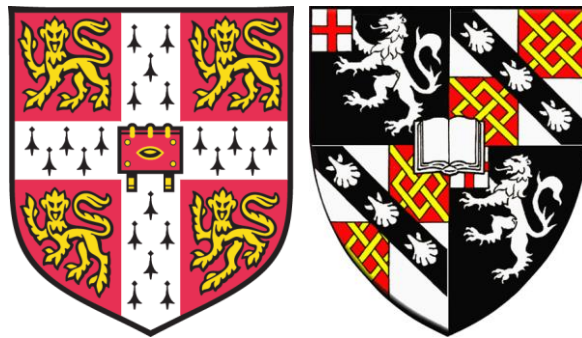


Understanding two-phase reaction processes in electrodes for Li-ion batteries

Hao Liu



Churchill College

University of Cambridge

June 2015

This dissertation is submitted for the degree of Doctor of
Philosophy

Declaration

This dissertation is the result of my own work and includes nothing which is the outcome of work done in collaboration except as declared in the Preface and specified in the text.

It is not substantially the same as any that I have submitted, or, is being concurrently submitted for a degree or diploma or other qualification at the University of Cambridge or any other University or similar institution except as declared in the Preface and specified in the text. I further state that no substantial part of my dissertation has already been submitted, or, is being concurrently submitted for any such degree, diploma or other qualification at the University of Cambridge or any other University of similar institution except as declared in the Preface and specified in the text

This dissertation does not exceed the regulation length of 60,000 words, including tables, bibliography and appendices, but excluding photographs and diagrams.

*Dedicated to my parents, Qingmin Liu and Fei Gao,
and my wife, Jingchen Hu,
who have inspired me to be a better person*

Acknowledgement

My greatest gratitude goes to my supervisor, Prof. Clare P. Grey, who has guided me through every obstacle during my PhD. She has been very supportive and always encourages me to experiment with new ideas and methods, especially when there are setbacks. She is a role model that teaches me what it takes to be a good scientist. It is truly a privilege to have been able to study with her as a PhD student.

This thesis could not have been finished without the generous help that I have received from other members of the group. I would like to thank Fiona Strobridge for many fruitful discussions on LiFePO_4 and her kind help with proofreading the reports, proposals, papers and thesis I have written. I want to thank Xiao Hua, Phoebe Allan, Sylvia Britto, Ieuan Seymour and Wei Meng for keeping me company on various trips to synchrotron facilities. My thanks also go to Rosa Robert, Elizabeth Castillo and Matthew Dunstan for Rietveld refinement related discussions. I frequently turned to Lina Zhou and Oliver Pecher for help with NMR experiments, and I owe them a great deal for helping me getting through most of my NMR sessions. Besides, Michal Leskes, Elodie Salager, John Griffin, Nicole Trease, Gunwoo Kim, Yunxu (Ben) Zhu, Yanyan Hu and Andy Pell were always willing to troubleshoot any NMR problems I had, for which I am very thankful. I want to thank Tao Liu for taking the SEM pictures of many of my samples and Michael Gaultois for kindly proofreading my thesis chapters. I also want to extend my thanks to Zigeng Liu, Hao Wang, Derek Middlemiss, Alex Forse, Luke Sperrin, Amy King, Raphaële Clément and Shou-hang Bo.

It has been a great learning experiment for me to have collaborated with people of different backgrounds. I would like to thank Olaf Borkiewicz, Gregory Halder, Kamila Wiaderek, Karena Chapman and Peter Chupas for indispensable assistance during my beam time at the APS. Bernardo Orvananos, Min-Ju Cho, Rahul Malik, Aziz Abdellahi, Raul Enrique, Hui-Chia Yu, Katsuyo Thornton and Gerbrand Ceder have offered invaluable insights on the theoretical and modelling aspects of LiFePO_4 , so I want to thank them for this. I would also like to thank Laurence Croguennec and her students for kindly providing us with the LiVPO_4F sample.

Last but not least, I am indebted to my lovely wife, Jingchen Hu, who brings so much joy and happiness to my life. Her encouragement and support have carried

me through the difficult times of my PhD. Besides, I want to thank my parents for their continuing care and support.

Publications

The material in Chapter 3 is based on the work that is in preparation for the following paper:

Hao Liu, Min-Ju Choe, Raul Enrique, Bernardo Orvananos, Hui-Chia Yu, Katsuyo Thornton, Clare P. Grey, “Li isotope exchange process of LiFePO₄ investigated by NMR and simulation”, in preparation

The material in Chapter 4 is based on the work that was published in the following paper:

Hao Liu, Fiona C. Strobridge, Olaf J. Borkiewicz, Kamila M. Wiaderek, Karena W. Chapman, Peter J. Chupas, Clare P. Grey, “Capturing metastable structures during high-rate cycling of LiFePO₄ nanoparticle electrodes”, *Science* 344, 1252817 (2014)

The material in Chapter 5 is based on the work that is in preparation for the following paper:

Hao Liu, Olaf J. Borkiewicz, Kamila M. Wiaderek, Peter J. Chupas, Karena W. Chapman, Clare P. Grey, “In situ X-ray diffraction studies of the high-rate charge and discharge processes of anatase TiO₂ at room and elevated temperatures”, in preparation

Understanding two-phase reaction processes in electrodes for Li-ion batteries

Summary

The occurrence of a phase separation, which induces substantial structural rearrangements and large volume changes, is generally considered to limit the high rate application of any battery electrode material. Contrary to this perception, nanoparticulate LiFePO_4 exhibits exceptionally high rates although the large Li miscibility gap in the Li-composition phase diagram dictates that delithiation takes place by a kinetically limited nucleation and growth process. It remains controversial as to whether the delithiation process is fundamentally different than expected from thermodynamics. This dissertation is set out to resolve this controversy and explore the implications in the (de)lithiation process of other phase separating electrode materials, such as TiO_2 and LiVPO_4F .

In this dissertation, LiFePO_4 is treated as the model compound that exemplifies the issues of Li diffusion and phase transitions in phase separating electrode, where a second phase is formed upon Li extraction/insertion. Li diffusion in LiFePO_4 was examined via a cation exchange process between ^6Li and ^7Li ions. The results indicate a single-file diffusion for Li along the diffusion channel, yet the Li diffusion was found to be rapid enough to allow for fast delithiation.

The phase transition process of LiFePO_4 nanoparticles was investigated by *in situ* synchrotron X-ray powder diffraction (XRD). At high cycling rates, the transition between LiFePO_4 ($Pnma$) and FePO_4 ($Pnma$) was found to proceed continuously via metastable solid solution phases, instead of a phase separation. Phase transition through this facile non-equilibrium path is thought to be essential in realising the high rate capability of nanoparticulate LiFePO_4 .

To explore the availability of the non-equilibrium continuous phase transition path in other materials, the (de)lithiation processes of anatase TiO_2 and LiVPO_4 at high cycling rates were also examined with *in situ* synchrotron XRD. Phase separation was found to occur, even at high rates, for transitions TiO_2 ($I4_1/amd$) \rightarrow $\text{Li}_{0.5}\text{TiO}_2$ ($Imma$) and $\text{Li}_{0.67}\text{VPO}_4$ ($P-1$) \rightarrow VPO_4 ($C2/c$), where the two end member phases adopt different, albeit group-subgroup related, symmetries. As with LiFePO_4 , a continuous phase transition was observed during the high rate cycling of LiVPO_4F ($P-1$) \rightarrow $\text{Li}_{0.67}\text{VPO}_4\text{F}$ ($P-1$), where both phases adopt the same symmetry.

Table of Contents

1	Introduction	1
1.1	Motivation	1
1.2	Introduction to rechargeable Li-ion batteries	2
1.3	Thermodynamics of Li-ion batteries	4
1.4	Issues of phase separating electrode: the case of LiFePO_4	6
1.4.1	Structure, thermodynamic and electrochemistry of LiFePO_4	6
1.4.2	The (de)lithation mechanism of $(\text{Li})\text{FePO}_4$	9
1.4.3	Li diffusivity: local migration vs. long range diffusion	12
1.5	Phase transition in phase separating electrodes.....	14
1.6	Objective	15
2	X-ray powder diffraction and nuclear magnetic resonance spectroscopy	17
2.1	X-ray powder diffraction (XRD).....	17
2.1.1	Position and intensity of a Bragg reflection.....	17
2.1.2	Broadening due to finite crystal size and lattice distortion	19
2.1.3	Diffraction peak profile deconvolution.....	22
2.1.4	Structure and microstructure refinement.....	23
2.1.5	Scattering by distorted domains	24
2.1.6	<i>In situ</i> synchrotron XRD	25
2.2	Nuclear magnetic resonance (NMR) spectroscopy	27
2.2.1	The basics of NMR spectroscopy	27
2.2.2	Chemical shift and solid state NMR spectroscopy	29
2.2.3	Li NMR of LiFePO_4	30
3	Determination of the Li tracer diffusivity in LiFePO_4 from Li isotope exchange experiment.....	33
3.1	Introduction	33
3.2	Theory	35

3.2.1	Ion exchange for LiFePO ₄	35
3.2.2	Relationship between tracer exchange and isotopic abundance	36
3.3	Experimental method	39
3.3.1	Materials synthesis and preparation.....	39
3.3.2	Li solid state NMR measurement	40
3.3.3	X-ray powder diffraction and Rietveld refinement.....	42
3.4	Results and discussion.....	43
3.4.1	Sample characterisation	43
3.4.2	The evolution of the ⁶ Li abundance of LiFePO ₄ under soaking condition 48	
3.4.3	Tracer exchange	52
3.4.4	Single-file mobility and tracer diffusivity of Li.....	55
3.5	Conclusion.....	58
4	Phase transition of LiFePO ₄ nanoparticles during high rate cycling	59
4.1	Introduction	59
4.2	Experimental methods.....	61
4.2.1	Materials synthesis and characterisation.....	61
4.2.2	<i>In situ</i> X-ray diffraction measurement.....	61
4.2.3	Whole powder pattern fitting method of the <i>in situ</i> X-ray diffraction data 62	
4.2.4	Simulations of XRD reflection profile.....	64
4.3	Results and Discussion.....	64
4.3.1	Material characterisation.....	64
4.3.2	Intermediate Li _x FePO ₄ phases induced at high currents	66
4.3.3	Continuous distribution of Li _x FePO ₄ phases beyond the thermodynamic miscibility gap.....	70
4.3.4	Proof of the metastable nature of the Li _x FePO ₄ phase.....	76
4.3.5	Verification of the whole pattern fitting method	78

4.3.6	Discussion	79
4.4	Conclusion.....	80
5	Phase transition of anatase TiO ₂ at high rates	81
5.1	Introduction	81
5.2	Experimental methods	83
5.2.1	Materials and electrode preparation	83
5.2.2	<i>In situ</i> XRD measurement.....	83
5.3	Results and Discussion	84
5.3.1	Particle size and electrochemistry of anatase TiO ₂	84
5.3.2	Phase evolution of anatase TiO ₂ under various conditions.....	86
5.3.3	Microstructural evolution of anatase TiO ₂ particles during discharge.....	96
5.3.4	Discussion on the nature of the instantaneous phase transition of 25 nm TiO ₂ particles	106
5.4	Conclusion.....	107
6	Phase transitions of LiVPO ₄ F at high rates of charge.....	109
6.1	Introduction	109
6.2	Experimental	111
6.2.1	Materials and electrode preparation.....	111
6.2.2	<i>In situ</i> XRD measurement.....	111
6.3	Results and Discussion	111
6.3.1	Electrochemistry upon charging LiVPO ₄ F	111
6.3.2	<i>In situ</i> XRD measured during 1 C, 2 C and 5 C charging of LiVPO ₄ F.....	113
6.3.3	Quantifying the phase transition	118
6.3.4	Discussion on the possibility of a continuous phase transition.....	121
6.4	Conclusion.....	122
6.5	Appendix	123
7	Conclusions	125

8 Bibliography 127

List of Figures

Figure 1.1 Comparison of the gravimetric power and energy densities for different rechargeable battery technologies (figure reproduced with permission from reference [2]).	1
Figure 1.2. The construction of a lithium-ion battery. The arrows indicate the direction of the charge carriers' movement.	2
Figure 1.3. Illustration of the intercalation mechanism for the LiCoO ₂ /graphite battery. Li ions are removed from the layers between the CoO ₂ sheets and intercalated into the graphite layers during charge.	3
Figure 1.4. The relationship between the Gibbs free energy and the cell voltage. (A) and (B) illustrate the case where a constant voltage plateau is observed, while (C) and (D) illustrate the case where the voltage changes with the Li composition.	5
Figure 1.5. (A) The lithiation process when two phases coexist. The reaction proceeds by varying the relative fraction of the two phases via propagation of the phase boundary. (B) The lithiation process when the particle remains as a single-phase. Li ions progressively occupy the vacant sites in the lattice by forming a solid solution with the host lattice M.	6
Figure 1.6. The crystal structure of LiFePO ₄ . The edges of the unit cell are shown by the black lines. The green, red, brown and purple spheres represent Li, O, Fe and P atoms, respectively.	7
Figure 1.7. The phase diagram of Li _x FePO ₄ as a function of temperature and Li composition [12].	8
Figure 1.8 Typical charge and discharge voltage profiles of LiFePO ₄ . Voltage is referenced against the redox potential of Li ⁺ /Li ⁰ .	8
Figure 1.9. The phase boundary is formed in the <i>bc</i> plane and propagates in the direction perpendicular to the Li diffusion (in the direction of the <i>a</i> -axis).	9
Figure 1.10. The Gibbs free energy diagram as a function of the Li composition assuming ΔG_A is negligible (red) and significant (green). The red curve indicates the energy of Li _x FePO ₄ if it is maintained as a single homogeneous phase. The black line indicates the energy as a linear combination of $G(x_a)$ and $G(x_b)$, i.e. the case when the particle size is big or the phase separation occurs between and not within particles. The green curve indicates the energy for nanoparticles where phase separation occurs within particles (intra-particle), introducing an additional interfacial energy ΔG_A . The	

extent of the solid solution range is exaggerated for clarity. In reality, x_α and x_β are close to 1 and 0, respectively.	10
Figure 1.11. Illustration of (A) the intra-particle vs. (B) the inter-particle phase separation in a multi-particle system. α and β are used to denote two different phases.	12
Figure 1.12. (A) A single Li-Fe antisite defect (red ellipse) and the possible paths (dashed black curves) for Li crossover between channels. (B) Li trapped (shaded region) between two Fe atoms in the diffusion channel.	13
Figure 2.1 Illustration of diffraction by Bragg's law. The incident and diffracted beams are denoted by black and red arrow lines, respectively. d_{hkl} is the interplanar spacing, and θ is the scattering angle. s_0 and s are the unit vectors of the incident and diffracted beam, respectively.	17
Figure 2.2 (A) Diffraction by a randomly oriented crystalline powder sample (yellow dots) produces a series of cones of diffracted beams (red), with semi-vertex angles of 2θ . (B) Variation of the diffraction intensity against 2θ for a crystalline powder sample.	18
Figure 2.3. Effects of strain and microstrain on a Bragg reflection. (A) Peak profile free from stain and microstrain. (B) Peak profile due to strain only. (C) Peak profile due to microstrain only.	21
Figure 2.4. Three profiles that are involved in the convolution of the Bragg reflection profile. $f(2\theta)$ is the profile solely due to various imperfections in the sample. $g(2\theta)$ is the instrumental profile for an incident X-ray beam of double wavelengths. $h(2\theta)$ is the profile that is actually measured by the diffractometer.	23
Figure 2.5. A typical setup for <i>in situ</i> XRD at a synchrotron. Either area or strip detector is used for fast data acquisition. A dissection of the electrochemical cell is also shown.	26
Figure 2.6. Diffraction geometry with an area detector. The sample is placed at point O, and the area detector is placed at a distance L_{sd} from the sample. The detector plane is perpendicular to the incident X-ray beam. The width of a pixel on the detector is w and subtends a small angle σ at the sample. The red lines trace the X-ray beam.	27
Figure 2.7. Illustration of a simple NMR experiment. (A) An r.f. pulse rotates the net magnetisation \mathbf{M} (along z) by $\pi/2$ into the y axis, and the magnetisation will precess in the transverse plane (x - y plane). (B) The oscillating signal acquired by the coil when the magnetisation precesses about the z direction in the transverse plane. (C) The NMR	

spectrum is obtained by FT of the signal in time domain. Figure modified from reference [68]	28
Figure 2.8. Illustration of the orientation dependence of the chemical shift. The crystals highlighted in green, yellow and red, have different orientations and giving rise to peaks indicated by the respective colour. Figure modified from reference [71].	30
Figure 2.9 (A) Schematic illustration of magic angle spinning (MAS), where a powder sample spins about the axis that makes an angle of 54.7° (“magic angle”) to the external magnetic field (\mathbf{B}^0). (B) The ^{31}P MAS NMR spectrum at a spinning speed of 40 kHz in comparison with the static NMR spectrum of LiFePO_4 powder. The spinning side bands are indicated by stars. Figure adapted, with permission, from my colleague Dr. Oliver Pecher.	30
Figure 2.10. The red spectrum shows the fully excited ^7Li NMR spectrum of a LiFePO_4 powder. When a long r.f. pulse is used, only part of the spectrum will be excited as illustrated schematically by the blue spectrum. Figure adapted, with permission, from my colleague Dr. Oliver Pecher.....	31
Figure 3.1 The edge sharing LiO_6 octahedral chain of LiFePO_4 . The blue and red spheres represent Li and O, respectively. The wavy dashed green curve indicates the Li diffusion path.....	34
Figure 3.2 The distributions of Li in a single channel that has (red) and has not (cyan) been exchanged with the Li in the electrolyte at time t and $t+\Delta t$ after the start of exchange. The tracer exchange γ defined as the fraction of ions in the channel that have undergone exchange, i.e. the ratio between the length of the red region and the length of the entire channel (red + cyan). The position of a Li in the channel is normalised against the channel length and is described by the dimensionless fractional coordinate x	37
Figure 3.3 A sealed NMR tube containing the wrapped ^6Li -enriched LiFePO_4 powder immersed in 1 M LiPF_6 in EC and DMC electrolyte solution.	42
Figure 3.4 XRD patterns of the pristine (as-synthesised) ^6Li -enriched LiFePO_4 particles synthesised in (A) EG and (B) PEG. Calculated diffraction patterns for the Rietveld-refined structures are shown in red. The difference (observed – calculated) curves are shown in grey. The green ticks indicate the positions of the Bragg reflections.....	45

Figure 3.5 SEM images showing the LiFePO ₄ crystals synthesised in (A) EG and (B) PEG.	47
Figure 3.6 Histogram of the measured thickness along the short axis determined from 26 LiFePO ₄ crystals synthesised in PEG.	47
Figure 3.7 The ⁶ Li static NMR spectra of ⁶ Li-enriched Mircon pristine LiFePO ₄ particles in DMC solvent. The spectrum in red is obtained by summing up the ⁶ Li static spectra acquired at carrier frequencies of 50 kHz (~ 1130 ppm), 0 kHz, -50 kHz and -100 kHz (~ -2270 ppm).	48
Figure 3.8 <i>In situ</i> static ⁶ Li NMR spectra measured with spin echo for the pristine (A) Nano- and (C) Micron-plate LiFePO ₄ powder samples. $\pi/2$ pulses of 11.25 μ s and 7 μ s are for the Nano- and Micron-plate samples, respectively. Image plots of the <i>in situ</i> ⁶ Li NMR spectra collected while LiFePO ₄ particles are immersed in the electrolyte for the (B) Nano- and (D) Micron-plate samples, the graphs next to the image plots are the corresponding integrated spectral intensities. The acquisition for the first spectrum started at 15 min after LiFePO ₄ had been immersed in the electrolyte.	50
Figure 3.9 The ⁶ Li abundance of different LiFePO ₄ samples as a function of immersion time of the ⁶ Li-enriched LiFePO ₄ particles in the LiPF ₆ electrolyte solution.....	52
Figure 3.10 The tracer exchange curves for the (A) Nano- and (B) Micron-plate samples presented in logarithmic scale. The green curves are the best fit with $\gamma(t)=At^{1/4}$ to the lower limit data with A as the only fitting parameter. The solid red curves are the best fit with (3.3), which has a slope equal to 0.5 in logarithmic scale.....	54
Figure 3.11. Average single-file mobility factor F against the Li occupancy Θ . The blue curve is the best fit by $F = B(1 - \Theta)/\Theta$ with $B = 2.6 \pm 0.5 \times 10^{-13} \text{ cm}^2 \text{ s}^{-1/2}$	57
Figure 3.12. The blue curve shows the relationship between the time taken to remove 95 % Li in the channel and the channel length. The Li diffusivity is taken as $2.4 \times 10^{-10} \text{ cm}^2 \text{ s}^{-1}$	58
Figure 4.1 The X-ray powder diffraction pattern of as-synthesised LiFePO ₄ powder (wavelength is 0.39996 Å).	65
Figure 4.2 (A) Scanning electron microscope (SEM) image of as-synthesised LiFePO ₄ powder. (B) Particle size distribution based on an analysis of 95 particles observed in the SEM images.	66
Figure 4.3 <i>In situ</i> XRD patterns during galvanostatic charge and discharge at a rate of 10 C. (A) The image plot of diffraction patterns for (200), (211), (020), and (301)	

reflections during the first five charge-discharge cycles. The horizontal axis represents the selected 2θ regions, and time is on the vertical axis. The diffraction intensity is colour coded with the scale bar shown on top. The corresponding voltage curve is plotted to the right. LFP, LiFePO_4 ;FP, FePO_4 ; a.u., arbitrary units. (B) Selected individual diffraction patterns during the first two cycles stacked against the voltage profile. The baseline is represented by horizontal dashed gray lines. Black vertical lines mark the positions of LiFePO_4 peaks at the start of reaction; red vertical lines mark the position of FePO_4 peaks formed during the first cycle. 67

Figure 4.4 *In situ* X-ray diffraction pattern of LiFePO_4 under different electrochemical cycling conditions. (A), (B) and (C) show the second galvanostatic cycle at 5 C, 10 C, and 20 C, respectively. (D) shows the evolution of the charge-relax experiment, where a current equivalent to 10 C is applied for 90 s, equivalent to 0.25 Li extraction per f.u. of LiFePO_4 , (highlighted with the horizontal pink bands) followed by an open-circuit relaxation of 10 mins. The dashed white lines indicate the peak positions of the LiFePO_4 (LFP) and FePO_4 (FP) phases at the end of the second relaxation period, which are used to draw the boundaries of the miscibility gap as determined from the (200) and (301) reflections..... 69

Figure 4.5 Development of peak asymmetry for the reflections from LiFePO_4 (LFP). The (200), (211)/(020), and (301) reflections from LiFePO_4 asymmetrically broaden towards higher 2θ angles, while the (101) reflection asymmetrically broadens towards lower angles. The same reflections from FePO_4 (FP) are marked by dashed lines. ... 70

Figure 4.6 Typical whole powder pattern fitting results. This pattern is taken at 720 s, corresponding to the global composition of $\text{Li}_{0.43}\text{FePO}_4$. (A) Only symmetrical peak profile is used. (B) Symmetrical peak profiles convoluted with the hkl-dependent exponential function..... 71

Figure 4.7 Refinement result of the scale factors of the LiFePO_4 and FePO_4 phases during the first two cycles. 72

Figure 4.8 Contour plot of refined LiFePO_4 and FePO_4 lattice parameter distributions as a function of time during the first two charge-discharge cycles at a 10 C rate. The relative population density is coded in colour, with the lowest contour corresponding to 7.5 % of the intensity at the position indicated by the black solid circle. The corresponding voltage profile is shown at the bottom. The dashed lines mark the positions where lattice parameter distributions are most asymmetrical..... 73

Figure 4.9 Simulated (200) reflection profiles for different interface widths between LiFePO₄ (LFP) and FePO₄ (FP). The left panel compares the simulated profiles with the experimentally measured one (top). The right panel shows the corresponding Li composition (shaded area) and the *a* lattice parameter profiles (solid black line) used in the simulation for various interfacial widths. The particle dimension along the *a*-axis is 186 nm, and the interface is positioned in the centre. (A) shows the result based on a discrete Li composition profile (mechanical strain only). (B) shows the result based on a continuous Li compositional variation..... 75

Figure 4.10 Contour plot of refined LiFePO₄ and FePO₄ lattice parameter distributions as a function of time during the intermittent charging experiment. The application of a 10 C current pulse for 90 s (corresponding to the removal of 0.25 Li per LiFePO₄ formula unit), is followed by a 10 min relaxation in open circuit mode. The low FePO₄ phase fraction during the first relaxation period is responsible for the greater fluctuation in the lattice parameters. The relative population density is colour coded (see top). The lowest contour is drawn at 7.5% intensity of the maximum population density for the FePO₄ phase at the end of the second relaxation period (indicated by the solid black circles). In the bottom graph, voltage (red lines) and current (blue lines) are plotted as a function of time..... 77

Figure 4.11 Phase population distribution obtained from multi-peak fitting. (A) shows the result for (200) reflection and (B) for the (301) reflection. 79

Figure 5.1. The crystal structures of (A) tetragonal α -TiO₂, (B) orthorhombic β -Li_{0.5}TiO₂ and (C) tetragonal γ -LiTiO₂. The half-filled green/white spheres denote sites which are randomly occupied by either Li or vacancy with equal probability..... 82

Figure 5.2. Typical voltage profile of anatase TiO₂ during discharge. The kinetically restricted lithiation to form γ -LiTiO₂ becomes more prominent with decreasing particle size. Figure adapted from reference [119]. 82

Figure 5.3 SEM images obtained for as-purchased (A) 100 nm and (B) 25 nm anatase TiO₂ samples. Pictures were taken by Dr. Tao Liu from our group. 85

Figure 5.4 Voltage profiles for the discharge-charge cycles performed during the *in situ* XRD experiment. (A) Room temperature (RT) and (B) 80 °C cycling for 100 nm particles. (C) Room temperature and (D) 80 °C cycling for 25 nm particles. 86

Figure 5.5 Image plots showing the time evolution of the *in situ* XRD patterns at *room temperature* for (A-C) 100 nm and (D-F) 25 nm TiO₂ particles at various cycling rates.

The intensity scale is shown by the colour bar. The electrochemical profile is shown in the graph to the right of each image. The 2θ region for the (024) reflection of α -TiO₂ and the (204) reflection of β -Li_{0.5}TiO₂ is shown. The (204) reflection of β -Li_{0.5}TiO₂ is barely visible in B and C due to the formation of a very limited amount of β -Li_{0.5}TiO₂, and the equally spaced intensity contours (11 levels in total) are drawn in black to aid visual inspection. 88

Figure 5.6 Image plots showing the time evolution of the *in situ* XRD patterns collected at *elevated temperature* ($\sim 80^\circ\text{C}$) for (A-C) 100 nm and (D-F) 25 nm TiO₂ particles at various cycling rates. The intensity scale is shown by the colour bar. The electrochemical profile is shown in the graph to the right of each image. The 2θ region for the (024) reflection of α -TiO₂ and the (204) reflection of β -Li_{0.5}TiO₂ is shown. Equally spaced intensity contours (11 levels in total) are drawn in black in B, C and F to aid visual inspection. 89

Figure 5.7. Typical fitting results obtained from Rietveld refinement for *in situ* XRD patterns collected for (A) 100 nm and (B) 25 nm particles. The green ticks mark the Bragg reflection positions of the corresponding phases. The asterisks indicate the Bragg reflections due to Li metal. The insets show the magnified $16.5^\circ - 19^\circ$ and $27^\circ - 28^\circ$ 2θ regions. The regions not accounted for by the calculated curves are excluded from the refinement. The blue dots represent the measured intensity, red curves are the calculated intensities from the refined models and grey curves are the differences between the measured and calculated intensities. 90

Figure 5.8 The R_{wp} factors in the Rietveld refinements for (A) 100 nm and (B) 25 nm particles. RT is short for room temperature. 91

Figure 5.9 Lattice parameters of both α -TiO₂ (highlighted in yellow and labelled with the subscript α) and β -Li_{0.5}TiO₂ (highlighted in green and labelled with the subscript β) phases obtained from Rietveld refinements for both the room temperature (RT) and the 80°C discharge processes. 93

Figure 5.10 The lattice parameters of TiO₂, Li_{0.5}TiO₂ and LiTiO₂ as reported in reference [116]. Only the c lattice parameter varies linearly with x across the entire Li composition range. 94

Figure 5.11 Evolution of the Li composition in α -TiO₂ and β -Li_{0.5}TiO₂ for (A-B) 100 nm and (C-D) 25 nm particles during discharge. Room temperature (RT) results are shown in A and B, and elevated temperature experiments are shown in B and D. The

dashed grey lines indicate the positions for Li solubilities of 0.025 and 0.5, which are considered as the boundaries of the thermodynamic Li solubility[116]. The error bars are smaller than the symbols..... 94

Figure 5.12 Normalised scale factors (normalised against the scale factor of α -TiO₂ at the start of lithiation) for (A) 100 nm and (B) 25 nm particles as a function of the overall Li composition. (C) and (D) show the overall Li composition determined from XRD as a function of the overall Li composition determined from electrochemistry for 100 nm and 25 nm particles, respectively. The dashed grey lines have a slope of 1. RT represent room temperature. 96

Figure 5.13. The evolution of the FWHM of select reflections from both α -TiO₂ and β -Li_{0.5}TiO₂ (i-ii), the domain size determined from the FWHM of the (116) reflection for α -TiO₂ and the (011) reflection for β -Li_{0.5}TiO₂ (iii), and scale factor (iv) as a function of the overall inserted Li for 100 nm particles during discharge at cycle rates of (A) 1C, (B) 2C and (C) 5C at room temperature..... 99

Figure 5.14 The evolution of the FWHM of select reflections from both α -TiO₂ and β -Li_{0.5}TiO₂ (i-ii), the domain size determined from FWHM of the (116) reflection for α -TiO₂ and the (011) reflection for β -Li_{0.5}TiO₂ (iii), and scale factor (iv) as a function of the overall inserted Li for 100 nm particles during discharge at cycle rates of (A) 5C, (B) 10C and (C) 20C at 80°C..... 100

Figure 5.15 Typical peak fitting patterns for 100 nm particles during room temperature charge at cycles rates of (A-B) 2 C and (C) 5 C. Blue dots are the experimental data, and red curves represent the overall fit. 100

Figure 5.16 Schematic illustration of the phase transition occurring in 100 nm anatase TiO₂ particles during high rate discharge. Lithiation proceeds firstly by a solid solution reaction in the α -TiO₂ phase (i) followed by the nucleation of β -Li_{0.5}TiO₂ (ii). The β -Li_{0.5}TiO₂ domains grow in size until the entire particle comprises a single phase (iii-iv). 101

Figure 5.17. The evolution of the FWHM of select reflections from both α -TiO₂ and β -Li_{0.5}TiO₂ (i-ii), the domain size determined from the FWHM of the (116) reflection for α -TiO₂ and the (011) reflection for β -Li_{0.5}TiO₂ (iii), and scale factor (iv) as a function of the overall inserted Li for 25 nm particles during discharge at cycle rates of (A) 1C, (B) 2C and (C) 5C discharge at room temperature. 103

Figure 5.18. The evolution of the FWHM of select reflections from both α -TiO₂ and β -Li_{0.5}TiO₂ (i-ii), the domain size determined from the FWHM of the (116) reflection for α -TiO₂ and the (011) reflection for β -Li_{0.5}TiO₂ (iii), and scale factor (iv) as a function of the overall inserted Li for 25 nm particles during discharge at cycle rates of (A) 5C, (B) 10C and (C) 20C discharge at 80 °C..... 104

Figure 5.19 Representative peak fitting patterns for 25 nm particles during charge at cycle rates of (A-B) 2 C at room temperature and (C-D) 5 C at 80°C..... 105

Figure 5.20. Schematic illustration of the phase transition occurring in 25 nm anatase TiO₂ particles during high rate discharge. Lithiation proceeds firstly by a solid solution reaction in the α -TiO₂ phase (i) followed by the sequential (particle-by-particle) transformation from α -TiO₂ to β -Li_{0.5}TiO₂ particles (ii-iv). 105

Figure 5.21. Illustration of the change in Gibbs free energy for various phase transition paths. The solid black line represents a continuous structural transition (second-order phase transition), and the critical point is marked by *O* (solid yellow circle). The dashed black line is the projected energy curve if there is no reduction to lower symmetry. The solid green line is the common tangent construction that determines the lowest possible energy of a system with a mixture of α -TiO₂ and β -Li_{0.5}TiO₂ not coexisting in the same particle. The solid red line is the modified energy of a system with a mixture of α -TiO₂ and β -Li_{0.5}TiO₂ separated by a phase boundary..... 107

Figure 6.1 The voltage profile during charge and discharge of LiVPO₄F at C/50. Two voltage plateaus (4.24 V and 4.28 V) are observed on charge while only one voltage plateau is observed on discharge. Figure reproduced from reference [129]. 110

Figure 6.2. The crystal structures of (A, B) LiVPO₄F and (C, D) VPO₄F. The structures in A and B are viewed from the side of the V-F-V chains while those in C and D are viewed along the chains. 110

Figure 6.3. (A) The electrochemical profile during charge (delithiation) of LiVPO₄F at 1 C, 2 C and 5 C, the inset shows the plateau region. (B) The dQ/dV (the first derivative of capacity, which is proportional to the number of Li extracted, with respect to voltage) plot for charging rates of 1 C, 2 C and 5 C. The “1 C smooth” in (A) is the smoothed voltage profile for 1 C charge by averaging over 50 adjacent data points, and its corresponding dQ/dV curve is shown as “1 C smooth” in (B). 113

Figure 6.4. *In situ* XRD patterns collected during the (A) 1 C, (B) 2 C and (C) 5 C charging of LiVPO₄F. Three 2 θ regions are selected to study the phase evolution. The

graphs on the right show the electrochemical profile at the respective rate. The dashed grey line in the electrochemical profile indicates the transition between the first and the second plateaus; no line is drawn for 1 C as there is no distinct low voltage plateau. The dashed white lines indicate the positions of the indicated reflections. LVPF, $\text{Li}_{0.67}\text{VPF}$ and VPF are abbreviations for LiVPO_4F , $\text{Li}_{0.67}\text{VPO}_4\text{F}$ and VPO_4F , respectively. 114

Figure 6.5 Individual *in situ* XRD patterns at different states of charge during (A) 1C, (B) 2C and (C) 5C charge. LVPF, $\text{Li}_{0.67}\text{VPF}$ and VPF are abbreviations for LiVPO_4F , $\text{Li}_{0.67}\text{VPO}_4\text{F}$ and VPO_4F , respectively. The number to the right of each pattern indicate the corresponding number of Li extracted per f.u. of LiVPO_4F 115

Figure 6.6 Typical fitting results for the $(1\bar{1}0)$ reflection of $\text{Li}_x\text{VPO}_4\text{F}$ (*P-I*). The blue dots represent the observed intensities, the red curves are the fitted profiles and the grey curves are the background. 120

Figure 6.7. (A) Contour plots of the $\text{Li}_x\text{VPO}_4\text{F}$ phase population extracted from fitting the $(1\bar{1}0)$ reflection profile during the charge at different rates. The spacing between two adjacent contour lines is equal to one tenth of the maximum density. The respective electrochemical profile is shown at the bottom. (B) Integrated intensities and (C) FWHMs of the $\text{Li}_x\text{VPO}_4\text{F}$ (Li_xVPF) (110) and the VPO_4F (VPF) (020), (021) and $(\bar{2}0\bar{2})$ reflections. (D) Voltage profiles during 1 C, 2 C and 5 C charging. 120

Figure 6.8 Typical peaking fitting results obtained for the (020), (021) and $(\bar{2}0\bar{2})$ reflections of VPO_4F and the (110) reflection for $\text{Li}_{0.67}\text{VPO}_4\text{F}$. The blue dots are the observed intensities, the red curves are the fitted profiles, the green curves show the individual profiles and the grey curve is the background. 121

List of Tables

Table 3.1 ^6Li and ^7Li abundance of all Li containing species at the onset of the ion exchange experiment ($t = 0$, i.e. no contact between the LiFePO_4 powder and the LiPF_6 electrolyte).....	42
Table 3.2 LiFePO_4 lattice parameters obtained from the Rietveld refinement for various samples.	45
Table 3.3 Literature unit cell volumes obtained for nearly stoichiometric LiFePO_4 .	46
Table 3.4 The volume weighted size (determined by Scherrer formula) of the sample synthesised in EG along the a , b , c crystal axes.....	47
Table 3.5 The ^6Li abundance of LiFePO_4 measured for different immersion time in the LiPF_6 electrolyte (natural ^6Li and ^7Li abundance) by the <i>ex situ</i> NMR measurement.	51
Table 3.6 Coefficients A obtained from fitting the tracer exchange curves with $\gamma(t) = A \cdot t^{1/4}$	54
Table 3.7. The single-file mobility factors obtained from the fitting coefficients.....	57

List of Abbreviations

0-D	Zero dimensional
1-D	One dimensional
2-D	Two dimensional
A_m	Molar interfacial area
ADP	Atomic displacement parameter
AMPIX	Argonne's multi-purpose in situ X-ray
B^0	External magnetic field
c	Speed of light
C_{ij}	Refined coefficients of the symmetrised spherical harmonics
CSA	Chemical shift anisotropy
CV	Cyclic voltammetry
D	Tracer diffusivity
\tilde{D}	Chemical diffusivity
D'	Inter diffusion coefficient
D_{cm}	Centre of mass diffusivity
D_{Li}	Li tracer diffusivity
DMC	Dimethyl carbonate
d_{hkl}	Interplaner spacing of the fictitious (hkl) crystal plane
E^0	Voltage against the standard hydrogen electrode
E	Energy
e	Elementary charge
E_{cell}	Voltage of the battery cell
EC	Ethylene carbonate

EG	Ethylene glycol
EIS	Electrochemical impedance spectroscopy
F	Single file mobility factor
\mathcal{F}	Faraday's constant
f	Diffraction peak profile due to sample
f_j	Atomic structure factor of j th atom
f_i	${}^6\text{Li}$ abundance of the electrolyte
f_s	${}^6\text{Li}$ abundance of LiFePO_4
\tilde{f}_s	Local ${}^6\text{Li}$ abundance profile of LiFePO_4
F_{hkl}	Structure factor of the (hkl) Bragg reflection
F_m	Structure factor of the m th unit cell
FID	Free induction decay
FP	FePO_4
FT	Fourier transform
f.u.	Formula unit
G	Gibbs free energy
g	Diffraction peak profile due to instrument
GITT	Galvanostatic intermittent titration technique
H_D	Full width at half maximum due to lattice distortion
H_G	Full width at half maximum of a Gaussian peak
H_L	Full width at half maximum of a Lorentzian peak
H_S	Full width at half maximum due to finite crystal size
H_{total}	Full width at half maximum due to both crystal size and lattice distortion
h	Observed diffraction peak profile

I	Nuclear spin quantum number
I_0	Incident X-ray beam intensity
I_{inter}	Interpolated intensity
K	Shape factor in Scherrer equation
k	Boltzmann constant
L	Volume weighted column length
l	Distance between successive jumps
L_0	Thickness of a plane sheet/Length of the diffusion channel
L_{sd}	Sample-to-detector distance
$\langle L_{hkl} \rangle_V$	Volume averaged column length along the (hkl) direction
LFP	LiFePO ₄
LP	Lorentz-polarisation factor
LIB	Li-ion batteries
LVPF	LiVPO ₄ F
M	Magnetisation
M_l	Moles of Li in the electrolyte
M_m	Molar mass
M_s	Moles of Li in the diffusion channel
m_e	Mass of electron
MAS	Magic angle spinning
NMR	Nuclear magnetic resonance
N	Number of unit cells
NPD	Neutron powder diffraction
PEG	Polyethylene glycol

PITT	Potentiostatic intermittent titration technique
PTEF	Polytetrafluoroethylene
r.f.	Radio frequency
RT	Room temperature
SEI	Solid electrolyte interface
SEM	Scanning electron microscope
T	Temperature
t	Time
T_{abs}	Absorption factor
T_c	Transition temperature
V	Unit cell volume
V_{exp}	Measured unit cell volume of LiFePO_4
V_{FP}	Unit cell volume of stoichiometric FePO_4
V_{LFP}	Unit cell volume of stoichiometric LiFePO_4
V_m	Molar volume
VPF	VPO_4F
Y_{ij}	Symmetrised spherical harmonics
w	Pixel width of the two-dimensional detector
XRD	X-ray powder diffraction

List of Symbols

μ	Chemical potential
γ_{int}	Interfacial energy
γ_{G}	Gyromagnetic ratio
γ_{a}	Thermodynamic activity
γ	Tracer exchange
Γ	Li Jump frequency
\hbar	Reduced Planck's constant
ν	Precession frequency of the nuclear spin
ν_{ref}	Precession frequency of the nuclear spin in a reference substance
δ	Chemical shift
σ	Angle subtended at the sample by the width of the pixel
τ_{rf}	Length of the 90° radio frequency pulse
ω	Excitation width of the radio frequency pulse
ω^0	Larmor frequency
Ω	Volume of the crystal
$\Delta\varphi$	Phase difference between two X-ray waves
λ	X-ray wavelength
ρ	Electron density
θ_{hkl}	Position of the hkl Bragg reflection
Θ	Site occupancy of the diffusion channel
ε	Refined strain parameter
ε_{app}	Apparent strain

ε_m Refined asymmetry parameter

ε_{\max} Maximum strain

η Order parameter

1 Introduction

1.1 Motivation

The importance of rechargeable Li-ion batteries (LIB) has been demonstrated by its indispensable role in powering portable electronics, such as smart phones and laptops. The rechargeable LIB technology prospered in the early 1990s when it was first commercially introduced by SONY. The success of LIB is a result of its high energy and power density in comparison to other competing batteries technologies, as shown in Figure 1.1. The high energy density is derived from the very negative redox potential of Li^+/Li^0 ($E^0(\text{Li}^+/\text{Li}^0) = -3.04 \text{ V}$ vs standard hydrogen electrode), and the high power density is attributed to the small ionic radius of Li, allowing for fast diffusion. Recently, as part of a concerted effort in reducing greenhouse gas emissions, the development of electrical vehicles to replace existing hydrocarbon fuel vehicles has called for high energy and power density energy storage technology, for which rechargeable LIB has been considered as a promising solution[1]. The energy density is determined by the capacity (the amount of charge that can be released/stored per unit weight) of the specific compounds used as the electrode materials in rechargeable LIB, and further improvement relies on the discovery of new compounds and/or chemistries; whereas the power density (the amount of energy that can be released/stored per unit time) can vary substantially for the same compound and is strongly dependent on the electrode kinetics, for example, Li ion diffusion. Therefore, it is imperative to understand the rate limiting kinetic factors to improve the power density of existing materials and facilitate the search for new ones.

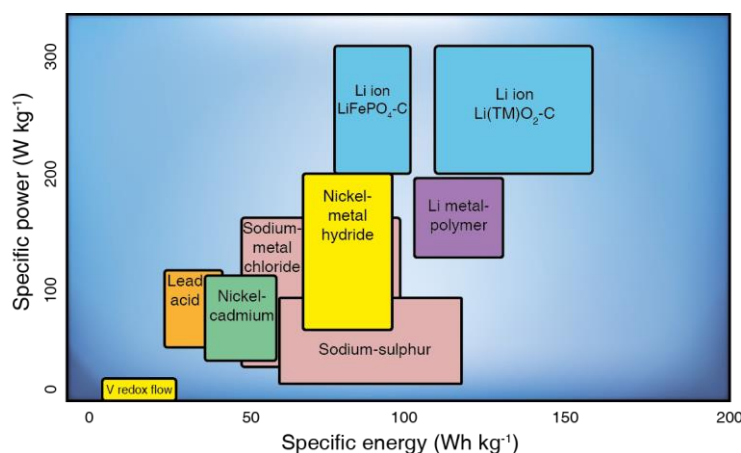


Figure 1.1 Comparison of the gravimetric power and energy densities for different rechargeable battery technologies (figure reproduced with permission from reference [2]).

1.2 Introduction to rechargeable Li-ion batteries

A battery consists of electrochemical cells that convert chemical energy into electrical energy through a redox reaction between the two electrodes. A battery is composed of three essential components: the cathode (positive electrode), the anode (negative electrode), and the electrolyte, as shown in Figure 1.2. In a rechargeable LIB, upon discharge, the cathode is reduced and the anode is oxidised whilst lithium ions are carried from the anode to the cathode by the electrolyte and the electrons travel from the anode to the cathode through the external circuit, which drives the electrical appliances. This process is reversed during charge. The reversible reactions occurring at both electrodes can take place via different mechanisms, such as conversion[3], alloying[4] and intercalation (insertion), with intercalation being the most common reaction pathway.

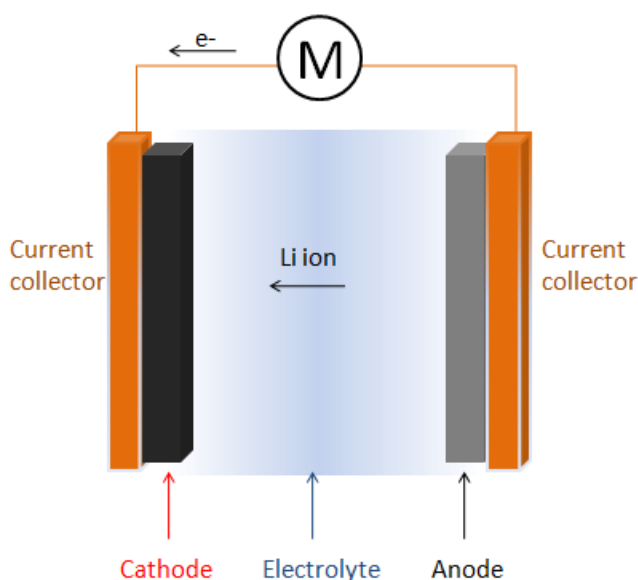
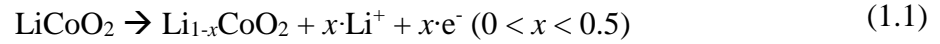


Figure 1.2. The construction of a lithium-ion battery. The arrows indicate the direction of the charge carriers' movement.

The intercalation mechanism is usually found in materials of layered structures or open channels that can accommodate Li^+ diffusion. The model example of intercalation materials is demonstrated by LiCoO_2 and graphite, which are used as the cathode and anode, respectively. They were used in the first LIB and still dominate in the commercial LIB today. Figure 1.3 illustrates the charging process, Li ions sandwiched between the CoO_2 layers are extracted and Co^{3+} is oxidised while Li ions are intercalated into the empty interplanar space between the layers in graphite. The reactions occurring at the cathode (LiCoO_2) and the anode (graphite) during charge are as follows:



Only 0.5 Li is able to be reversibly extracted from LiCoO_2 due to a structural transformation from the hexagonal to monoclinic symmetry upon further Li extraction[5].

The charge storage capacity is commonly used to compare different electrode materials. The theoretical capacity is defined as the amount of charge that can be utilised electrochemically per unit weight and is determined by

$$\text{Theoretical capacity} = \frac{\Delta x \cdot \mathcal{F}}{M_m} [\text{Coulomb/g}] = \frac{1000}{3600} \times \frac{\Delta x \cdot \mathcal{F}}{M_m} [\text{mAh/g}] \quad (1.3)$$

where Δx is the number of Li available for electrochemical insertion/extraction per formula unit of the corresponding compound, \mathcal{F} is the Faraday's constant (96,485 C/mol), and M_m is the molar mass of the compound in gram. The numerical factor 1000/3600 converts the value in the commonly quoted units of mAh/g.

The applied charge/discharge current is usually quoted in terms of the "C" rate. A rate of "C/n" corresponds to the current needed to either fully charge or discharge the electrode in n hours, hence the current is calculated by

$$\begin{aligned} & \text{Current}[\text{mA}] \\ & = \frac{\text{Theoretical capacity} \left[\frac{\text{mAh}}{\text{g}} \right] \times \text{active electrode mass}[\text{g}]}{n[\text{hour}]} \end{aligned} \quad (1.4)$$

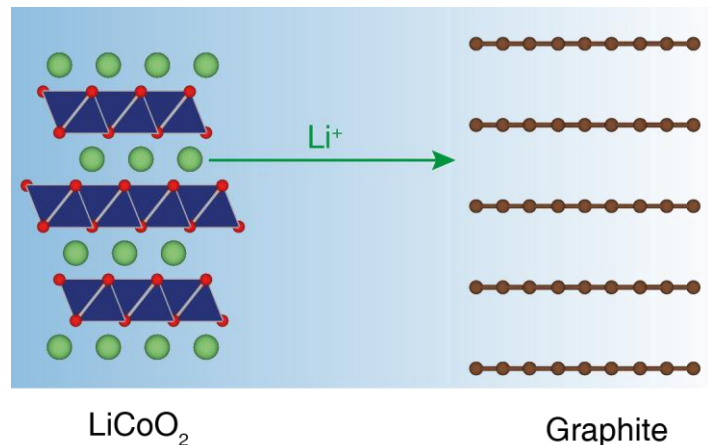


Figure 1.3. Illustration of the intercalation mechanism for the LiCoO_2 /graphite battery. Li ions are removed from the layers between the CoO_2 sheets and intercalated into the graphite layers during charge.

1.3 Thermodynamics of Li-ion batteries

The energy stored in a LIB depends on its capacity as well as its operating voltage. The equilibrium voltage of a LIB is dictated by the Li chemical potential difference between the two electrodes,

$$E_{cell}(x_C, x_A) = -\frac{\mu_{Li}^C(x_C) - \mu_{Li}^A(x_A)}{\mathcal{F}} \quad (1.5)$$

where $\mu_{Li}^C(x_C)$ and $\mu_{Li}^A(x_A)$ are the Li chemical potentials at the cathode and the anode, respectively, x_C and x_A are the Li compositions of the cathode and the anode, respectively, and \mathcal{F} is the Faraday's constant. In LIB research, Li metal is conventionally employed as the anode and the material of interest as the cathode. As a result, the chemical potential at the anode is invariant owing to its constant Li composition, and the cell voltage, E_{cell} , provides a direct measure of the Li chemical potential at the cathode (the material of interest):

$$E_{cell}(x_C) = -\frac{\mu_{Li}^C(x_C) - \mu_{Li}^{Li\ metal}}{\mathcal{F}} \quad (1.6)$$

Because the chemical potential is given by

$$\mu = \frac{\partial G}{\partial x} \quad (1.7)$$

where G and x are the molar Gibbs free energy and the Li composition of the compound, respectively, the Gibbs free energy of the cathode can be constructed by measuring the cell voltage at different Li compositions.

Depending on the nature of the Gibbs free energy, the cell voltage will be either invariant or changing with Li composition. The relationship between the Gibbs free energy and the cell voltage is illustrated in Figure 1.4. For a “W” shaped $G(x)$ shown as the red curve in Figure 1.4 A, the corresponding voltage changes with the Li composition in regions $0 < x < x_\alpha$ and $x_\beta < x < 1$, as shown in Figure 1.4 B. However, when the Li composition is in the range $x_\alpha < x < x_\beta$, the lowest energy state is not represented by the red curve and instead follows the common tangent construction shown by the black line, which represents the linear combination of the two phases of Li composition x_α and x_β , respectively. Consequently, the chemical potential and hence the cell voltage in the range $x_\alpha < x < x_\beta$ remains constant. The two-phase coexistence for $x_\alpha < x < x_\beta$ indicates a spontaneous phase separation process (formation of a second phase) when the Li

composition is within the range defined by $x_\alpha < x < x_\beta$. The delithiation process is illustrated in Figure 1.5 A and is usually referred to as a two-phase reaction. When $G(x)$ represents the lowest energy state for every x , as shown in Figure 1.4 C, the corresponding voltage in Figure 1.4 D simply manifests the slope of $G(x)$. Since only one phase is involved throughout the entire Li composition range, this phase is effectively a Li solid solution. The (de)lithiation reactions proceeds by simply varying the Li composition and is referred to as a single-phase (solid solution) reaction as illustrated in Figure 1.5 B.

The kinetics for a single-phase reaction are mainly determined by the Li diffusion and the electronic conduction of the electrode material. Whereas, the two-phase reaction mechanism is further complicated by the formation of a second phase, which is discussed in more detail in the next section.

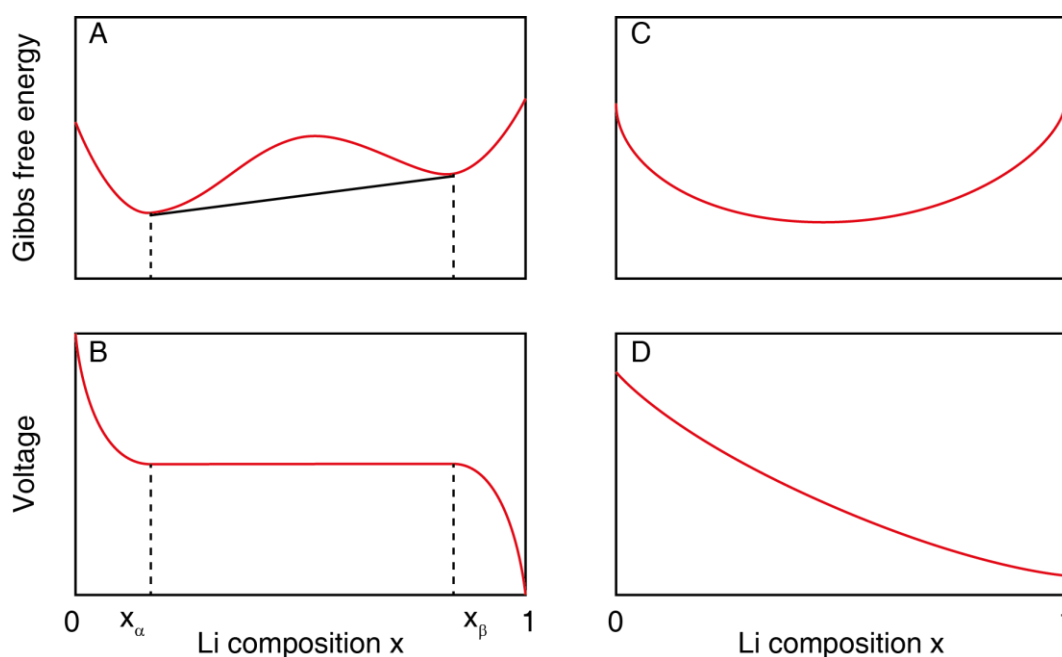


Figure 1.4. The relationship between the Gibbs free energy and the cell voltage. (A) and (B) illustrate the case where a constant voltage plateau is observed, while (C) and (D) illustrate the case where the voltage changes with the Li composition.

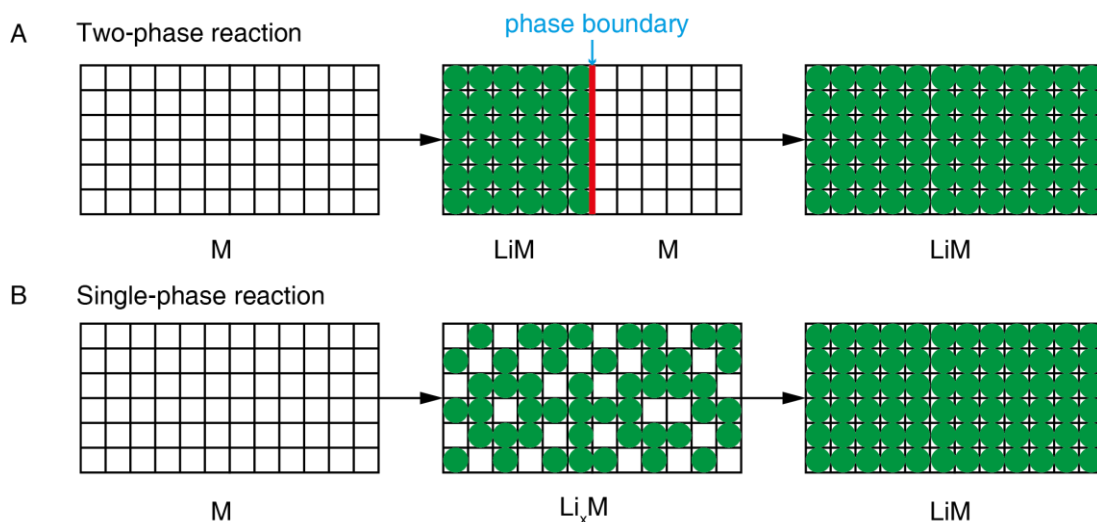


Figure 1.5. (A) The lithiation process when two phases coexist. The reaction proceeds by varying the relative fraction of the two phases via propagation of the phase boundary. (B) The lithiation process when the particle remains as a single-phase. Li ions progressively occupy the vacant sites in the lattice by forming a solid solution with the host lattice M.

1.4 Issues of phase separating electrode: the case of LiFePO₄

The two-phase reaction is usually considered to be more sluggish than the single-phase reaction due to the additional kinetic energy barrier introduced by the nucleation and growth of a second phase, hence electrodes with phase separating behaviour upon (de)lithiation are thought to be unsuitable for high rate applications. However, the phase separating LiFePO₄, which demonstrated very high rate capability, serves as a counterexample to this perception. Thus, it is crucial to understand the mechanisms that underlies its high rate capability. This section will highlight the issues of Li diffusion and the delithiation mechanism generally in the context of LiFePO₄ and identify the problems that must be addressed.

1.4.1 Structure, thermodynamic and electrochemistry of LiFePO₄

Since its first demonstration as a cathode material for LIB in 1997[6], LiFePO₄ has attracted tremendous attention as an alternative to LiCoO₂, due to its lower cost, lower toxicity and high safety. The olivine-type LiFePO₄ is crystallised in the space group *Pnma*, and its crystal structure is shown in Figure 1.6. When Li is extracted, LiFePO₄ is transformed to FePO₄, which adopts the same crystal structure with a contraction in the *a* and *b* lattice parameters and an expansion in the *c* lattice parameter.

The diffusion of Li is predominantly in the one-dimensional (1-D) channels parallel to the b direction[7–9], since the energy barrier for hopping between channels is predicted to be very high[8,10]. The intrinsic electronic conductivity is very low, and the conduction is carried out by polaron hopping[11]. The PO_4 tetrahedra between adjacent FeO_6 octahedra build up a high activation energy along the a axis, and the electronic conduction is restricted in the two-dimensional (2-D) plane of the FeO_6 octahedra (i.e. the bc -plane).

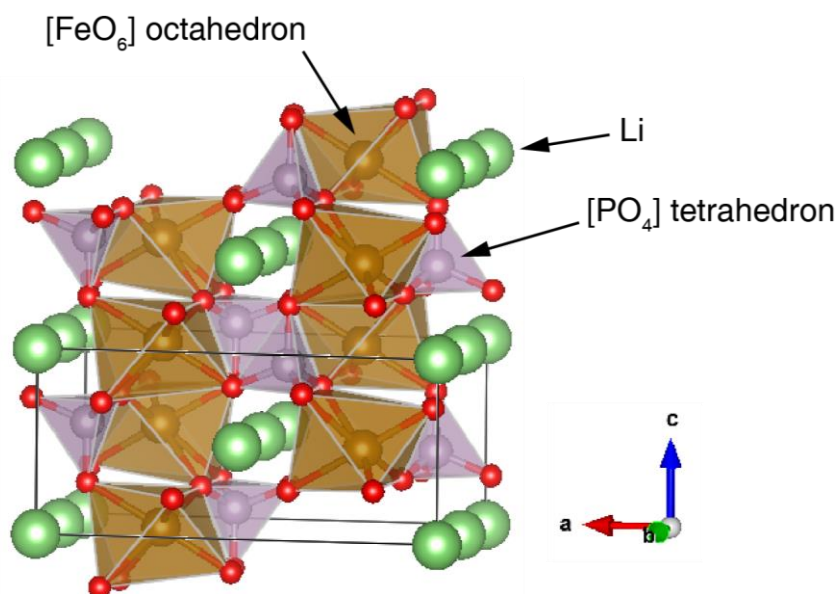


Figure 1.6. The crystal structure of LiFePO_4 . The edges of the unit cell are shown by the black lines. The green, red, brown and purple spheres represent Li, O, Fe and P atoms, respectively.

The phase diagram of Li_xFePO_4 as a function of Li composition and temperature was mapped out by X-ray powder diffraction[12] and is shown in Figure 1.7. At room temperature, the end member phases, $\text{Li}_\beta\text{FePO}_4$ and $\text{Li}_{1-\alpha}\text{FePO}_4$, have very limited Li solubilities, leaving a large miscibility gap that extends over almost the entire Li composition range[13]. Therefore, it is expected that the (de)lithiation of $(\text{Li})\text{FePO}_4$ proceeds by a two-phase reaction under ambient conditions.

Figure 1.8 shows a typical voltage profile during the charge and discharge cycle of LiFePO_4 . There is a very flat voltage plateau at ~ 3.45 V spanning almost the entire Li composition range, corresponding to the transition between $\text{Li}_\beta\text{FePO}_4$ and $\text{Li}_{1-\alpha}\text{FePO}_4$. The sloping voltage at the end of charge (discharge) is due mostly to the high kinetic barrier in extracting (inserting) the last few Li ions.

Given the 1-D Li diffusion, low electronic conduction and the two-phase reaction upon (de)lithiation, LiFePO_4 does not seem to possess the appealing properties for high rate applications. However, through particle size reduction and carbon coating, significant improvements have been made on the rate performance of LiFePO_4 . It has been shown that LiFePO_4 particles of 50 nm size can be discharged at 20 C (discharge in 3 min) over extended cycles while retaining more than 80 % of their theoretical capacity[14]. It turns out that the particle size reduction affects the thermodynamics of Li_xFePO_4 , the delithiation mechanism and the Li diffusion process, and has profound implications for the rate performance.

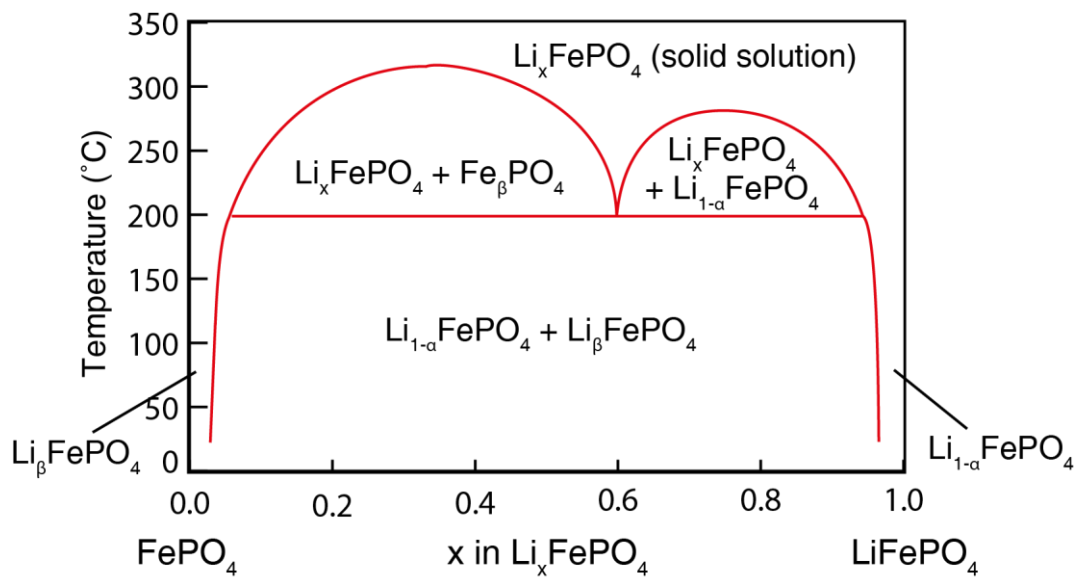


Figure 1.7. The phase diagram of Li_xFePO_4 as a function of temperature and Li composition[12].

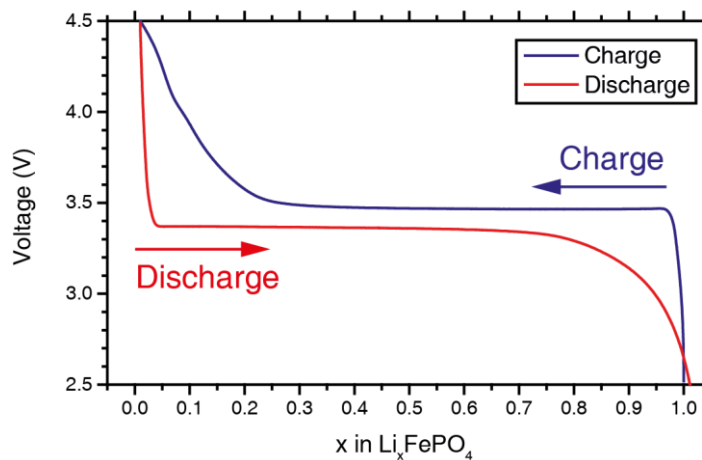


Figure 1.8 Typical charge and discharge voltage profiles of LiFePO_4 . Voltage is referenced against the redox potential of Li^+/Li^0 .

1.4.2 The (de)lithiation mechanism of (Li)FePO₄

Most of the earlier models[6,15,16] describing the Li (de)intercalation process of (Li)FePO₄ assumed isotropic Li diffusion and are considered relevant only to secondary LiFePO₄ particles, owing to the anisotropic diffusion of Li in LiFePO₄. The phase separating nature of LiFePO₄ requires the formation of a Li_{1- α} FePO₄/Li _{β} FePO₄ phase boundary when LiFePO₄ becomes partially delithiated. It is known that the two phase morphology may hinder the Li diffusion if the phase boundary is orientated perpendicular to the Li diffusion direction[17]. In LiFePO₄, the phase boundary prefers to align with the (101) and (100) crystallographic planes[18–21], which are parallel to the direction of Li diffusion along the *b* crystallographic axis. As illustrated in Figure 1.9, it was proposed that Li extraction/insertion takes place only at the Li_{1- α} FePO₄/Li _{β} FePO₄ interface and the phase boundary propagates along the direction perpendicular to the *b* axis[18]. Therefore, reducing the Li diffusion length by particle size reduction will improve the rate performance of LiFePO₄.

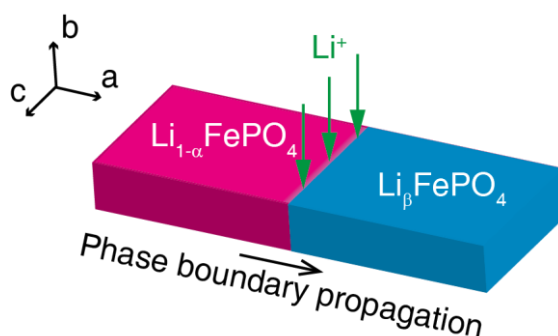


Figure 1.9. The phase boundary is formed in the *bc* plane and propagates in the direction perpendicular to the Li diffusion (in the direction of the *a*-axis).

The miscibility gap in Li_{*x*}FePO₄ is found to decrease with decreasing particle size[22,23]. Since the size of the miscibility gap is determined by the Gibbs free energy, $G(x)$, of Li_{*x*}FePO₄, the observed size effect indicates that $G(x)$ is also dependent on the particle size. This is rationalised by the increased contribution of the interfacial energy in nanoparticles[24]. Consider the molar Gibbs free energy, $G(x)$, of a single Li_{*x*}FePO₄ particle within the miscibility gap, where the two end member phases Li _{β} FePO₄ and Li_{1- α} FePO₄ are separated by an interface:

$$G(x) = x \cdot G_{\alpha} + (1 - x) \cdot G_{\beta} + \frac{A_m}{V_m} \gamma_{int} \quad (1.8)$$

where G_{α} and G_{β} are the molar Gibbs free energy of the Li_{1- α} FePO₄ and Li _{β} FePO₄ phases, respectively, A_m is the molar interfacial area, V_m is the molar volume of Li_{*x*}FePO₄, and γ_{int}

is the interfacial energy. A_m/V_m is equivalent to the interfacial area to volume ratio, which increases with decreasing particle size. The interfacial energy term, $\Delta G_A = \frac{A_m}{V_m} \gamma_{int}$, is negligible when the particle size is sufficiently large ($> 1 \mu\text{m}$). Otherwise, ΔG_A becomes appreciable and must be taken into account. The Gibbs free energy with the interfacial energy considered is shown as the green curve in Figure 1.10. Due to the additional interfacial energy, the single phase (red curve) has a lower energy than the phase separation in individual particles for $x_\alpha' < x < x_\alpha$ and $x_\beta < x < x_\beta'$ and becomes energetically unfavourable for $x_\beta' < x < x_\alpha'$. Since ΔG_A increases with decreasing particle size, the composition range defined by x_α' and x_β' , i.e. the miscibility gap, will shrink as the particle size decreases.

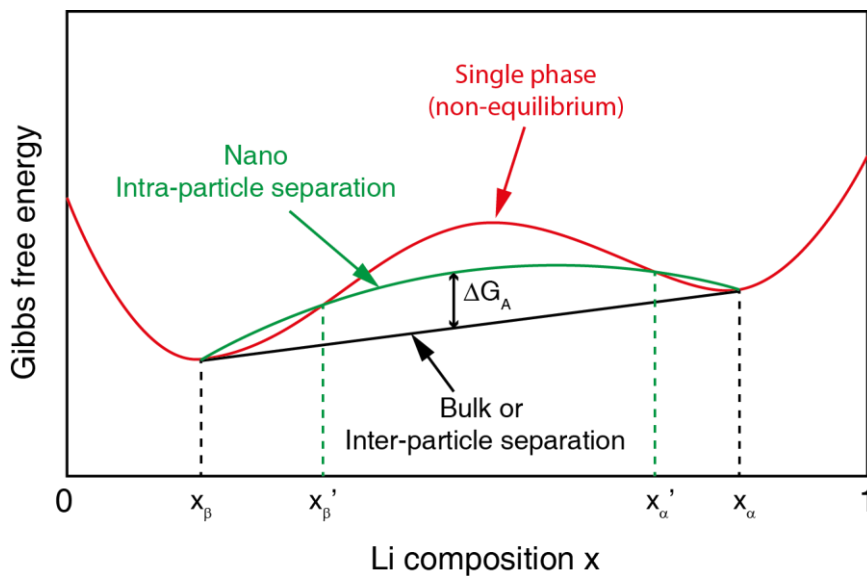


Figure 1.10. The Gibbs free energy diagram as a function of the Li composition assuming ΔG_A is negligible (red) and significant (green). The red curve indicates the energy of Li_xFePO_4 if it is maintained as a single homogeneous phase. The black line indicates the energy as a linear combination of $G(x_\alpha)$ and $G(x_\beta)$, i.e. the case when the particle size is big or the phase separation occurs between and not within particles. The green curve indicates the energy for nanoparticles where phase separation occurs within particles (intra-particle), introducing an additional interfacial energy ΔG_A . The extent of the solid solution range is exaggerated for clarity. In reality, x_α and x_β are close to 1 and 0, respectively.

The preceding argument involves only a single particle. In a real battery electrode, which is a multi-particle system, phase separation can occur either inside individual particles or between particles, which are illustrated by Figure 1.11 A and B, respectively. It is noted that the interface can be eliminated by adopting the inter-particle phase separation, which is the configuration of lower total energy. Hence, in a real electrode,

where Li ion transport between particles is possible, inter-particle phase separation will be the equilibrium configuration, when the interfacial energy is very high. Indeed, in partially delithiated electrodes made from particles of 50 ~ 300 nm in size, the majority of the particles assumes either the $\text{Li}_{1-\alpha}\text{FePO}_4$ or the $\text{Li}_\beta\text{FePO}_4$ phase, i.e. inter-particle phase separation occurs[25,26], whereas intra-particle phase separation was observed in micron-sized particles[18] or in nanoparticles delithiated by chemical methods[20] where Li^+ transport between particles is forbidden.

The observation of the inter-particle phase separation in *ex situ* samples, which are retrieved by disassembling the partially dis/charged battery cell, raises the question as to how the delithiation proceeds in nanoparticles. It was first proposed that the $\text{Li}_{1-\alpha}\text{FePO}_4/\text{Li}_\beta\text{FePO}_4$ interface is so unstable that it propagates throughout the particle almost instantaneously once a $\text{Li}_\beta\text{FePO}_4$ domain is nucleated[25], resulting in an electrode composed of either reacted or non-reacted particles. This is known as the “domino-cascade” model, which builds on the two-phase reaction. The “domino-cascade” model and other studies[27] have recognised that the (de)lithiation of nanoparticles of LiFePO_4 in a multi-particle electrode takes place sequentially. A recent theoretical study suggested that the delithiation may proceed by a single-phase reaction[28], as the nucleation energy barrier in nanoparticles (< 100 nm) was estimated to be too high for nucleation to occur. Additionally, the calculated formation energy of the solid solution Li_xFePO_4 , albeit not thermodynamically stable, turned out to be very low (< 15 meV per formula unit for all x at room temperature) in comparison with kT (~26 meV at room temperature). This finding inspired the proposition that the (de)lithiation of $(\text{Li})\text{FePO}_4$ may take the facile, non-equilibrium, solid solution path, provided there is a driving force, i.e. a small electrochemical overpotential ~ 10 mV, to initiate the (de)lithiation process. This proposed paradigm shift from the two-phase to the single-phase reaction for LiFePO_4 nanoparticles is echoed by continuum modelling studies[29]. Although thermodynamics dictate spontaneous phase separation when $\frac{\partial^2 G}{\partial x^2} < 0$ due to the local fluctuation in Li composition, the kinetics are dependent on the Li diffusion and the driving force for phase separation, which is determined by the exact form of single-phase $G(x)$. It was found that the solid solution phase could be kinetically stabilised in a Li_xFePO_4 particle if the rate at which Li is extracted or inserted is faster than the rate of phase separation.[29]

Due to a lack of direct experimental evidence in support of the proposed hypotheses, the issue remains as to whether the (de)lithiation of $(\text{Li})\text{FePO}_4$ nanoparticles

takes place by a single-phase or a two-phase reaction. The analysis of the kinetics of phase transition between LiFePO_4 to FePO_4 suggested that (de)lithiation takes place via the non-equilibrium single-phase reaction with small particles (< 100 nm) or a large overpotential (> 150 mV)[30]. Nonetheless, two-phase behaviour was reported by many *in situ* X-ray diffraction (XRD) studies during slow electrochemical cycling[31–35] or chemical delithiation[36], which show the growth of diffraction peaks of the $\text{Li}_\beta\text{FePO}_4$ phase accompanied by the disappearance of diffraction peaks of the $\text{Li}_{1-\alpha}\text{FePO}_4$ phase. Due to the sequential reaction mechanism, only a small fraction of the particles in the electrode is taking part in the reaction at a time during low rate cycling. Consequently, the small amount of reacting particles may not be captured by *in situ* XRD. In order to understand the (de)lithiation process of (Li)FePO₄ nanoparticles, *in situ* methods that capture reacting particles must be employed.

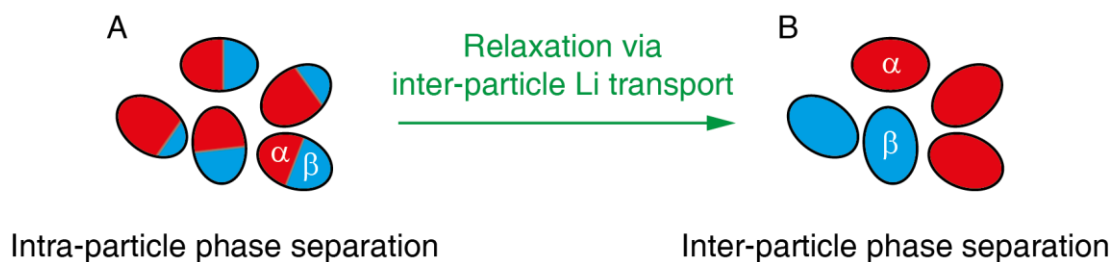


Figure 1.11. Illustration of (A) the intra-particle vs. (B) the inter-particle phase separation in a multi-particle system. α and β are used to denote two different phases.

1.4.3 Li diffusivity: local migration vs. long range diffusion

The room temperature Li diffusivity along the 1-D channel is predicted to be very high ($\sim 10^{-7}$ to 10^{-9} cm^2/s) from first-principle calculations[10,37]. However, these results are obtained for Li hopping to an adjacent vacant site, which occurs on the length scale of a few nanometres, and do not readily translate to long range Li migration if there are defects in the channel impeding or blocking the Li motion. Malik *et al.*[38] studied the effect of the $\text{Li}_{\text{Fe}}^- - \text{Fe}_{\text{Li}}^\bullet$ antisite defects, formed between nearest neighbouring Li and Fe, as shown in Figure 1.12 A. The Li-Fe antisite defects are the most common ones found in LiFePO_4 obtained from low temperature syntheses[39,40], but they can be avoided by synthesising at a higher temperature ($> 180^\circ\text{C}$ for hydrothermal synthesis)[39,41,42] or annealed out by post-synthesis thermal treatment (annealing at $> 500^\circ\text{C}$)[43]. This antisite defect blocks the Li motion in the same channel, and can be circumvented by crossing over to an adjacent channel, which poses a high energy barrier[8,10,37]. The presence of

antisite defects results in a decreased Li diffusivity measured over long range Li migration. In the presence of more than two Fe atoms in the same channel, as shown in Figure 1.12 B, the Li trapped between two Fe become inaccessible, leading to a reduced capacity. Obviously, for a given defect concentration, shorter channels have fewer trapped Li. Malik *et al.*[38] shows that the unblocked fraction of Li as well as the long range Li diffusivity increases with reducing channel length. Therefore, decreasing the particle size has at least a twofold improvement to the rate performance: a reduction in the Li diffusion length and an improvement in the effective Li diffusivity.

Li diffusion can be determined by either microscopic or macroscopic measurement. Microscopic methods probe Li hopping between adjacent sites and thus measure local Li migration, while macroscopic methods probe the diffusion process under a concentration gradient and thus measure long range Li diffusion. Measurement by microscopic methods, such as muon spin relaxation spectroscopy, have consistently yielded a Li diffusivity on the order of 10^{-10} cm^2/s [44–46]. However, macroscopic measurements, which are commonly carried out by electrochemical methods, have led to large discrepancies in the Li diffusivity of LiFePO_4 , ranging from 10^{-11} cm^2/s to 10^{-14} cm^2/s [47–50]. The challenges associated with obtaining an accurate measurement of the active surface area, where Li ion transfer between the electrode and the electrolyte takes place, in a multi-particle electrode has been recognised for underestimating the Li diffusivity determined by common electrochemical methods[51]. Therefore, new macroscopic techniques are required to measure the long range Li diffusion in LiFePO_4 to verify the rapid Li diffusivity obtained by microscopic measurements.

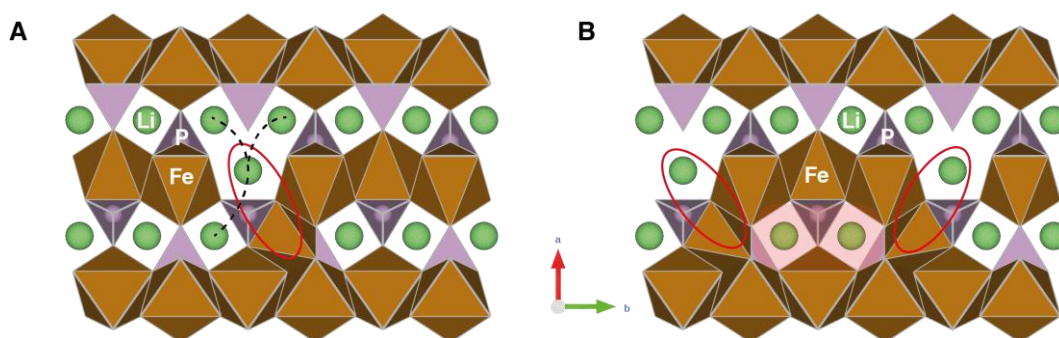


Figure 1.12. (A) A single Li-Fe antisite defect (red ellipse) and the possible paths (dashed black curves) for Li crossover between channels. (B) Li trapped (shaded region) between two Fe atoms in the diffusion channel.

1.5 Phase transition in phase separating electrodes

LIBs usually operate under constant temperature and pressure, hence, any phase transition in the electrode material is induced by changes in Li composition. For a phase separating electrode with a miscibility gap, the transition from one end member phase to the other phase, which undergoes via the nucleation and growth of a second phase, is characterised as a first-order phase transition.

The possibility of whether the two end member phases can be interconverted via a non-equilibrium, continuous structural transition by varying the Li composition depends on the crystal structures of the two phases and whether a continuous transition path exists. When both phases assume the same symmetry, a continuous transition can proceed via a solid solution phase of the same symmetry with the end member phases. For example, a continuous structural transition between $\text{Li}_{1-\alpha}\text{FePO}_4$ and $\text{Li}_\beta\text{FePO}_4$ can be realised by a hypothetical, non-equilibrium, solid solution phase Li_xFePO_4 .

When the two end member phases adopt different symmetries, one cannot construct a single solid solution phase bridging the two because there has to be a discontinuous change in symmetry somewhere within the Li miscibility gap. If the symmetries of the two end member phases do not correspond to a group-subgroup relationship, a continuous phase transition is prohibited. For a pair of phases with symmetries corresponding to a particular group-subgroup relationship, the possibility of whether or not a continuous structural phase transition, also known as second-order phase transition, will occur and can be assessed by Landau theory[52]. This assessment can be readily carried out by the programme ISOTROPY[53] if the crystal structures of the two phases are known. An example of phase transition between phases of group-subgroup related symmetries is given by anatase TiO_2 , which is used as an anode material for LIB[54]. When Li is intercalated into TiO_2 , it undergoes via a first-order transition from tetragonal TiO_2 to orthorhombic $\text{Li}_{0.5}\text{TiO}_2$, with a large Li miscibility gap between the two phases.

Both of the above scenarios can occur for the same electrode material during different stages of (de)lithiation. For example, during delithiation, LiVPO_4F transforms to $\text{Li}_{0.67}\text{VPO}_4\text{F}$ via an apparent first-order transition without symmetry changes, and further delithiation transforms $\text{Li}_{0.67}\text{VPO}_4\text{F}$ (triclinic) to VPO_4F (monoclinic) via a first-order phase transition that involves a change in symmetry.

1.6 Objective

To independently verify the fast long range Li diffusion in LiFePO_4 , a different method compared with the conventional electrochemical techniques should be employed. Cation exchange can be used to determine the diffusivity of the exchanging ions[55]. Since it is the Li diffusivity that is of interest to us, ^6Li and ^7Li isotopes can be used as the exchanging species. The amount of exchange can be measured by the nucleation magnetic resonance (NMR), which is able to distinguish between the two nuclei, to then derive the long range Li diffusivity

The controversy over the (de)lithiation mechanism of $(\text{Li})\text{FePO}_4$ requires further investigation to obtain a better understanding of how this material is able to achieve good capacity retention even at very high rates. The biggest debate is whether a single- or two-phase reaction occurs in individual LiFePO_4 nanoparticles. To eliminate any ambiguity in the interpretation of the results, *in situ* experiments, which capture the reacting particles, must be employed to obtain direct evidence for the proposed mechanisms. One strategy to capture the reacting particles is by inducing more particles to react at a time through high rates of cycling so that they can be measured with conventional techniques with high temporal resolution. *In situ* synchrotron X-ray diffraction is a powerful tool in characterising the structural changes in crystalline samples while retaining high temporal resolution. Hence, this technique is employed to investigate the (de)lithiation process of $(\text{Li})\text{FePO}_4$ nanoparticles.

Although the hypotheses on the (de)lithiation process were discussed for LiFePO_4 , it is interesting to investigate the applicability to other phase separating materials. Because LiFePO_4 represents the case where symmetry change is not involved during (de)lithiation, it is interesting to investigate the case where the symmetries of the end member phases during (de)lithiation correspond to a group-subgroup relationship. Therefore, as introduced in Section 1.5, the (de)lithiation processes of anatase TiO_2 and LiVPO_4F are also investigated in this thesis: TiO_2 being an example where lithiation involves group-subgroup related phases, and LiVPO_4F being an example where delithiation undergoes two first-order phase transitions.

2 X-ray powder diffraction and nuclear magnetic resonance spectroscopy

The main experimental techniques employed in this thesis include X-ray powder diffraction and nuclear magnetic resonance spectroscopy. This chapter gives a general introduction to these two techniques.

2.1 X-ray powder diffraction (XRD)

XRD is a widely used, non-invasive technique to investigate not only the crystal structures but also microstructures, such as crystal/domain size and lattice strain, of crystalline materials.

2.1.1 Position and intensity of a Bragg reflection

When a monochromatic X-ray beam is incident upon a crystalline sample, the X-ray beam is scattered by the electrons of atoms in the sample and produces a diffraction pattern. The criterion for diffraction is dictated by the well-known Bragg's law:

$$2d_{hkl}\sin\theta = n\lambda \quad (2.1)$$

where d_{hkl} is the interplanar spacing between two (hkl) planes, θ is the scattering angle as shown in Figure 2.1, λ is the wavelength of the X-ray beam and n is an integer.

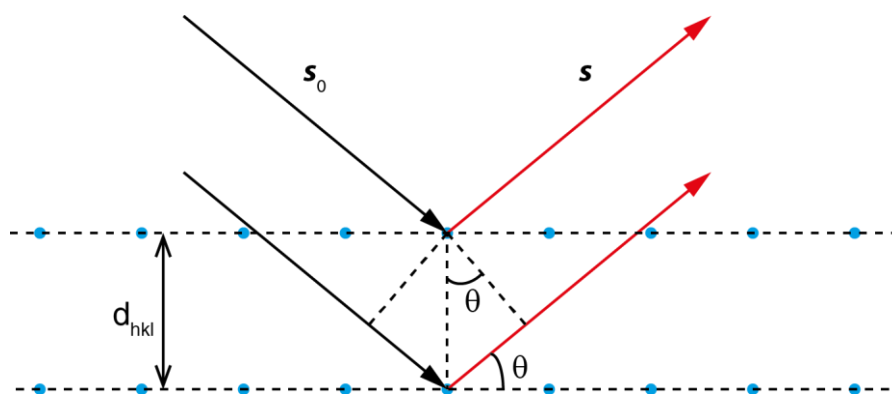


Figure 2.1 Illustration of diffraction by Bragg's law. The incident and diffracted beams are denoted by black and red arrow lines, respectively. d_{hkl} is the interplanar spacing, and θ is the scattering angle. s_0 and s are the unit vectors of the incident and diffracted beam, respectively.

For a randomly oriented crystalline powder sample, the diffracted X-rays form a series of cones, as shown in Figure 2.2 A, with semi-vertex angles of 2θ determined by

Bragg's law. Due to the random orientation of the crystals in the sample, the diffracted X-ray beams are uniformly distributed on each cone, and the diffraction intensity is conventionally presented as a function of 2θ , as illustrated in Figure 2.2 B. The diffraction pattern exhibits a series of sharp diffraction peaks at 2θ determined by Bragg's law, and the diffraction peaks are commonly referred to as Bragg reflections or peaks. As can be seen from (2.1), the position of a Bragg reflection is determined by the lattice parameters of the sample.

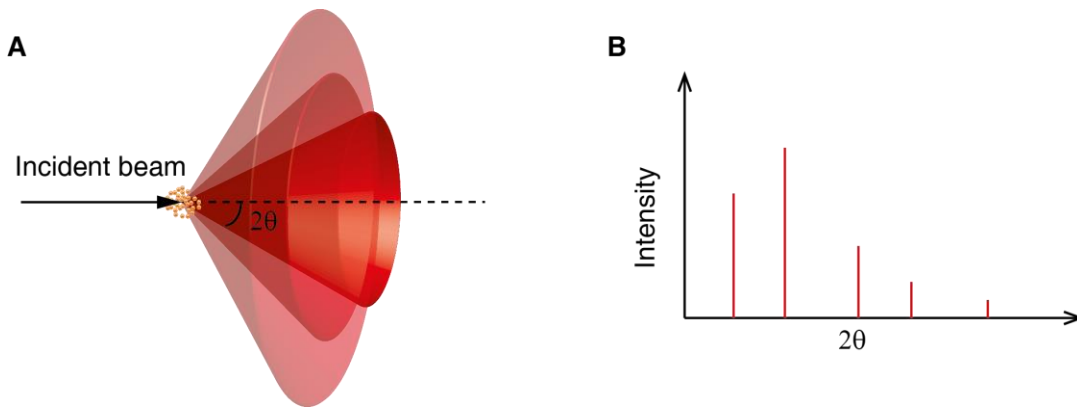


Figure 2.2 (A) Diffraction by a randomly oriented crystalline powder sample (yellow dots) produces a series of cones of diffracted beams (red), with semi-vertex angles of 2θ . (B) Variation of the diffraction intensity against 2θ for a crystalline powder sample.

The integrated intensity of a Bragg reflection corresponding to an (hkl) plane is given by[56]

$$I_{hkl} = I_0 \frac{\Omega e^4 \lambda^3}{V^2 m_e^2 c^4} LP \cdot T_{abs} \cdot |F_{hkl}|^2 \quad (2.2)$$

where I_0 is the intensity of the incident beam, Ω is the volume of the crystal, V is the volume of the unit cell, m_e is the mass of the electron, c is the speed of the light, e is the elementary charge, λ is the wavelength of the X-ray beam, LP is the Lorentz-polarisation factor, T_{abs} is the absorption factor, and F_{hkl} is the structure factor for the hkl reflection. LP depends on the diffraction geometry and T_{abs} depends on the X-ray absorption coefficient and porosity of the sample. F_{hkl} is determined by the crystal structure of the sample and is given by

$$\begin{aligned}
F_{hkl} &= \sum_{j=1}^n f_j(\mathbf{H}_{hkl}) \exp\left(2\pi i(h\mathbf{a}^* + k\mathbf{b}^* + l\mathbf{c}^*) \cdot (x_j\mathbf{a} + y_j\mathbf{b} + z_j\mathbf{c})\right) \\
&= \sum_{j=1}^n f_j(\mathbf{H}_{hkl}) \exp\left(2\pi i(hx_j + ky_j + lz_j)\right)
\end{aligned} \tag{2.3}$$

where \mathbf{a} , \mathbf{b} and \mathbf{c} are the basis vectors of the unit cell, \mathbf{a}^* , \mathbf{b}^* and \mathbf{c}^* are the basis vectors of the reciprocal lattice, x_j , y_j and z_j are the coordinates of the j th atom in the unit cell, and $f_j(\mathbf{H}_{hkl})$ is the atomic structure factor of the j th atom in the unit cell, and $\mathbf{H}_{hkl} = h\mathbf{a}^* + k\mathbf{b}^* + l\mathbf{c}^*$. The atomic structure factor of the j th atom is given by the Fourier transform of its electron density:

$$f_j(\mathbf{H}_{hkl}) = \int \rho_j(\mathbf{r}) \exp(2\pi i\mathbf{H}_{hkl} \cdot \mathbf{r}) dV \tag{2.4}$$

where $\rho_j(\mathbf{r})$ is the electron density of the j th atom and \mathbf{r} is a vector from the atomic centre to any point in space. The integration is taken over the entire space where the electron density of the corresponding atom is not zero. In essence, the integrated intensity of Bragg peaks contains the information about the crystal structure of the sample.

The Bragg peak also possesses a finite peak width, which is determined by the microstructure of the sample and the instrument. Different contributions to peak broadening are introduced in Sections 2.1.2 – 2.1.3.

2.1.2 Broadening due to finite crystal size and lattice distortion

In principle, Bragg peaks due to infinitely large, periodic crystals exhibit no broadening other than the broadening due to the instrument. When the crystal becomes finite in size or the periodicity of the crystal is interrupted, additional broadening of the Bragg peaks will be introduced. There are two mechanisms due to imperfections of the sample that can cause broadening to the Bragg peaks: finite crystal size and lattice distortion.

Broadening due to small crystal size is most pronounced in nanoparticles. The relation between the broadening and the crystal size is described by the Scherrer formula[57]

$$H_s(2\theta_{hkl}) = \frac{K\lambda}{L \cos\theta_{hkl}} \tag{2.5}$$

where H_s is the full width at half maximum (FWHM) of the (hkl) Bragg reflection due to finite crystal size, K is the shape factor that is close to unity, λ is the wavelength of the X-ray, θ_{hkl} is the position of the (hkl) Bragg peak and L is the volume weighted column

length perpendicular to the (hkl) crystal plane[58]. For spherical crystals, L is equivalent to the volume weighted crystal size. For crystals of non-spherical shapes, the column length varies with (hkl) , which will lead to the hkl -dependent (anisotropic) broadening of the Bragg reflections.

Broadening due to lattice distortion can appear in both large and small crystals. In an ideal crystal, the spacing between lattice planes is uniform across the crystal, and the diffraction condition dictated by Bragg's law for an (hkl) reflection is satisfied at only one 2θ angle, giving rise to a peak (Figure 2.3 A) whose shape/broadening is only affected by the particle size as determined by (2.5).

When a crystal is subject to strain, which is homogenous across the crystal, the interplanar spacing is still uniform across the crystal but its value will change. Consequently, the Bragg peak will only shift in position and retain the same shape (i.e. broadening), as illustrated in Figure 2.3 B.

However, when the strain is not homogeneous, i.e. the interplanar spacing in different parts of the crystal varies, and the average interplanar spacing is still the same, the Bragg peak will become broader but will not change in position (Figure 2.3 C). The effect of a small variation in the interplanar spacing or d-spacing, known as the microstrain, on the peak broadening is illustrated by differentiating the Bragg's law equation in (2.1):

$$d_{hkl} \cos\theta_{hkl} \Delta\theta_{hkl} + \sin\theta_{hkl} \Delta d_{hkl} = 0 \quad (2.6)$$

$$\Delta\theta_{hkl} = -\frac{\Delta d_{hkl}}{d_{hkl}} \tan\theta_{hkl}.$$

The above equation shows that a small change in the d-spacing will lead to a small shift in the peak position. If the deviation from the average d-spacing d_{hkl} follows a symmetrical distribution, this will lead to a broadening rather than a shift in the 2θ position. The broadening due to the apparent strain ε_{app} is expressed as[59]

$$H_D(2\theta) = \varepsilon_{app} \tan\theta = 4\varepsilon_{max} \tan\theta \quad (2.7)$$

where H_D is the FWHM due to microstrain and ε_{max} is the maximum strain[59]. (2.7) is derived on the basis of a symmetrical strain distribution, which also leads to a symmetrical peak broadening. However, the strain distribution can take a variety of forms and does not have to be symmetrical. Hence, the peak may not always broaden symmetrically if the strain distribution is not symmetrical. It must be pointed out that the "strain" discussed

here is interpreted broadly as lattice distortions that originate from, other than mechanical stress, various sources, such as compositional variations, dislocations and stacking faults.

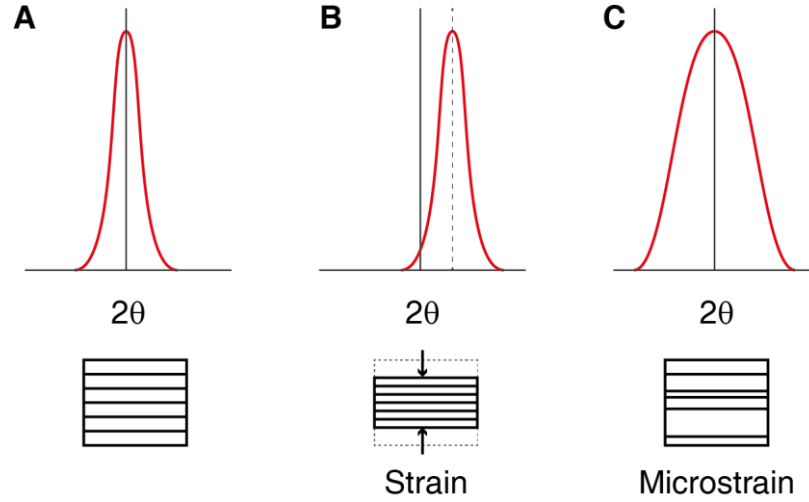


Figure 2.3. Effects of strain and microstrain on a Bragg reflection. (A) Peak profile free from stain and microstrain. (B) Peak profile due to strain only. (C) Peak profile due to microstrain only.

For small particles, broadening due to both size and distortion can be present simultaneously. Separation of the two effects is possible by making use of several orders of an (hkl) reflection. One simple and approximate method is to consider the different 2θ dependence of the broadening due to different mechanism. In this method, the total broadening of a Bragg reflection can be approximated as the sum of the broadenings due to size and distortion:

$$H_{total} = H_S + H_D = \frac{K\lambda}{L \cos\theta} + \varepsilon_{app} \tan\theta \quad (2.8)$$

Multiplying both sides by $\cos\theta$ yields:

$$H_{total} \cos\theta = \frac{K\lambda}{L} + \varepsilon_{app} \sin\theta \quad (2.9)$$

When $H_{total} \cos\theta$ (ordinate) is plotted against $\sin\theta$ (abscissa) for several peaks corresponding to the same crystallographic direction, for example (111), (222), (333), a straight line can be used to fit all the points on the plot, which is also known as the Williamson-Hall plot[60]. The slope yields the apparent strain and the intercept with the ordinate gives $K\lambda/L$.

A more rigorous and sophisticated method is developed by B.E. Warren and B.L. Averbach[61]. This method involves expressing the peak profile in Fourier series, and multiple reflections of the same crystallographic direction have to be considered. One

advantage of this method is that it is applicable to both symmetrically and asymmetrically broadened peaks. Since both methods rely on multiple peaks of the same crystallographic direction, their applications are usually found in materials of high symmetry, where the Bragg reflections are well separated from each other and their shape can be determined with more confidence. The severe overlap of the reflections of low symmetry phases presents a challenge to the determination of the individual peak shape and hence the use of both methods.

2.1.3 Diffraction peak profile deconvolution

The observed diffraction peak profile $h(2\theta)$ is a convolution of the instrumental profile $g(2\theta)$ and the sample profile $f(2\theta)$:

$$h(2\theta) = g(2\theta) \otimes f(2\theta) \quad (2.10)$$

which is illustrated in Figure 2.4.

The instrumental profile is characteristic of the particular instrument and the diffraction geometry, and is generally affected by wavelength distribution and geometrical aberrations. Hence, $g(2\theta)$ is independent of the sample under investigation and is usually determined experimentally by measuring a standard sample that is free from size and distortion effects.

The sample profile $f(2\theta)$ can be further deconvoluted into a variety of contributions that arise from any imperfections in the sample, such as finite crystal size and lattice distortion introduced in Section 2.1.2.

There are two ways to obtain the sample profile f : deconvolution and convolution approaches. The deconvolution approach unfolds the sample profile f from the observed profile h using the instrumental profile g [62]; whereas the convolution approach constructs the sample profile f by adjusting its shape through the least-square minimisation algorithm. The deconvolution process may fail or become inaccurate under some circumstances, while the convolution process is always stable but risks being trapped in a local minimum during the least-square fitting procedure. In addition, since a particular profile function for f has to be used for the least-square fitting, this method is not unbiased and introduces systematic errors if the models used are not adequate.

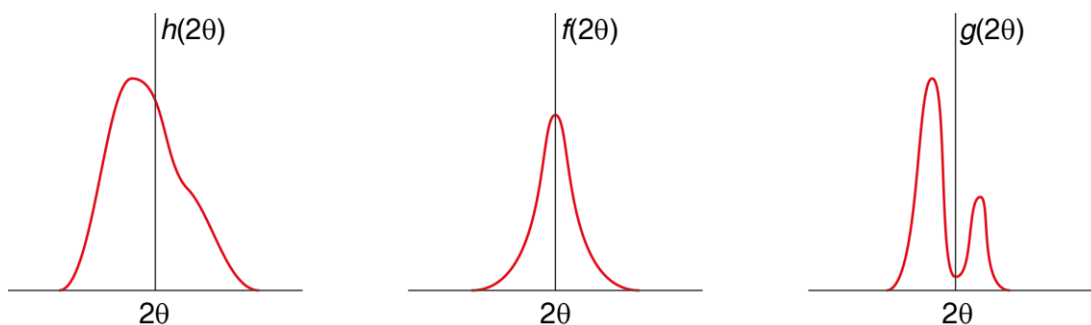


Figure 2.4. Three profiles that are involved in the convolution of the Bragg reflection profile. $f(2\theta)$ is the profile solely due to various imperfections in the sample. $g(2\theta)$ is the instrumental profile for an incident X-ray beam of double wavelengths. $h(2\theta)$ is the profile that is actually measured by the diffractometer.

2.1.4 Structure and microstructure refinement

It can be seen from (2.2) that the diffraction intensity is proportional to the squared magnitude of the structure factor, which contains the information about the number and type of atoms and atomic positions and occupancies. Bragg's law specifies a straightforward relation between the position of the Bragg reflection and the unit cell lattice constants. As a result, only the intensity and position of a Bragg reflection are relevant to the crystal structure. Refinement of the structure model is carried out by the well-known Rietveld method[63,64]. This method carries out a least-square minimisation that finds the best fit between the entire observed diffraction pattern and the calculated pattern based on the simultaneously refined models for the crystal structures, lattice parameters, instrumental factors, diffraction peak profile and other factors as may be desired and can be modelled. Hence, refinement of microstructure parameters, such as domain size and microstrain, can also be included in the Rietveld analysis if a relevant microstructure model is used to account for the various broadening mechanisms present in the sample.

Since microstructure information is embedded only in the broadening of the Bragg peaks, refinement of microstructure models can be done alone without reference to a crystal structure model. In this case, the whole powder pattern is systematically decomposed into its component Bragg reflections, a procedure called pattern decomposition, and the intensities of individual Bragg reflections are treated as independent parameters and do not carry any structure significance; meanwhile, the positions of the Bragg reflections are constrained by the unit cell parameters. This whole pattern fitting method, also carried out by least-square minimisation, without reference to a structure model is known as the Pawley method[65]. As with the Rietveld method,

refinement of the microstructure model is carried out by fitting the broadening of the Bragg reflections. If the crystal structure of the sample is not of interest or not well defined, a sample with a large variation in chemical composition for example, the Pawley method is better suited for microstructural analysis.

In both the Rietveld and the Pawley methods, microstructure refinement is carried out by refining the parameters of analytical functions that are assumed for the sample profile f as described in Section 2.1.3. Hence, the microstructure models are not unbiased and systematic errors are introduced, yet these effects can be mitigated through the identification of the dominant broadening mechanisms and adoption of relevant microstructure models.

2.1.5 Scattering by distorted domains

In a distorted structure, if the position \mathbf{r}_m of each atom m is known, the amplitude of the diffracted beam is equal to the summation of the scattering amplitude of each atom, and the diffraction intensity is given by the product of the summed amplitude and its complex conjugate:

$$I_{scatter} = \sum_m f_m e^{(\frac{2\pi i}{\lambda})(s-s_0) \cdot \mathbf{r}_m} \sum_n f_n e^{-(\frac{2\pi i}{\lambda})(s-s_0) \cdot \mathbf{r}_n} \quad (2.11)$$

where s_0 is the unit vector of the incident beam, s is the unit vector of the diffraction beam as illustrated in Figure 2.1, $f_{m(n)}$ is the atomic structure factor of the $m(n)$ th atom, and $\mathbf{r}_{m(n)}$ is the position vector of the $m(n)$ th atom. f_m now takes the general form:

$$f_m = \int \rho_m(\mathbf{r}) \exp\left(2\pi i \frac{\mathbf{s} - \mathbf{s}_0}{\lambda} \cdot \mathbf{r}\right) dV \quad (2.12)$$

This approach is applicable when the number of atoms in a particle is not very large, such as nanoparticles of a few nanometres in size. However, when the particle size is relatively big, this approach is not practical because it is difficult and unnecessary to know the exact positions of all the atoms in the system. For such a system, the diffraction amplitude by the distorted domain is obtained by summing the scattering amplitude, i.e. the structure factor, of each unit cell. If F_m is the structure factor of the unit cell m at position \mathbf{R}_m , the diffraction intensity can be written as[66]:

$$\begin{aligned}
I_{scatter} &= \sum_m F_m e^{\left(\frac{2\pi i}{\lambda}\right)(s-s_0) \cdot R_m} \sum_n F_n^* e^{-\left(\frac{2\pi i}{\lambda}\right)(s-s_0) \cdot R_n} \\
&= \sum_m \sum_n F_m F_n^* e^{\left(\frac{2\pi i}{\lambda}\right)(s-s_0) \cdot (R_m - R_n)}
\end{aligned} \tag{2.13}$$

where $F_{m(n)}$ is the structure factor of the $m(n)$ th unit cell and is given by

$$F_m = \sum_{j=1}^n f_j \exp\left(2\pi i \frac{\mathbf{s} - \mathbf{s}_0}{\lambda} \cdot \mathbf{r}\right) \tag{2.14}$$

where f_j is the atomic structure factor of the j th atom in the unit cell as given by (2.12). The above equation expressed in terms of the structure factors can be very convenient in cases where exact atomic positions are not known nor sought after. For example, a concentration gradient across the particle can be modelled by a gradient in the unit cell structure factor without knowing the exact crystal structure at different concentration.

2.1.6 *In situ* synchrotron XRD

A typical setup for an *in situ* XRD investigation of an operating battery at the synchrotron facility is illustrated in Figure 2.5. Diffraction is usually carried out in transmission geometry, where the direction of the incident X-ray beam and the position of the electrochemical cell are fixed. As the X-ray beam has to transmit through the electrochemical cell, beryllium metal[33] or glassy carbon[67] disks are commonly used as the X-ray windows on both sides of the cell to minimise scattering and absorption of the incident beam. The diffracted intensity can be collected by various detectors, including 2-dimensional (2-D) area detectors, 1-dimensional (1-D) strip detectors and 0-dimensional (0-D) point detectors, which collect data by scanning across the 2θ region of interest and is not suitable for time-resolved experiment. For 1-D and 0-D detectors, the angular resolution is mostly dependent on the resolving power of the detector itself since the radius of the goniometer, i.e. the sample-to-detector distance, is fixed. However, the angular resolution of a 2-D detector can be tuned if the detector is allowed to translate along the direction of the incident X-ray beam.

The diffraction geometry with a flat area detector is illustrated in Figure 2.6. The detector plane is perpendicular to the incident X-ray beam and is placed at a distance L_{sd} away from the sample at point O. The intensity of the diffracted beam is measured by the pixels on the detector. Since each pixel has a finite width w , it measures the entire intensity over the angle σ subtended at the sample by the width of the pixel. Hence, the angular resolution is determined by σ . As the pixel width (on the order of $\sim 100 \mu\text{m}$) is

much smaller than the sample-to-detector distance L_{sd} (a few hundred mm), σ can be expressed as:

$$\sigma(\theta) = \frac{w \cos(2\theta)}{L_{sd}/\cos(2\theta)} = \frac{w}{L_{sd}} \cos^2(2\theta) \quad (2.15)$$

It is obvious that when the size of the pixel (w) is fixed, the angular resolution at the same diffraction angle can be improved by increasing the sample-to-detector distance. However, increasing L_{sd} comes with two costs. (i) The measured angular range is reduced because the angle subtended by the detector at the sample decreases with increasing L_{sd} . This effect can be partially mitigated by offsetting the detector from its centre within the detector plane, yet only part of the diffraction circle can be measured. (ii) The intensity measured by each pixel becomes less because of a smaller σ , which is proportional to the intensity of the diffraction beam. This will lead to a poorer signal-to-noise ratio.

Detector (area or strip detector)

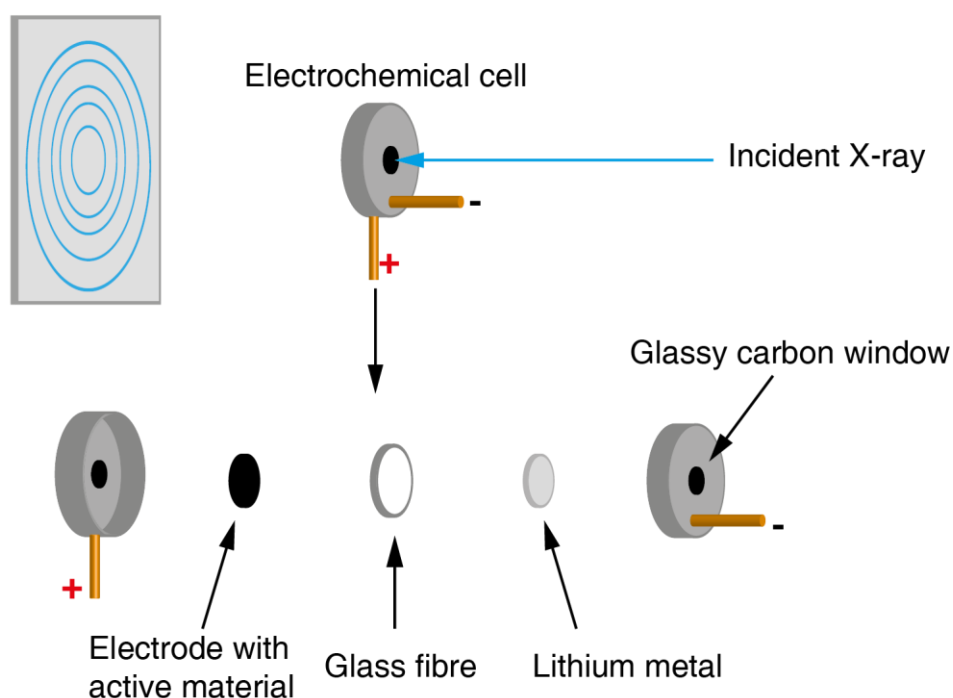


Figure 2.5. A typical setup for *in situ* XRD at a synchrotron. Either area or strip detector is used for fast data acquisition. A dissection of the electrochemical cell is also shown.

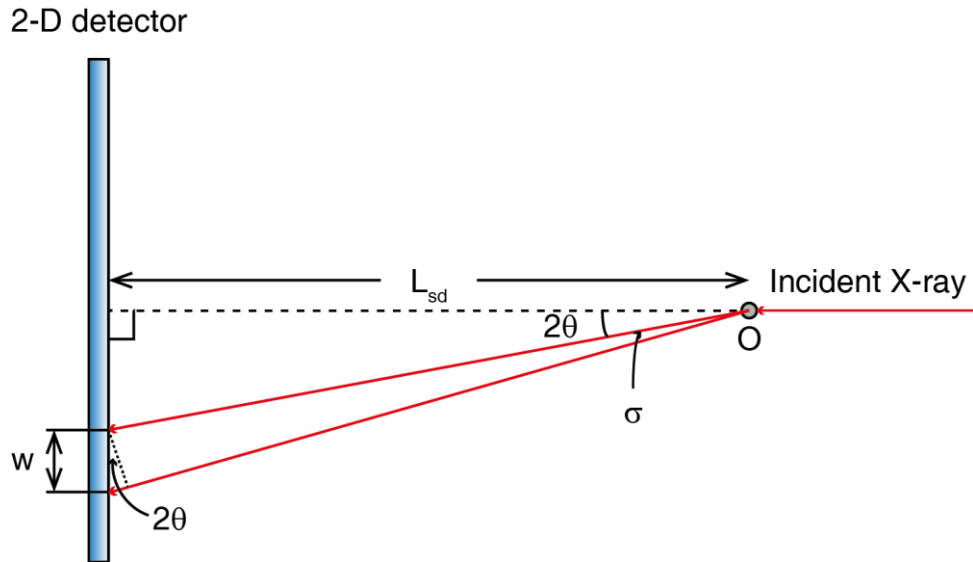


Figure 2.6. Diffraction geometry with an area detector. The sample is placed at point O, and the area detector is placed at a distance L_{sd} from the sample. The detector plane is perpendicular to the incident X-ray beam. The width of a pixel on the detector is w and subtends a small angle σ at the sample. The red lines trace the X-ray beam.

2.2 Nuclear magnetic resonance (NMR) spectroscopy

2.2.1 The basics of NMR spectroscopy

Most atomic nuclei possess spin, which is denoted by the spin quantum number I . For a nuclear spin I , there are $(2I+1)$ degenerate nuclear spin states. Each nuclear spin is associated with an angular momentum, \mathbf{I} , of magnitude $\hbar\sqrt{I(I+1)}$ (\hbar is the reduced Planck's constant), which gives rise to a magnetic moment, $\boldsymbol{\mu}$, described by:

$$\boldsymbol{\mu} = \gamma_G \mathbf{I} \quad (2.16)$$

where γ_G is the nucleus specific gyromagnetic ratio. When an external magnetic field, \mathbf{B}^0 , is applied along the z axis, the energy due to the interaction between the magnetic moment and the applied magnetic field is given by:

$$E = -\boldsymbol{\mu} \cdot \mathbf{B}^0 = -\gamma_G \mathbf{I} \cdot \mathbf{B}^0 = -\gamma_G I_z B^0 \quad (2.17)$$

It follows from quantum mechanics that $I_z = m\hbar$ (m takes integer values between $-I$ and I), so the interaction energy becomes:

$$E = -m\gamma_G \hbar B^0; m = -I, -I+1, \dots, I-1, I \quad (2.18)$$

Hence, the degeneracy of the nuclear spin states breaks down in the presence of an external field. The energy difference between two adjacent states is:

$$\Delta E = \gamma_G \hbar B^0 \quad (2.19)$$

The product of γ_G and B^0 defines the Larmor frequency, ω^0 :

$$\omega^0 = -\gamma_G B^0 \quad (2.20)$$

The Larmor frequency can be interpreted in the classical context as the precession frequency of the nuclear spin in the presence of the magnetic field.

For a sample that contains an ensemble of randomly oriented nuclear spins, it exhibits no macroscopic magnetisation. In the absence of B^0 , the energies of all nuclear spin states are degenerate, and the nuclear spin states are equally populated. When B^0 is applied, the degeneracy is lifted and the low energy nuclear spin states are more populated than the high energy nuclear spin states at thermal equilibrium. A direct consequence is the build-up of a net magnetisation, M , of the nuclear spin ensemble in the same direction with B^0 , i.e. along the z axis.

In an NMR experiment, the sample is placed inside a homogeneous magnetic field. A radio frequency (r.f.) pulse is applied to rotate the vertical magnetisation of the sample by $\pi/2$ into the transverse plane as defined by the x - y plane in Figure 2.7 A. The precession of the transverse magnetisation about the vertical axis produces a rotating magnetic field, which induces an oscillating current in a nearby coil. This oscillating current induced by the precession of the transverse magnetisation, illustrated in Figure 2.7 B and known as the free induction decay (FID), is acquired as the NMR signal. The NMR signal is Fourier transformed (FT) to obtain the information in the frequency domain that is presented in a normal NMR spectrum schematically shown in Figure 2.7 C.

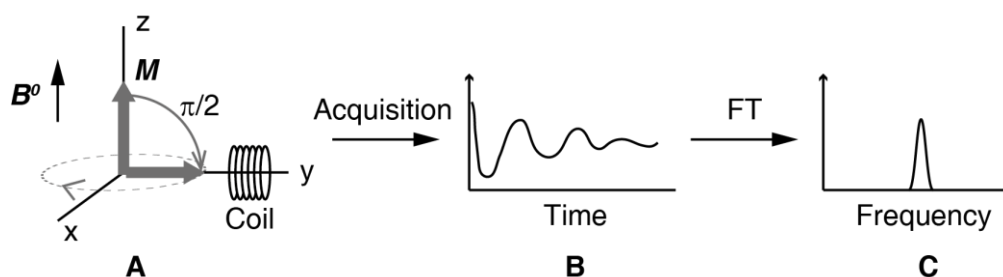


Figure 2.7. Illustration of a simple NMR experiment. (A) An r.f. pulse rotates the net magnetisation M (along z) by $\pi/2$ into the y axis, and the magnetisation will precess in the transverse plane (x - y plane). (B) The oscillating signal acquired by the coil when the magnetisation precesses about the z direction in the transverse plane. (C) The NMR spectrum is obtained by FT of the signal in time domain. Figure modified from reference [68]

2.2.2 Chemical shift and solid state NMR spectroscopy

Because a nucleus is surrounded by electrons, which also possess magnetic moments, the application of the external field (\mathbf{B}^0) will induce currents of electrons, which generate a magnetic field that either adds to or subtracts from \mathbf{B}^0 at the nucleus. This perturbation in the magnetic field experienced by the nucleus causes a shift in the nuclear spin precession frequency, known as the chemical shift. The total frequency of the nuclear spin becomes the sum of the Larmor frequency and the frequency shift due to the chemical shift. In practice, the chemical shift of a nuclear spin is expressed with respect to the frequency of the same spin in a reference substance. If the frequency of the nuclear spin of interest is ν and the frequency of the same spin in a reference substance is ν_{ref} , the chemical shift, δ , which is quoted in ppm, is given by

$$\delta = \frac{\nu - \nu_{ref}}{\nu_{ref}} \quad (2.21)$$

In frequency units (Hz), the chemical shift is directly given by $\nu - \nu_{ref}$.

Because the induced local field depends on the relative orientation of the molecule or crystal to \mathbf{B}^0 , the chemical shift is also orientation dependent or anisotropic. In liquid NMR, the molecules rapidly tumble through every possible orientation with equal probability, which removes the chemical shift anisotropy (CSA). Consequently, only a single peak is observed with a shift corresponding to the averaged value referred to as the isotropic shift. In contrast, a static powder sample, where crystals are randomly orientated, the CSA will result in a distribution of the chemical shift and a broadening in the NMR spectrum, as shown in Figure 2.8.

CSA due to a powder sample can be removed by the application of magic angle spinning (MAS) in solid state NMR[69]. MAS is carried out by spinning the powder sample about an axis that makes an angle $\theta_r=54.7^\circ$, known as the “magic angle”, to the external magnetic field (\mathbf{B}^0), as shown in Figure 2.9 A. The CSA can be completely removed when the spinning speed is greater than the size of the CSA, resulting in the observation of only isotropic shift; when the spinning speed is less than the CSA, a series of peaks start to appear at frequencies of integer multiples of the spinning speed from the isotropic shift, due to the incomplete averaging of the CSA. These peaks are known as the spinning side bands. Figure 2.9 B shows an example of the ^{31}P MAS NMR spectrum of LiFePO_4 powder.

For paramagnetic materials, such as LiFePO_4 , the dominant internal contribution to the local magnetic field at the nucleus comes from the unpaired electrons of the paramagnetic ions [70]. This interaction leads to a line shape that resembles CSA and can also be removed by MAS.

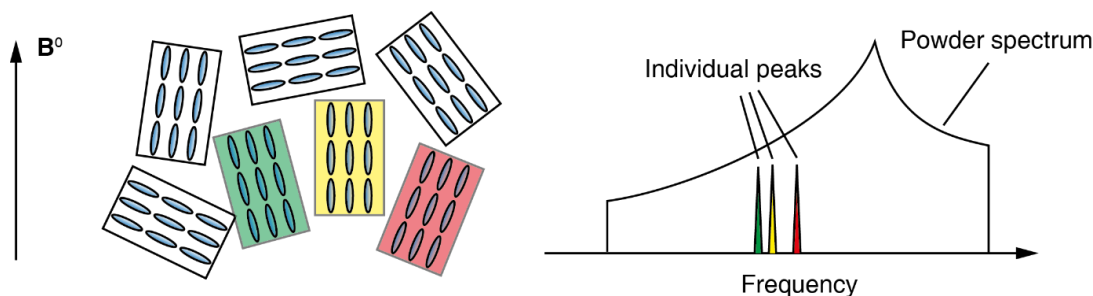


Figure 2.8. Illustration of the orientation dependence of the chemical shift. The crystals highlighted in green, yellow and red, have different orientations and giving rise to peaks indicated by the respective colour. Figure modified from reference [71].

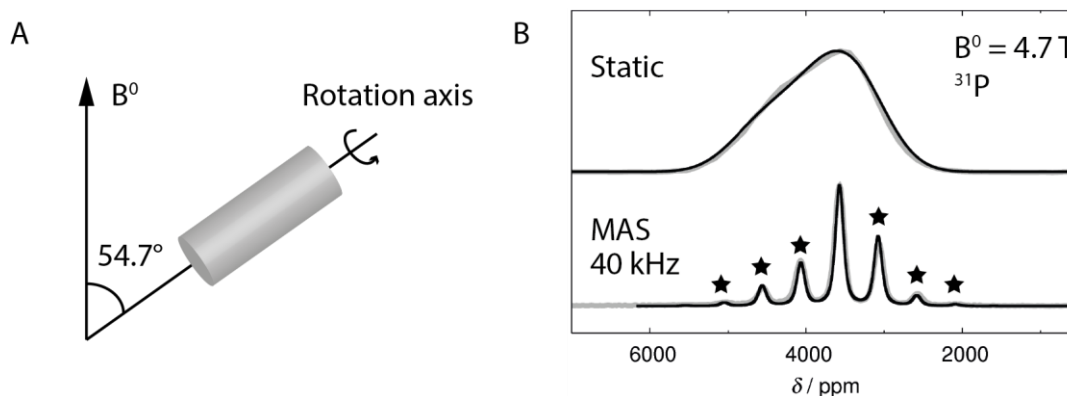


Figure 2.9 (A) Schematic illustration of magic angle spinning (MAS), where a powder sample spins about the axis that makes an angle of 54.7° (“magic angle”) to the external magnetic field (B^0). (B) The ^{31}P MAS NMR spectrum at a spinning speed of 40 kHz in comparison with the static NMR spectrum of LiFePO_4 powder. The spinning side bands are indicated by stars. Figure adapted, with permission, from my colleague Dr. Oliver Pecher.

2.2.3 Li NMR of LiFePO_4

There are two NMR active Li isotopes, ^6Li ($I = 1$) and ^7Li ($I = 3/2$), that can be used for the Li NMR measurement of LiFePO_4 . The interaction between the Li nuclei and the average magnetic moment of the unpaired electrons causes a large broadening in the powder spectrum, as shown by the red spectrum in Figure 2.10. Due to the finite length of the r.f. pulse, only nuclear spins within a finite frequency range centred about the carrier frequency will be excited. To obtain a spectrum where the intensity at the edge of

the excited spectrum is reduced to 90% of the full intensity, the r.f. pulse length is given by[72]

$$\tau_{rf} = \frac{0.4}{\omega} \quad (2.22)$$

where τ_{rf} is the r.f. pulse length required to rotate the nuclear spin by 90° , and ω is the excitation width defined by the difference between the frequency at the edge of spectrum and the carrier frequency. According to (2.22), to excite the entire ${}^7\text{Li}$ NMR spectrum of LiFePO_4 as shown in Figure 2.10 when the carrier frequency is at 0 kHz, ω is equal to 500 kHz and the corresponding r.f. pulse length is $0.8 \mu\text{s}$. Therefore, for r.f. pulses that are longer than $0.8 \mu\text{s}$, the spectrum will only be partially excited as schematically illustrated by the blue spectrum in Figure 2.10.

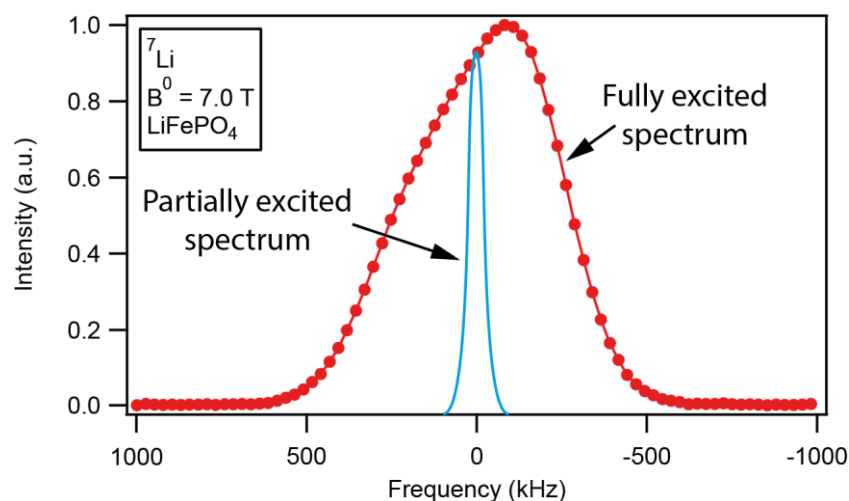


Figure 2.10. The red spectrum shows the fully excited ${}^7\text{Li}$ NMR spectrum of a LiFePO_4 powder. When a long r.f. pulse is used, only part of the spectrum will be excited as illustrated schematically by the blue spectrum. Figure adapted, with permission, from my colleague Dr. Oliver Pecher.

3 Determination of the Li tracer diffusivity in LiFePO₄ from Li isotope exchange experiment

3.1 Introduction

Solid state Li-ion diffusion plays an important role in understanding the rate capability of any Li-ion battery electrode. Despite being the subject of both theoretical[10,37] and experimental[44–49,73,74] investigations, reported values for the Li diffusivity in LiFePO₄ span from 10⁻¹⁴ cm² s⁻¹ to 10⁻⁸ cm² s⁻¹. The large disparity in the literature values can be attributed, at least in part, to the different methods (microscopic vs. macroscopic methods) used in obtaining the Li diffusivity.

In microscopic methods, diffusion is assumed to occur by random jumps of Li between adjacent sites on a lattice. The relationship between the tracer diffusivity, D , and the Li jump frequency, Γ , is given by:

$$D = \frac{1}{2} l^2 \Gamma \quad (3.1)$$

where l is the distance between successive jumps. Since Li diffusion in LiFePO₄ is well established experimentally[7] and theoretically[8,9] to follow a one-dimensional (1-D) wavy path, as shown in Figure 3.1, l is well defined by the crystal structure. Hence, microscopic measurement of diffusion largely hinges on the determination of Li jump frequency and yields the *tracer diffusivity*: theoretical calculations predict a tracer diffusivity on the order of 10⁻⁸ cm² s⁻¹, while muon spin relaxation measurements[44–46] consistently yield values on the order of 10⁻¹⁰ cm² s⁻¹.

In contrast, the macroscopic method treats diffusion as described by Fick's law of diffusion and relates diffusion flux with the concentration gradient. The diffusivity is determined by matching the experimental observables, such as flux, with theoretical solutions of Fick's diffusion equations subject to certain boundary conditions. The macroscopic method is commonly adopted by electrochemical techniques: measurements by cyclic voltammetry (CV)[47,48], galvanostatic/potentiostatic titration techniques (GITT/PITT)[47,49,73,74], and electrochemical impedance spectroscopy (EIS)[47], yield Li diffusivity in the range 10⁻¹⁴ ~ 10⁻¹¹ cm² s⁻¹. Since the above measurements (CV, GITT/PITT and EIS) are carried out with a gradient in Li concentration, the measured diffusivity is the *chemical diffusivity* of Li, which is related to the *tracer diffusivity* by:

$$\tilde{D} = D \left(1 + \frac{d \ln \gamma}{d \ln X} \right) \quad (3.2)$$

where D is the tracer diffusivity, \tilde{D} is the chemical diffusivity, γ is the thermodynamic activity coefficient and X is the mole fraction of the diffusing species. Notwithstanding the inherent difference between tracer and chemical diffusivity, the large discrepancy in the Li chemical diffusivity of LiFePO_4 obtained from the electrochemical methods also arises from the difficulty in the accurate determination of the active surface area (the surface that allows Li transport between LiFePO_4 and the electrolyte), which is needed as a parameter to calculate the Li chemical diffusivity from the theoretical solution to Fick's equations. Another inadequacy of the electrochemical methods arises from the assumption of a single-phase reaction. This leads to the theoretical solution used to calculate the chemical diffusivity, whereas delithiation of LiFePO_4 nominally takes place by a two-phase reaction. Yet, this problem can be overcome if measurements are carried out only within the single-phase regime of LiFePO_4 . As a consequence of the above inadequacies, the measured Li chemical diffusivity becomes more of a reflection of the electrode architecture than a real assessment of the Li diffusion in LiFePO_4 .

In principle, measurement of the same type of diffusion, for example tracer diffusivity, should yield the same value regardless of the methods employed. To independently check the validity of the high tracer diffusivity obtained from microscopic measurements, a different macroscopic method that exploits the cation (Li^+) exchange between Li^+ in the liquid LiPF_6 electrolyte solution (with 92.5 % ^7Li and 7.5 % ^6Li) and Li^+ in the solid LiFePO_4 (with 4 % ^6Li and 96 % ^7Li) particles is adopted to determine the Li tracer diffusivity in LiFePO_4 . Details of the model are described in the next section.

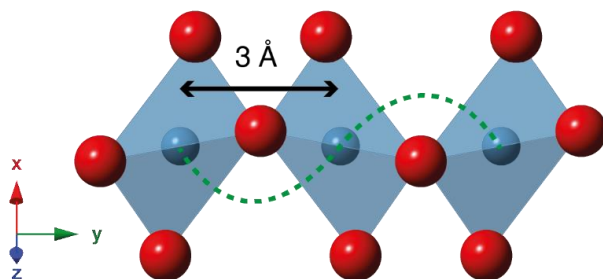


Figure 3.1 The edge sharing LiO_6 octahedral chain of LiFePO_4 . The blue and red spheres represent Li and O, respectively. The wavy dashed green curve indicates the Li diffusion path.

3.2 Theory

3.2.1 Ion exchange for LiFePO₄

The ion exchange usually takes place via inter diffusion between ions in the liquid and the solid phases, which are tagged with two different isotopic species. For an infinite plane with thickness L , the fraction of ions in the solid that has exchanged with ions in the liquid after an exchange time t , known as tracer exchange and denoted by $\gamma(t)$, can be solved from Fick's diffusion equations and expressed as[75]

$$\gamma(t) = 1 - \frac{8}{\pi^2} \sum_{n=0}^{\infty} \frac{1}{(2n+1)^2} \exp\left(-\frac{(2n+1)^2 \pi^2 D' t}{L^2}\right) \quad (3.3)$$

where D' is the inter diffusion coefficient for the out-going (from solid to liquid) and incoming (from liquid to solid) ions. Under the assumption that the isotopic effect is negligible, the inter diffusion coefficient (D') can be replaced by the tracer diffusivity of the isotope.

In LiFePO₄, since each LiO₆ (Figure 3.1) octahedron accommodates at most one Li, a jump to an adjacent Li site is only possible when that adjacent site is vacant. This introduces a correlation between Li motion along the LiO₆ chain, and the Li diffusion cannot be described as random jumps since the possibility of the Li jump now depends on the occupancy of the adjacent site. Diffusion in such a system, where the diffusing species cannot overtake its neighbours, is known as single-file diffusion. Consequently, (3.3) is not valid in describing ion exchange subject to single-file diffusion as exchange cannot take place by inter diffusion of Li due to the exclusion of mutual passages of Li along the diffusion channel. Instead, ion exchange can only take place at both ends of the channel: expelling an ion from the terminal site of the channel creates a vacancy which can then be occupied by an ion from the liquid. Li diffusion between channels is predicted to be several orders of magnitude lower than Li diffusion within channels[8,10,37], and is not considered to substantially affect the single-file diffusion process.

Tracer exchange subject to single-file diffusion has been worked out by Vasenkov *et al.*[76]:

$$\gamma(t) = \frac{4}{L} \sqrt{\frac{F}{\pi}} t^{1/4} \quad (3.4)$$

where L is the length of the channel and F is the single-file mobility factor defined as

$$F = \sqrt{\frac{\Gamma}{2\pi} \frac{1 - \Theta}{\Theta}} l^2 \quad (3.5)$$

with Γ being the frequency of the attempted jump, l being the distance between two adjacent sites, and Θ being the occupancy of available sites in the channel. An attempted jump is successful only when the jump is directed to an adjacent vacant site and is equivalent to the jump frequency given in (3.1). Although the diffusion coefficient has little significance in single-file diffusion, the fundamental parameters l and Γ can be used to obtain F or vice versa if Θ is known. A distinct character of tracer exchange, subject to single-file diffusion, is the dependence on $t^{1/4}$.

Since tracer exchange will approach 1 at longer times, it cannot increase with $t^{1/4}$ indefinitely as described in (3.4). At very long times, tracer exchange deviates from $t^{1/4}$ dependence and follows (3.3) with D' being replaced by the centre of mass diffusivity (D_{cm}) given by [77,78]:

$$D_{cm} = \frac{(1 - \Theta)D}{L\Theta} \quad (3.6)$$

3.2.2 Relationship between tracer exchange and isotopic abundance

Since tracer exchange is usually obtained through the measurement of the isotopic abundance in the solid and/or liquid, the relationship between tracer exchange and isotopic abundance needs to be established. If ions in the liquid are tagged only by one isotope, for example ^7Li , and are infinite in number relative to the ions in the solid, which are tagged only by a different isotope, for example ^6Li , tracer exchange is simply given by the fraction of ^7Li nuclei in the solid. When the number of ions in the liquid is not infinitely large in comparison to ions in the solid, the isotope abundance in the liquid changes as ion exchange takes place and tracer exchange is not directly given by the isotope abundance in the solid.

Consider a single-file channel with M_s moles of Li, of which the ^6Li abundance is f_s , immersed in a liquid with M_l moles of Li, of which the ^6Li abundance is f_l . Since the ^6Li abundance in both the solid and liquid changes with time and is a function of time, for the sake of clarity, the ^6Li abundance in the solid and the liquid before any ion exchange takes place is denoted by $f_s(0)$ and $f_l(0)$ (assuming $f_l(0) < f_s(0)$ for the sake of argument), respectively. If the channel is described with a fractional coordinate x that

ranges from 0 at one end to 1 at the other end of the channel, a tracer exchange $\gamma(t)$ is equivalent to the fraction of the channel that has undergone ion exchange, as illustrated in Figure 3.2. To relate tracer exchange $\gamma(t)$ to the ${}^6\text{Li}$ abundance of the channel $f_s(t)$, $f_s(t)$ can be expressed by integrating the local ${}^6\text{Li}$ abundance profile $\tilde{f}_s(x, t)$ (x defined between 0 and 1) across the channel while noting $\tilde{f}_s(x, t) = f_s(0)$ in the unexchanged region:

$$f_s(t) = \int_0^1 \tilde{f}_s(x, t) dx = \int_0^{\gamma(t)} \tilde{f}_s(x, t) dx + f_s(0) \cdot (1 - \gamma(t)) \quad (3.7)$$

where the integral between 0 and $\gamma(t)$ is performed over the red region as shown in Figure 3.2. Since $\gamma(t)$ is contained in the integral $\int_0^{\gamma(t)} \tilde{f}_s(x, t) dx$ and $\tilde{f}_s(x, t)$ varies with x in the exchanged region, solving for $\gamma(t)$ is not trivial in this case. Hence, only the upper and lower limits of $\gamma(t)$ are derived here.

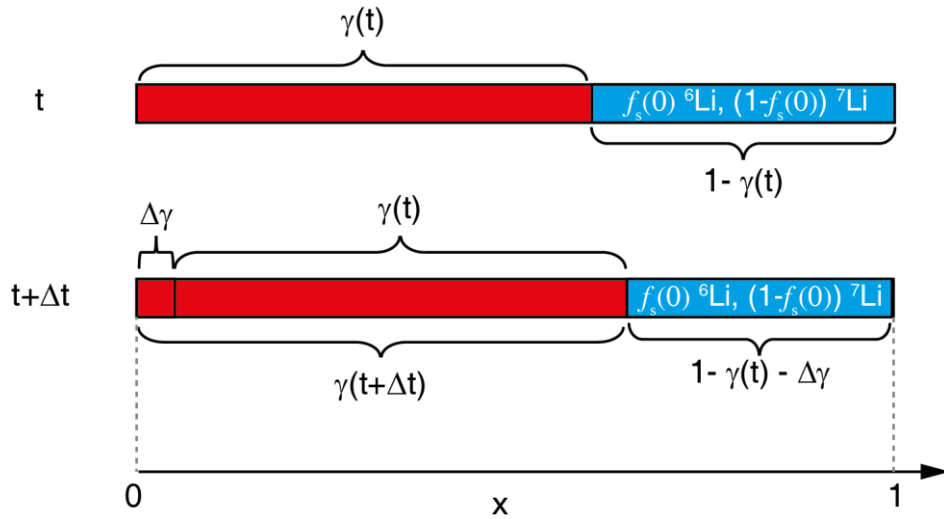


Figure 3.2 The distributions of Li in a single channel that has (red) and has not (cyan) been exchanged with the Li in the electrolyte at time t and $t+\Delta t$ after the start of exchange. The tracer exchange γ defined as the fraction of ions in the channel that have undergone exchange, i.e. the ratio between the length of the red region and the length of the entire channel (red + cyan). The position of a Li in the channel is normalised against the channel length and is described by the dimensionless fractional coordinate x .

The upper limit can be obtained by noting that the ${}^6\text{Li}$ abundance in the liquid, $f_l(t)$, increases with time (since it has been previously assumed that $f_l(0) < f_s(0)$), hence, $\tilde{f}_s(x, t)$ must be less than or equal to $f_l(t)$ anywhere in the in the exchanged fraction of the channel:

$$\int_0^{\gamma(t)} \tilde{f}_s(x, t) dx \leq \int_0^{\gamma(t)} f_l(t) dx = f_l(t) \cdot \gamma \quad (3.8)$$

Substituting (3.8) into (3.7) yields the following inequality:

$$f_s(t) \leq f_l(t) \cdot \gamma + f_s(0) \cdot (1 - \gamma(t)) \quad (3.9)$$

Noting $f_l(t) < f_s(0)$, rearranging the above inequality gives:

$$\gamma(t) \leq \frac{f_s(0) - f_s(t)}{f_s(0) - f_l(t)} \quad (3.10)$$

which defines the upper limit of $\gamma(t)$.

To estimate the lower limit of $\gamma(t)$, consider the change in f_s after a small time increment Δt :

$$\begin{aligned} \Delta f_s(t) &= f_s(t + \Delta t) - f_s(t) \\ &= \int_{\Delta\gamma}^{\Delta\gamma + \gamma(t)} \tilde{f}_s(x, t + \Delta t) dx + \int_0^{\Delta\gamma} \tilde{f}_s(x, t + \Delta t) dx - \int_0^{\gamma(t)} \tilde{f}_s(x, t) dx - f_s(0) \cdot \Delta\gamma \end{aligned} \quad (3.11)$$

where the relationship between $\gamma(t)$ and $\Delta\gamma$ is illustrated in Figure 3.2. Since the total amount of ${}^6\text{Li}$ in the region $\Delta\gamma < x < \gamma(t) + \Delta\gamma$ at $t + \Delta t$ is no less than ${}^6\text{Li}$ in the region $0 < x < \gamma(t)$ at t , the difference between the integrals $\int_{\Delta\gamma}^{\Delta\gamma + \gamma(t)} \tilde{f}_s(x, t + \Delta t) dx - \int_0^{\gamma(t)} \tilde{f}_s(x, t) dx$ is always non-negative. In addition, ${}^6\text{Li}$ abundance in the incremental exchanged region $\Delta\gamma$ cannot exceed the ${}^6\text{Li}$ abundance of the liquid, hence, $\tilde{f}_s(x, t + \Delta t) \geq f_l(t)$ for $0 < x < \Delta\gamma$. Substituting both relations into (3.11) yields the inequality (noting $\Delta f_s(t) < 0$):

$$\Delta f_s(t) + f_s(0) \cdot \Delta\gamma \geq \int_0^{\Delta\gamma} f_l(t) dx = f_l(t) \cdot \Delta\gamma \quad (3.12)$$

$$\Delta\gamma \geq -\frac{\Delta f_s(t)}{f_s(0) - f_l(t)} \quad (3.13)$$

Since $\gamma(t) = \int_0^t d\gamma$ can be approximated by a summation of $\Delta\gamma$, the lower limit of $\gamma(t)$ can be expressed by the inequality below:

$$\gamma(t) = \int_0^t d\gamma \cong \sum_i \Delta\gamma(t_i) \geq \sum_i -\frac{\Delta f_s(t)}{f_s(0) - f_l(t)} \quad (3.14)$$

When the ${}^6\text{Li}$ abundance of the liquid (f_l) is kept constant over time, the limits given by (3.10) and (3.14) becomes identical and yield the exact result for $\gamma(t)$.

The ${}^6\text{Li}$ abundance of the electrolyte can be obtained on the basis of conservation of matter in closed system (ions in the channel and the liquid):

$$f_s(0) \cdot M_s + f_l(0) \cdot M_l = f_s(t) \cdot M_s + f_l(t) \cdot M_l \quad (3.15)$$

As $f_s(0)$ and $f_l(0)$ are known from the starting solid and liquid, respectively, one only needs to obtain at least one of $f_s(t)$ and $f_l(t)$ in order to estimate the lower and upper limits of tracer exchange.

The above derivations show that experimentally measurable parameters, such as ${}^6\text{Li}/{}^7\text{Li}$ abundance, can be related to the desired tracer exchange used in ion exchange models if the ${}^6\text{Li}$ abundance in the starting liquid and solid phases and the molar ratio of Li in the liquid and solid phase are known.

3.3 Experimental method

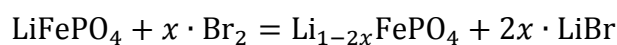
3.3.1 Materials synthesis and preparation

Since ion exchange is a macroscopic method, knowledge of the microstructure of the sample is still required to obtain the attempted jump frequency of Li. According to (3.4), the diffusion channel length (L) of the sample is needed to obtain the single-file mobility factor (F), from which the attempted jump frequency (Γ) can be determined through (3.5) if the Li occupancy in the diffusion channel is known. To reduce the uncertainty of the attempted jump frequency due to errors in L and Θ , it is important to use samples with well-defined L and Θ and perform ion exchange experiment over different L and Θ pairs. Samples with well-defined crystal facets are preferred for obtaining accurate diffusion channel length. Solvothermal syntheses[79,80] have been shown to produce LiFePO_4 crystals of platelet morphology with the short axis parallel to the Li diffusion channel and were adopted in this study. The use of ethylene glycol (EG)[80] and polyethylene glycol (PEG)[79] as synthesis solvents has been shown to produce nano (35 nm thick) and micron (a few hundred nm thick) platelets, respectively, which would give two different L values.

For the synthesis carried out with EG solvent, 0.0016 mol $\text{FeSO}_4 \cdot 7\text{H}_2\text{O}$ (Fisher Scientific) and 0.004 mol ^6Li -enriched $\text{LiOH} \cdot \text{H}_2\text{O}$ (Cambridge Isotope, 96 % ^6Li) were separately dissolved in 8 mL EG by sonication. The FeSO_4 EG solution was added to 0.0016 mol phosphoric acid (85wt% aqueous solution, Sigma Aldrich). LiOH EG solution was further added dropwise to the acidic FeSO_4 solution under mechanical stirring, resulting in the formation of dark green precipitates. The mixture was stirred for 5 min before being transferred to a 22 mL Teflon sleeve in an autoclave. The autoclave was heated at 180 °C for 10 hours. LiFePO_4 particles were collected by centrifuge, washed with water and ethanol and dried in a vacuum oven at 100 °C overnight.

For the synthesis carried out with PEG solvent, 0.00225 mol H_3PO_4 (85 wt% aqueous solution, Sigma Aldrich) was mixed with 2.25 mL deionised water and 9 mL PEG. 0.00675 mol ^6Li enriched $\text{LiOH} \cdot \text{H}_2\text{O}$ (Cambridge Isotope, 96% ^6Li) and 0.00225 mol $\text{FeSO}_4 \cdot 7\text{H}_2\text{O}$ (Fisher Scientific) were dissolved in 6.75 mL and 4.5 mL deionised water, respectively. FeSO_4 solution was added dropwise to the H_3PO_4 solution under mechanical stirring, resulting in the formation of white precipitates. LiOH solution was subsequently introduced dropwise into the mixture, and the precipitates turned a light green colour. The mixture was stirred for a further 5 min before being transferred to a 45 mL Teflon sleeve. The mixture in the Teflon sleeve was purged with Ar for 2 min, sealed in a Parr reactor, and kept at 180 °C for 24 hours. The product was collected by centrifuge, washed with water and ethanol and dried in a vacuum oven at 100 °C overnight.

To prepare samples of different Li occupancy (Θ), the sample synthesised in EG was partially delithiated by Br_2 via the following reaction[18]:



Two batches of 0.043 g pristine sample synthesised in EG were reacted with approximately 0.02 mmol and 0.01 mmol Br_2 , respectively, in 5 mL acetonitrile with constant stirring, and the partially delithiated samples are referred to as EG A and EG B, respectively. The partially delithiated samples were sequentially washed with acetone and then ethanol, and dried at 100 °C in vacuum overnight.

3.3.2 Li solid state NMR measurement

The evolution of the Li isotope concentration in LiFePO_4 was measured with both *ex situ* and *in situ* methods. The spin-echo pulse sequence ($90^\circ - \tau - 180^\circ - \tau - \text{acquire}$) was used

to acquire the Li spectra in both methods, and all spectra were referenced to 1 M LiCl solution at 0 ppm.

For a typical *in situ* NMR measurement, 15 mg of ^6Li -enriched LiFePO_4 powder was wrapped in a piece of tissue paper (KIMTECH delicate task wipers) to keep the sample fixed in space. The wrapped sample was inserted into a 5 mm NMR tube. The NMR tube (with the wrapped LiFePO_4 sample inside) was dried in a vacuum oven at 100 °C overnight before being taken into the Ar-filled glove box. 0.5 mL 1 M LiPF_6 (natural ^6Li and ^7Li abundance) in EC and DMC electrolyte solution was quickly added to the NMR tube using a syringe, and the LiFePO_4 powder was completely immersed in the electrolyte while the powder sample was still kept in place due to the tissue paper. The NMR tube was sealed with a cap, taken out of the glove box and placed inside the NMR coil of a static probe. The ^6Li and ^7Li abundance of the starting LiFePO_4 and LiPF_6 electrolyte are summarised in Table 3.1. Figure 3.3 shows an image of a sealed NMR tube. The static probe was used on a Bruker 300 spectrometer for measurement. *In situ* ^6Li NMR spectra were recorded continuously to monitor the evolution of the ^6Li population in the sample as a function of immersion time. The ^6Li NMR spectra were acquired with a spin-echo pulse sequence with a recycle delay of 0.1 s, and the measurement of each spectrum took 60 min. The short recycle delay suppresses the ^6Li signal from the electrolyte, and only ^6Li signal from LiFePO_4 was measured in practice. Due to the time required to transfer sample from the glove box to the NMR probe, the acquisition of the first *in situ* NMR spectrum was started only after the LiFePO_4 powder had been immersed in the electrolyte and undergone exchange for approximately 15 min. Since the ^6Li signal intensity is only proportional to the ^6Li population, the evolution of the ^6Li signal intensity is also only proportional to, but does not provide a direct measurement of the evolution of ^6Li abundance. To obtain the ^6Li abundance from ^6Li NMR signal intensity, one only needs to know the ^6Li abundance at any one of the points measured by *in situ* NMR experiment to obtain the proportionality between ^6Li abundance and intensity. This can be done by the *ex situ* NMR measurement of a sample that has undergone the same exchange process as any one of the points from *in situ* NMR measurement.

For a typical *ex situ* NMR measurement, 15 mg of ^6Li -enriched LiFePO_4 powder was immersed in 0.5 mL 1 M LiPF_6 (natural ^6Li and ^7Li abundance) in ethylene carbonate (EC) and dimethyl carbonate (DMC) electrolyte solution in an Ar-filled glove box for a desired period of time, after which the electrolyte was removed and the LiFePO_4 powder

was washed with DMC three times and dried in vacuum. Magic angle spinning (MAS) ^6Li and ^7Li NMR spectra were acquired on a Bruker 300 spectrometer. A spin-echo pulse sequence was applied with a recycle delay of 0.1 s and a spinning speed of 25 kHz. The ^6Li to ^7Li molar ratio of the immersed sample was determined by comparing the integrated intensities of the ^6Li and ^7Li spectra with those obtained for the pristine LiFePO_4 sample with known ^6Li (96%) and ^7Li (4%) abundances.

Table 3.1 ^6Li and ^7Li abundance of all Li containing species at the onset of the ion exchange experiment ($t = 0$, i.e. no contact between the LiFePO_4 powder and the LiPF_6 electrolyte).

	Number of Li nuclei (x 10^{-4} mol)	^6Li abundance	^7Li abundance
LiPF_6	5	7.5 %	92.5 %
LiFePO_4	0.96	96 %	4 %
$\text{LiPF}_6 + \text{LiFePO}_4$	5.96	22 %	78 %

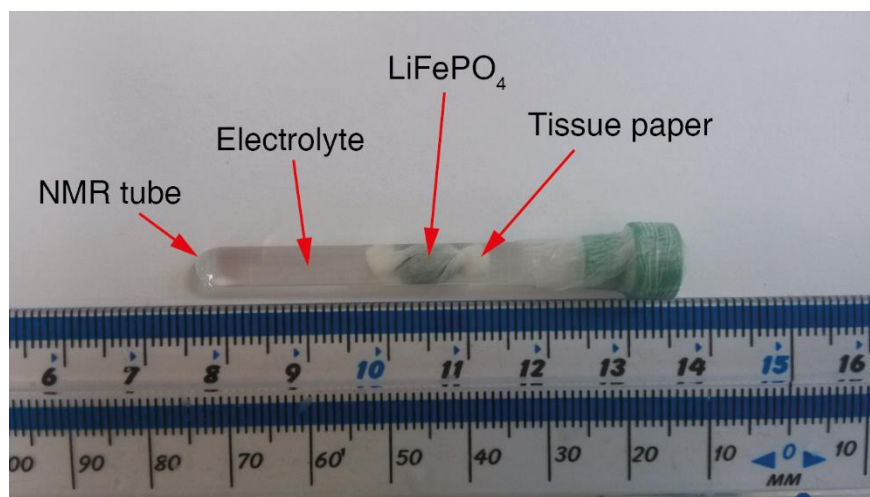


Figure 3.3 A sealed NMR tube containing the wrapped ^6Li -enriched LiFePO_4 powder immersed in 1 M LiPF_6 in EC and DMC electrolyte solution.

3.3.3 X-ray powder diffraction and Rietveld refinement

The XRD patterns of synthesised LiFePO_4 were collected at room temperature using a Panalytical Empyrean diffractometer equipped with $\text{Cu K}\alpha$. Measurements were taken with a step size of 0.0167° in Bragg-Brentano reflection geometry.

Rietveld refinements were performed with the TOPAS software package[81] in the 2θ range 10° -- 90° . The background was modelled with a Chebyshev polynomial with 6 coefficients. The scale factor and the sample displacement were refined. The Thompson-Cox-Hasting pseudo-Voigt peak profile was used for LiFePO_4 synthesised in PEG, and preferred orientation along the $(0k0)$ direction was included. For LiFePO_4 synthesised in EG, the peak profile was modelled with anisotropic size broadening (Lorentzian shape) and isotropic strain broadening (Gaussian shape). The anisotropic size broadening is described by

$$H_L = \frac{\lambda}{\cos\theta} \sum_{ij} C_{ij} Y_{ij} \quad (3.16)$$

where H_L is the full width at half maximum (FWHM) of a Lorentzian peak, λ is the X-ray wavelength, Y_{ij} are the symmetrised spherical harmonics[82], and C_{ij} are the refined parameters. The volume averaged length along a certain crystal axis, $\langle L_{hkl} \rangle_V$, can be obtained by

$$\langle L_{hkl} \rangle_V = \frac{2}{\pi \sum_{ij} C_{ij} Y_{ij}} \quad (3.17)$$

The isotropic strain broadening is described by

$$H_G = \varepsilon \tan\theta \quad (3.18)$$

where H_G is the FWHM of a Gaussian peak, and ε is the refined isotropic strain parameter. The structure was described in the $Pnma$ space group, and unit cell and atomic positions were refined. Isotropic atomic displacement parameters (ADP) were refined for Fe, P and O atoms, where the ADP for O atoms at different sites were constrained to be identical. The ADP for Li was fixed at 1.5 and not refined.

3.4 Results and discussion

3.4.1 Sample characterisation

The XRD patterns of the pristine ^6Li -enriched LiFePO_4 particles are shown in Figure 3.4. All reflections are indexed in the $Pnma$ space group, which is adopted by LiFePO_4 . No impurity phases were observed. Table 3.2 summarises the LiFePO_4 lattice parameters obtained from the Rietveld refinements. The unit cell volume for the sample synthesised in PEG are similar to the values obtained for a defect-free LiFePO_4 determined by X-ray diffraction from prior studies ($V = 291.4 \text{ \AA}^3$ [39]). However, the pristine sample synthesised in EG shows noticeably smaller lattice parameters. The contraction in lattice

parameters is usually attributed to the existence of Fe^{3+} through a partial delithiation process when LiFePO_4 is exposed to water/moisture or oxidative atmosphere[83,84] and/or the formation of Fe vacancies usually found for the low temperature (~ 100 °C) precipitation synthesis[85,86]. As expected, the partial delithiation of the pristine particles synthesised in EG by Br_2 results in a substantial decrease in the lattice volume. Assuming the unit cell contraction is due solely to the decrease in the Li occupancy, the Li occupancy can be interpolated from the unit cell volumes by Vegard's law:

$$\Theta = \frac{V_{exp} - V_{FP}}{V_{LFP} - V_{FP}} \quad (3.19)$$

where V_{exp} is the unit cell volume of LiFePO_4 sample in this study, and V_{LFP} and V_{FP} are the unit cell volumes of stoichiometric LiFePO_4 and FePO_4 , respectively. Since Θ is more sensitive to V_{LFP} than to V_{FP} when Θ is close to 1, the choice of V_{LFP} is critical. Table 3.3 tabulates the unit cell volumes of nearly stoichiometric LiFePO_4 from the literature, and $V_{LFP} = 291.18 \text{ \AA}^3$ [42], which is obtained for hydrothermally synthesised LiFePO_4 with < 0.5 % Fe on Li site and 0.99 Li occupancy, is used in this study. The unit cell volume of stoichiometric FePO_4 is also taken from literature, and $V_{FP} = 271.7 \text{ \AA}^3$ [23], obtained from XRD of electrochemically delithiated FePO_4 , is adopted. Li occupancy deduced from Vegard's law is shown in Table 3.2. The uncertainty in Li occupancy resulting from the errors in the refined lattice parameters is only ~ 0.1 %. Nonetheless, given the difference between the reported values ($V_{LFP} = 291.4 \text{ \AA}^3$ [39] and $V_{LFP} = 291.18(1) \text{ \AA}^3$ [42] for stoichiometric LiFePO_4), which gives rise to ~ 1 % difference in Li occupancy, 1% is taken as a measure of the uncertainty in Li occupancy.

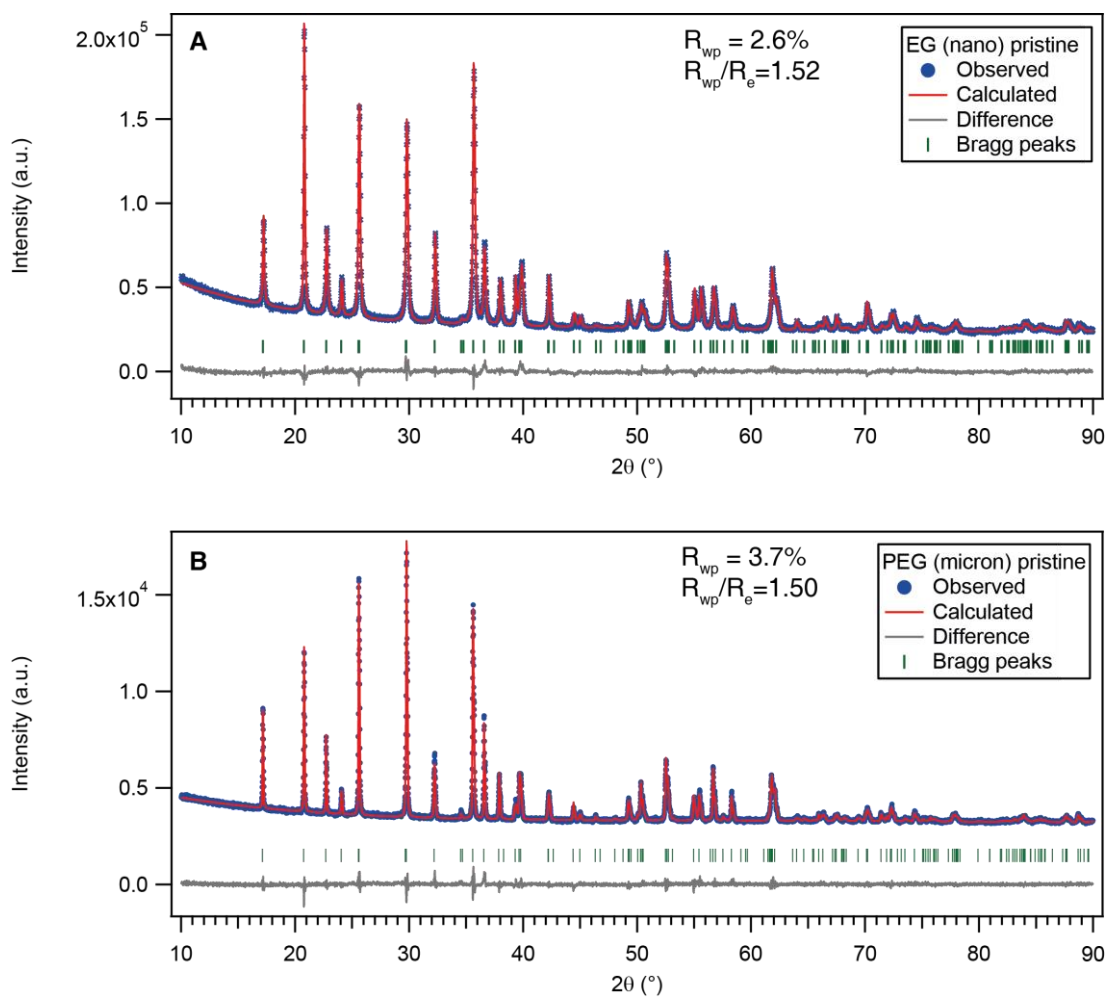


Figure 3.4 XRD patterns of the pristine (as-synthesised) ${}^6\text{Li}$ -enriched LiFePO_4 particles synthesised in (A) EG and (B) PEG. Calculated diffraction patterns for the Rietveld-refined structures are shown in red. The difference (observed – calculated) curves are shown in grey. The green ticks indicate the positions of the Bragg reflections.

Table 3.2 LiFePO_4 lattice parameters obtained from the Rietveld refinement for various samples.

Synthesis medium	$a / \text{Å}$	$b / \text{Å}$	$c / \text{Å}$	$V / \text{Å}^3$	Θ
EG (pristine)	10.3108(2)	5.9989(1)	4.6982(1)	290.60(1)	$97 \pm 1 \%$
PEG (pristine)	10.3373(1)	6.00195(5)	4.69758(7)	291.456(6)	-- ^a
EG A (delithiated)	10.2980(3)	5.9936(2)	4.7006(1)	290.13(2)	$94 \pm 1 \%$
EG B (delithiated)	10.3006(4)	5.9945(3)	4.6999(2)	290.20(2)	$95 \pm 1 \%$

^a Since its value is almost identical to the literature value, its vacancy concentration is close to zero.

Table 3.3 Literature unit cell volumes obtained for nearly stoichiometric LiFePO₄

Reference	Unit cell volume / Å ³	Synthesis method	Characterisation method	Fe defect on Li site	Li occupancy
[39]	291.4	Hydrothermal	Lab XRD	0	Unknown
[42]	291.18	Hydrothermal	Synchrotron XRD	< 0.5 %	0.99
[41]	291.16	Hydrothermal	Synchrotron XRD and neutron powder diffraction (NPD)	2 %	0.95
[87]	290.76	Solid state	NPD	0	1

The SEM images (Figure 3.5) of both samples show the expected [79,80] platelet morphology with the short axis being parallel to the Li diffusion channel (*b* axis). Due to the small crystal size, the microstructure of the sample synthesised in EG is quantified by the Scherrer analysis of the anisotropic diffraction peak broadening, which is implemented in the Rietveld refinement, and the volume weighted size along the three principal crystal axes are given in Table 3.4. The average length along the *b* axis is 50 nm. However, the crystal size of the sample synthesised in PEG is too large to contribute to substantial broadening of the XRD peaks, hence the size distribution for the short axis is measured from the SEM image. A total 26 crystals were measured, and histogram in Figure 3.6 shows the frequency that a crystal with a certain thickness along the short axis is observed. The average size of the short axis of the crystals is 255 nm. The samples synthesised in EG and PEG are henceforth referred to as Nano- and Micron-plate LiFePO₄, respectively, and the delithiated EG A and EG B samples are henceforth referred to as Nano-plate A and B, respectively.

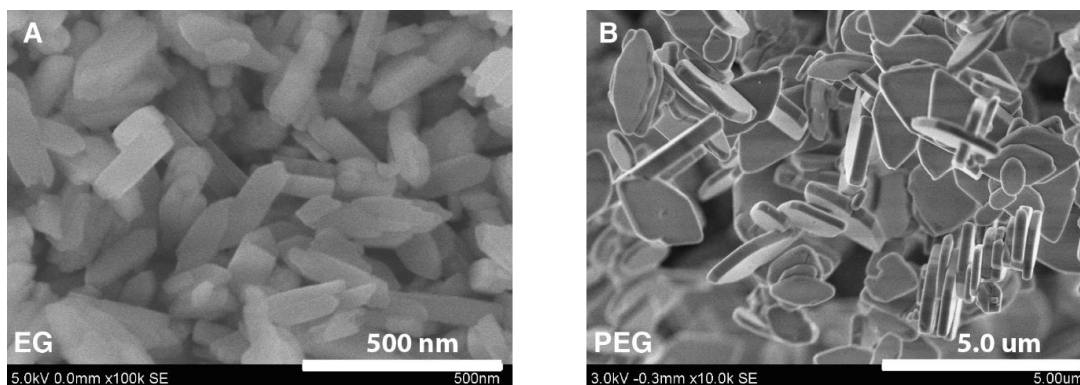


Figure 3.5 SEM images showing the LiFePO_4 crystals synthesised in (A) EG and (B) PEG.

Table 3.4 The volume weighted size (determined by Scherrer formula) of the sample synthesised in EG along the a , b , c crystal axes.

Orientation	$(h00)$	$(0k0)$	$(00l)$
Size (nm)	59	50	132

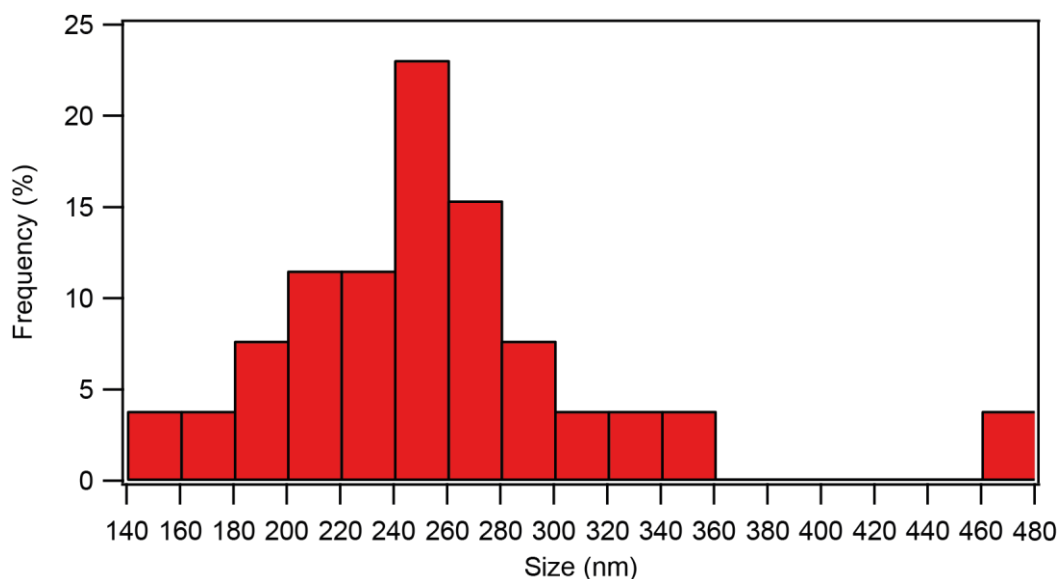


Figure 3.6 Histogram of the measured thickness along the short axis determined from 26 LiFePO_4 crystals synthesised in PEG.

Due to the large dipolar interactions between the Li nuclei and the unpaired electron of Fe^{2+} , it is difficult to excite and acquire the entire static ${}^6\text{Li}$ NMR spectrum for LiFePO_4 at a single carrier frequency. Instead, ${}^6\text{Li}$ NMR spectra acquired at different frequencies were added up to yield the complete static ${}^6\text{Li}$ NMR spectrum of LiFePO_4 . Figure 3.7 shows the summed spectrum (red) and the sub-spectra measured at various carrier frequencies measured on a Micron pristine LiFePO_4 sample immersed in DMC solvent to mimic the magnetic susceptibility of the EC/DMC electrolyte solvent. The

large span of the summed ${}^6\text{Li}$ spectrum is consistent with previous reports[88,89] for this material.

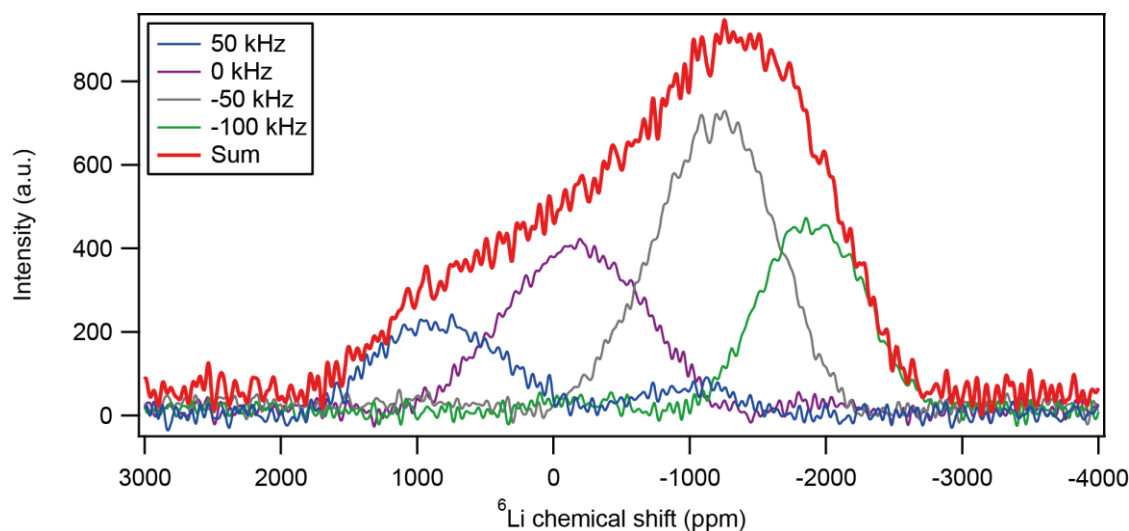


Figure 3.7 The ${}^6\text{Li}$ static NMR spectra of ${}^6\text{Li}$ -enriched Micron pristine LiFePO_4 particles in DMC solvent. The spectrum in red is obtained by summing up the ${}^6\text{Li}$ static spectra acquired at carrier frequencies of 50 kHz (~ 1130 ppm), 0 kHz, -50 kHz and -100 kHz (~ -2270 ppm).

3.4.2 The evolution of the ${}^6\text{Li}$ abundance of LiFePO_4 under soaking condition

To track the amount of ${}^6\text{Li}$ in LiFePO_4 when it is immersed in the naturally abundant ${}^6\text{Li}$ (7.5%) and ${}^7\text{Li}$ (92.5%) electrolyte, *in situ* static ${}^6\text{Li}$ NMR spectra were acquired continuously at a fixed carrier frequency equal to 0 ppm (0 kHz). Since the LiFePO_4 powder sample wrapped with tissue paper is fixed in space, the full spectrum (the red pattern in Figure 3.7) will not change in shape and will only decrease in intensity when exchange between ${}^6\text{Li}$ and ${}^7\text{Li}$ occurs. Therefore, although only a portion of the total ${}^6\text{Li}$ nuclei in the LiFePO_4 powder sample can be measured in the *in situ* NMR experiment, the population of the measured ${}^6\text{Li}$ nuclei is a fixed proportion to the entire ${}^6\text{Li}$ population and can still be used to represent the ${}^6\text{Li}$ population of the entire LiFePO_4 sample. The static ${}^6\text{Li}$ NMR spectra for pristine Nano- and Micron-plate LiFePO_4 powder samples in LiPF_6 electrolyte solution are shown in Figure 3.8 A and C, respectively. The difference in the peak width is due to the different pulse lengths applied during the measurements ($\pi/2$ pulse lengths of 11.25 μs and 7 μs for Nano- and Micron-plate samples, respectively), which lead to different excitation band widths. Figure 3.8 B and D show the *in situ* ${}^6\text{Li}$ NMR spectra obtained during the immersion of pristine Nano- and Micron-plate samples, respectively, in the LiPF_6 electrolyte solution. Acquisition of the first NMR spectrum

started at 15 min after LiFePO_4 had been immersed in the electrolyte. As each spectrum took 60 min to acquire, the average of the starting and finishing time for each spectral acquisition is taken to be the corresponding immersion time. For example, the first *in situ* NMR spectrum (acquisition started at 15 min and finished at 75 min after immersion) corresponds to an immersion time of $(15+75)/2 = 45$ min. It is noted that the ^6Li resonance due to LiPF_6 , which is expected to appear as a very sharp peak at ~ 0 ppm, is suppressed due to the short recycle delay, and only the broad peak due to ^6Li in LiFePO_4 is observed. The intensity of the $^6\text{LiFePO}_4$ peak for the Nano-plate LiFePO_4 (Figure 3.8 B) decreases over time, indicating a loss of ^6Li nuclei in LiFePO_4 . The intensity decrease for the Micron-plate sample (Figure 3.8 D) appears to be much less. Since LiFePO_4 does not react with the LiPF_6 electrolyte solution, the total amount of Li in LiFePO_4 should remain constant. The decrease of the ^6Li spectral intensity in LiFePO_4 is hence compensated for by an increase of ^7Li in LiFePO_4 via exchange between Li in LiFePO_4 and Li in the electrolyte.

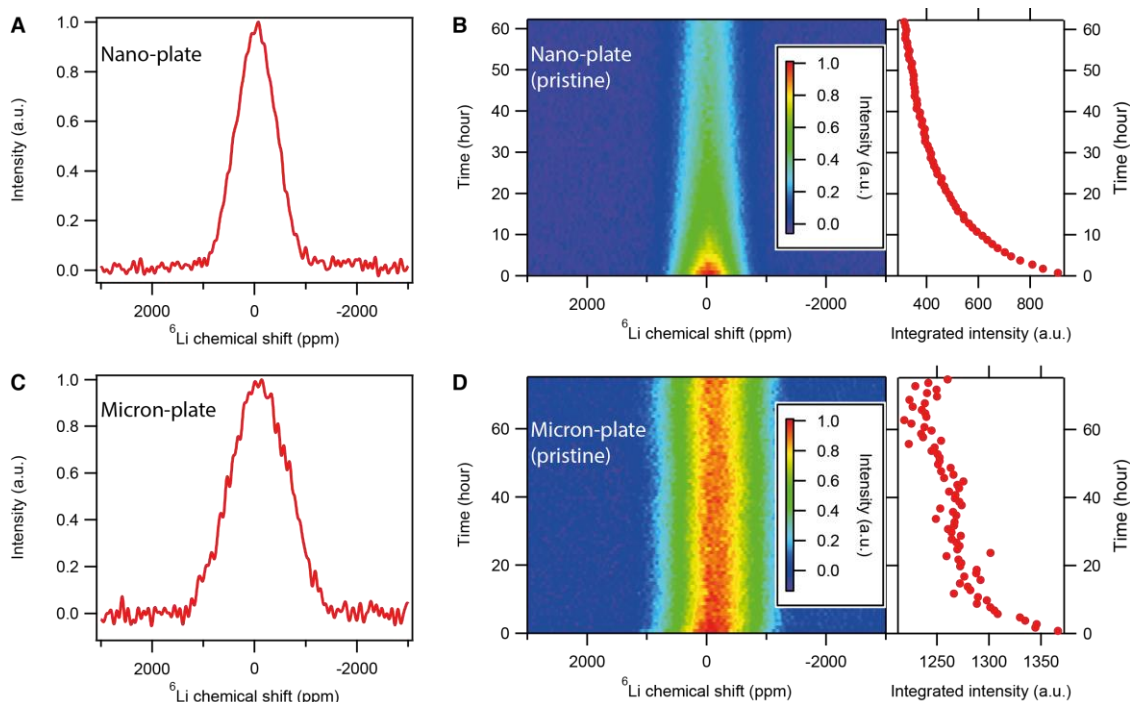


Figure 3.8 *In situ* static ${}^6\text{Li}$ NMR spectra measured with spin echo for the pristine (A) Nano- and (C) Micron-plate LiFePO_4 powder samples. $\pi/2$ pulses of $11.25\ \mu\text{s}$ and $7\ \mu\text{s}$ are for the Nano- and Micron-plate samples, respectively. Image plots of the *in situ* ${}^6\text{Li}$ NMR spectra collected while LiFePO_4 particles are immersed in the electrolyte for the (B) Nano- and (D) Micron-plate samples, the graphs next to the image plots are the corresponding integrated spectral intensities. The acquisition for the first spectrum started at 15 min after LiFePO_4 had been immersed in the electrolyte.

Since it is not known from the *in situ* spectra what the ${}^6\text{Li}$ abundance of LiFePO_4 is at the time when the first NMR spectrum was taken, *ex situ* ${}^6\text{Li}$ and ${}^7\text{Li}$ NMR spectra were measured to correlate the integrated intensities of the *in situ* ${}^6\text{Li}$ NMR spectra with the ${}^6\text{Li}$ abundance of LiFePO_4 . Taking the *in situ* NMR result of Nano-plate LiFePO_4 as an example (Figure 3.8 B), the integrated intensity of the first NMR spectrum (at $t = 45$ min) is 908, and *ex situ* NMR measurement of Nano-plate LiFePO_4 subject to the same time (45 min) and immersion conditions yields a ${}^6\text{Li}$ abundance of 0.68. The ${}^6\text{Li}$ abundance corresponding to the sample measured at $t = 45$ min in the *in situ* NMR experiment is assigned a value of 0.68 and the ${}^6\text{Li}$ abundance of the subsequent *in situ* points can be obtained by multiplying the integrated intensity with the conversion factor $\frac{0.68}{908} = 7.49 \times 10^{-4}$. For Micron-plate and Nano-plate A and B, since the immersion time for the *ex situ* measurement does not coincide the time of any of the *in situ* NMR spectra, the integrated spectral intensity, used to calculate the conversion factor, was obtained by linear interpolation between two adjacent integrated spectral intensities from the *in situ* NMR measurement. Taking the *in situ* NMR result for the Micron-plates (Figure 3.8 D)

as an example, the integrated spectral intensities for the first two spectra are 1366 and 1344, corresponding to 44 min and 104 min, respectively. Linear interpolation of the intensity at time t is carried out by

$$I_{inter}(t) = I_1 + \frac{t - t_1}{t_2 - t_1} (I_2 - I_1) \quad (3.20)$$

where I_{inter} and t represent the intensity and time, respectively, and the subscripts 1 and 2 denote two adjacent points, respectively. Applying the above relation, the interpolated intensity at 60 min is 1360. As the ${}^6\text{Li}$ abundance at 60 min determined from *ex situ* measurement is 0.95, the conversion factor is $\frac{0.95}{1360} = 6.99 \times 10^{-4}$.

Figure 3.9 shows the ${}^6\text{Li}$ abundance of various ${}^6\text{Li}$ -enriched LiFePO_4 samples as a function of the immersion time of LiFePO_4 particles in the electrolyte. The ${}^6\text{Li}$ abundance of the Nano-plate particles decreases much more rapidly than the Micron-plate particles. When the particle size is the same, a lower Li occupancy leads to a faster drop in the ${}^6\text{Li}$ abundance, as observed for the Nano-plate particles. Since the change of ${}^6\text{Li}$ abundance is caused by the Li exchange process, the result shows that the Li exchange process becomes faster as the diffusion channel length decreases and the Li occupancy decreases. At longer times (> 4000 min), the ${}^6\text{Li}$ abundances of the Nano-plate A and B appear to asymptotically approach ~ 0.2 , which is effectively the expected ${}^6\text{Li}$ abundance at long times, i.e. the ${}^6\text{Li}$ abundance of the system ($\text{LiFePO}_4 + \text{LiPF}_6$) in Table 3.1. The ability of Nano-plate samples to reach the theoretical ion exchange limit indicates that the Li diffusion channels are not affected by the Li-Fe anti-site defect, which will block Li diffusion in the channel.[38] The different decay rates for the Nano-plate samples indicate the Li exchange is not limited by the Li exchange across the solid/liquid interface.

Table 3.5 The ${}^6\text{Li}$ abundance of LiFePO_4 measured for different immersion time in the LiPF_6 electrolyte (natural ${}^6\text{Li}$ and ${}^7\text{Li}$ abundance) by the *ex situ* NMR measurement.

Immersion time / min	${}^6\text{Li}$ abundance			
	Nano-plate	Nano-plate A	Nano-plate B	Micron-plate
45	0.68	--	--	--
60	--	0.59	0.64	0.95

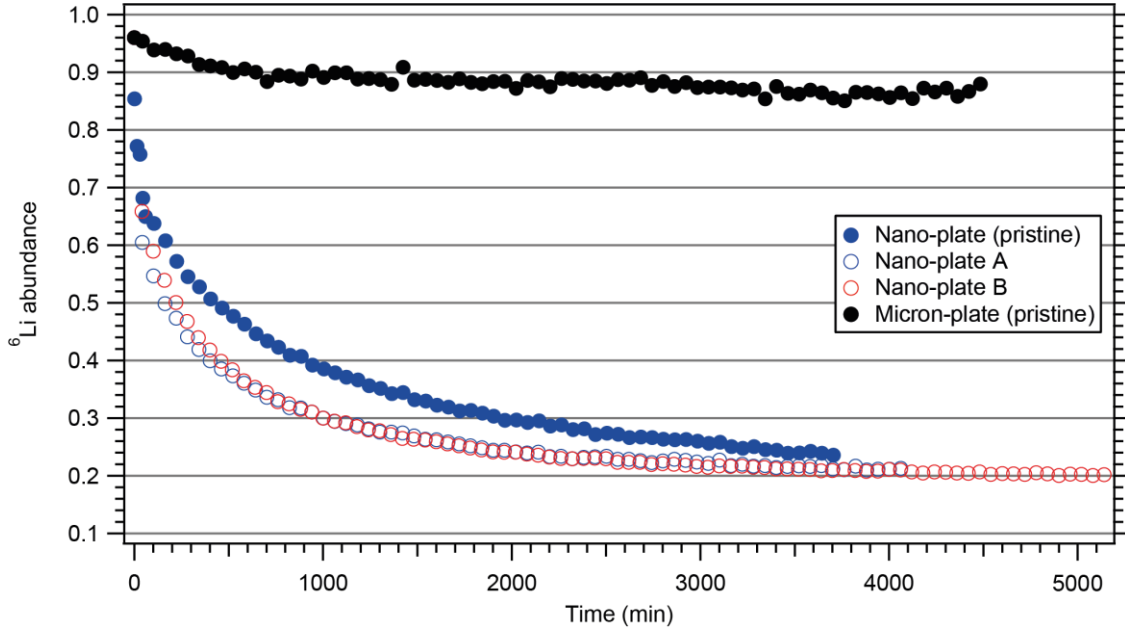


Figure 3.9 The ${}^6\text{Li}$ abundance of different LiFePO_4 samples as a function of immersion time of the ${}^6\text{Li}$ -enriched LiFePO_4 particles in the LiPF_6 electrolyte solution.

3.4.3 Tracer exchange

The lower and higher values of the tracer exchange estimated with (3.10) and (3.14) are shown in Figure 3.10 on a log-log scale. For the Nano-plate samples (Figure 3.10 A), $\log(\gamma)$ increases linearly with $\log(t)$ until ~ 1000 min, after which the slope becomes less steep and tracer exchange enters the long time limit as introduced in Section 3.2.2. Since the difference between the upper and lower limits of estimated tracer exchange becomes substantial in the long time limit, only the time regime (< 1000 min) where tracer exchange (on a log-log scale) shows a linear behaviour is considered. This linear relationship suggests γ can be described by a power function of t . The best fit to the first 1000 min data for the pristine Nano-plate sample by a general power function of t

$$\gamma(t) = \gamma(0) + A \cdot t^b \quad (3.21)$$

yields $\gamma(0) = 0.004 \pm 0.014$, $A = 0.11 \pm 0.01$ and $b = 0.27 \pm 0.01$. The form of this best fit function is in good agreement with the analytical expression for the tracer exchange under the single-file diffusion as given by (3.4)[76]. Therefore, the observed tracer exchange is consistent with the single-file diffusion mechanism. The tracer exchange during the first 1000 min for all Nano-platelet samples are fitted by

$$\gamma(t) = A \cdot t^{1/4} \quad (3.22)$$

For clarity, only the best fits to the lower estimated values are shown in Figure 3.10 A as green lines. The fitted coefficients are listed in Table 3.6.

If the tracer exchange is controlled by the normal diffusion not subject to single-file restriction, the tracer exchange should follow (3.3) as introduced in Section 3.2.1. The red trace in Figure 3.10 A shows the best fit of (3.3) to the lower limits of the data from the pristine Nano-plate sample for $t < 1000$ min with D'/L^2 as the only fitting parameter. The relationship between $\log(\gamma)$ and $\log(t)$ is also linear for the fitted data range, however, the slope of the line is 0.5, which is distinctively different from 0.25 and characteristic for tracer exchange subject to normal diffusion. This confirms that Li diffusion in LiFePO_4 cannot be described by a normal diffusion process.

The lower and upper values of the tracer exchange for the pristine Micron-platelet sample shown in Figure 3.10 B are almost identical. This is due to the small changes in the ^6Li abundance of the electrolyte, so the equality relations of (3.10) and (3.14) are approached. The tracer exchange is much slower and reaches only a little more than 10 % even after an immersion time of more than 4000 min. The best fit to the lower limit of tracer exchange by (3.21) yields: $\gamma(0) = -0.008 \pm 0.008$, $A = 0.011 \pm 0.004$ and $b = 0.285 \pm 0.035$, which also justifies the use of (3.22) in describing the tracer exchange behaviour. The green line in Figure 3.10 B shows the best fit to the lower limit of tracer exchange with equation (3.22), and the coefficients are shown in Table 3.6. In comparison, the solid red curve shows the best fit obtained by (3.3) for tracer exchange subject to normal diffusion, and the dashed red line indicates a slope of 1/2 on a log-log scale. It is noted that tracer exchange during the first 300 min cannot be fitted well by either model, nonetheless, tracer exchange at longer times (> 300 min) is better described by the single-file diffusion model.

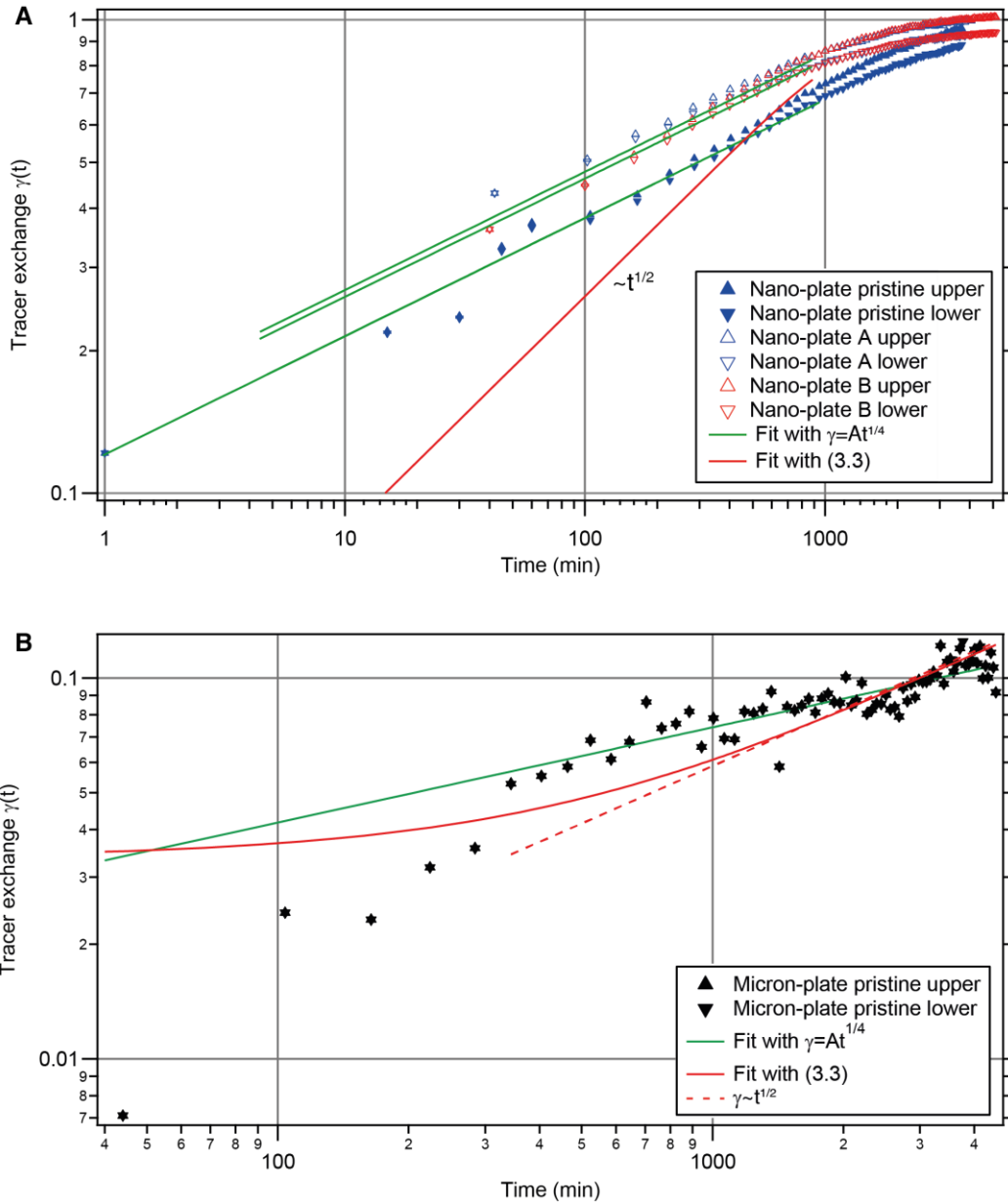


Figure 3.10 The tracer exchange curves for the (A) Nano- and (B) Micron-plate samples presented in logarithmic scale. The green curves are the best fit with $\gamma(t)=At^{1/4}$ to the lower limit data with A as the only fitting parameter. The solid red curves are the best fit with (3.3), which has a slope equal to 0.5 in logarithmic scale.

Table 3.6 Coefficients A obtained from fitting the tracer exchange curves with $\gamma(t) = A \cdot t^{1/4}$.

	A (lower limit) / $\text{min}^{-1/4}$	A (upper limit) / $\text{min}^{-1/4}$
Nano-plate (pristine)	0.1207 ± 0.0008	0.127 ± 0.001
Nano-plate A	0.151 ± 0.001	0.1572 ± 0.0007
Nano-plate B	0.1461 ± 0.0005	0.1529 ± 0.0009
Micron-plate (pristine)	0.0132 ± 0.0002	0.0132 ± 0.0002

3.4.4 Single-file mobility and tracer diffusivity of Li

The tracer exchange described by (3.4) is valid only for a system of uniform channel length, which is not realised in the powder sample used in this study. However, Γ , Θ and l , on which F is dependent, can be assumed to be homogenous in a single sample, thus the tracer exchange for a sample with a distribution of L becomes:

$$\gamma(t) = \sum_i c_i \gamma_i = \sum_i \frac{V_i}{V} \frac{4}{L_i} \sqrt{\frac{F}{\pi}} t^{1/4} = 4 \left\langle \frac{1}{L} \right\rangle_V \sqrt{\frac{F}{\pi}} t^{1/4}, \quad (3.23)$$

where c_i , γ_i , V_i denote the molar fraction, tracer exchange and the volume of channels of length L_i , V is the total volume of the sample, and $\left\langle \frac{1}{L} \right\rangle_V$ is the volume weighted average of $\frac{1}{L}$. Comparing (3.23) and (3.22), the single-file mobility factor F is related to the fitting coefficient A through:

$$F = \pi \left(\frac{A}{4 \left\langle \frac{1}{L} \right\rangle_V} \right)^2 \quad (3.24)$$

Hence, the determination of F requires that $\left\langle \frac{1}{L} \right\rangle_V$ or the volume weighted distribution of L , from which $\left\langle \frac{1}{L} \right\rangle_V$ can be easily derived, is known. For the Nano-plate samples, the size obtained from X-ray diffraction by the Scherrer equation is the volume weighted average, i.e. $\langle L \rangle_V$, and the approximation $\left\langle \frac{1}{L} \right\rangle_V \approx \frac{1}{\langle L \rangle_V}$ is used although $\left\langle \frac{1}{L} \right\rangle_V \neq \frac{1}{\langle L \rangle_V}$ in general. The distribution in Figure 3.6 for the Micron-plate sample is based on the frequency of occurrence and not weighted by volume, nonetheless, $\left\langle \frac{1}{L} \right\rangle_V$ is approximated by the non-weighted average $\langle \frac{1}{L} \rangle$, which is $4.13 \times 10^{-3} \text{ nm}^{-1}$. In comparison, $\frac{1}{\langle L \rangle}$, which is equal to $3.92 \times 10^{-3} \text{ nm}^{-1}$, is 5% smaller than $\langle \frac{1}{L} \rangle$. Hence, it is reasonable to assume a $\pm 10\%$ uncertainty in $\left\langle \frac{1}{L} \right\rangle_V$ for all samples. Table 3.7 shows the calculated values for F from the upper and lower limits of A in Table 3.6 and the estimated errors based on $\pm 10\%$ variation in $\left\langle \frac{1}{L} \right\rangle_V$. However, the single-file mobility factor does not provide a straightforward estimation of the (de)lithiation time since F is dependent on Θ , which is constantly changing during (de)lithiation, according to (3.5). It is more relevant to obtain the Li attempt jump frequency and tracer diffusivity, which are quoted conventionally as indicators for the rate of (de)lithiation. Assuming a constant Γ within the composition range of all samples,

F should be proportional to $\frac{1-\Theta}{\Theta}$ and the proportional coefficient can be used to obtain Γ according to (3.5). The average F (mean value of the upper and lower limits) against Θ is plotted in Figure 3.11. To estimate the Li occupancy Θ for the Micron-plate sample, the upper limit is assumed to contain 0.3 % vacancies as determined previously from stoichiometric LiFePO₄[90], the lower limit is assumed to be given by the literature value for a sample after long time exposure to ambient air ($\Theta=0.983$)[84], and Li occupancy is given by the average value of the upper and lower estimates and the uncertainty is given by the difference, which are shown in Table 3.7. The best fit by (3.5) (the blue curve in Figure 3.11) yields the Li attempt jump frequency $\Gamma = 5.4 \pm 1.1 \times 10^5 \text{ s}^{-1}$, which, invoking (3.1), leads to a Li tracer diffusivity $D_{\text{Li}} = 2.4 \pm 0.5 \times 10^{-10} \text{ cm}^2 \text{ s}^{-1}$. Despite the very generous assumption on the uncertainties in both $\langle \frac{1}{L} \rangle_V$ and Θ , the values of both Γ and D_{Li} are on the same orders of magnitude with the ones obtained by microscopic methods, such as muon spin relaxation measurements[44–46]. This good agreement between macroscopic and microscopic methods in turn validates the single-file diffusion mechanism in LiFePO₄.

The Li attempt jump frequency and diffusivity can be used to estimate the rate performance as a function of the channel length. It is found that even under the single-file condition, the desorption of the diffusing atoms within the single-file channel is still governed by the same equation derived for normal 1-D diffusion as given by (3.3)[91], where γ and D' are replaced by $1-\Theta$ and D_{Li} , respectively. For 95% delithiation ($\gamma = 1 - \Theta = 0.95$), there exists a relationship between Li tracer diffusivity (D_{Li}), the channel length (L) and the delithiation time (t):

$$\gamma(t, L, D') = 1 - \frac{8}{\pi^2} \sum_{n=0}^{\infty} \frac{1}{(2n+1)^2} \exp\left(-\frac{(2n+1)^2 \pi^2 D_{\text{Li}} t}{L^2}\right) = 0.95 \quad (3.25)$$

For $D_{\text{Li}} = 2.4 \times 10^{-10} \text{ cm}^2 \text{ s}^{-1}$, $Z(t, L) = \gamma(t, L) - 0.95 = 0$ becomes an implicit function of t and L only, and the relationship between t and L (solved numerically) is shown as the blue curve in Figure 3.12. For $L = 50 \text{ nm}$ and 250 nm , 95 % delithiation takes only 0.04 s and 1 s, respectively. Such short delithiation time is consistent with the high-rate capability of LiFePO₄, which has demonstrated cycling performance at rates as high as 400 C ($\sim 9 \text{ s}$ to fully delithiate) in 50 nm particles[14].

Table 3.7. The single-file mobility factors obtained from the fitting coefficients

	Θ	$F / \times 10^{-15} \text{ cm}^2 \text{ s}^{-1/2}$		Error $\Delta F / \times 10^{-15} \text{ cm}^2 \text{ s}^{-1/2}$
		lower limit	upper limit	
Nano-plate (pristine)	0.97 ± 0.01	9.2	10.1	2.4
Nano-plate A	0.94 ± 0.01	14.4	15.7	3.7
Nano-plate B	0.95 ± 0.01	13.5	14.8	3.5
Micron-plate (pristine)	0.99 ± 0.014	2.6	2.6	1.1

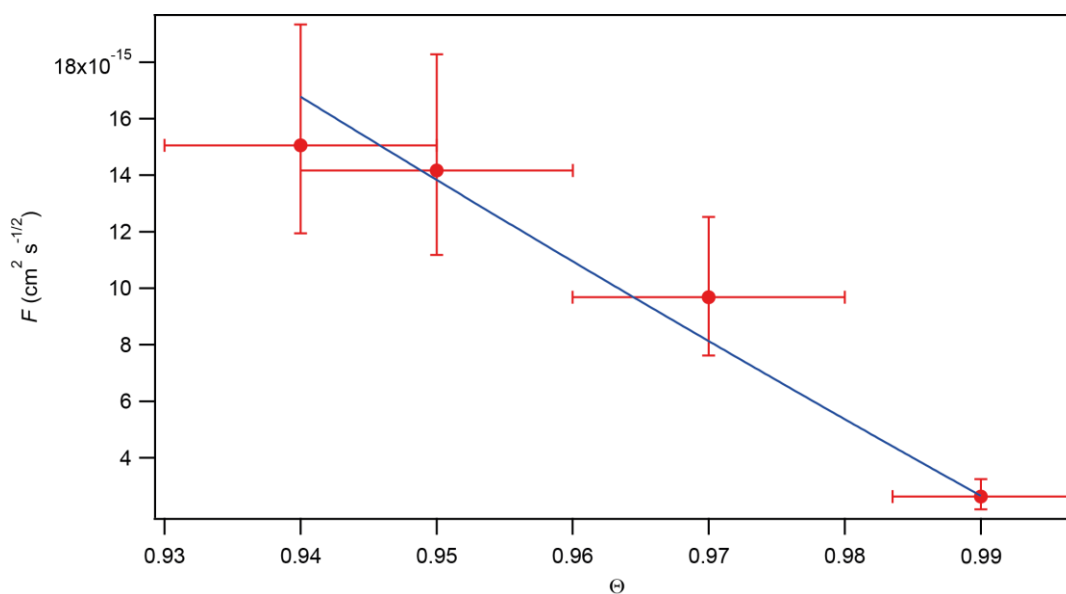


Figure 3.11. Average single-file mobility factor F against the Li occupancy Θ . The blue curve is the best fit by $F = B \frac{1-\Theta}{\Theta}$ with $B = 2.6 \pm 0.5 \times 10^{-13} \text{ cm}^2 \text{ s}^{-1/2}$.

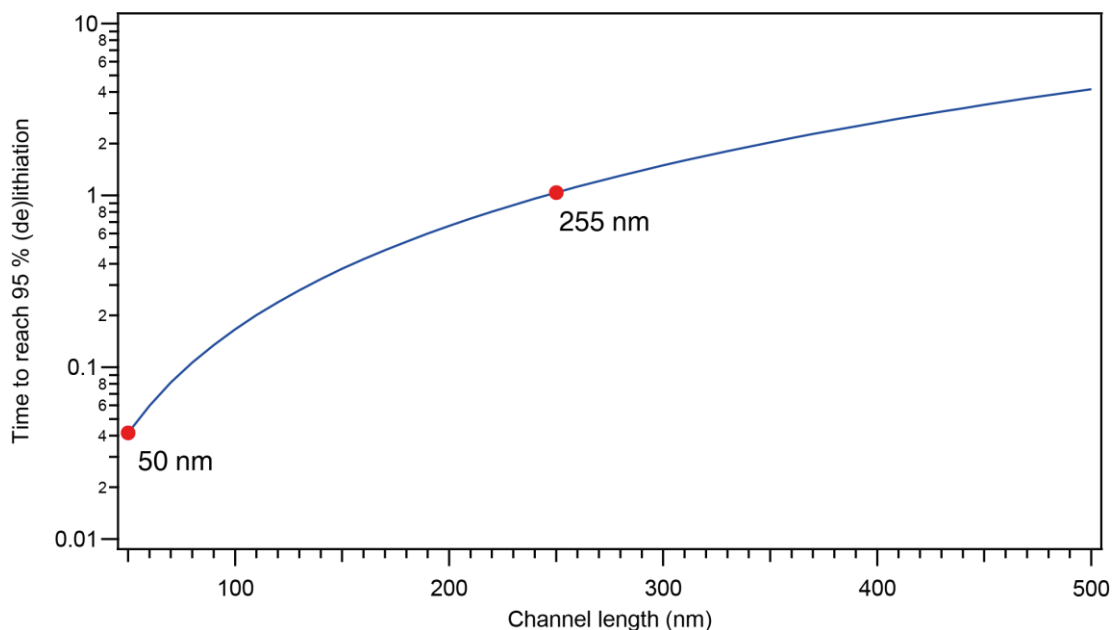


Figure 3.12. The blue curve shows the relationship between the time taken to remove 95 % Li in the channel and the channel length. The Li diffusivity is taken as $2.4 \times 10^{-10} \text{ cm}^2 \text{ s}^{-1}$.

3.5 Conclusion

By labelling the solid LiFePO_4 and the liquid LiPF_6 electrolyte solution with different Li isotopes, ^6Li solid state NMR has elucidated the Li exchange process between the two phases at room temperature. The $t^{1/2}$ dependence of the Li tracer exchange, regardless of the Li diffusion channel length, provides compelling evidence that the Li diffusion in LiFePO_4 is governed by a single-file mechanism, which is consistent with the 1-D diffusion channel allowed by its crystal structure. Fitting the tracer exchange curve with the analytical expression yields the single file mobility factor, from which the Li attempt jump frequency $\Gamma \sim 10^5 \text{ s}^{-1}$ and Li tracer diffusivity $D_{\text{Li}} \sim 10^{-10} \text{ cm}^2 \text{ s}^{-1}$ are obtained. The obtained values are in good agreement with the ones measured by microscopic methods and justifies the use of the single-file ion exchange model. The high diffusivity allows (de)lithiation to occur in times as short as $\sim 0.1 \text{ s}$ and $\sim 1 \text{ s}$ for 50 nm and 255 nm, respectively, and underpins the high rate capability of LiFePO_4 .

4 Phase transition of LiFePO₄ nanoparticles during high rate cycling

4.1 Introduction

High-rate lithium-ion battery electrode compounds generally form solid solutions with Li over a large composition range so that no phase transition is induced during (de)lithiation. Phase transformations, if they occur during cycling, are associated with small or negligible volume changes. For example, the layered compound, LiNi_{1/3}Mn_{1/3}Co_{1/3}O₂, reacts via a single solid solution phase[92,93], and the undoped Li_xCoO₂ only shows a weak first-order phase transformation, induced by the insulator-metal transition[94], between $x = 0.75$ and 0.94 with very little structural change. LiFePO₄[6] represents an exception to this paradigm, because it displays excellent high-rate performance when nano-sized[14], despite it undergoing a first-order phase transition to FePO₄ upon delithiation, a process involving a volume change of 6.8 %[6]. The very limited Li solubility in LiFePO₄ and FePO₄ suggests that (de)lithiation occurs via a two-phase reaction[18,19,95–97], where the relative LiFePO₄ : FePO₄ phase ratio is changed by a moving phase boundary, and not via a solid solution. Although the Li solubility is found to increase with decreasing particle size[22,23] as a result of an increased interfacial energy per volume, substantial Li miscibility gap still exists. Taking this interfacial energy into consideration, *ex situ* diffraction studies of LiFePO₄ nanoparticles propose that once an energetically unfavourable LiFePO₄ - FePO₄ interface is formed, this interface will quickly propagate through the particle so as to return to the most stable LiFePO₄ or FePO₄ state (the “domino-cascade” mechanism)[25], explaining why only LiFePO₄ and FePO₄ particles are observed *ex situ*[26]. Thus, at any time during the charge cycling, only a very small subset of particles should be reacting, making it difficult to observe this mechanism *in situ*. Although the energetics for nanoparticles are different from bulk particles, the thermodynamic properties of the system unequivocally leads to the conclusion that LiFePO₄ reacts via a two-phase mechanism.

Because all electrochemical processes operate at an overpotential, the pathways taken during the reaction are not necessarily governed by the thermodynamic properties of the system. As LiFePO₄ and FePO₄ phases coexist under equilibrium, an overpotential that lowers the Li chemical potential of one phase relative to the other, is required to drive the reaction. It has been postulated that this reaction overpotential modifies the phase

transition pathway. *Ab initio* calculations[28] have predicted that instead of forming an interface, the (de)lithiation of a single particle proceeds via a non-equilibrium single-phase Li_xFePO_4 ($0 < x < 1$), which bypasses nucleation and proceeds at a much lower overpotential. Once the overpotential is removed, the non-equilibrium Li_xFePO_4 particle relaxes to form the thermodynamic LiFePO_4 and FePO_4 phases releasing or taking in Li^+ ions from the electrolyte. Taking this into consideration, continuum modelling has suggested that a higher fraction of the electrode will react simultaneously via the non-equilibrium solid solution at high rates than at low rates[98]. A second continuum modelling study has argued that LiFePO_4 - FePO_4 phase separation (within a single particle) is not seen at high rates due to the dynamic stabilisation of the intermediate phases[29].

Diffraction methods using neutron or X-ray sources are commonly used for *in situ* characterisation of the structural changes that occur in the crystalline phases within the electrode during electrochemical cycling. Recent *in situ* X-ray diffraction (XRD) studies of micron-sized LiFePO_4 at high current rates have shown the appearance of a metastable crystalline phase with an intermediate lithium composition of $\text{Li}_{0.6-0.75}\text{FePO}_4$ [99]. However, investigations of smaller particles have been limited to low (< 0.1 C, n C is the current required to fully charge/discharge the electrode in 1/n hours)[34] and moderate (1 C)[100] current rates, and only small deviations in stoichiometry from LiFePO_4 and FePO_4 were observed (via changes in lattice parameters) during cycling. Since nanoparticles generally have faster transport kinetics, a higher current rate is required to reach the kinetic limit of a phase transition.

Our approach involves the use of a dilute electrode in a customized electrochemical cell[67], which is capable of achieving high cycling rates, with high reproducibility over multiple cycles, and an *in situ* XRD set-up with high X-ray intensity and a fast read detector to allow the reaction to be probed with high time resolution. The use of the dilute electrode improves both the electronic conductivity and the ion diffusion within the electrode composite[101,102], and is critical to probe the process intrinsic to the active material, LiFePO_4 . By forcing the nanoparticles to transform under high current rates, we are able to induce enough particles to transform simultaneously so that the reacting particles can be detected and the nature of the phase transitions that occur at an overpotential can be determined.

4.2 Experimental methods

4.2.1 Materials synthesis and characterisation

LiFePO₄/carbon composites were synthesised by a solid state reaction developed by Kobayashi *et al.*[23]. 0.556 g lithium carbonate (Li₂CO₃ Aldrich 99.997%), 2.6812 g iron(II) oxalate dihydrate (Fe(II)C₂O₄•H₂O Aldrich 99%), 1.7144 g ammonium dihydrogen phosphate (NH₄H₂PO₄ Aldrich 99.999%) and 0.2612 g Ketjen black (EC-600JD AkzoNobel) were high-energy ball-milled for 40 mins to produce homogeneously mixed precursors. The precursors were then pressed into pellet and sintered at 600 °C for 6 hours under flowing Ar gas.

Ex situ X-ray powder diffraction was performed in transmission geometry at ID31, ESRF, Grenoble, France. The wavelength was calibrated as 0.39996 Å. Rietveld refinement was performed with TOPAS software package in the 2θ range 4 - 30°. The background was modelled by a Chebyshev polynomial with 9 coefficients. The scale factor and zero point were refined. The peak profile was modelled by isotropic broadening due to size and strain. The θ dependence of the full width at half maximum (FWHM) of the Voigt peak profile due to isotropic size broadening is given by

$$H_{size} = \frac{\lambda}{L \cdot \cos\theta} \quad (4.1)$$

where H_{size} is FWHM of a Voigt peak, λ is the wavelength, and L is the refined particle size. The θ dependence of FWHM of the Voigt peak due to isotropic strain broadening is given by

$$H_{strain} = \varepsilon \cdot \tan\theta \quad (4.2)$$

where H_{strain} is FWHM of a Voigt peak and ε is the refined isotropic strain parameter. The structure was described in the *Pnma* space group, and the unit cell and atomic positions were refined. Isotropic atomic displacement parameters (ADPs) were refined for Li, Fe, P and O atoms, where the ADPs for crystallographically different O atoms were constrained to be identical.

4.2.2 *In situ* X-ray diffraction measurement

The AMPIX electrochemical cells[67] were used in this experiment. To ensure optimal high-rate performance, the proportion of active material in the electrode was halved compared to typical experiments. 3 mg LiFePO₄ powder was mixed with Super P carbon

(Alfa Aesar), carbon black (Vulcan XC-72, Cabot Corporation) and polytetrafluoroethylene (PTFE) binder (Sigma-Aldrich) in the mass ratio 3:3:3:1 and was pressed (1.6-1.8 ton) into a pellet (13 mm in diameter, ~150 μm in thickness). The electrode pellet was assembled into the AMPIX cell with Li foil as the anode, glass fibre as the separator and 1 M LiPF_6 in 1:1 ethylene carbonate/dimethyl carbonate (Tomiya Pure Chemical Industries) as the liquid electrolyte. The cells were cycled under conditions as described in the text.

In situ synchrotron X-ray powder diffraction measurements were performed in transmission geometry at beamline 17-BM of the Advanced Photon Source at Argonne National Laboratory (wavelength 0.7270 \AA , 500 μm diameter beam). A 2-D area detector (Perkin-Elmer) consisting of 2048×2048 pixels of $200 \mu\text{m} \times 200 \mu\text{m}$ in size was used. Measurements were performed at two sample-to-detector distances optimized for improved 2θ resolution (900 mm, detector offset 130 mm from the scattered beam, covering 2θ for $1^\circ - 25^\circ$, for the 10 C charge/discharge cycling presented in the main text; and data collection time for each pattern was 4 s, corresponding to a change of 0.011 Li per formula unit per pattern of LiFePO_4) or for a larger 2θ range (500 mm, detector centred at the scattered beam, covering 2θ for $1^\circ - 29^\circ$, for 5 C, 10 C, 20 C cycling and the intermittent 10 C charge/discharge cycling; and data collection time for each pattern was 3 s, corresponding to a change of 0.004 Li, 0.008 Li and 0.017 Li per formula unit per pattern of LiFePO_4 at 5 C, 10 C, and 20 C, respectively).

4.2.3 Whole powder pattern fitting method of the *in situ* X-ray diffraction data

The background profile was measured for an assembled AMPIX cell without either electrode, and then was modelled with 7 split pseudo-Voigt functions. These 7 peaks were then used to describe the background of the *in situ* patterns, and only the peak intensities were varied to account for the gradual changes in the background intensity. Since the sample thickness is less than the beam size, the instrumental broadening is dominated by the beam size. The instrumental profile was determined from the diffraction pattern of a thin layer of LaB_6 powder (SRM 660a) placed in the same geometry as the LiFePO_4 electrode.

The sample profile is a convolution of the size and the strain effects and is modelled separately. A Lorentzian peak profile is used to model the size broadening, and

the apparent size is assumed to be isotropic with respect to different (hkl) reflections. The dependence of FWHM, H_s , on θ is given by

$$H_s = \frac{\lambda}{L \cdot \cos \theta_{hkl}} \quad (4.3)$$

where λ is the wavelength, and L the refined apparent size parameter. Since the strain/compositional effect induces an asymmetrical profile, it is described by a convolution of a symmetrical and an asymmetrical profile function. A Gaussian profile peak function is chosen to model the symmetrical broadening due to strain, and this strain is also assumed to be isotropic with respect to different (hkl) reflections. The θ dependence of FWHM is given by

$$H_D = \varepsilon \cdot \tan \theta \quad (4.4)$$

where ε is the refined symmetrical strain parameter. The asymmetrical profile is modelled by an exponential function:

$$f(\theta) = \exp\left(-\frac{2\theta - 2\theta_{hkl}}{\varepsilon_m}\right) \quad (4.5)$$

where ε_m is the refined parameter and θ is defined in the range $[0, +\infty]$ if $\varepsilon_m > 0$ and $[-\infty, 0]$ if $\varepsilon_m < 0$. Due to the anisotropic change in the lattice parameters from LiFePO_4 to FePO_4 , where a and b lattice parameters contract and c lattice parameter expands, we have to include an hkl-dependent description of the asymmetrical profile, which is done by including symmetrized spherical harmonics series in ε_m :

$$\varepsilon_m = \sum_{ij} C_{ij} Y_{ij} \tan \theta_{hkl} \quad (4.6)$$

where Y_{ij} are the symmetrized spherical harmonics that can be found in references[82,103] and C_{ij} are the refined parameters.

The purely strain-induced profile for a certain (hkl) reflection is obtained by convolving the symmetrical Gaussian function and the exponential function defined at the corresponding θ_{hkl} . This profile is scaled by the peak area of the respective phase to represent the population density distribution. The whole powder pattern fitting of the *in situ* diffraction patterns within the 2θ range between 7.5° and 22.95° was carried out sequentially in the TOPAS structural refinement package[81].

4.2.4 Simulations of XRD reflection profile

Since it has been shown by experiment[18] that the LiFePO_4 - FePO_4 phase boundary is in the bc plane, we only considered the case of a one-dimensional 186 nm particle along the (h00) direction composed of unit cells that continuously vary in a lattice parameter, as described by (4.9) in Section 4.3.3. Each unit along the (h00) direction is assigned with a unique index. We followed the treatment of small coherent domains with continuously varying unit cell parameters by Warren[104]. For an (h00) reflection, the diffraction power as a function of diffraction angle 2θ can be expressed as

$$P(2\theta) = \frac{K'}{\sin^2 \theta} \sum_{m'} \sum_m F_{m'} F_m e^{(2\pi i / \lambda)(2 \sin \theta)(R_{m'} - R_m)} \quad (4.7)$$

where the subscripts m and m' represent the indices of the unit cells, F_m is the structure factor of unit cell m , R_m is the position coordinate of unit cell m , λ is the X-ray wavelength, and K' is a factor independent of θ . The summation is performed over all unit cells in the one-dimensional particle. The structure factor F_{200} for the (200) reflection is assumed to vary linearly with the Li composition x [105]:

$$F_{200}(x) = (1 - x) \cdot F_{200}(0) + x \cdot F_{200}(1) \quad (4.8)$$

where $F_{200}(0)$ is the structure factor for the (200) reflection of FePO_4 , and $F_{200}(1)$ for that of LiFePO_4 .

4.3 Results and Discussion

4.3.1 Material characterisation

Figure 4.1 shows the X-ray powder diffraction (XRD) pattern of the as-synthesised LiFePO_4 powder, and no impurity phase is observed. The particle size obtained from Rietveld refinement is 186 nm. Figure 4.2 A shows the particle morphology examined by scanning electron microscope (SEM). As the particles do not exhibit spherical morphology, ellipsoidal particle shape was assumed in measuring the particle size distribution, which is shown Figure 4.2 B. The particle size is represented by the diameter of a circle with the same area as measured from the SEM images, and the average particle size is 160 nm. It must be pointed out that it is very challenging to obtain a true particle size distribution or the average particle size: the model used for line broadening analysis of the XRD pattern assumes isotropic, i.e. spherical, particle shape, which is not the case for this sample; SEM only presents a two-dimensional image and lacks the three-

dimensional topographical information of the particles. Nonetheless, results from both methods indicate the average particle size is well above 100 nm, and the average particle size is likely to be between 150 nm and 200 nm.

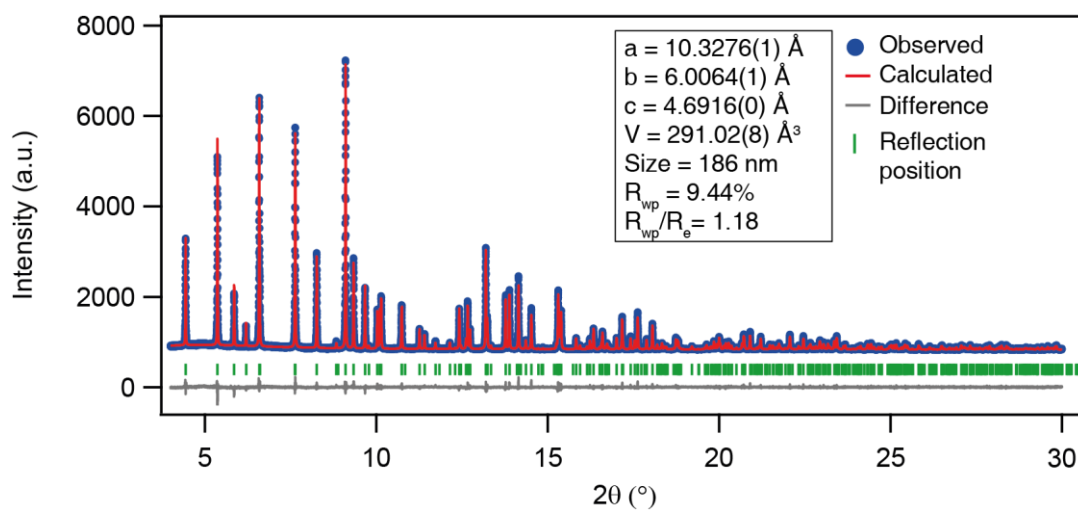


Figure 4.1 The X-ray powder diffraction pattern of as-synthesised LiFePO_4 powder (wavelength is 0.39996 \AA , ID31 ESRF, Grenoble)

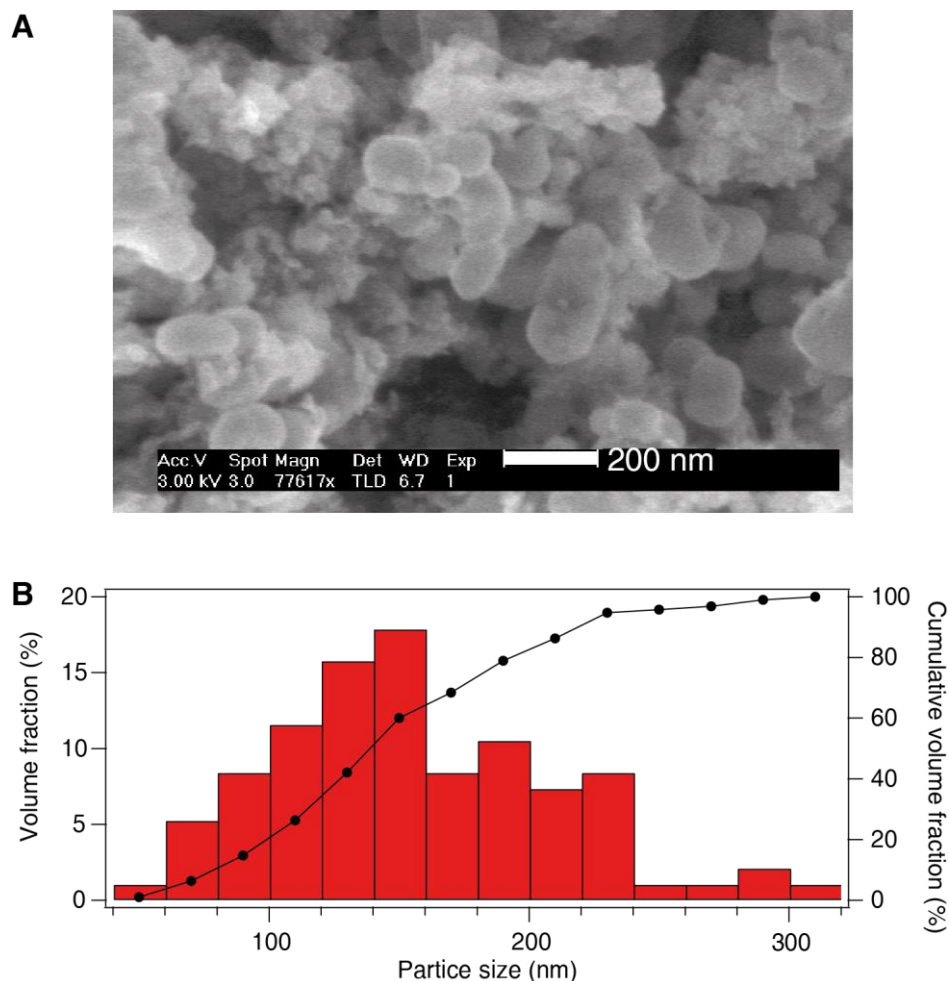


Figure 4.2 (A) Scanning electron microscope (SEM) image of as-synthesised LiFePO₄ powder. (B) Particle size distribution based on an analysis of 95 particles observed in the SEM images.

4.3.2 Intermediate Li_xFePO₄ phases induced at high currents

In situ diffraction patterns during the first 5 cycles of a 10 C galvanostatic charge-discharge of LiFePO₄ nanoparticles are shown in Figure 4.3 A, where the contributions from the cell background and polytetrafluoroethylene (PTFE) peaks are subtracted for clarity. All diffraction peaks can be indexed to either the Li-rich Li_{1- α} FePO₄ phase, or the Li-poor Li _{β} FePO₄ phase in the space group *Pnma*. As expected, Li_{1- α} FePO₄ peaks disappear on charge and are restored on discharge; conversely, Li _{β} FePO₄ peaks start to form and grow on charge and disappear on discharge. Unexpectedly we observe the development of appreciable positive intensities within the 8.15-8.4°, 13.95-14.1° and 15.15-15.4° 2 θ ranges, which indicate the existence of phases with lattice parameters that deviate from those of LiFePO₄ and FePO₄ under equilibrium. A closer examination of individual diffraction patterns for selected 2 θ regions is provided in Figure 4.3 B. The

phenomenon is more pronounced at high current rates: Figure 4.4 compares the results obtained at 5 C, 10 C, 20 C rates.

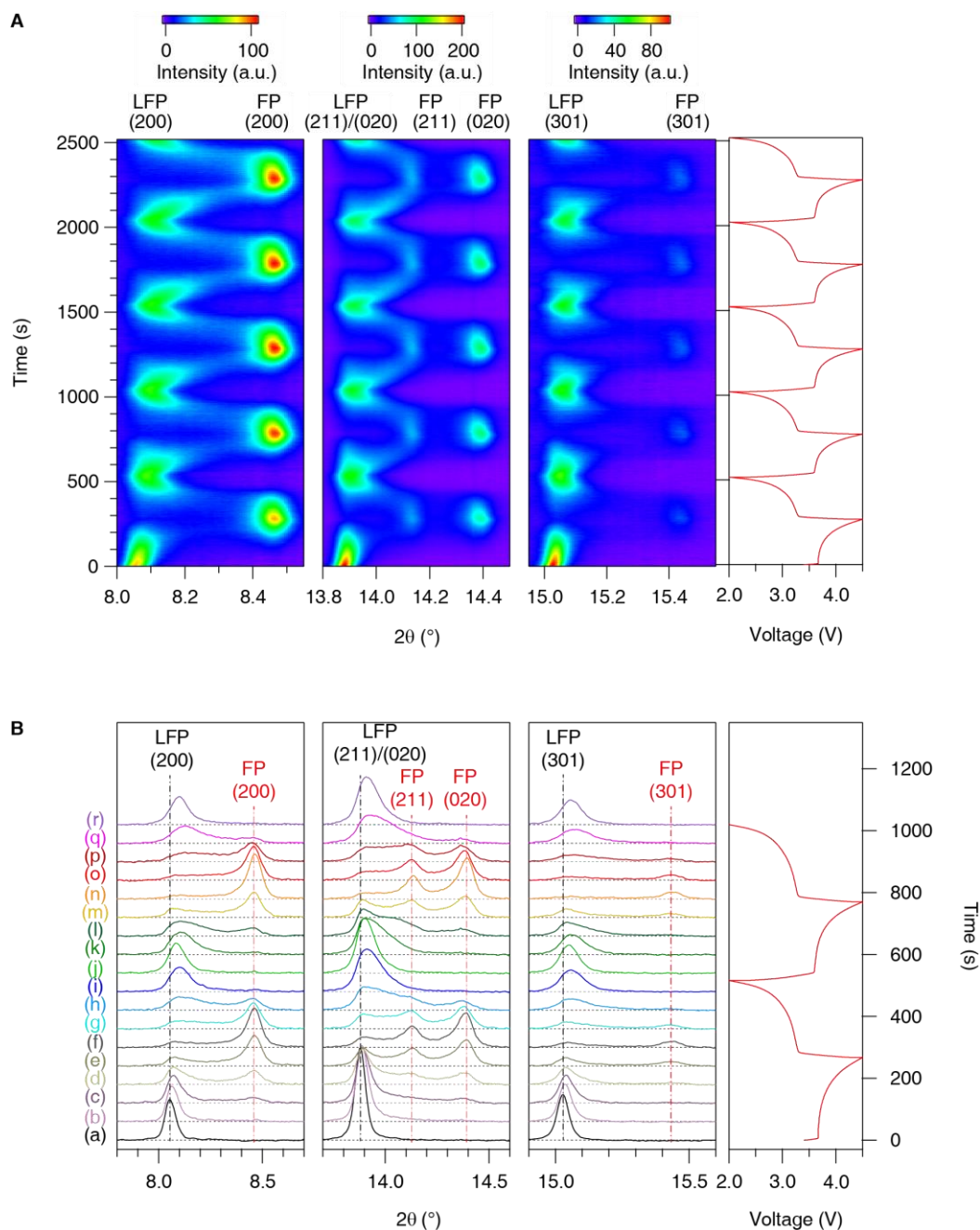


Figure 4.3 *In situ* XRD patterns during galvanostatic charge and discharge at a rate of 10 C. (A) The image plot of diffraction patterns for (200), (211), (020), and (301) reflections during the first five charge-discharge cycles. The horizontal axis represents the selected 2θ regions, and time is on the vertical axis. The diffraction intensity is colour coded with the scale bar shown on top. The corresponding voltage curve is plotted to the right. LFP, LiFePO_4 ; FP, FePO_4 ; a.u., arbitrary units. (B) Selected individual diffraction patterns during the first two cycles stacked against the voltage profile. The baseline is represented by horizontal dashed gray lines. Black vertical lines mark the positions of LiFePO_4 peaks at the start of reaction; red vertical lines mark the position of FePO_4 peaks formed during the first cycle.

All the reflections exhibit highly symmetrical profiles at the onset of the first charge, shown in Figure 4.3 B, pattern (i), but as charging proceeds, the LiFePO_4 (200) and (301) reflections start to broaden asymmetrically towards higher angles (pattern (d)). The most severe asymmetrical broadening is shown on discharge in patterns (f) and (g), where the (200) reflections from both phases are connected by a positive intensity band. Similar behaviour is also found in the second cycle (most notably, patterns (l) and (p)). Neither the peak position nor the peak shape of LiFePO_4 restores to that of the original state by the end of the second cycle. As shown in pattern (r), all selected peaks shifting towards higher angle and broadening. The peak shift indicates a decrease in the unit cell volume, which is attributed to the reduced accessible capacity at high rates. Since the lithium composition is not restored to LiFePO_4 at the end of each cycle, a solid solution, $\text{Li}_{1-\alpha}\text{FePO}_4$, is formed, which has a smaller unit cell volume than stoichiometric LiFePO_4 . This phase is also more disordered/has a shorter coherence length than LiFePO_4 , resulting in peak broadening.

The unusual evolution of peak shapes comes as a result of the microstructural changes induced during high rate cycling. In diffraction theory[104], the peak shape is a convolution of the instrumental profile, which is symmetrical in this case, and the sample induced profile due to small crystallite sizes and/or lattice distortions that can originate from strain, composition variations, etc. The size effect produces a symmetrical profile, whereas the lattice distortion effect can give rise to either a symmetrical or asymmetrical profile[104], depending on the nature and distribution of the distortion. Thus the development of an asymmetrical peak profile in this system is solely attributed to lattice distortions/compositional distributions. The experimental peak asymmetry exhibits a certain hkl dependence, the (200), (210), (211), (020) and (301) reflections skewing in the opposite direction to the skew observed for the (101) reflection (Figure 4.5), this dependence being consistent with that predicted for varying lithium composition between FePO_4 and LiFePO_4 , i.e., a solid solution. Some anisotropic peak shift and/or asymmetry could also be induced by a mechanical strain built up from the coherent interface between the LiFePO_4 and the FePO_4 domains during the reaction, which although of different physical origin, will also cause variations in lattice parameters.

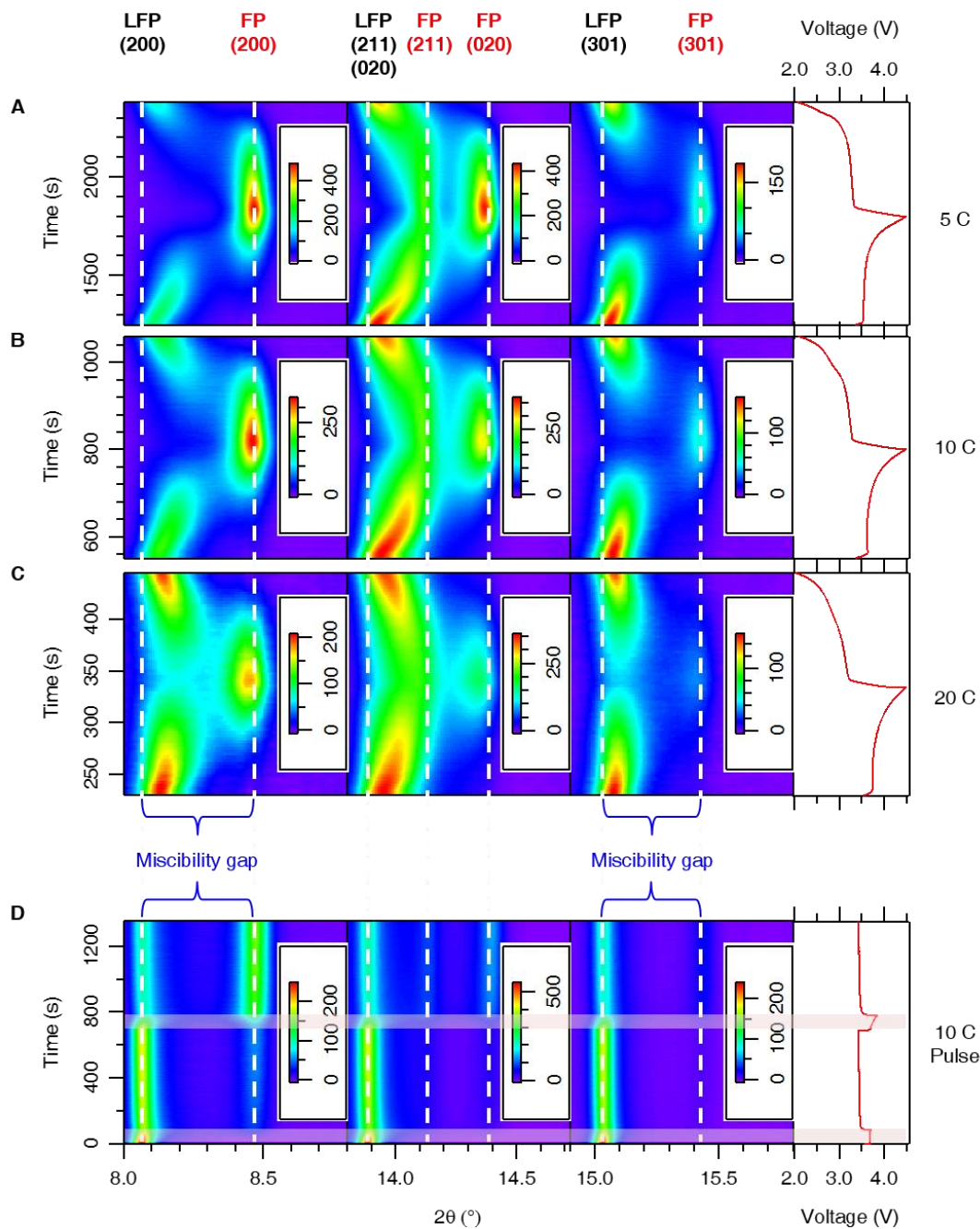


Figure 4.4 *In situ* X-ray diffraction pattern of LiFePO_4 under different electrochemical cycling conditions. (A), (B) and (C) show the second galvanostatic cycle at 5 C, 10 C, and 20 C, respectively. (D) shows the evolution of the charge-relax experiment, where a current equivalent to 10 C is applied for 90 s, equivalent to 0.25 Li extraction per f.u. of LiFePO_4 , (highlighted with the horizontal pink bands) followed by an open-circuit relaxation of 10 mins. The dashed white lines indicate the peak positions of the LiFePO_4 (LFP) and FePO_4 (FP) phases at the end of the second relaxation period, which are used to draw the boundaries of the miscibility gap as determined from the (200) and (301) reflections.

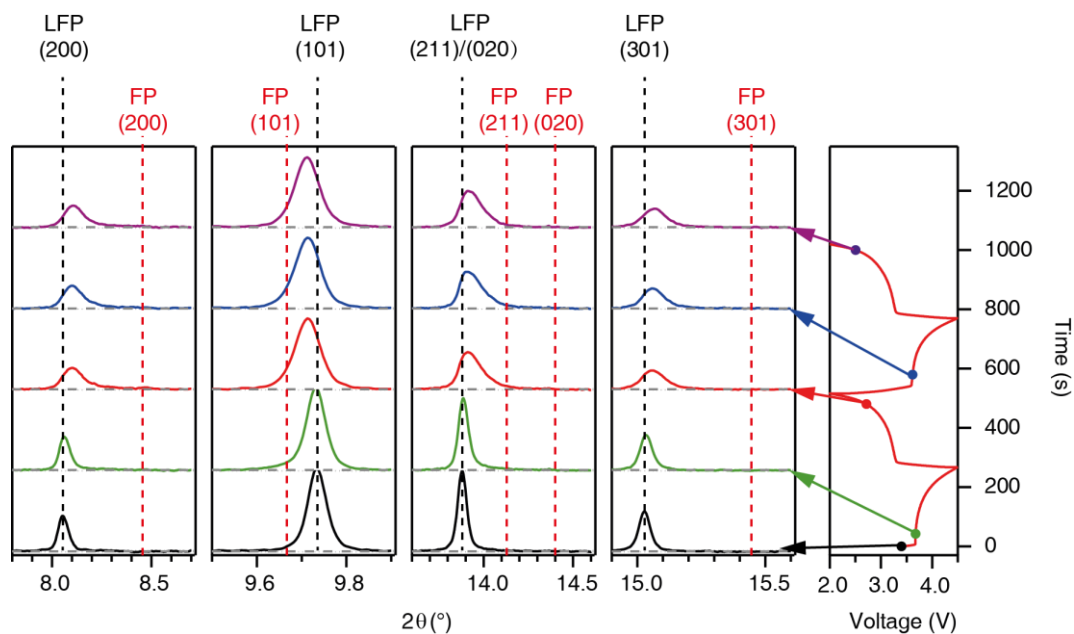


Figure 4.5 Development of peak asymmetry for the reflections from LiFePO_4 (LFP). The (200), (211)/(020), and (301) reflections from LiFePO_4 asymmetrically broaden towards higher 2θ angles, while the (101) reflection asymmetrically broadens towards lower angles. The same reflections from FePO_4 (FP) are marked by dashed lines.

4.3.3 Continuous distribution of Li_xFePO_4 phases beyond the thermodynamic miscibility gap

The distribution of lattice parameters can be quantified if its contribution to the peak profile can be separated from other sources. One common approach to treat an asymmetrical profile is to deconvolute contributions due to size and lattice parameter variations by applying a Warren-Averbach Fourier analysis[104] to a series of diffraction peaks arising from the same class of reflection. This is difficult to implement in our system due to the low crystal symmetry and severe peak overlap. An alternative approach, adopted here, involves fitting the peak profile by convoluting separate contributions from size and lattice parameter variations with appropriate analytical functions. To carry this out, Pawley whole powder pattern fitting[65] was performed with two phases representing LiFePO_4 and FePO_4 . The effect on the profile from the small crystallite size was modelled by an isotropic size broadening term, while that due to lattice parameter variations was modelled by convoluting an isotropic microstrain-like broadening term, accounting for the symmetrical distribution of lattice parameters, with spherical harmonics to fit the hkl -dependent asymmetry[106] caused by the asymmetrical lattice parameter distribution. The size and lattice parameter variations were then refined in the fitting process, using the TOPAS structural refinement package[81] and satisfactory fits

to the observed profile were achieved (Figure 4.6), which demonstrates the success of our model in accounting for the asymmetrical peak profile. The calculated patterns capture the asymmetry of all the classes of reflections (Figure 4.6; see for example the (200), (211), (020) and (301) reflections), which indicates the lattice spacing variation is not limited to only a few crystallographic directions. The scale factor of $\text{LiFePO}_4 + \text{FePO}_4$ remains constant during the reaction (Figure 4.7), providing evidence that our model is able to capture the bulk of the sample, even during the phase transformation. Instead of a single set, a distribution of all lattice parameters can be obtained for each diffraction pattern from this analysis.

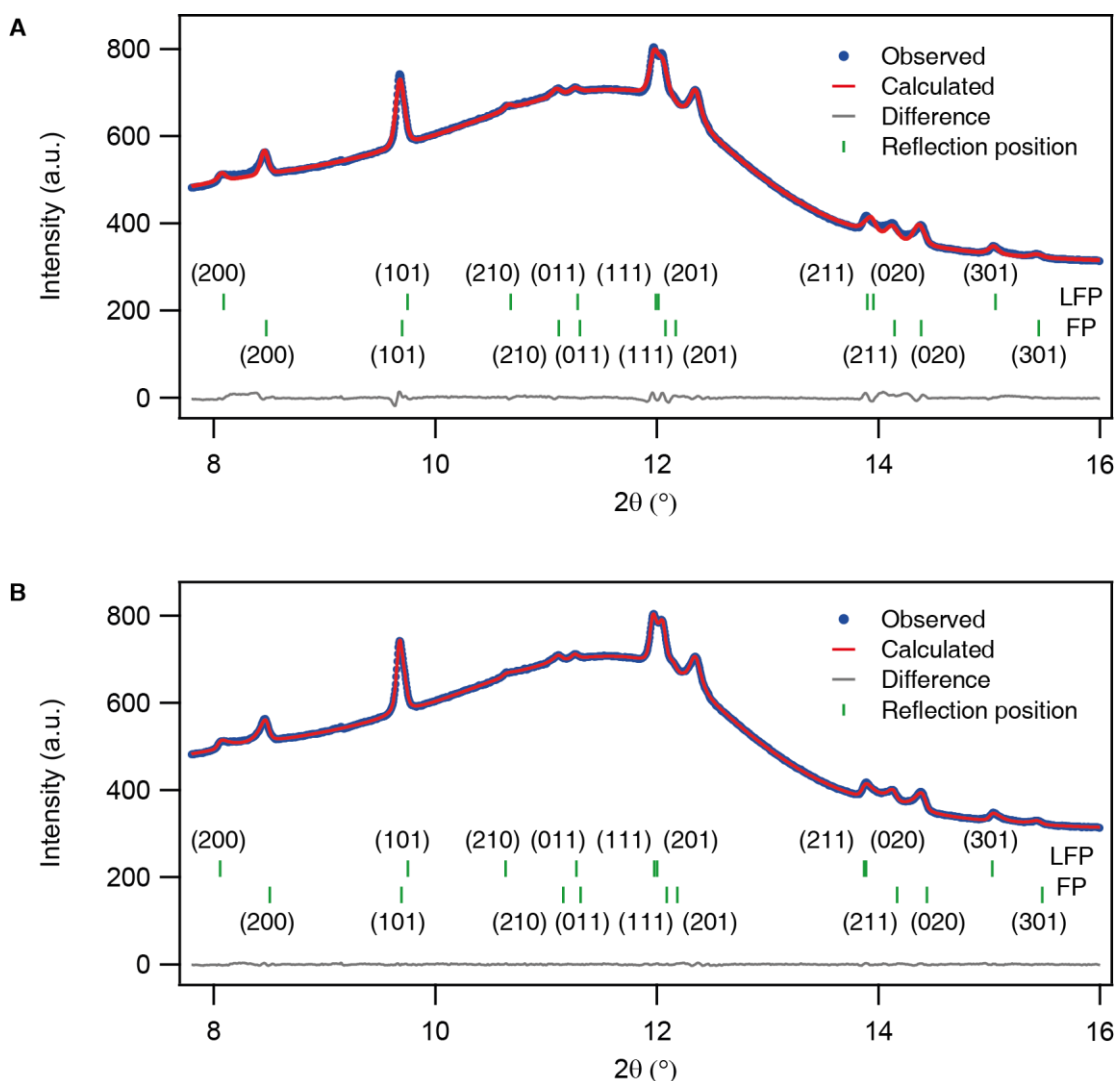


Figure 4.6 Typical whole powder pattern fitting results. This pattern is taken at 720 s, corresponding to the global composition of $\text{Li}_{0.43}\text{FePO}_4$. (A) Only symmetrical peak profile is used. (B) Symmetrical peak profiles convoluted with the hkl-dependent exponential function. Wavelength is 0.7270 \AA (17 BM APS).

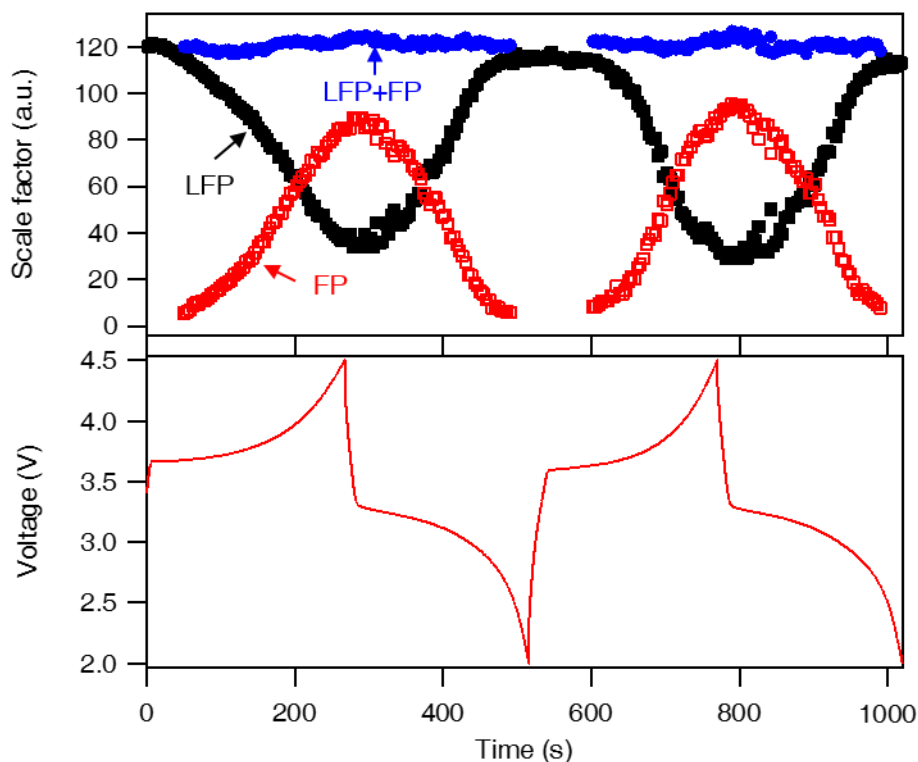


Figure 4.7 Refinement result of the scale factors of the LiFePO_4 and FePO_4 phases during the first two cycles. The cycling rate is 10 C.

Contour plots in Figure 4.8 show the population density distribution of a , b , and c lattice parameters from both phases during the first 2 cycles. The LiFePO_4 phase initially has a very narrow lattice parameter distribution, but during the first charge, the lattice parameters from both LiFePO_4 and FePO_4 become more widely distributed, but with an asymmetric tail towards the cell parameters corresponding to the lower and the higher Li compositions, respectively. Although analogous features are found in subsequent discharge and charge cycles, the Li composition range between $x = 0.2$ and 0.8 in the middle of (dis)charge becomes more populated than in the first charge. Verification of the results obtained from the whole pattern fitting method is presented in Section 4.3.5.

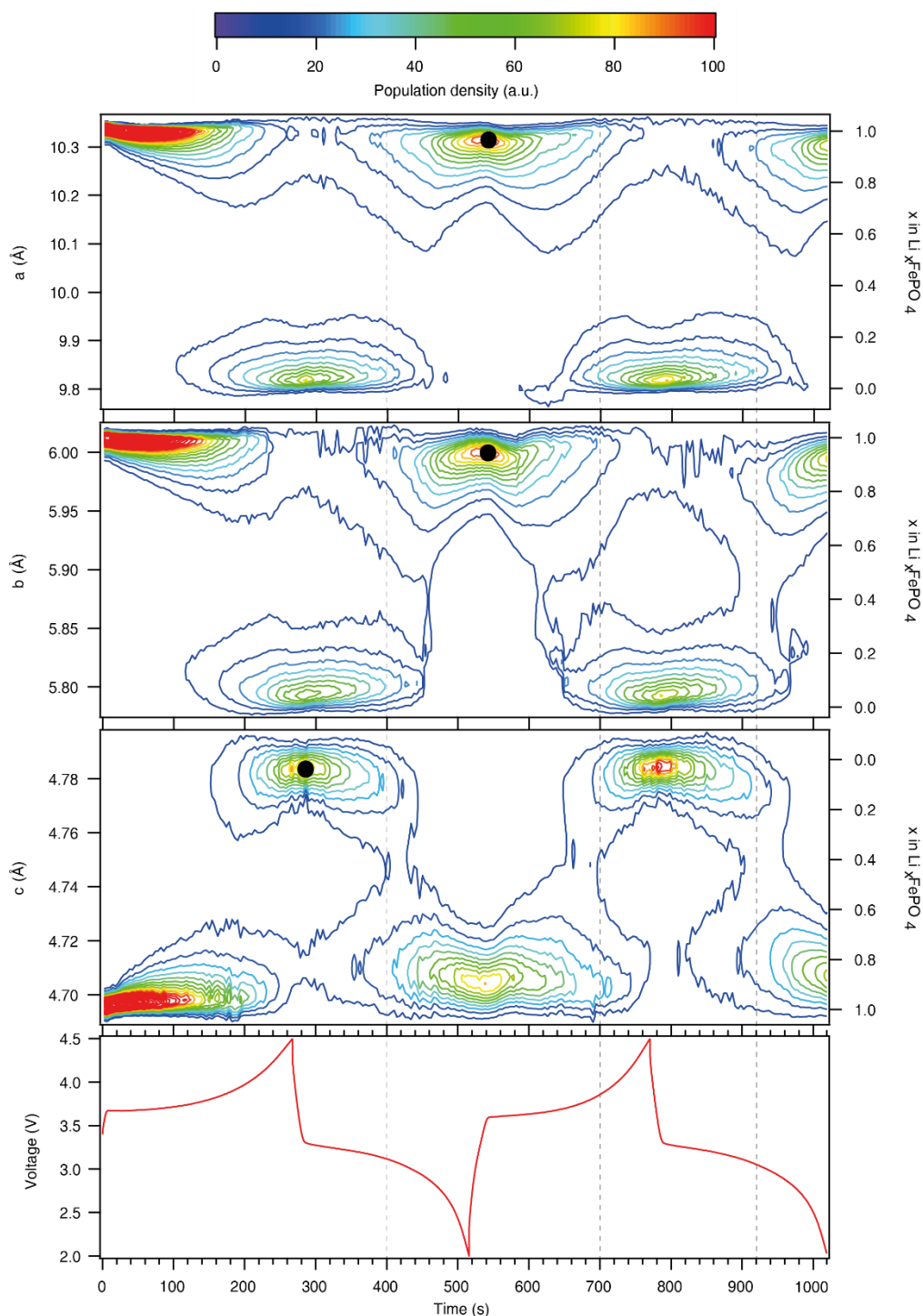


Figure 4.8 Contour plot of refined LiFePO_4 and FePO_4 lattice parameter distributions as a function of time during the first two charge-discharge cycles at a 10 C rate. The relative population density is coded in colour, with the lowest contour corresponding to 7.5 % of the intensity at the position indicated by the black solid circle. The corresponding voltage profile is shown at the bottom. The dashed lines mark the positions where lattice parameter distributions are most asymmetrical.

To identify the dominant cause for the asymmetrical distribution of lattice parameters, we need to separate the effects of compositional variations and strain between two different lattices (LiFePO_4 and FePO_4). The following observations indicate that the

compositional variation mechanism dominates. First, we note that the peak asymmetry of reflections from LiFePO_4 persists even in the absence of any reflections from FePO_4 , as shown in patterns (i) and (k) of Figure 4.3 B; this can only be caused by compositional variation since an interface requires the coexistence of both phases. Second, we consider the effect of a possible region affected by the strain introduced by a coherent interface between LiFePO_4 and FePO_4 on the XRD patterns. Since the interface has been shown to align with the bc plane by transmission electron microscopy (TEM) studies[18], it is most relevant to examine the effect of the interface width on the (200) reflections. Figure 4.9 shows the simulated (200) reflection profiles for a series of widths of the bc interface in a particle that is 186 nm long along the a -axis. We used the strain distribution derived from a coherent twin boundary[107], which leads to the a lattice parameter profile at an interface along the a -axis as:

$$a = \frac{a_0 + a_1}{2} + \frac{a_1 - a_0}{2} \tanh\left(\frac{2x}{L}\right) \quad (4.9)$$

where a_0 and a_1 are the a lattice parameters of FePO_4 and LiFePO_4 , respectively, L is the interfacial width, x is the distance from the centre of the interface. The Li composition profile (and also the structure factor) is discrete and remains constant on either side of the interface, as shown in the right panel of Figure 4.9 A. We find that for a 10 nm interface, which is approximately the relaxed interface width found in both a micron-sized[18] and a 172 nm[95] particle, the (200) profile remains almost unaffected. Although the simulated profile shows more asymmetry as the interface becomes wider, the asymmetry is mostly associated with the FePO_4 reflection, which is opposite to the experimental observation where the asymmetrical broadening is more associated with the LiFePO_4 reflection. When the Li composition (and also the structure factor) is allowed to vary continuously across the interface, the a lattice parameter distribution profile follows the exact form described by (4.9) if (a) Vegard's law is assumed (i.e., a linear change in the lattice parameters is observed as the lithium composition varies between FePO_4 and LiFePO_4), and (b) the regular solution model[108] is assumed (Li and vacancy ordering is random). The simulated profile in Figure 4.9 B finds much better agreement with the experimentally observed one, but only for interfaces of 100 nm or wider, i.e., of the same order of magnitude as the size of the crystallites. Hence, the experimental profile cannot be explained by an interface maintained solely by mechanical strains, as suggested by the "domino-cascade" argument[25], and must be associated with continuous compositional

variations. This is only plausible for a system that can form a solid solution – in this case only under non-equilibrium conditions.

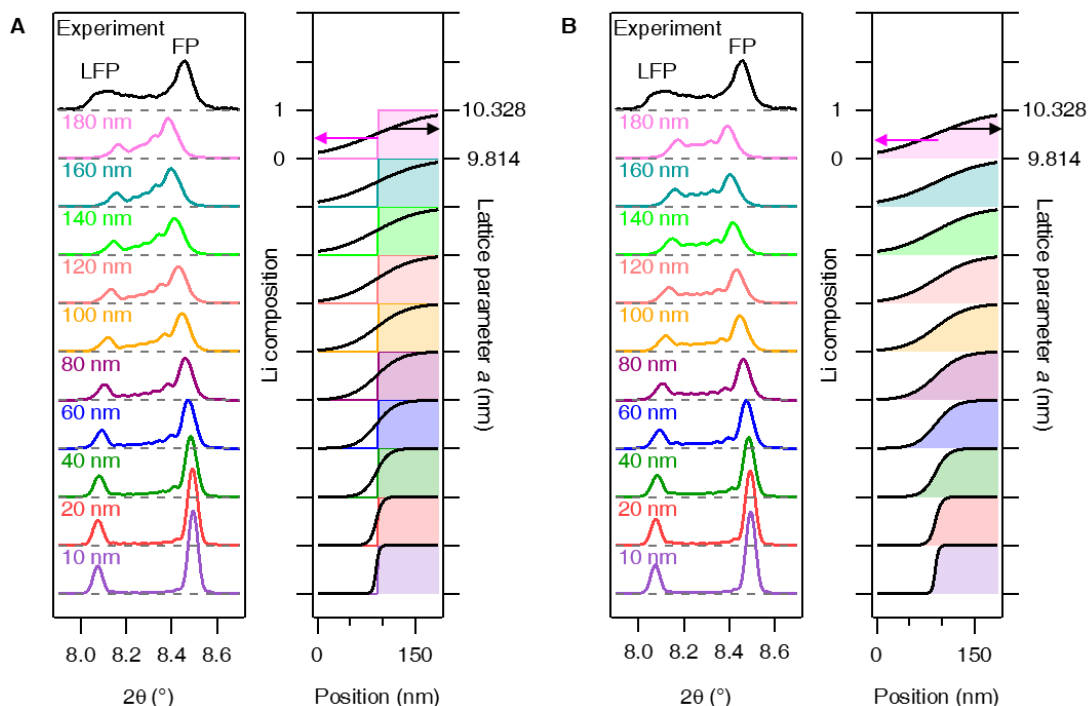


Figure 4.9 Simulated (200) reflection profiles for different interface widths between LiFePO_4 (LFP) and FePO_4 (FP). The left panel compares the simulated profiles with the experimentally measured one (top). The right panel shows the corresponding Li composition (shaded area) and the a lattice parameter profiles (solid black line) used in the simulation for various interfacial widths. The particle dimension along the a -axis is 186 nm, and the interface is positioned in the centre. (A) shows the result based on a discrete Li composition profile (mechanical strain only). (B) shows the result based on a continuous Li compositional variation.

In a real system, more interfaces/reaction fronts may exist within a single particle, which will lead to an even more homogenous Li composition distribution within a single particle. Furthermore, increased inhomogeneity may result from the finite one-dimensional Li^+ transport in the one-dimensional tunnels of the olivine structure. Li^+ concentration gradients in the electrolyte induced by the high current rate will also give rise to an inhomogeneous state of lithiation across the electrode[102]; that is the Li composition varies between particles. Consequently, the asymmetrical broadening of the observed reflection profile cannot be solely attributed to the Li compositional variation within a particle, and at least a substantial part of the broadening is due to compositional variation between particles and across the electrode.

It should be noted that a wide distribution of particle size could potentially lead to asymmetrical peak profiles, due to the particle-size dependent Li solubility[20,22,23],

which could lead to a composition variation based on the particle size. However, the change in the Li solubility is substantial only when the particle size is smaller than 50 nm. Although there are some particles smaller than 50 nm in the sample (Figure 4.2 B), their volumetric fraction is negligible. Since the phase fraction by X-ray diffraction scales with the total volume of the respective phase, the very small particles (< 50 nm) in the sample will contribute almost no intensity to the diffraction pattern and will not appreciably affect the peak profile.

4.3.4 Proof of the metastable nature of the Li_xFePO_4 phase

The lithium composition interpolated by Vegard's law is shown on the right axes in Figure 4.8. It is noted that at around 400 s, 700 s and 920 s (corresponding to an overall composition of $\text{Li}_{0.68}\text{FePO}_4$, $\text{Li}_{0.49}\text{FePO}_4$, and $\text{Li}_{0.74}\text{FePO}_4$, respectively), where the asymmetrical lattice parameter distribution is most pronounced, approximately 20% of the entire electrode probed by the X-ray beam exists with a composition between that of $\text{Li}_{0.25}\text{FePO}_4$ and $\text{Li}_{0.65}\text{FePO}_4$. In comparison, the solubilities obtained by Vegard's law in 35 nm and 140 nm particles with coexisting LiFePO_4 and FePO_4 domains are $\text{Li}_{\sim 0.9}\text{FePO}_4$ and $\text{Li}_{\sim 0.1}\text{FePO}_4$, and $\text{Li}_{>0.95}\text{FePO}_4$ and $\text{Li}_{<0.05}\text{FePO}_4$, respectively, even by taking the most generous estimation[20]. The application of a high current rate thus extends the solid solution into the regime that is thermodynamically prohibited and exists only under non-equilibrium conditions.

To confirm the metastability of the extended solid solution, we carried out an intermittent charging experiment and collected diffraction patterns during both the 10 C charging and the relaxation processes (Figure 4.4 D). The same whole powder pattern fitting method was used to generate the a , b , c lattice parameter distribution contour plots (Figure 4.10). As expected, asymmetry in the lattice parameter distribution develops on the LiFePO_4 side in the shaded region that highlights the periods during which current is applied, and the distribution gradually becomes more symmetrical once the current is removed and the system is allowed to equilibrate.

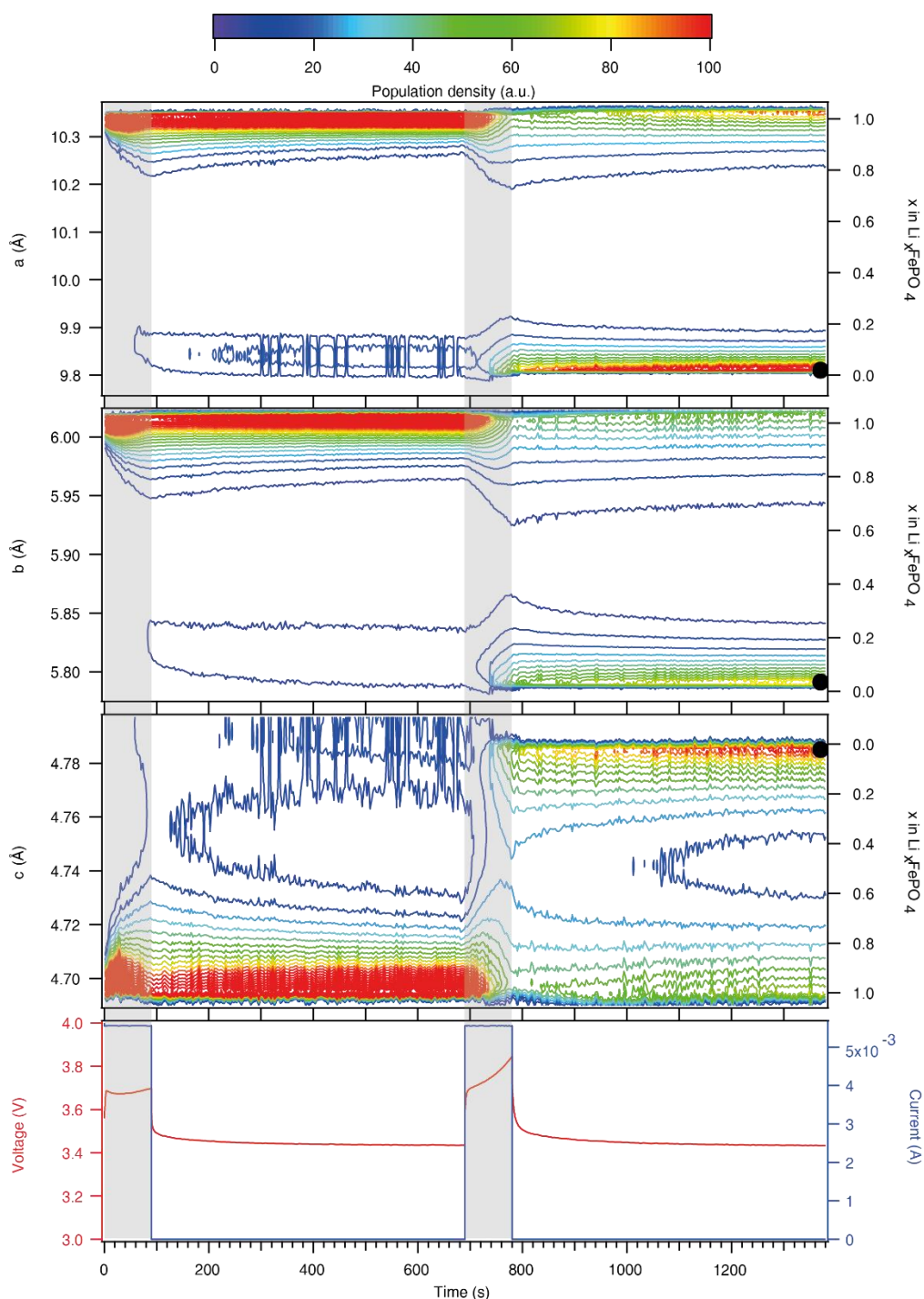


Figure 4.10 Contour plot of refined LiFePO_4 and FePO_4 lattice parameter distributions as a function of time during the intermittent charging experiment. The application of a 10 C current pulse for 90 s (corresponding to the removal of 0.25 Li per LiFePO_4 formula unit), is followed by a 10 min relaxation in open circuit mode. The low FePO_4 phase fraction during the first relaxation period is responsible for the greater fluctuation in the lattice parameters. The relative population density is colour coded (see top). The lowest contour is drawn at 7.5% intensity of the maximum population density for the FePO_4 phase at the end of the second relaxation period (indicated by the solid black circles). In the bottom graph, voltage (red lines) and current (blue lines) are plotted as a function of time

4.3.5 Verification of the whole pattern fitting method

To verify the validity of the fitting results obtained in Figure 4.8, the peak asymmetry of (200) and (301) reflections were treated by fitting the selected regions with a series of peaks to model reflections from phases of varying lithium composition. The (200) and (301) reflections were chosen based on the fact that reflections from the LiFePO_4 and the FePO_4 phases are well separated to give a better resolution of the asymmetrical profile.

Peak positions of the two end phases, LiFePO_4 and FePO_4 , are obtained from the whole pattern fitting of the pattern at the beginning and the end of first charge, respectively. By trial and error, it was found that at least 8 intermediate phases are needed to achieve a good fitting of the reflection profile. The 8 intermediate reflections are distributed equally in d-spacing between the LiFePO_4 and the FePO_4 reflections, therefore, a total of 10 reflections are employed to fit each of the (200) and the (301) reflection profiles. In the fitting process, the refined parameters are the intensities of individual peaks and a single width parameter for all 10 peaks; all peak positions are fixed.

Extraction of relative phase population is based on the work by Rudman[105]. The integrated intensity of the (hkl) reflection corresponding to the composition Li_xFePO_4 is given by

$$I_{hkl}(x) = K'' \cdot |F_{hkl}(x)|^2 \cdot T_{abs} \cdot LP(\theta) \cdot N(x) \quad (4.10)$$

where K'' is a constant, $F_{hkl}(x)$ is the structure factor of Li_xFePO_4 , T_{abs} is the absorption factor, $LP(\theta)$ is the Lorentz-polarisation factor, and $N(x)$ is the number of unit cells of Li_xFePO_4 in the irradiated volume. Since the reflection profile of interest spans only over a small 2θ range ($\Delta(2\theta) < 1^\circ$), to a first approximation, T_{abs} and $LP(\theta)$ can be considered as constant. Hence,

$$I_{hkl}(x) \propto |F_{hkl}(x)|^2 \cdot N(x) \quad (4.11)$$

and $F_{hkl}(x)$ is treated as a linear combination of the experimentally determined $F_{hkl}(0)$ and $F_{hkl}(1)$ (structure factors of LiFePO_4 and FePO_4 , respectively) given by (4.8).

The relative phase population extracted from the integrated intensity of (200) and (301) reflections are shown in Figure 4.11 A and B, respectively. Figure 4.11 B appears to be noisier than Figure 4.11 A because of the lower intensity of the (301) reflections. It

can be seen that Figure 4.11 is in very good agreement with the result obtained from the whole pattern fitting method shown in Figure 4.8.

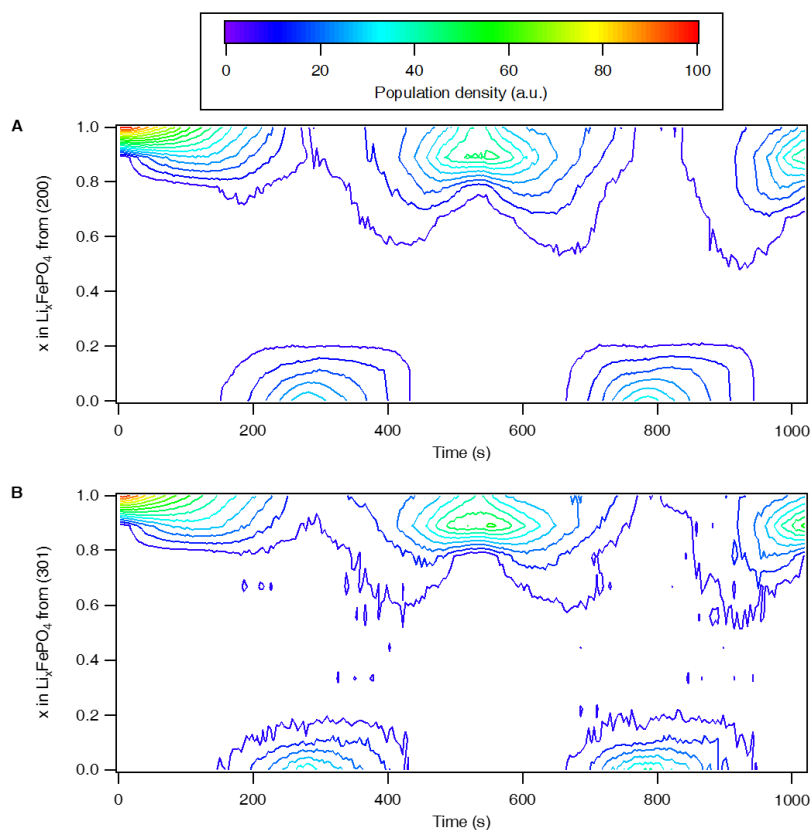


Figure 4.11 Phase population distribution obtained from multi-peak fitting. (A) shows the result for (200) reflection and (B) for the (301) reflection.

4.3.6 Discussion

In contrast to the formation of an intermediate $\text{Li}_{0.6-0.75}\text{FePO}_4$ phase under high cycling rates in micron-sized particles[99], our model reveals the development of a continuous solid solution that extends from the two end member phases into the thermodynamic miscibility gap. A higher fraction is distributed on the LiFePO_4 than on the FePO_4 side in good agreement with the non-equilibrium stability phase diagram constructed from the phase-field simulation[29], which predicts an asymmetrically vanishing spinodal region with increasing current rate. This asymmetry is also consistent with the thermodynamic phase diagram with greater lithium solubility on the LiFePO_4 side at room temperature[22,23] and a higher solid solution formation temperature on the low Li composition side[12,109], which indicates a higher energy barrier to form a homogeneous solid solution with low Li composition. Phase transformation via a single-phase solid solution mechanism is generally thought to manifest itself in diffraction studies as a continuous shift in the peak position. The distribution of Li compositions is a consequence

of the inhomogeneous nature in the reacting nanoparticulate electrode, which has been shown in various studies to react particle by particle[25,26,110,111]. The high current rate induces more particles to undergo phase transition at the same time, but not to the same state of lithiation, which causes the Li composition to vary both between the particles and within the particle[112]. Detection of the solid solution by powder diffraction is, however, very difficult due to the small number of reacting particles at any one time. The application of a high current not only induces an overpotential that is large enough to deliver a dynamic phase transformation pathway but also increases the number of reacting particles, so that they can be observed via a bulk measurement technique. However, a large portion of the electrode still remains inactive at any one time, and the diffraction pattern is still dominated by the equilibrium phases, LiFePO_4 and FePO_4 .

4.4 Conclusion

In situ X-ray powder diffraction of LiFePO_4 nanoparticles at 10 C rate has shown a phase transition that deviates from the classical nucleation and growth process. The whole powder pattern fitting approach to model the severely skewed diffraction peaks has revealed the existence of continuously distributed solid solutions (Li_xFePO_4) deeply extended into the thermodynamic miscibility gap. The intermittent charging experiment has confirmed the non-equilibrium nature of the solid solutions formed within the miscibility gap. The existence of a non-equilibrium single-phase transition pathway in LiFePO_4 explains its exceptionally high-rate performance. Provision of the non-equilibrium solid solution phase may also underpin high-rate capability of other materials that nominally operate via two-phase reactions.

5 Phase transition of anatase TiO₂ at high rates

5.1 Introduction

To explore whether the formation of non-equilibrium solid solution phases is unique to LiFePO₄ or a general phenomenon of the intercalation process at high rates, it is necessary to investigate the phase transition of other compounds. Hence, the phase transitions of anatase TiO₂ and LiVPO₄F, both known to undergo first-order phase transitions during Li⁺ (de)intercalation at low rates, i.e. at close to thermodynamic equilibrium conditions, were investigated at high cycling rates. This chapter is focused on the phase transition of anatase TiO₂. The results from a study of LiVPO₄F are presented in the next chapter.

Anatase, TiO₂, is used as an anode material for lithium ion batteries and, in theory, can accommodate a maximum of 1 Li per formula unit (f.u.). Initial Li intercalation into anatase TiO₂ from $x = 0$ to 0.025 (x in Li _{x} TiO₂) proceeds by a single phase, solid solution reaction. When Li is further intercalated, there is a two-phase reaction in the composition range $0.025 < x < 0.5$ (x in Li _{x} TiO₂) between tetragonal Li _{$a \approx 0.025$} TiO₂ ($I4_1/amd$, No. 141, Figure 5.1 A)[113], denoted as the α -TiO₂ phase, and orthorhombic Li _{$b \approx 0.5$} TiO₂ ($Imma$, No. 74, Figure 5.1 B)[114], denoted as the β -Li_{0.5}TiO₂ phase. Further intercalation for $x > 0.5$ is kinetically restricted by slow Li ion diffusion[115,116], and as a result, transformation to LiTiO₂ ($I4_1/amd$, Figure 5.1 C), denoted as γ -LiTiO₂, is only observed for very small nanoparticles (~7 nm) and on the surface layer of bigger particles at room temperature[117]. As shown in Figure 5.2, the discharge (Li insertion) voltage profile shows two distinct process: a well-defined voltage plateau at 1.78 V[118] corresponding to the two phase reaction of α -TiO₂ \rightarrow β -Li_{0.5}TiO₂, and a sloping voltage due to the kinetically restricted two-phase reaction of β -Li_{0.5}TiO₂ \rightarrow γ -LiTiO₂ occurring at the particle surface. The thermodynamics of the system are also dependent on the particle size: for large particles, both the α -TiO₂ and β -Li_{0.5}TiO₂ phases coexist in a single particle; for small particles, such phase coexistence is not stable and each crystallite is composed entirely of either the α -TiO₂ or the β -Li_{0.5}TiO₂ phase[117]. The effect of particle size on the reaction mechanism at a very low rate (C/120) was recently investigated by *in situ* XRD[119]. It was found that both small (15 nm) and large (130 nm) particles react sequentially and that the large particles transform by a moving boundary. The same study, despite being carried out at a low rate, also reveals a non-equilibrium nature during the transition between α -TiO₂ and β -Li_{0.5}TiO₂ in small (15 nm) particles: the Li composition of α -TiO₂ and β -Li_{0.5}TiO₂ measured during the transition process of TiO₂ \rightarrow Li_{0.5}TiO₂ is

different than the Li composition measured under equilibrium at the same state of overall lithiation. Hence, it would be interesting to explore whether the deviation from the equilibrium Li composition could be large enough at high rates to achieve a continuous phase transition between α -TiO₂ and β -Li_{0.5}TiO₂. To this end, the phase transition of anatase TiO₂ during electrochemical cycling under different cycling rates and temperatures was investigated by *in situ* synchrotron XRD.

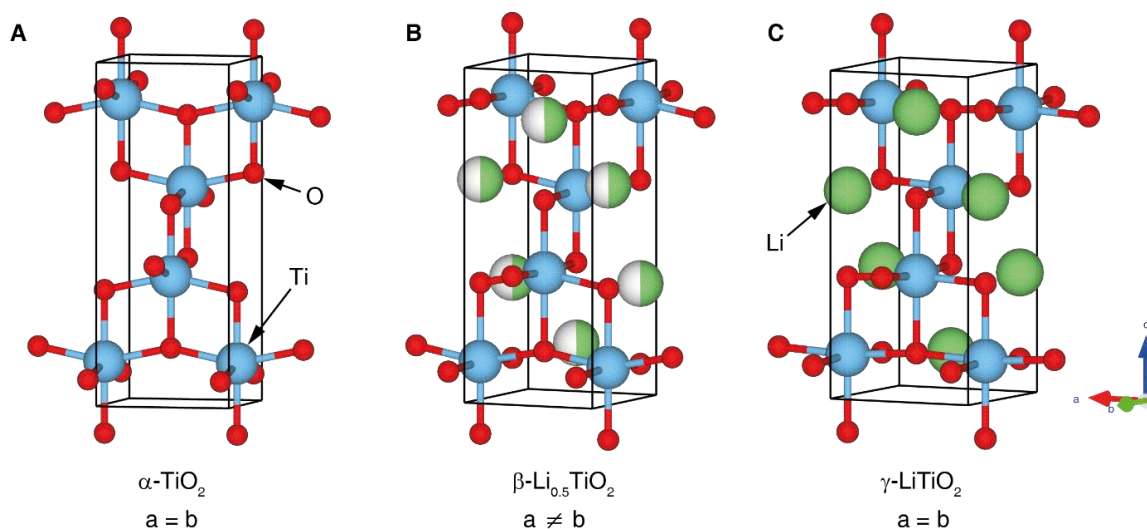


Figure 5.1. The crystal structures of (A) tetragonal α -TiO₂, (B) orthorhombic β -Li_{0.5}TiO₂ and (C) tetragonal γ -LiTiO₂. The half-filled green/white spheres denote sites which are randomly occupied by either Li or vacancy with equal probability.

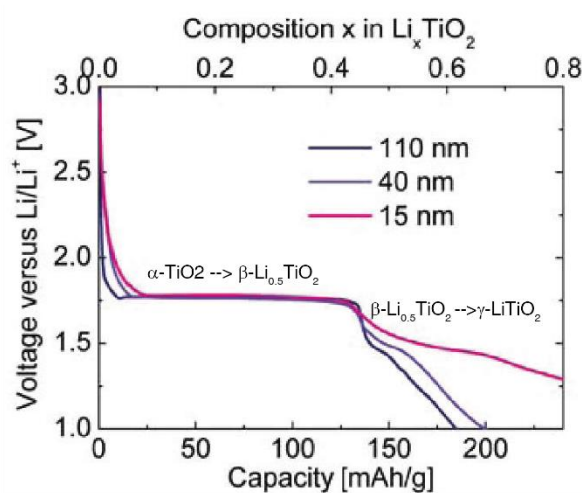


Figure 5.2. Typical voltage profile of anatase TiO₂ during discharge. The kinetically restricted lithiation to form γ -LiTiO₂ becomes more prominent with decreasing particle size. Figure adapted from reference [120].

5.2 Experimental methods

5.2.1 Materials and electrode preparation

The 25 nm and 100 nm TiO₂ powders were purchased from Sigma Aldrich. The electrode was prepared with a high proportion of carbon additives, to improve the electrochemical performance of the active material at high rates (by increasing the electronic conductivity). For a typical electrode, 3 mg of the active material powder was mixed with Super P carbon (Alfa Aesar), carbon black (Vulcan XC-72, Cabot Corporation) and polytetrafluoroethylene (PTFE) binder (Sigma-Aldrich) in the mass ratio 3:3:3:1 and was pressed (1.6-1.8 ton) into a pellet of 13 mm in diameter.

5.2.2 *In situ* XRD measurement

The electrode pellet was assembled into the AMPIX cell[67] with Li foil as the anode, glass fibre as the separator and 1 M LiPF₆ in 1:1 ethylene carbonate/dimethyl carbonate (Tomiyaama Pure Chemical Industries) as the liquid electrolyte. For high temperature electrochemical cycling, the cell was heated up with a heating tape whose temperature was set to 80°C by a thermostat. *In situ* synchrotron XRD measurements were performed in transmission geometry at beamline 17-BM of the Advanced Photon Source at Argonne National Laboratory (wavelength 0.72779 Å, 500 μm diameter beam). A 2-D area detector (Perkin-Elmer) consisting of 2048 × 2048 pixels of 200 μm × 200 μm in size was used and was placed 400 mm away from the AMPIX cell. The same electrode was used for the *in situ* measurement at different cycling rates, with measurements taken in the order from low to high rate. The data collection time of each pattern for 1 C, 2 C, 5 C, 10 C and 20 C cycling rates was 30 s, 12 s, 6 s, 3 s, and 3 s, respectively, which correspond to a change of 0.004 Li, 0.003 Li, 0.004 Li, 0.004 Li and 0.008 Li, respectively, per formula unit (f.u.) of TiO₂. The C-rate is calculated based on the theoretical capacity of 0.5 Li insertion per f.u., which is 168 mAh/g. LaB₆ powder was measured to obtain the instrumental broadening profile.

Rietveld refinements were performed with TOPAS software package in the 2θ range 10.3° – 35.5°. The background was modelled by 4 asymmetrical pseudo-Voigt peaks at positions ~11.7°, ~20.1°, ~25.0°, ~34.8°, respectively, with full width at half maximum (FWHM), intensity, shape parameter being refined, to account for the diffraction background intensity from glassy carbon, glass fibre separator and the liquid electrolyte, on top of the function $B/2\theta$, where B was refined. Two phases corresponding

to α -TiO₂ (*I4₁/amd*) and β -Li_{0.5}TiO₂ (*Imma*) were included in the refinement. The scale factors, unit cell parameters, atomic coordinates and isotropic atomic displacement parameters (ADP) for Ti and O atoms were refined. Ti and O atoms in both phases were constrained to have the same ADP for each atomic species. The peak profile was modelled by the convolution of isotropic size-like broadening (both Lorentzian and Gaussian) with anisotropic strain-like broadening (both Lorentzian and Gaussian). The Voigt peak profile is used to describe the isotropic size-like broadening:

$$H_{iso} = S/\cos(\theta) \quad (5.1)$$

where H_{iso} is the full width at half maximum (FWHM) of the Voigt profile, S is the refined parameter. The anisotropic strain-like broadening is described by

$$H_{aniso} = \sum_{ij} C_{ij} Y_{ij} \tan(\theta) \quad (5.2)$$

where H_{aniso} is the full width at half maximum (FWHM) of the Voigt peak profile, Y_{ij} is the symmetrised spherical harmonics[82], and C_{ij} are the refined parameters. Since the peak broadening was modelled empirically to obtain a good refinement, no microstructural information about the sample was obtained.

5.3 Results and Discussion

5.3.1 Particle size and electrochemistry of anatase TiO₂

The particle size of the as-purchased TiO₂ samples was checked by scanning electron microscope (SEM). Figure 5.3 A and B show the SEM images for the as-purchased TiO₂ powder specified as 100 nm and 25 nm, respectively, and the particle size is in agreement with the specification. Henceforward, the two TiO₂ samples are referred to by their particle size: 100 nm and 25 nm, respectively.

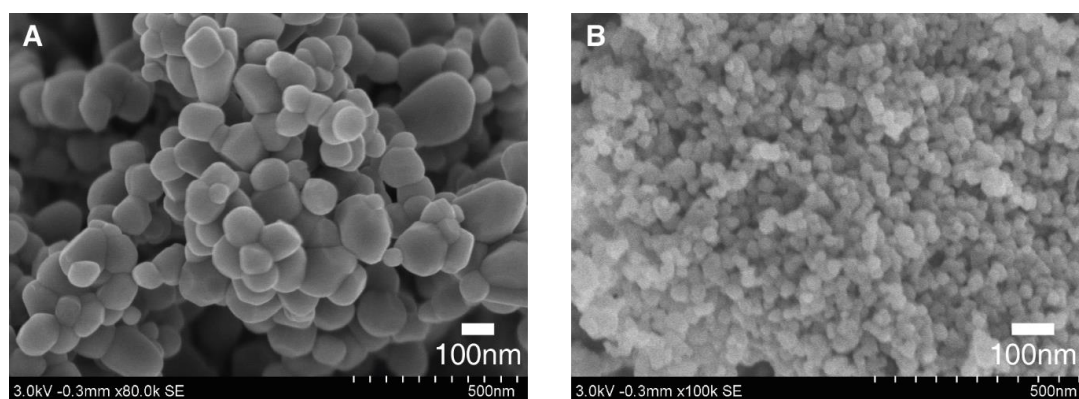


Figure 5.3 SEM images obtained for as-purchased (A) 100 nm and (B) 25 nm anatase TiO_2 samples. Pictures were taken by Dr. Tao Liu from our group.

In situ XRD measurements were conducted for both TiO_2 samples at cycle rates of 1 C, 2 C and 5 C at room temperature and at cycle rates of 5 C, 10 C and 20 C at 80°C . The same 25 nm electrode was used for both room temperature and 80°C cycles, while two 100 nm electrodes were used for room temperature and 80°C cycles, respectively. Cycles were carried out in the order of increasing rates at each temperature, for example, 1 C, 2 C and 5 C cycles were carried out sequentially at room temperature. For 25 nm particles, cycling at 80°C was performed after all the cycling at room temperature had been completed. Discharge and charge were limited within the voltage window 1.0 V – 3.5 V, except for 1 C and 2 C cycles of 25 nm particles at room temperature, where the low cut-off voltage was accidentally set to 1.2 V. The voltage profiles vs. overall cycled Li per f.u. of TiO_2 during the *in situ* XRD experiment are shown in Figure 5.4. For 100 nm at 1 C cycling at room temperature (Figure 5.4 A), the discharge voltage profile displays similar characteristics as the one shown in Figure 5.2: a steep drop in voltage is followed by a voltage plateau at 1.7 V between 0.05 and 0.25 overall cycled Li, indicating the transition from $\alpha\text{-TiO}_2$ to $\beta\text{-Li}_{0.5}\text{TiO}_2$. The sloping voltage profile towards the end of discharge (from 0.3 to 0.45 overall cycled Li) is attributed to further Li insertion exceeding $\text{Li}_{0.5}\text{TiO}_2$ [121,122] and electrolyte decomposition at low voltages[123,124] to form a protective layer of solid electrolyte interphase (SEI), which cannot be reversed on charge. Except for the irreversible SEI formation, the aforementioned process is reversed on charge. The small voltage bump at 0.57 overall cycled Li is associated with a kinetic barrier, such as nucleation of a second phase or the slow Li diffusion in $\gamma\text{-LiTiO}_2$ which may form on the surface layer. It can be seen that the voltage profiles under other cycling conditions exhibit similar behaviour.

It is noted that the irreversible capacity is mostly associated with the first cycle, i.e. the cycle of lowest rate in each graph in Figure 5.4. The irreversible capacity between discharge and charge during a 1 C cycle for 100 nm particles at room temperature (Figure 5.4 A), a 5 C cycle for 100 nm particles at 80°C (Figure 5.4 B), a 1 C cycle for 25 nm particles at room temperature (Figure 5.4 C) and a 5 C cycle for 25 nm particles at 80°C (Figure 5.4 D) is equal to 0.1, 0.3, 0.05 and 0.15 overall cycled Li per f.u., respectively. The small irreversible capacity during a 1 C cycle for 25 nm particles at room temperature is possibly due to the higher than average cut-off voltage at 1.2 V, which reduces the amount of electrolyte decomposition. The irreversible capacity found for subsequent cycles to the first one is less than 0.05 overall cycled Li per f.u.. Since SEI is amorphous and does not affect the crystal structure of the electrode material, it does not directly interfere with the interpretation of the *in situ* XRD results.

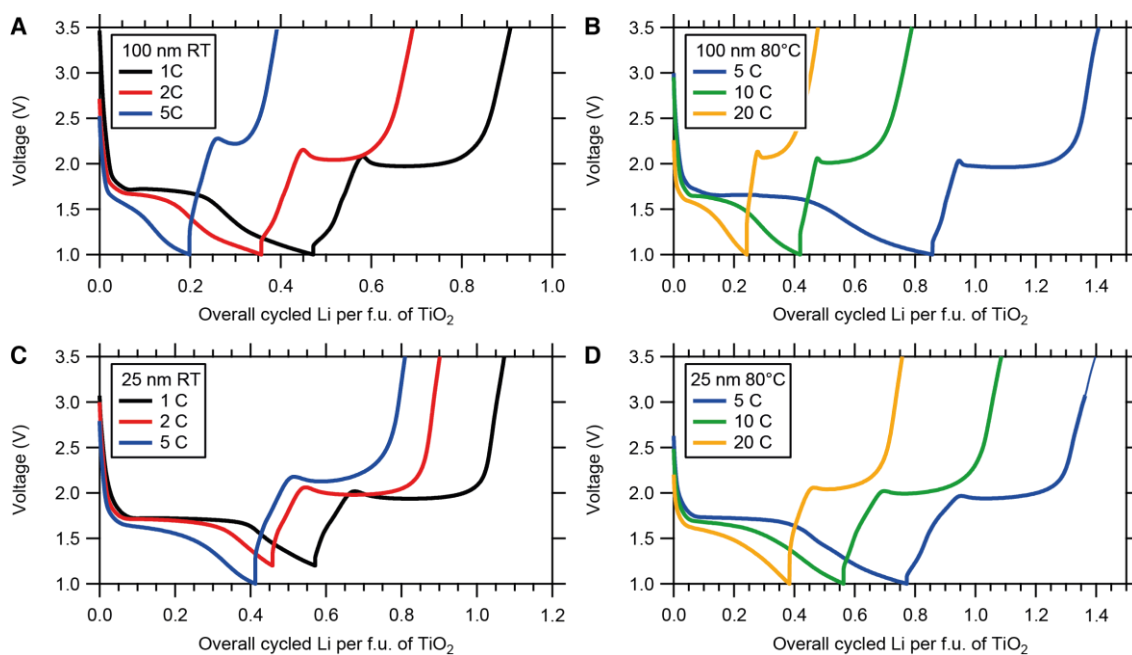


Figure 5.4 Voltage profiles for the discharge-charge cycles performed during the *in situ* XRD experiment. (A) Room temperature (RT) and (B) 80 °C cycling for 100 nm particles. (C) Room temperature and (D) 80 °C cycling for 25 nm particles.

5.3.2 Phase evolution of anatase TiO₂ under various conditions

Image plots of the time-resolved *in situ* XRD patterns for the evolution of the (024) reflection of α -TiO₂ and the (204) reflection of β -Li_{0.5}TiO₂ during high rate cycling at room temperature are shown in Figure 5.5 A-C for 100 nm particles and Figure 5.5 D-F for 25 nm particles. (024) and (204) are symmetry equivalent reflections in tetragonal α -TiO₂, and when the symmetry is lowered to orthorhombic β -Li_{0.5}TiO₂, they appear as two

distinct peaks in a powder XRD pattern. If the transition from the tetragonal to the orthorhombic phase is continuous, one would expect to observe, in the *in situ* XRD patterns, first the splitting of the (024) reflection into two reflections, (204) and (024), then the continuous shift of these reflections towards the 2θ values of the β -Li_{0.5}TiO₂ (204) and (024) reflections, respectively. For clarity, the (024) reflection of β -Li_{0.5}TiO₂, which appears at a lower 2θ angle but overlaps with other peaks, is not shown. For the discharge of 100 nm particles at a cycle rate of 1 C (Figure 5.5 A), the (024) reflection of α -TiO₂ shifts to a lower 2θ angle (0 – 0.07 overall cycled Li per f.u.) at the beginning of discharge, indicating an increasing Li composition of α -TiO₂ by the single-phase reaction; further discharge shows the characteristic two-phase reaction, where the (204) reflection of β -Li_{0.5}TiO₂ grows at the expense of the (024) reflection of α -TiO₂. On discharge, the (204) reflection of β -Li_{0.5}TiO₂ decreases in intensity and the (024) reflection of α -TiO₂ is restored. Similar evolution of the (024) reflection of α -TiO₂ is observed also for the 100 nm particles at cycle rates of 2 C and 5 C as shown in Figure 5.5 B and C, respectively; however, due to the formation of the small amount of β -Li_{0.5}TiO₂ on discharge at higher rates, the intensity of the (204) reflection of β -Li_{0.5}TiO₂ becomes very weak at 2 C, as shown by a single contour level corresponding to ~ 9 % maximum intensity of the image (Figure 5.5 B), and is barely visible at 5 C, where its maximum intensity is less than ~ 9 % of the maximum intensity of the image (Figure 5.5 C). The diffraction patterns shown in Figure 5.5 D-F are qualitatively the same as the ones for 100 nm particles and also display a two-phase feature. The 25 nm particles show improved kinetics as indicated by the higher fraction of the β -Li_{0.5}TiO₂ formed and the higher discharge capacity at the end of discharge in comparison to the 100 nm particles at equivalent rate: for example, the discharge capacity of 25 nm particles at 5 C corresponds to the insertion of 0.4 Li per f.u. as opposed to 0.2 Li for 100 nm particles at the same rate.

Since the (dis)charge process at room temperature terminates prematurely at higher rates (≥ 5 C), to probe the phase transition at rates above 5 C, electrochemical cycling was performed at an elevated temperature (~80°C) to improve the Li diffusion and the reaction kinetics. The *in situ* XRD patterns collected at 80°C during high rate cycling are shown in Figure 5.6 A-C for 100 nm particles and Figure 5.6 D-F for 25 nm particles. There is a noticeable improvement in the rate performance of both 100 nm and 25 nm particles with the formation of a substantial amount of β -Li_{0.5}TiO₂ at the end of the 20 C discharge, yet the XRD patterns still exhibit characteristic two-phase behaviour for both particles sizes.

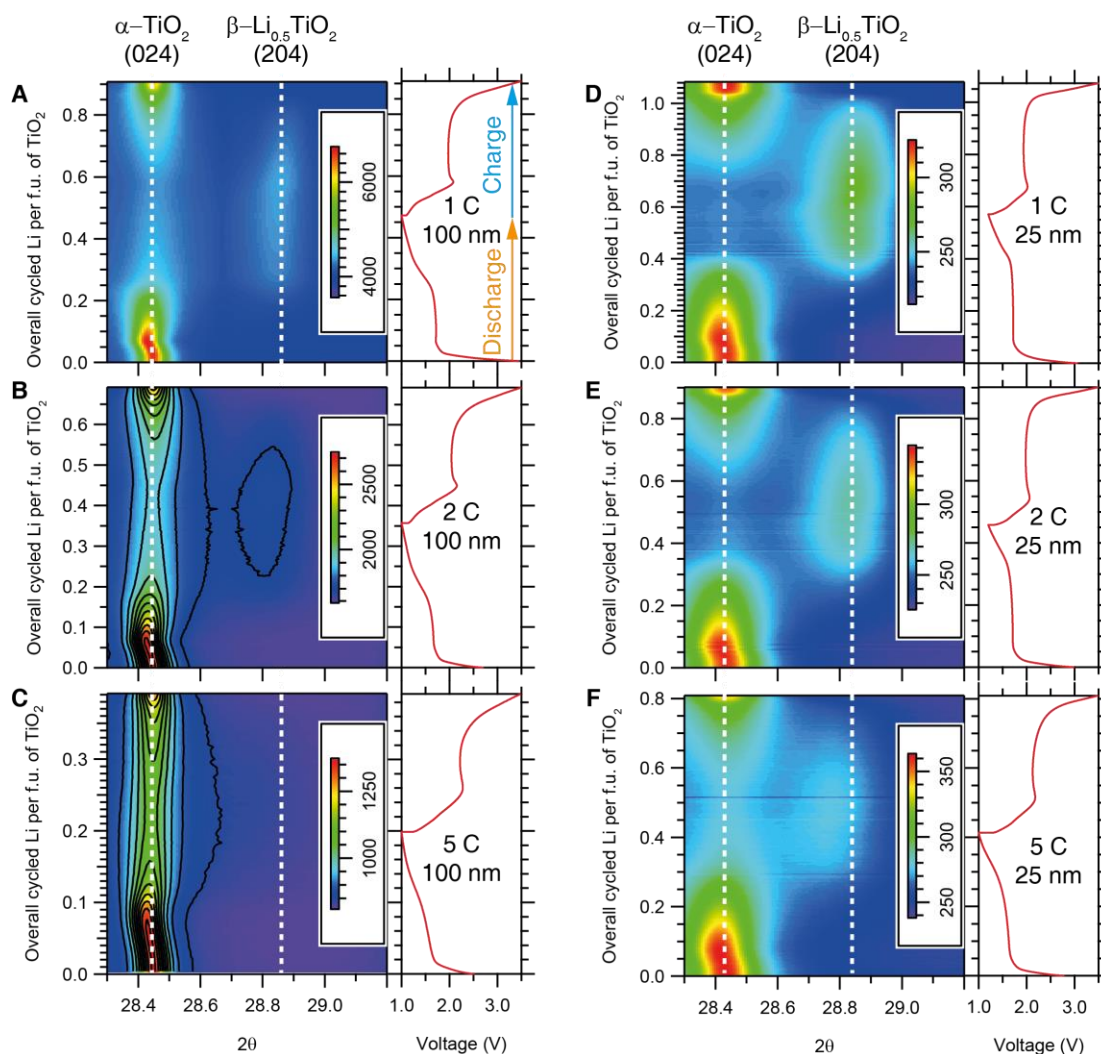


Figure 5.5 Image plots showing the time evolution of the *in situ* XRD patterns at room temperature for (A-C) 100 nm and (D-F) 25 nm TiO_2 particles at various cycling rates. The intensity scale is shown by the colour bar. The electrochemical profile is shown in the graph to the right of each image. The 2θ region for the (024) reflection of $\alpha\text{-TiO}_2$ and the (204) reflection of $\beta\text{-Li}_{0.5}\text{TiO}_2$ is shown. The (204) reflection of $\beta\text{-Li}_{0.5}\text{TiO}_2$ is barely visible in B and C due to the formation of a very limited amount of $\beta\text{-Li}_{0.5}\text{TiO}_2$, and the equally spaced intensity contours (11 levels in total) are drawn in black to aid visual inspection.

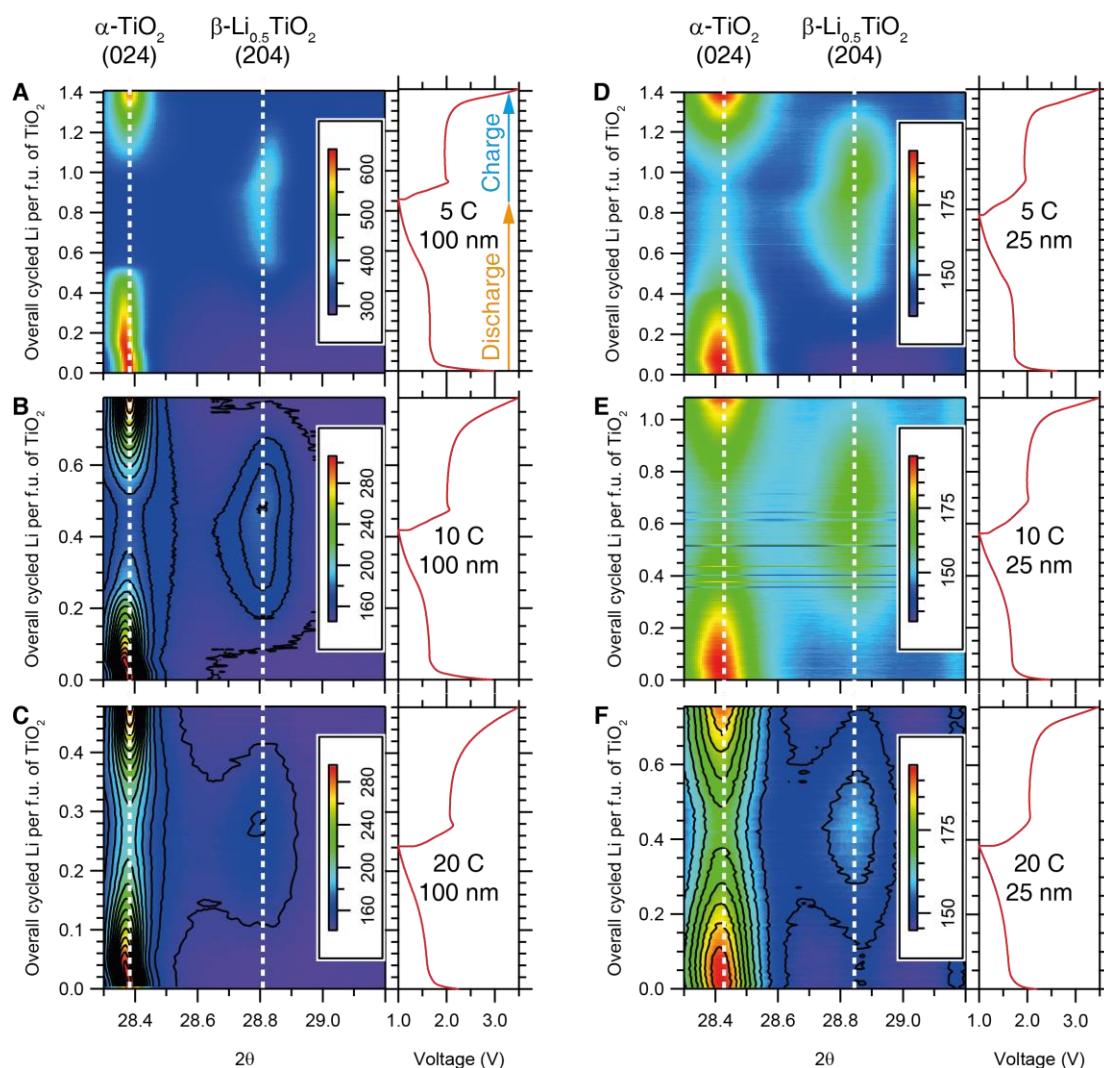


Figure 5.6 Image plots showing the time evolution of the *in situ* XRD patterns collected at *elevated temperature* ($\sim 80^{\circ}\text{C}$) for (A-C) 100 nm and (D-F) 25 nm TiO_2 particles at various cycling rates. The intensity scale is shown by the colour bar. The electrochemical profile is shown in the graph to the right of each image. The 2θ region for the (024) reflection of $\alpha\text{-TiO}_2$ and the (204) reflection of $\beta\text{-Li}_{0.5}\text{TiO}_2$ is shown. Equally spaced intensity contours (11 levels in total) are drawn in black in B, C and F to aid visual inspection.

Rietveld refinements were carried out to follow the evolution of the $\alpha\text{-TiO}_2$ and $\beta\text{-Li}_{0.5}\text{TiO}_2$ lattice parameters and capture any quantitative differences in the phase transition between the various cycling conditions. Figure 5.7 A and B show typical fitting patterns obtained from Rietveld refinement for the 100 nm particles at 0.33 overall cycled Li per f.u. and 25 nm particles at 0.24 overall cycled Li per f.u., respectively, during 2 C discharge at room temperature (RT). Reflections overlapped with the Li metal ones are not included in the refinement. The dips at $\sim 28^{\circ}$ are due to the presence of less efficient pixels of the detector and are also excluded from the refinement. The two big humps at $\sim 11^{\circ}$ and $\sim 20^{\circ}$, 2θ , arise from the glassy carbon window and the liquid electrolyte in the

cell[67] and are treated as background. The extremely small R_{wp} factors ($<1\%$), which indicate the quality of fit, are due to the relatively high background intensities with respect to the intensities of the Bragg reflections. Figure 5.8 shows the R_{wp} factors in all Rietveld refinements carried out in this study. It can be seen that R_{wp} stays almost constant for all refinements carried out for each cycling condition, except for the cycling at room temperature for 25 nm particles, where R_{wp} increases with the overall Li composition but still remains in the same range with R_{wp} obtained for cycling at 80°C for 25 nm particles.

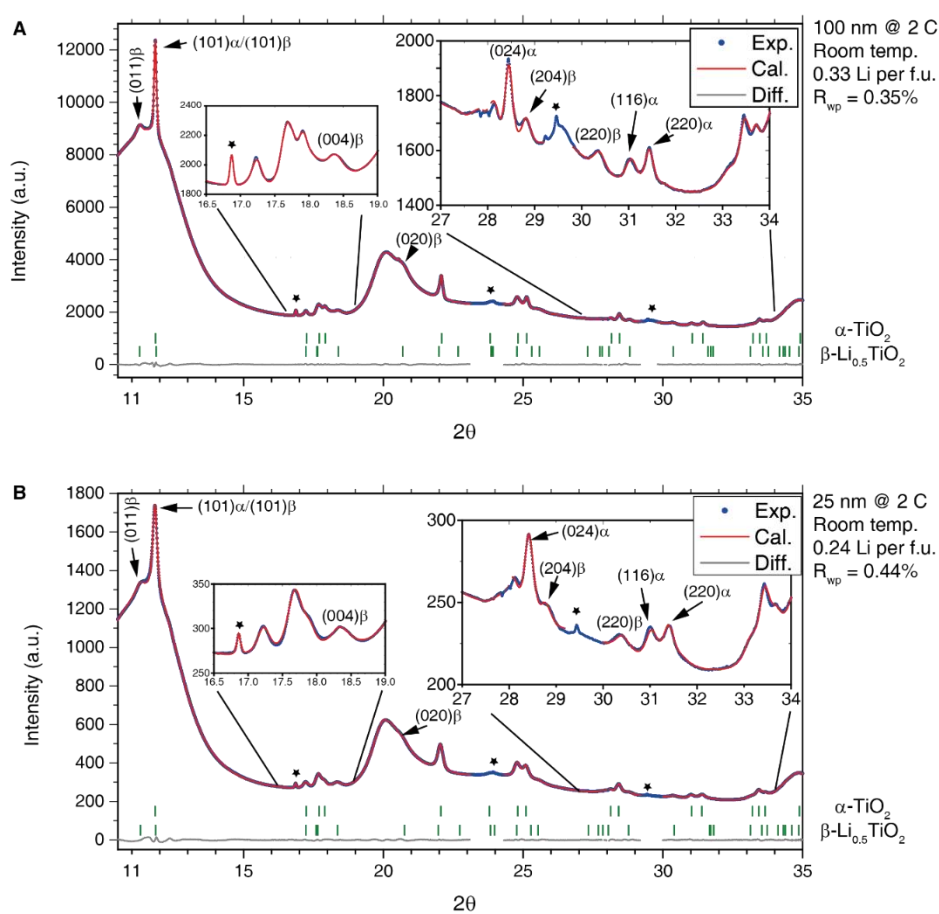


Figure 5.7. Typical fitting results obtained from Rietveld refinement for *in situ* XRD patterns collected for (A) 100 nm and (B) 25 nm particles. The green ticks mark the Bragg reflection positions of the corresponding phases. The asterisks indicate the Bragg reflections due to Li metal. The insets show the magnified $16.5^\circ - 19^\circ$ and $27^\circ - 28^\circ$ 2θ regions. The regions not accounted for by the calculated curves are excluded from the refinement. The blue dots represent the measured intensity, red curves are the calculated intensities from the refined models and grey curves are the differences between the measured and calculated intensities.

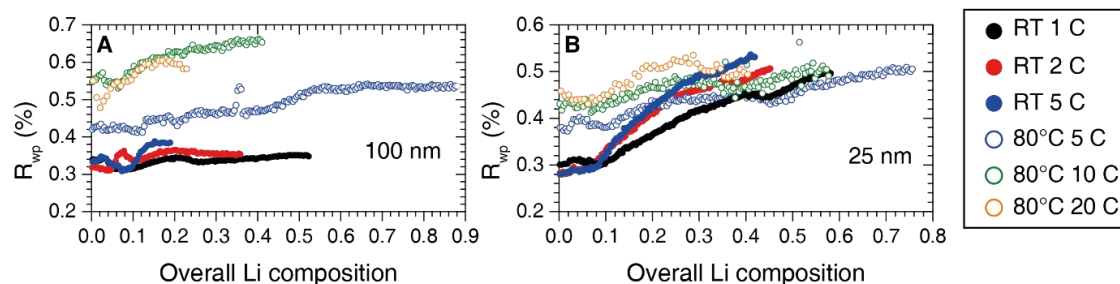


Figure 5.8 The R_{wp} factors in the Rietveld refinements for (A) 100 nm and (B) 25 nm particles. RT is short for room temperature.

The refined lattice parameters as a function of the overall Li composition determined from the electrochemistry during discharge are shown in Figure 5.9. The evolution of the α -TiO₂ lattice parameters exhibits two different regimes: (i) an initial steep increase (decrease) of the a (c) lattice parameter within the first ~ 0.1 overall Li composition, followed by (ii) a much gradual increase (decrease) of the a (c) lattice parameter until the end of discharge. Regime (i) is in line with the single-phase reaction within the limited Li solubility, where the insertion of Li only changes the Li composition of the α -TiO₂ phase. Upon entering regime (ii), the β -TiO₂ phase starts to form after the α -TiO₂ phase becomes saturated with Li.

The Li composition of each phase can be interpolated under the assumption of Vegard's law; here, it is based on the interpolation of the c lattice parameter since it has been shown to vary linearly across the stoichiometries of α -TiO₂, β -Li_{0.5}TiO₂, and γ -LiTiO₂[117] (Figure 5.10). The evolution of the Li composition of each phase during discharge is shown in Figure 5.11, where the dashed grey lines indicate the thermodynamic Li solubility limits determined from neutron diffraction studies of 120 nm particles.[117] It is noted, for example, in Figure 5.11 A for the discharge processes of 100 nm at room temperature, that the Li composition of the saturated α -TiO₂ (at the overall Li composition of ~ 0.07) and the emerging β -Li_{0.5}TiO₂ phase (at the overall Li composition of ~ 0.15) exceeds the thermodynamic Li solubility limit. Furthermore, as also shown in Figure 5.11 A, the Li composition of the saturated α -TiO₂ phase (at the overall Li composition of $0.07\sim 0.1$) increases progressively with cycle rate: the maximum Li composition of the α -TiO₂ phase before the formation of the β -TiO₂ phase is found to be $x = 0.042$, 0.045 , and 0.054 for 1 C, 2 C and 5 C, respectively, where x is the Li composition of Li _{x} TiO₂. This rate-dependent solubility is similar to what was observed[125] and predicted[29] for LiFePO₄ at moderately high rates, and is attributed to the overpotential induced by the high current. In comparison, the same, yet less

pronounced, rate-induced solubility is observed at higher temperature: for example, for the 100 nm particles cycled at 5 C at 80°C (Figure 5.11 B), the maximum Li composition of the α -TiO₂ phase before the β -Li_{0.5}TiO₂ phase is formed is less than that at room temperature (Li_{0.035}TiO₂ is observed at an overall Li composition of ~0.17 at 80°C, whereas Li_{0.054}TiO₂ is seen at an overall Li composition of 0.1 in Figure 5.11 A). The Li composition of the emerging β -Li_{0.5}TiO₂ phase is also closer to the thermodynamic limit than that at room temperature. A similar observation is also made for the 25 nm particles at 80°C in Figure 5.11 D.

The less pronounced rate-induced Li solubility at higher temperature reflects the kinetic nature of this phenomenon, which is associated with the finite Li diffusivity in the α -TiO₂ and β -Li_{0.5}TiO₂ phases. This can be understood from the fact that a system not subject to kinetic limitations will always be found in its thermodynamic equilibrium state, therefore, the Li composition of the α -TiO₂ and β -Li_{0.5}TiO₂ phases will never exceed their thermodynamic solubilities if the Li diffusion, which is found to be limited by the Li migration across the α -TiO₂/ β -Li_{0.5}TiO₂ interface[17], is infinitely fast. As the diffusion of Li becomes faster with increasing temperature, the Li solubilities of α -TiO₂ and β -Li_{0.5}TiO₂ will approach their thermodynamic limits.

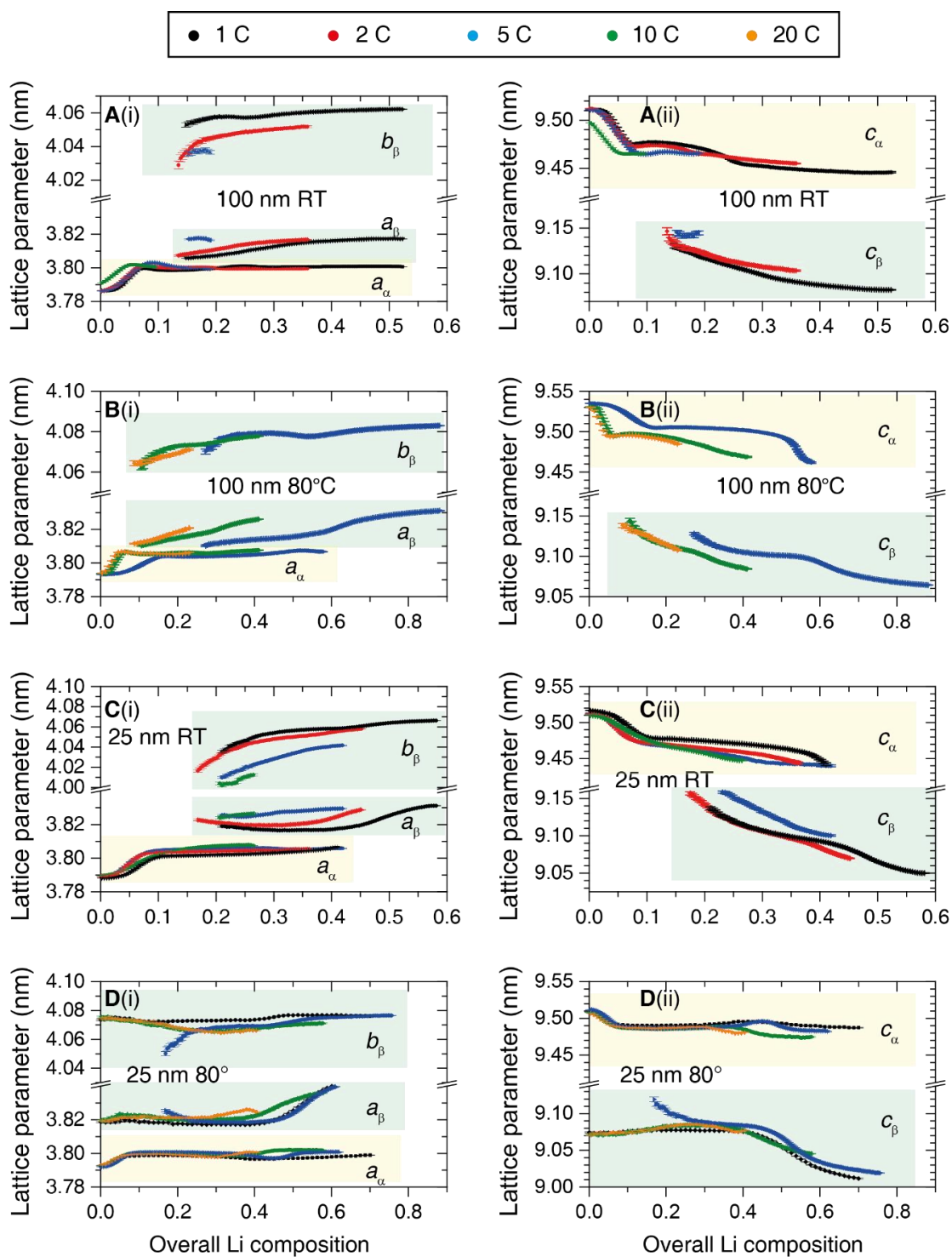


Figure 5.9 Lattice parameters of both α -TiO₂ (highlighted in yellow and labelled with the subscript α) and β -Li_{0.5}TiO₂ (highlighted in green and labelled with the subscript β) phases obtained from Rietveld refinements for both the room temperature (RT) and the 80°C discharge processes.

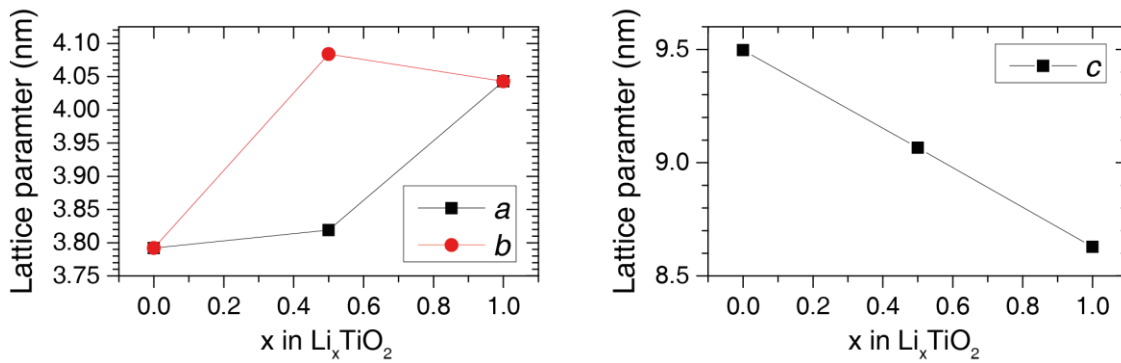


Figure 5.10 The lattice parameters of TiO_2 , $\text{Li}_{0.5}\text{TiO}_2$ and LiTiO_2 as reported in reference [117]. Only the c lattice parameter varies linearly with x across the entire Li composition range.

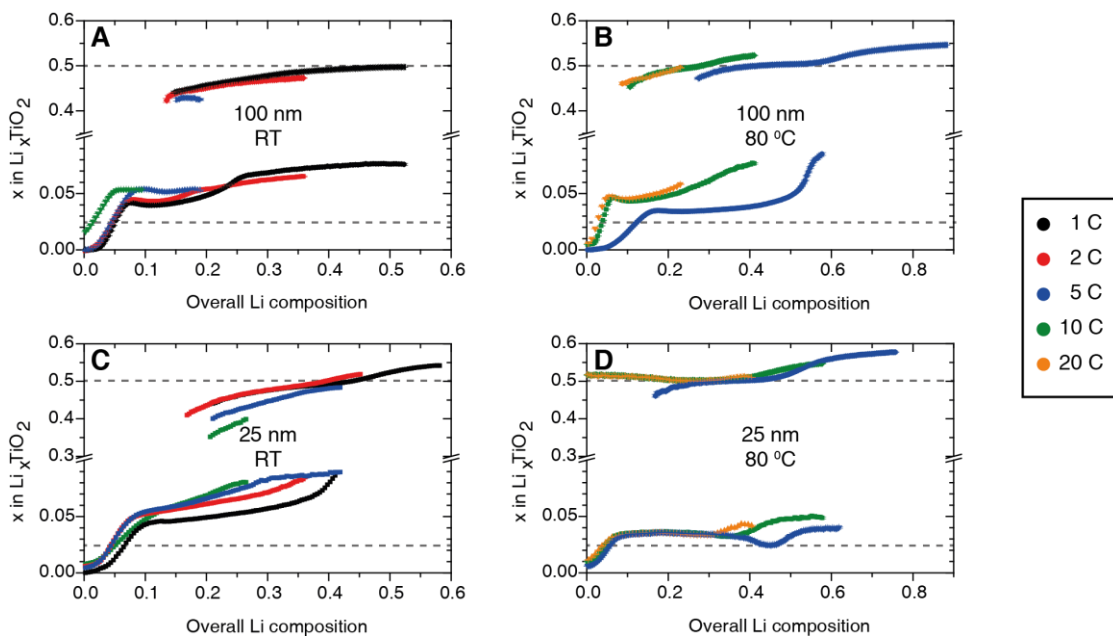


Figure 5.11 Evolution of the Li composition in $\alpha\text{-TiO}_2$ and $\beta\text{-Li}_{0.5}\text{TiO}_2$ for (A-B) 100 nm and (C-D) 25 nm particles during discharge. Room temperature (RT) results are shown in A and B, and elevated temperature experiments are shown in B and D. The dashed grey lines indicate the positions for Li solubilities of 0.025 and 0.5, which are considered as the boundaries of the thermodynamic Li solubility [117]. The error bars are smaller than the symbols.

The normalised scale factors (normalised against the scale factor of $\alpha\text{-TiO}_2$ at the start of lithiation) of both $\alpha\text{-TiO}_2$ and $\beta\text{-Li}_{0.5}\text{TiO}_2$ phases are shown in Figure 5.12 A and B for 100 nm and 25 nm particles, respectively. It can be seen that the $\alpha\text{-TiO}_2$ phase increases while the $\beta\text{-Li}_{0.5}\text{TiO}_2$ phase decreases with increasing overall Li composition. Because the scale factor and the Li composition (Figure 5.11) are known for both phases, the overall Li composition can also be determined by

$$\begin{aligned} \text{Overall Li composition} = & (\text{Normalised scale factor})_{\alpha} \times (\text{Li composition})_{\alpha} \\ & + (\text{Normalised scale factor})_{\beta} \times (\text{Li composition})_{\beta} \end{aligned} \quad (5.3)$$

where the subscripts α and β denote the α -TiO₂ and β -Li_{0.5}TiO₂ phases, respectively. The overall Li composition determined from Rietveld refined parameters is shown as a function of the overall Li composition determined from electrochemistry in Figure 5.12 C and D for 100 nm and 25 nm particles, respectively. If there is no side reaction, an increment in the overall Li composition determined from electrochemistry should, in principle, correspond to an equal increment in the overall Li composition determined from Rietveld refined parameters, i.e. the points in Figure 5.12 C and D should follow a linear relationship with a slope of one. Any deviation from the linear relationship with a slope of one indicates the presence of side reactions, unrealistic Rietveld refined parameters and/or the formation of amorphous phase not captured by XRD. It is noted that substantial deviation from the linear relationship (indicated by the dashed grey lines) occurs only for 1 C cycling for 100 nm at room temperature (Figure 5.12 C) for more than 0.3 overall Li composition determined from electrochemistry. This deviation is consistent with its electrochemistry shown in Figure 5.4 A, as discussed in Section 5.3.1, that the sloping voltage observed for more than 0.3 overall cycled Li is, at least in part, due to side reactions involved in the formation of the solid electrolyte interphase.

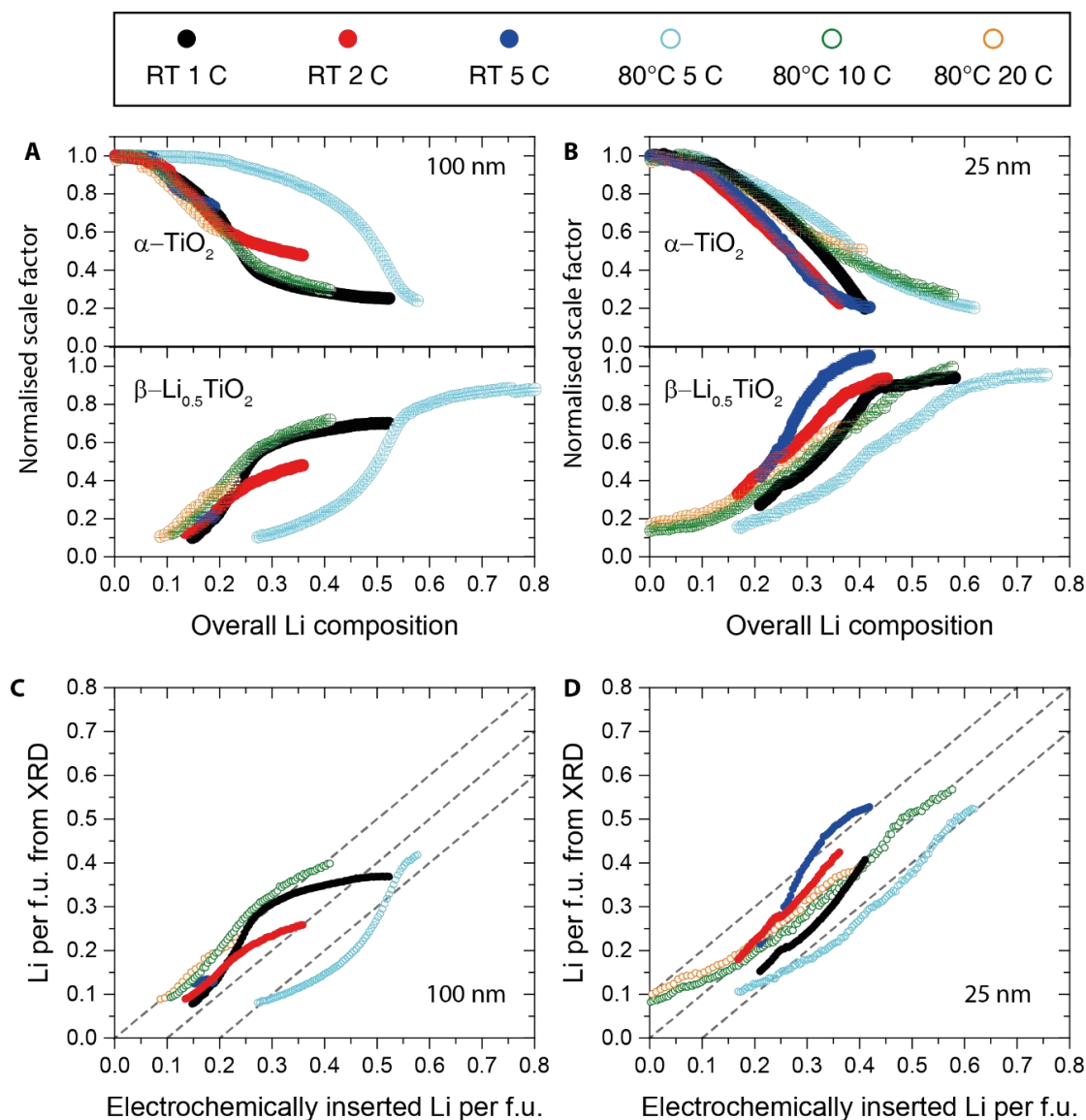


Figure 5.12 Normalised scale factors (normalised against the scale factor of $\alpha\text{-TiO}_2$ at the start of lithiation) for (A) 100 nm and (B) 25 nm particles as a function of the overall Li composition. (C) and (D) show the overall Li composition determined from XRD as a function of the overall Li composition determined from electrochemistry for 100 nm and 25 nm particles, respectively. The dashed grey lines have a slope of 1. RT represents room temperature.

5.3.3 Microstructural evolution of anatase TiO_2 particles during discharge

Although the *in situ* XRD patterns clearly show the presence of only two phases, it is not obvious as to what occurs on the particle level: does the reaction proceed particle by particle or simultaneously in all particles? To answer this question, microstructural analysis was performed based on the full width at half maximum (FWHM) of the (024), (116) and (220) reflections of the $\alpha\text{-TiO}_2$ phase and the (011), (204) and (220) reflections of the $\beta\text{-Li}_{0.5}\text{TiO}_2$ phase. These reflections were selected on the criterion that there is no

or only a small amount of overlap with other reflections, in order to minimise ambiguity and correlation in the peak fitting process. The results from fitting individual reflections including FWHM and domain size calculated from Scherrer formula, and the phase fractions obtained from Rietveld refinements are presented and discussed below.

5.3.3.1 100 nm TiO₂ particles

The fitting results for 100 nm particles are shown in Figure 5.13 and Figure 5.14 for the discharge at room temperature and 80 °C, respectively. Typical fitting patterns are shown in Figure 5.15. For 100 nm particles cycled at a rate of 1 C at room temperature (Figure 5.13 A(i)), the (024), (116) and (220) reflections of the α -TiO₂ phase become broader as more Li is inserted. Meanwhile, as shown in Figure 5.13 A(ii), the (011) reflection of the β -Li_{0.5}TiO₂ phase decreases in FWHM, while the (204) reflection remains almost constant in FWHM and the (220) reflection shows an increase in FWHM for more than 0.25 overall Li composition. Since β -Li_{0.5}TiO₂ is the newly formed phase, its domain size will only increase (in case of the two-phase reaction with intra-particle phase separation) or remain constant (in case of the particle by particle reaction) as lithiation proceeds, resulting in the narrowing or the invariance of the peak width, respectively. The reduction in symmetry from tetragonal (α -TiO₂) to orthorhombic (β -Li_{0.5}TiO₂) gives rise to different *a* and *b* lattice constants. Previous studies find an increase in the length of the zig-zag Ti-O-Ti chain along the *b* axis when Li is intercalated.[113] Therefore, a variation in the Li composition of the β -Li_{0.5}TiO₂ phase could lead to distortions in the Ti-O-Ti chain and variations in the *b* lattice parameter of β -Li_{0.5}TiO₂. Since the (220) plane is not parallel to the *b* axis, distortions in the *b* axis could introduce variations in the inter-plane spacing of the (220) planes, and hence the broadening of the (220) reflection. Consequently, the increase in FWHM of the (220) reflection of the β -Li_{0.5}TiO₂ phase is attributed to the microstrain effect. If the broadening of all the select reflections, except the (220) reflection of β -Li_{0.5}TiO₂, is due largely to the finite domain size effect, the domain size of each phase can be deduced using the Scherrer formula. Figure 5.13 A(iii) shows the evolution of the domain size deduced from FWHM of the (116) reflection of α -TiO₂ and the (011) reflection of β -Li_{0.5}TiO₂. It is seen that the domain size of α -TiO₂ decreases from 80 nm to 73 nm from an overall Li composition of 0 to 0.07. This slight initial decrease of 7 nm in the domain size of α -TiO₂ is again attributed to the microstrain induced by Li composition variation within the limited solid solution of α -TiO₂, since α -TiO₂ is the only phase present when the overall Li composition is between 0 and 0.07, i.e.

there is no size induced broadening. Further Li insertion results in a drastic decrease in the domain size of α -TiO₂ from 73 nm to 16 nm towards the end of lithiation, while the domain size of β -Li_{0.5}TiO₂ grows to 30 nm. The growth of the β -Li_{0.5}TiO₂ domain at the expense of the α -TiO₂ one is expected for a two-phase reaction with the nucleation and growth of a second phase within the particles of the first phase. The fact that this process is captured by powder XRD, which measures a large number of crystallites at a time, indicates the two-phase reaction occurs simultaneously in all particles. Although the domain size of β -Li_{0.5}TiO₂ at the end of lithiation appears to be small even though it constitutes 70% of the total phase fraction (Figure 5.13 A(iv)), the small domain size (30 nm) of β -Li_{0.5}TiO₂ could be the result of more than one α -TiO₂/ β -Li_{0.5}TiO₂ interface per particle[17] and/or a concurrent microstrain broadening due to the Li composition variation of β -Li_{0.5}TiO₂. As shown in Figure 5.13 B and C, increasing the cycling rate to 2 C and 5 C does not qualitatively change the behaviour of FWHM of the reflections: the α -TiO₂ reflections increase while the β -Li_{0.5}TiO₂ reflections decrease or remain constant in FWHM with increasing overall Li composition, indicating the same two-phase reaction with the 1 C discharge. It is noted that FWHM of the β -Li_{0.5}TiO₂ reflections increases with the cycling rate: for example, as shown in Figure 5.13, the FWHM of the (204) reflection of β -Li_{0.5}TiO₂ is 0.19°, 0.36° and 0.4° for 1 C, 2 C and 5 C, respectively, suggesting the formation of smaller β -Li_{0.5}TiO₂ domains or larger microstrain with increasing rate. Broad reflections with weak intensities can lead to large uncertainties in the determination of FWHM, as can be seen in the fitting pattern in Figure 5.15 C for the overall Li composition of 0.19 during 5 C discharge at room temperature. As with discharge at room temperature, cycles at 80°C for 100 nm particles (Figure 5.14) still proceed by the two-phase reaction: the decrease of the α -TiO₂ domain size and the increase of the β -Li_{0.5}TiO₂ domain size with increasing overall Li composition.

A previous room temperature *in situ* XRD study[119] performed at C/120 rate reported a sequential nucleation mechanism for the phase transition of 130 nm anatase TiO₂ particles, i.e. the reaction was shown not to take place simultaneously in all particles. The difference in the reaction mechanism could be attributed to the different rates applied in the experiment. Prior simulation studies[126] demonstrate that a higher fraction of an ensemble of electrode particles, which transform sequentially at lower rates, transform simultaneously at higher rates. The lithiation process of 100 nm TiO₂ particles is summarised in Figure 5.16: (i) lithiation starts with a single phase reaction in the α -TiO₂

phase, followed by (ii) the simultaneous nucleation of β - $\text{Li}_{0.5}\text{TiO}_2$ domains in all particles; (iii) the β - $\text{Li}_{0.5}\text{TiO}_2$ domains continue to grow until all the α - TiO_2 domains are transformed into β - $\text{Li}_{0.5}\text{TiO}_2$.

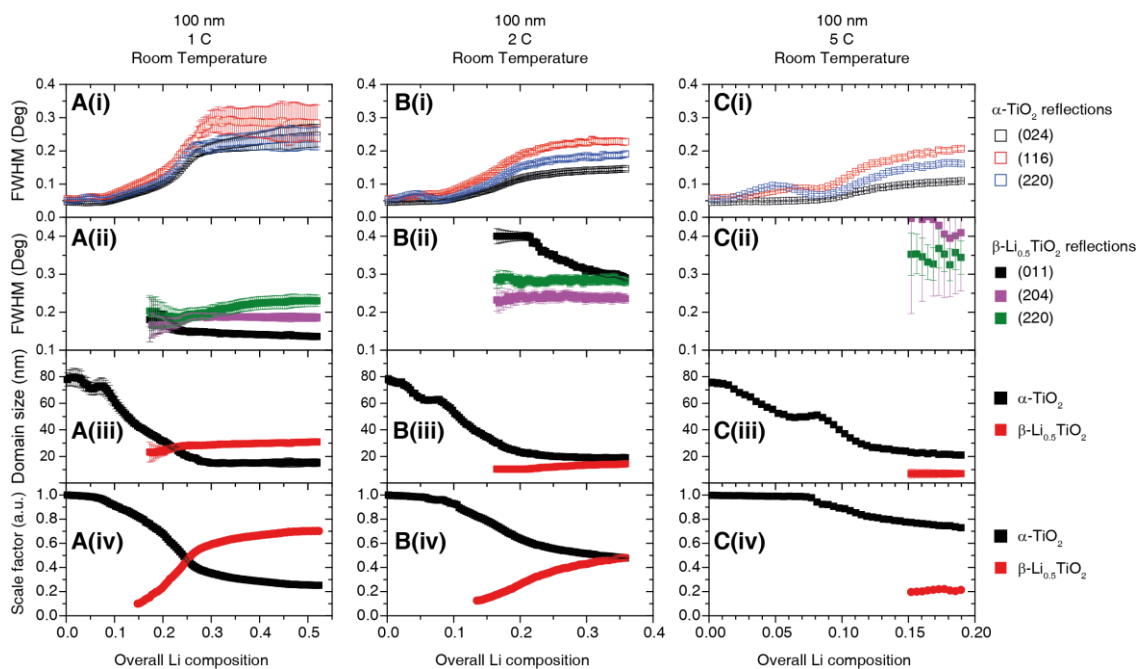


Figure 5.13. The evolution of the FWHM of select reflections from both α - TiO_2 and β - $\text{Li}_{0.5}\text{TiO}_2$ (i-ii), the domain size determined from the FWHM of the (116) reflection for α - TiO_2 and the (011) reflection for β - $\text{Li}_{0.5}\text{TiO}_2$ (iii), and scale factor (iv) as a function of the overall inserted Li for 100 nm particles during discharge at cycle rates of (A) 1C, (B) 2C and (C) 5C at room temperature.

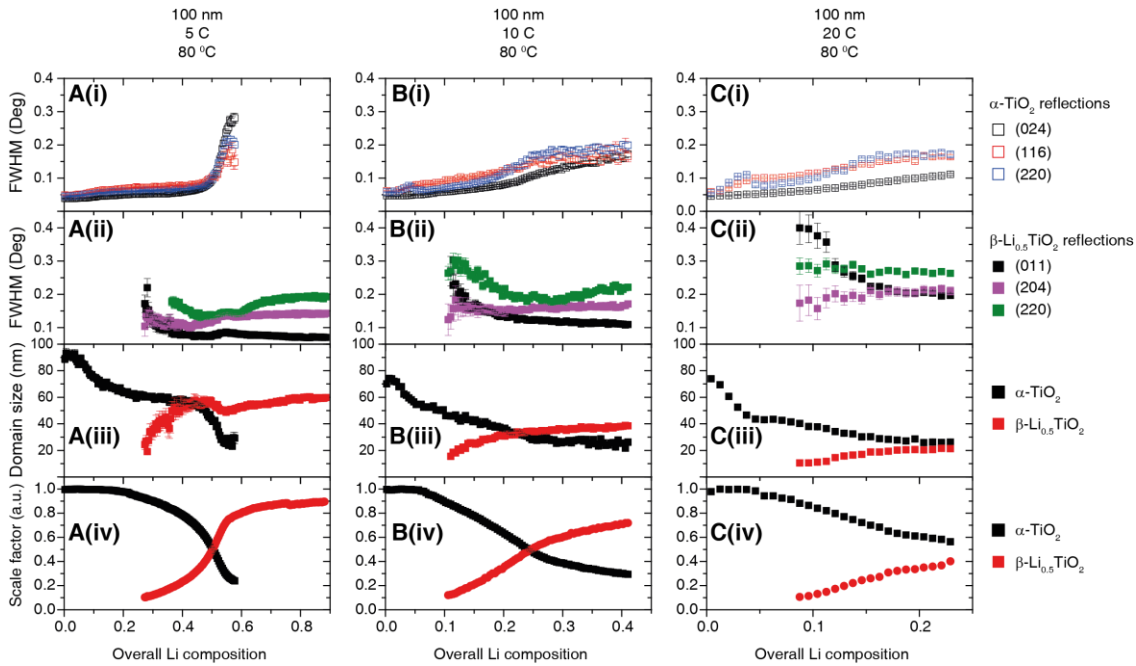


Figure 5.14 The evolution of the FWHM of select reflections from both α -TiO₂ and β -Li_{0.5}TiO₂ (i-ii), the domain size determined from FWHM of the (116) reflection for α -TiO₂ and the (011) reflection for β -Li_{0.5}TiO₂ (iii), and scale factor (iv) as a function of the overall inserted Li for 100 nm particles during discharge at cycle rates of (A) 5C, (B) 10C and (C) 20C at 80°C.

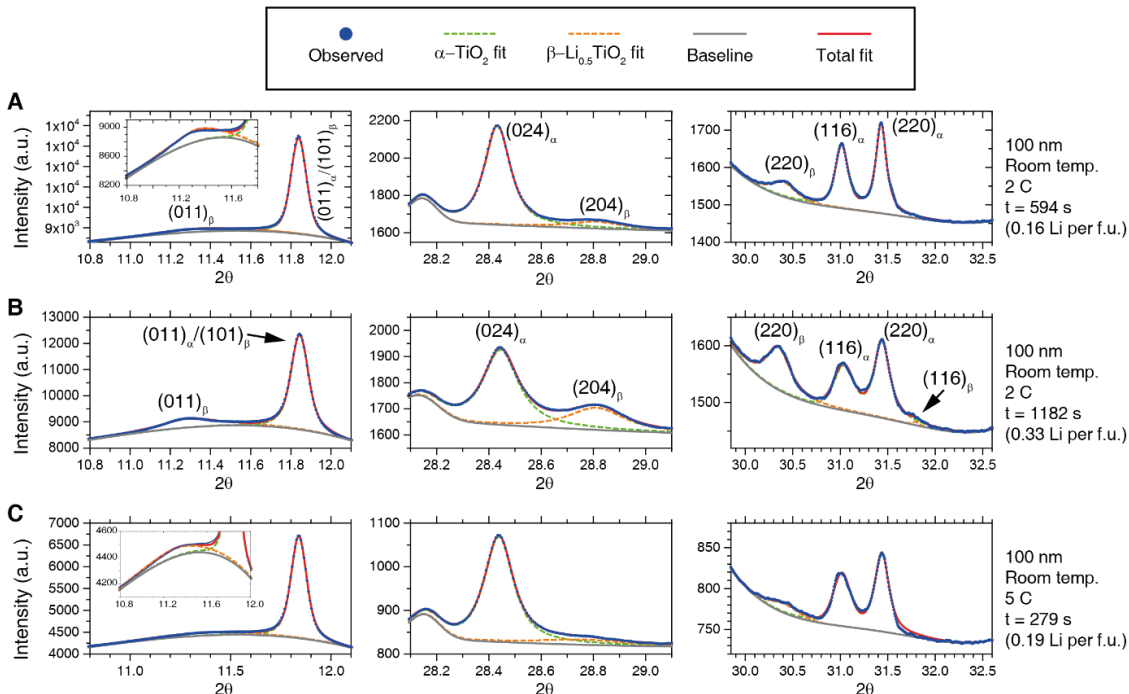


Figure 5.15 Typical peak fitting patterns for 100 nm particles during room temperature charge at cycles rates of (A-B) 2 C and (C) 5 C. Blue dots are the experimental data, and red curves represent the overall fit.

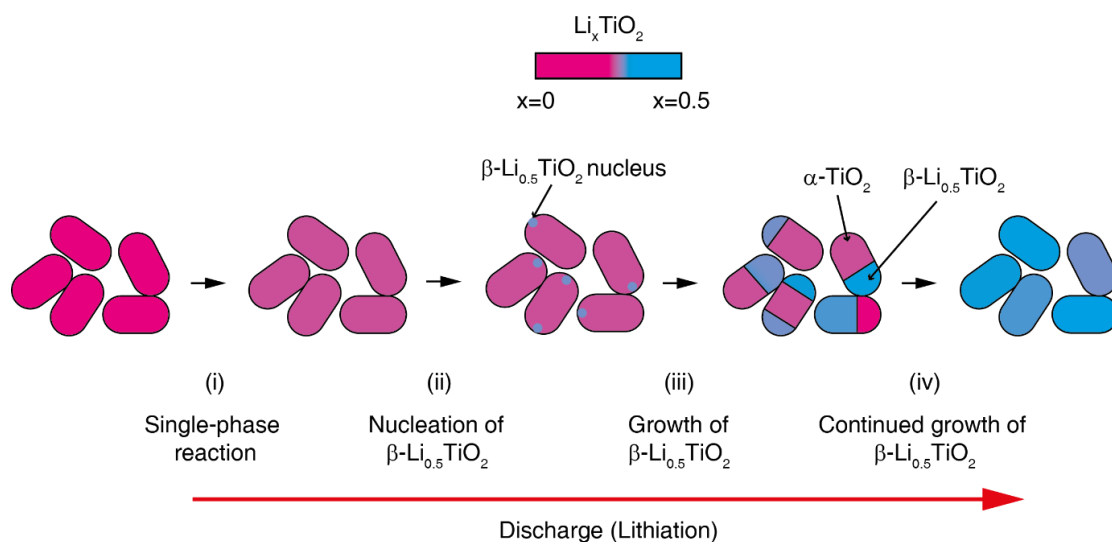


Figure 5.16 Schematic illustration of the phase transition occurring in 100 nm anatase TiO_2 particles during high rate discharge. Lithiation proceeds firstly by a solid solution reaction in the $\alpha\text{-TiO}_2$ phase (i) followed by the nucleation of $\beta\text{-Li}_{0.5}\text{TiO}_2$ (ii). The $\beta\text{-Li}_{0.5}\text{TiO}_2$ domains grow in size until the entire particle comprises a single phase (iii-iv).

5.3.3.2 25 nm TiO_2 particles

The fitting results for 25 nm particles are shown in Figure 5.17 and Figure 5.18 for cycles at room temperature and 80°C , respectively. Typical peak fitting results are shown in Figure 5.19. During the discharge at a cycle rate of 1 C at room temperature (Figure 5.17 A(i)) the FWHM of the $\alpha\text{-TiO}_2$ reflections increases from 0.2° to 0.3° from an overall Li composition of 0 to 0.4. The evolution of $\beta\text{-Li}_{0.5}\text{TiO}_2$ reflections, shown in Figure 5.17 A(ii), follows the same trend as observed for the 100 nm particles: the FWHM of the (011) and (204) reflections decreases with increasing overall Li composition, while the FWHM of the (220) reflection decreases first until the overall Li composition reaches 0.45, after which it increases again. Figure 5.17 A(iii) shows the domain size as a function of overall Li composition deduced from the FWHM of the (116) reflection of $\alpha\text{-TiO}_2$ and the (011) reflection of $\beta\text{-Li}_{0.5}\text{TiO}_2$. As shown in Figure 5.17 A(iii) for 1 C discharge, the domain size of $\alpha\text{-TiO}_2$ decreases from 23 nm to 15 nm when the overall Li composition increases from 0 to 0.4, meanwhile the phase fraction of $\alpha\text{-TiO}_2$ decreases by 80 %. If the two phases in a spherical particle assume a core-shell morphology, where the core is $\alpha\text{-TiO}_2$ and the shell is $\beta\text{-Li}_{0.5}\text{TiO}_2$, the volume fraction of a 15 nm diameter spherical core of $\alpha\text{-TiO}_2$ in a 23 nm diameter spherical particle would correspond to 28 %, which is very close to the 20 % phase fraction of the $\alpha\text{-TiO}_2$ phase. However, this core-shell arrangement would yield a shell ($\beta\text{-Li}_{0.5}\text{TiO}_2$) thickness of 4 nm, which is far less than the value, 17 nm, determined from the Scherrer formula. Therefore, the only plausible

explanation is that the lithiation takes place particle by particle and the decrease in the domain size of α -TiO₂ from 23 nm to 15 nm is associated with the microstrain developed in α -TiO₂. This microstrain could result from the distortion present in the α -TiO₂ phase and/or the Li composition variation between different α -TiO₂ particles. The particle-by-particle mechanism also stipulates a constant domain size for β -Li_{0.5}TiO₂, hence, the very large broadening at the point where the β -Li_{0.5}TiO₂ peaks emerge is also associated with the microstrain effect, which is likely to be caused by compositional variation between β -Li_{0.5}TiO₂ particles. Reactions at higher rates, shown in Figure 5.17 B for 2 C and Figure 5.17 C for 5 C, exhibit qualitatively similar behaviour and also proceed particle by particle. It is noted in Figure 5.17 C for 5 C discharge that the domain size of β -Li_{0.5}TiO₂ is 12 nm at the overall Li composition of 0.4, well below 20 nm observed at the end charge for cycle rates of 1 C and 2 C, despite the dominant presence of the β -Li_{0.5}TiO₂ phase. Hence, this provides a direct evidence for the presence of microstrain in β -Li_{0.5}TiO₂.

When the temperature is raised to 80°C, for example, for the cycle rate of 5 C as shown in Figure 5.18 A(i), the FWHM of the (024) reflection of α -TiO₂ remains almost constant at ~0.18° throughout the entire overall Li composition, while the FWHM of the (116) and (220) reflections of α -TiO₂, after a rapid initial increase from 0 to 0.07 overall Li, which is attributed to the microstrain effect, also shows very little change over the rest of the overall Li composition range. As shown in Figure 5.18 A(ii), the FWHM of the (011) reflection of β -Li_{0.5}TiO₂ decreases monotonically with increasing overall Li composition, whereas the FWHM of the (204) and (220) reflections decreases from 0.2 to 0.45 overall Li composition and increases from 0.45 overall Li composition onwards. The increase in the FWHM of the (204) reflection, in addition to the (220) reflection, of β -Li_{0.5}TiO₂ is attributed to the microstrain effect. As shown in Figure 5.18 A(iii), the domain size of α -TiO₂ determined from FWHM of the (116) reflection of α -TiO₂ remains effectively invariant at ~20 nm except the small initial drop from 23 nm to 20 nm from 0 to 0.07 overall Li composition. Since the 10 C and 20 C discharge was carried out consecutively on the same cell after the cycle at 5 C, a small amount (~10%) of the β -Li_{0.5}TiO₂ phase (residual β -Li_{0.5}TiO₂), which did not transform back to α -TiO₂, was present at the beginning of 10 C and also 20 C discharge (shown in Figure 5.19 C for 10 C charge). The presence of the residual β -Li_{0.5}TiO₂ phase complicates the interpretation of the FWHM of the β -Li_{0.5}TiO₂ reflections: the increase, as opposed to the decrease as observed at all other rates, in the FWHM of the β -Li_{0.5}TiO₂ reflections, as shown in Figure

5.18 B(ii) and C(ii) for 10 C and 20 C, respectively, is attributed to the formation of β - $\text{Li}_{0.5}\text{TiO}_2$ particles that are not compositionally homogenous. Nonetheless, interpretation of the FWHM of the α - TiO_2 reflections and the deduced domain size of α - TiO_2 , is not affected: the effectively invariant domain size (~ 20 nm) of α - TiO_2 throughout the entire overall Li composition for the 10 C and 20 C discharge, shown in Figure 5.18 B(iii) and C(iii), respectively, is consistent with the particle by particle reaction mechanism.

The particle by particle reaction mechanism is in agreement with the previous findings from *in situ*[119] and *ex situ*[117] XRD studies of anatase TiO_2 nanoparticles (15 nm and < 40 nm, respectively), and is attributed to the high energy of the α - TiO_2/β - $\text{Li}_{0.5}\text{TiO}_2$ interface, whose disappearance reduces the total energy of the system. Figure 5.20 summarises the lithiation process: (i) the initial lithiation involves the single phase reaction in the α - TiO_2 phase, and (ii) further lithiation triggers the instantaneous transformation of an entire α - TiO_2 domain into a β - $\text{Li}_{0.5}\text{TiO}_2$ one (stages (ii-iv)), which does not occur simultaneously in all particles but proceeds from particle to particle until every particle is transformed.

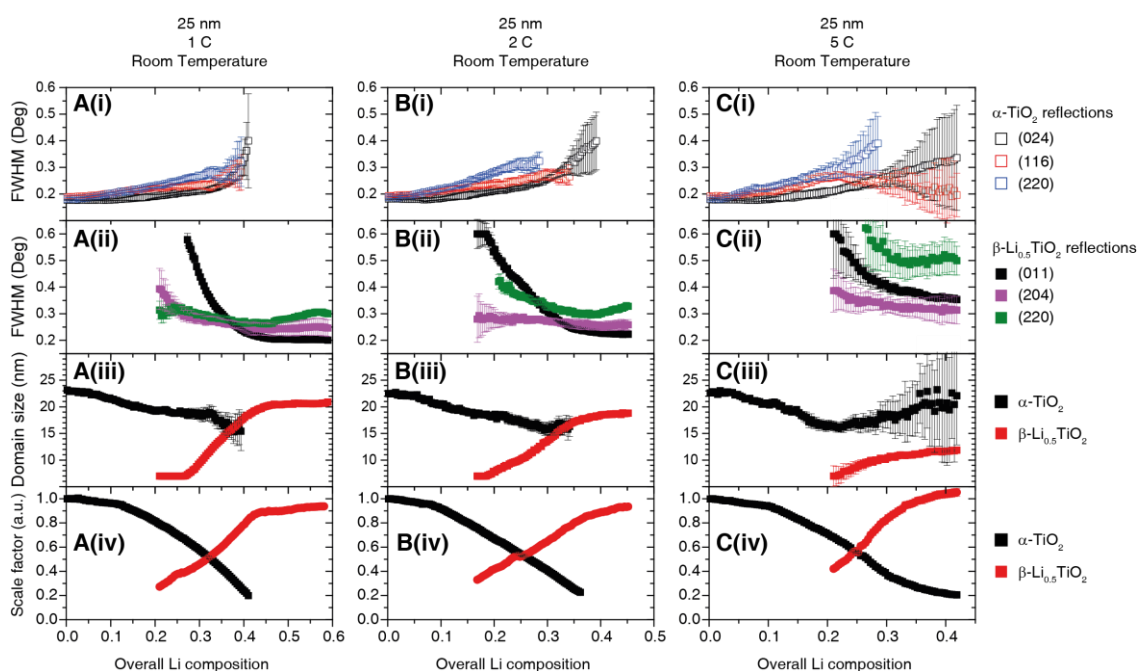


Figure 5.17. The evolution of the FWHM of select reflections from both α - TiO_2 and β - $\text{Li}_{0.5}\text{TiO}_2$ (i-ii), the domain size determined from the FWHM of the (116) reflection for α - TiO_2 and the (011) reflection for β - $\text{Li}_{0.5}\text{TiO}_2$ (iii), and scale factor (iv) as a function of the overall inserted Li for 25 nm particles during discharge at cycle rates of (A) 1C, (B) 2C and (C) 5C discharge at room temperature.

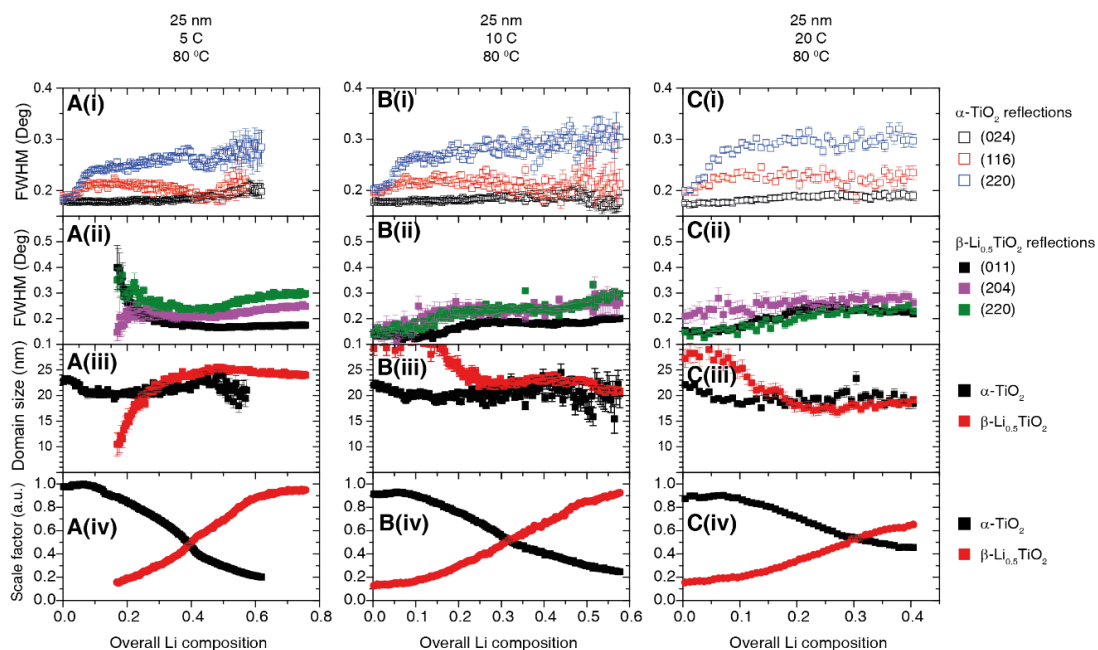


Figure 5.18. The evolution of the FWHM of select reflections from both α -TiO₂ and β -Li_{0.5}TiO₂ (i-ii), the domain size determined from the FWHM of the (116) reflection for α -TiO₂ and the (011) reflection for β -Li_{0.5}TiO₂ (iii), and scale factor (iv) as a function of the overall inserted Li for 25 nm particles during discharge at cycle rates of (A) 5C, (B) 10C and (C) 20C discharge at 80 °C.

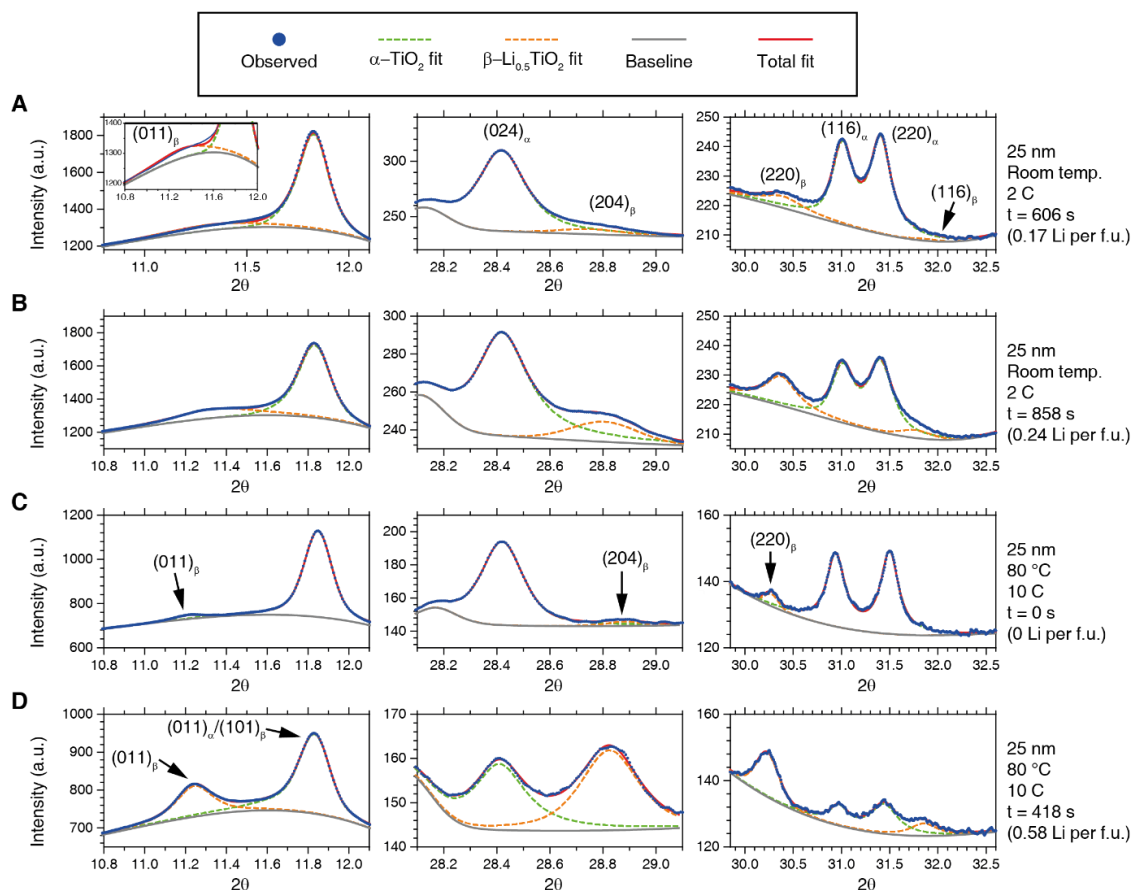


Figure 5.19 Representative peak fitting patterns for 25 nm particles during charge at cycle rates of (A-B) 2 C at room temperature and (C-D) 5 C at 80°C.

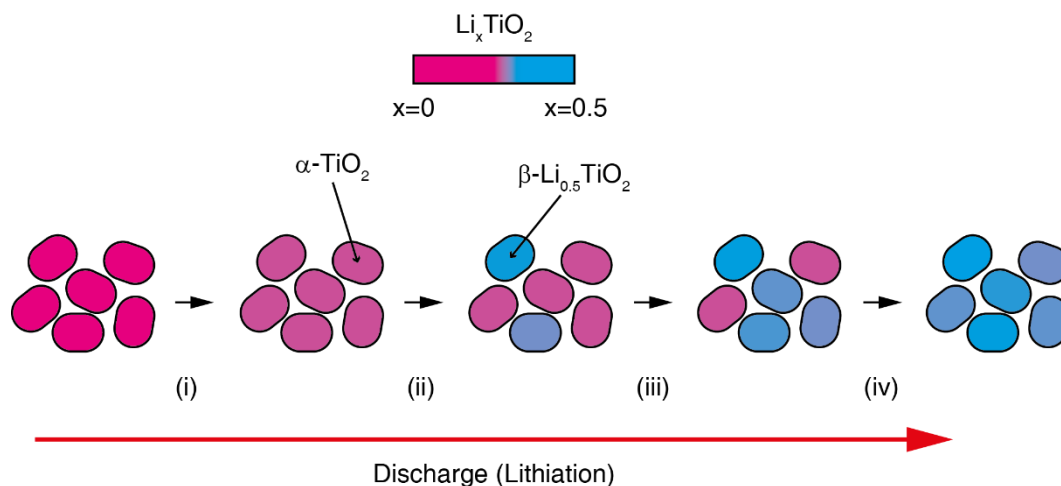


Figure 5.20. Schematic illustration of the phase transition occurring in 25 nm anatase TiO_2 particles during high rate discharge. Lithiation proceeds firstly by a solid solution reaction in the $\alpha\text{-TiO}_2$ phase (i) followed by the sequential (particle-by-particle) transformation from $\alpha\text{-TiO}_2$ to $\beta\text{-Li}_{0.5}\text{TiO}_2$ particles (ii-iv).

5.3.4 Discussion on the nature of the instantaneous phase transition of 25 nm TiO₂ particles

What remains unanswered from the preceding sections is the microscopic process by which an entire α -TiO₂ domain transforms into a β -Li_{0.5}TiO₂ one. Analogous to the case for LiFePO₄ nanoparticles, two mechanisms need to be examined: (i) phase transition by a continuous structure change from α -TiO₂ to β -Li_{0.5}TiO₂, and (ii) nucleation of β -Li_{0.5}TiO₂ in α -TiO₂ domain followed instantaneously by the fast propagation of the phase boundary.

Since the transformation from α -TiO₂ to β -Li_{0.5}TiO₂ involves a change in crystal symmetry from $I4_1/amd$ to $Imma$, corresponding to a group-subgroup relationship, a continuous path, if there is one, between the two phases must undergo a second-order phase transition. Although continuous structure transition between α -TiO₂ and β -Li_{0.5}TiO₂ is found, with the use of the programme ISOTROPY[53], to be allowed by Landau theory[52], whether it will occur depends on the energetics and kinetics of various transition pathways.

The Gibbs free energy diagram for different phase transition paths is displayed in Figure 5.21. If the transformation from α -TiO₂ to β -Li_{0.5}TiO₂ proceeds by a continuous structural phase transition, the energy will evolve along the solid black curve during lithiation: the initial lithiation involves the single-phase reaction of α -TiO₂ until it reaches the critical point O , beyond which the energy for the high symmetry phase (α -TiO₂) becomes higher than the low symmetry one (β -Li_{0.5}TiO₂). Therefore, traversing across point O from left to right, the entire nanoparticle will spontaneously transform to β -Li_{0.5}TiO₂. This transition should manifest itself in the XRD measurement as a continuous splitting of the $(0kl)$ (l can be 0) reflections into $(0kl)$ and $(k0l)$ reflections, in the case studied here, the splitting of the (024) reflection of α -TiO₂ into the (024) and (204) reflections of β -Li_{0.5}TiO₂. Further lithiation beyond the transition point O proceeds as a single-phase reaction of β -Li_{0.5}TiO₂. If the transformation takes place via a nucleation and growth mechanism, the Li composition in the nanoparticle will evolve along the solid red curve, which differs from the equilibrium energy (solid green) only by an α -TiO₂/ β -Li_{0.5}TiO₂ interfacial energy, ΔG_1 . Phase separation will be induced within the composition between A and B , i.e. between the points where the red curve crosses the black curve.

The absence of any continuous splitting of the (024) reflection of α -TiO₂ in the *in situ* XRD patterns presented in Figure 5.5 and Figure 5.6 suggests the transformation takes place by a nucleation and growth mechanism. Kinetics aside, the transformation should take the route that lies lower in energy, and it is possible that the energy barrier for the second-order phase transition (solid black curve) is too high for it to occur. In addition, the interfacial energy, ΔG_1 , can be minimised by forming an interface along a zero-strain plane[115], hence favouring the two-phase mechanism with a fast propagation of the interface.

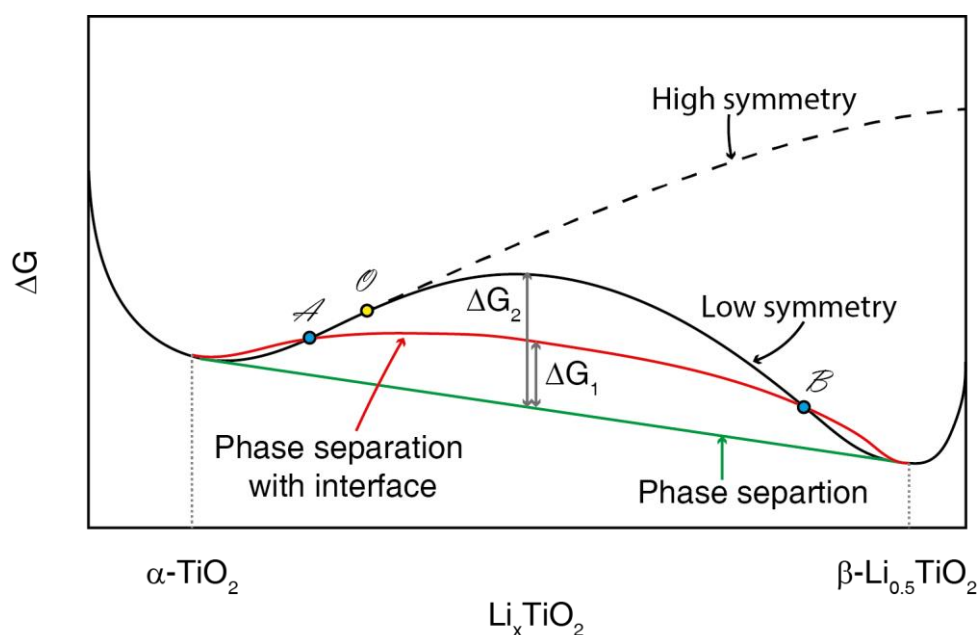


Figure 5.21. Illustration of the change in Gibbs free energy for various phase transition paths. The solid black line represents a continuous structural transition (second-order phase transition), and the critical point is marked by *O* (solid yellow circle). The dashed black line is the projected energy curve if there is no reduction to lower symmetry. The solid green line is the common tangent construction that determines the lowest possible energy of a system with a mixture of α -TiO₂ and β -Li_{0.5}TiO₂ not coexisting in the same particle. The solid red line is the modified energy of a system with a mixture of α -TiO₂ and β -Li_{0.5}TiO₂ separated by a phase boundary.

5.4 Conclusion

The lithiation mechanism of anatase TiO₂ particles during Li insertion was investigated by *in situ* XRD as a function of rate, particle size and cycling temperature. Li solubilities of the end member phases, α -TiO₂ and β -Li_{0.5}TiO₂, are found to increase noticeably with increasing rate, yet no continuous transition from α -TiO₂ to β -Li_{0.5}TiO₂ is observed, even at a cycle rate of 20 C. An increase in temperature from room temperature to 80°C results a significant improvement in the electrode's electrochemical performance although the

reaction proceeds by a two-phase reaction. The Li solubility exceeds the thermodynamic limit and increases with cycling rate for both the α -TiO₂ and β -Li_{0.5}TiO₂ phases, due to the kinetic limitation imposed by the finite Li diffusivity. Domain size information obtained from the line broadening analysis reveals a change in the phase transition mechanism brought about by a reduction in particle size from 100 nm to 25 nm: the 100 nm particles react simultaneously via a conventional nucleation and growth mechanism, while the 25 nm particles react sequentially via a two-phase mechanism.

6 Phase transitions of LiVPO₄F at high rates of charge

6.1 Introduction

LiVPO₄F[127,128] can be cycled reversibly between LiVPO₄F and VPO₄F utilising the V³⁺/V⁴⁺ redox couple. However, the reaction on the charge (from LiVPO₄F to VPO₄F) takes a different reaction pathway than on the discharge (from VPO₄F to LiVPO₄F): the charge (Li extraction) process of LiVPO₄F proceeds by two, distinct two-phase reactions between LiVPO₄F and Li_{0.67}VPO₄F and between Li_{0.67}VPO₄F and VPO₄F at voltages of 4.24 V and 4.28 V, respectively, while discharging process (Li insertion) of VPO₄F proceeds by only one two-phase reaction between VPO₄F and LiVPO₄F.[129][130] The typical charge and discharge voltage profile is shown in Figure 6.1. It is not clear what causes the difference between the charging and discharging processes. The first-order phase transition from LiVPO₄F and Li_{0.67}VPO₄F does not induce a change in crystal symmetry and both phases adopt the space group *P-1* (triclinic), while the first-order phase transition from Li_{0.67}VPO₄F to VPO₄F raises the symmetry from *P-1* to *C2/c* (monoclinic). The crystal structures of LiVPO₄F (triclinic *P-1*, No. 2) and VPO₄F (monoclinic *C2/c*, No. 15) are shown in Figure 6.2 A-B and C-D, respectively.[127,130,131] The change in the crystal symmetry from LiVPO₄F (*P-1*) to VPO₄F (*C2/c*) is accompanied by the unit cell transformation, which is described by

$$\begin{pmatrix} a_m \\ b_m \\ c_m \end{pmatrix} = \begin{pmatrix} -1 & -1 & 0 \\ 1 & -1 & 0 \\ 1 & 1 & 1 \end{pmatrix} \begin{pmatrix} a_t \\ b_t \\ c_t \end{pmatrix} \quad (6.1)$$

where the subscripts *t* and *m* denote the triclinic (LiVPO₄F, *P-1*) and monoclinic (VPO₄F, *C2/c*) systems, respectively. Since one of the two two-phase reactions during charge involves a change in crystal symmetry while the other does not, the charging process provides the unique opportunity to study the phase transition both in the presence and the absence of a change in crystal symmetry. In this chapter, the phase transitions of LiVPO₄F during charge at different rates were investigated by *in situ* synchrotron XRD.

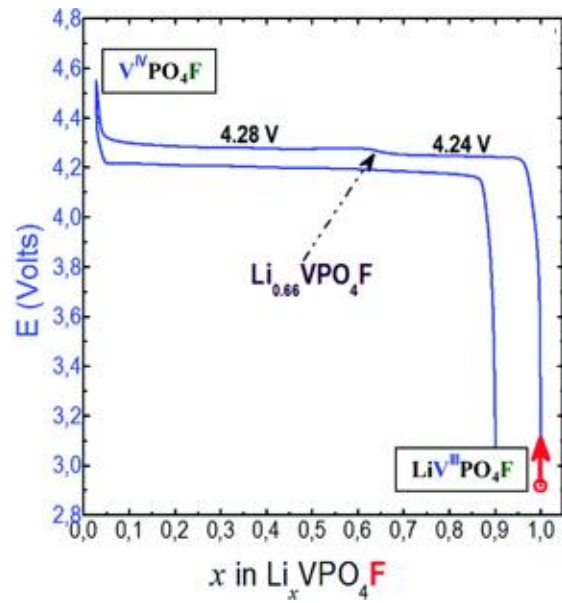


Figure 6.1 The voltage profile during charge and discharge of LiVPO_4F at C/50. Two voltage plateaus (4.24 V and 4.28 V) are observed on charge while only one voltage plateau is observed on discharge. Figure reproduced from reference [130].

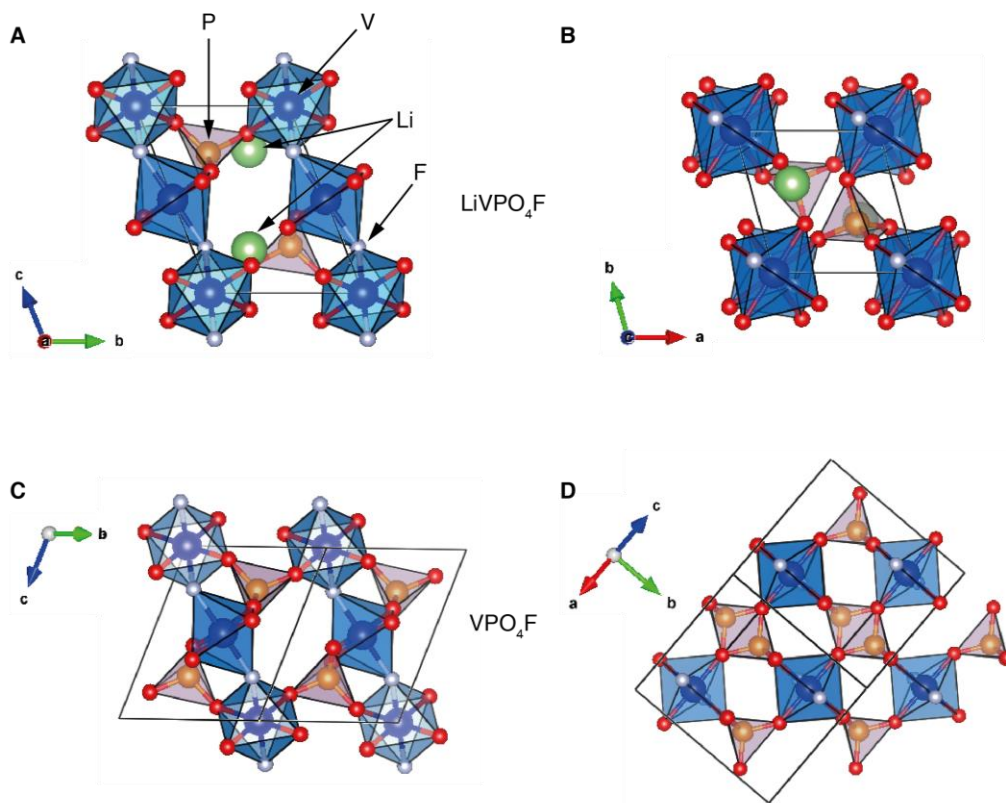


Figure 6.2. The crystal structures of (A, B) LiVPO_4F and (C, D) VPO_4F . The structures in A and B are viewed from the side of the V-F-V chains while those in B and D are viewed along the chains.

6.2 Experimental

6.2.1 Materials and electrode preparation

LiVPO₄F powder was provided by Dr. Laurence Croguennec's group at the University of Bordeaux. The electrode was prepared with a high proportion of carbon additives, to improve the electrochemical performance of the active material at high rates (by increasing the electronic conductivity). For a typical electrode, 3 mg of LiVPO₄F powder was mixed with Super P carbon (Alfa Aesar), carbon black (Vulcan XC-72, Cabot Corporation) and polytetrafluoroethylene (PTFE) binder (Sigma-Aldrich) in the mass ratio 3:3:3:1 and was pressed (1.6-1.8 ton) into a pellet of 13 mm in diameter.

6.2.2 *In situ* XRD measurement

The electrode pellet was assembled in a homemade *in situ* Swagelok cell with Li foil as the anode, glass fibre as the separator and 1 M LiPF₆ in ethylene carbonate/dimethyl carbonate (1:1 vol%, Solvionic) as the liquid electrolyte. *In situ* synchrotron XRD measurements were performed at beamline I11 Diamond, UK (wavelength 0.825974 Å), with transmission geometry. The time-resolved position sensitive detector (Mythen2) was used to minimise the time for data collection. The data collection time of each pattern for 1 C, 2 C and 5 C cycling rates were 33.13 s, 18.8 s and 18 s, respectively, which correspond to 0.009 Li, 0.010 Li and 0.025 Li, respectively, per formula unit (f.u.) of LiVPO₄F.

6.3 Results and Discussion

6.3.1 Electrochemistry upon charging LiVPO₄F

In situ XRD measurements were carried out during charge (delithiation) of LiVPO₄F at cycle rates of 1 C, 2 C and 5 C. Figure 6.3 A shows the corresponding voltage profiles during charge. The sloping voltage up to ~4.25 V, corresponding to 0.4, 0.3 and 0.2 Li extracted per f.u. of LiVPO₄F for 1 C, 2 C and 5 C charging, respectively, is attributed to the capacitive process arising from the large surface area due to the 60 wt% carbon in the electrode and/or side reactions involving the formation of solid electrolyte interphase (SEI)[132], hence no Li is expected to be extracted from LiVPO₄F. The low voltage plateau (at 4.23 V at low cycle rate) that corresponds to the phase transition from LiVPO₄F to Li_{0.67}VPO₄F cannot be easily identified for 1 C charge but is discernable

between 0.3 and 0.5 Li extracted for 2 C charge and between 0.25 and 0.25 Li extracted for 5 C charge. The high voltage plateau (at 4.27 V at low cycle rate) that corresponds to the two-phase reaction from $\text{Li}_{0.67}\text{VPO}_4\text{F}$ to VPO_4F can be clearly identified over the range of 0.5 – 1.5, 0.6 – 1.1 and 0.5 – 0.9 Li extraction for 1 C, 2 C and 5 C charge, respectively. The sloping voltage profile after the high voltage plateau could be associated with voltage polarisation. Although there is only one Li available per f.u. of LiVPO_4F for extraction, the number of Li extracted from the electrochemistry appears to be much greater than one: ~ 1.9 Li for 1 C charge and ~ 1.4 Li for 2 C and 5 C charge. However, the number of Li extracted during the plateau region (both low and high voltage plateaus) corresponds to ~ 1 Li (from 0.5 to 1.5), ~ 0.7 Li (from 0.3 to 1) and ~ 0.7 Li (from 0.2 to 0.9) per f.u. of LiVPO_4F for 1 C, 2 C and 5 C charge, respectively, suggesting the electrochemical extraction of Li from LiVPO_4F does not exceed the maximum number of Li available in LiVPO_4F .

To determine the voltage plateaus during charge accurately, the first derivative of the charge capacity (Q) with respect to voltage (V), henceforth referred to as dQ/dV , is plotted against voltage in Figure 6.3 B. Since the charge capacity is proportional to the number of Li extracted, the dQ/dV plot is essentially the first derivative of abscissa with respect to the ordinate of Figure 6.3 A: a voltage plateau in Figure 6.3 A translates into a peak in Figure 6.3 B, at the position corresponding to the voltage of the plateau. By definition, the integrated area under the peak yields the capacity of the voltage plateau. It is noted in Figure 6.3 B that there is a weak yet distinguishable peak centred at 4.26 V for 1 C charge, indicating the occurrence of the transition from LiVPO_4F to $\text{Li}_{0.67}\text{VPO}_4\text{F}$. It is not clear as to why the low voltage plateau gives so little capacity during the initial cycle at 1 C. The large noise for 1C charge between 4.3 V and 4.4 V is due to too many data points measured within the voltage plateau region: when the actual voltage change (dV) between two successive data points is less than the noise level of the measurement, dV effectively reflects the noise in voltage and can be either negative or positive. As a result, dQ/dV (dQ is always positive) alternates randomly between positive and negative values, which gives rise to the observed large noise in the dQ/dV . To reduce noise, each voltage data point for 1 C charge is averaged over 50 adjacent data points, i.e. the value at the centre of 50 consecutive data points is equal to the average of the 50 data points, before carrying out the dQ/dV operation for voltages above 4.30 V. The smoothed voltage profile up to 4.5 V is shown as dashed line in Figure 6.3 A: the smoothed voltage

reproduces the profile for the voltage plateau but exhibits deviation for voltage below 4.30 V. dQ/dV was carried out for smooth voltages above 4.30 V, and the result is shown as the “1C smooth” curve in Figure 6.3 B, where an intense peak centred at 4.33 V, corresponding to the high voltage plateau, is observed. Two peaks corresponding to the low and high voltage plateaus are observed for 2 C and 5 C charge. The shift of the dQ/dV peak to higher voltage with increasing rate of charge is due to the larger voltage polarisation associated with higher current.

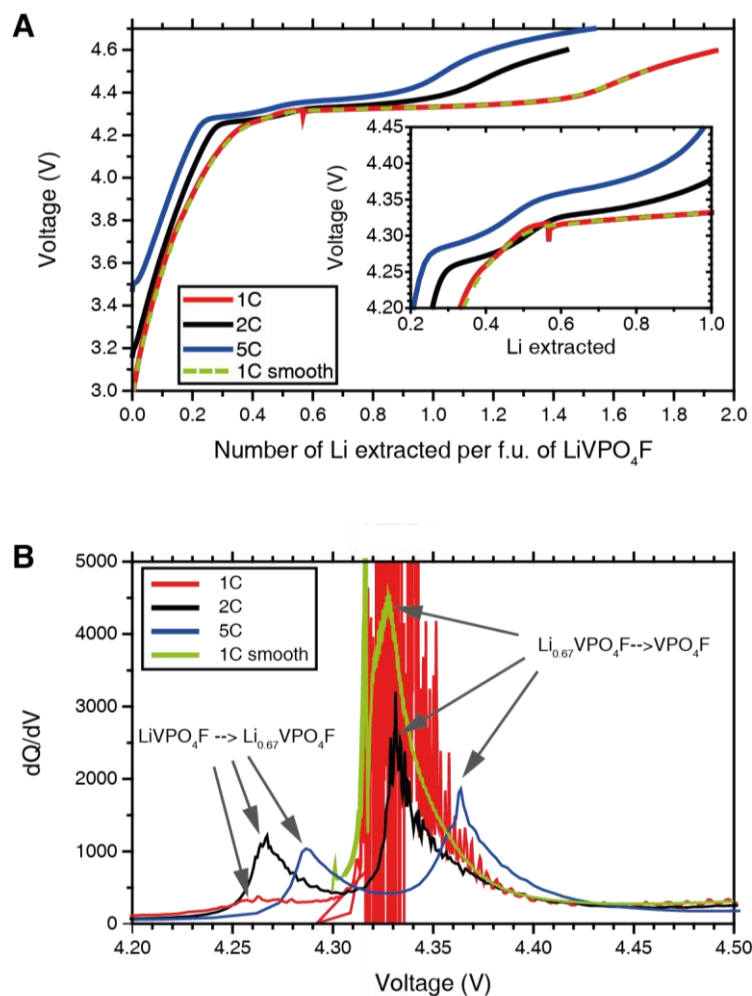


Figure 6.3. (A) The electrochemical profile during charge (delithiation) of LiVPO_4F at 1 C, 2 C and 5 C, the inset shows the plateau region. (B) The dQ/dV (the first derivative of capacity, which is proportional to the number of Li extracted, with respect to voltage) plot for charging rates of 1 C, 2 C and 5 C. The “1 C smooth” in (A) is the smoothed voltage profile for 1 C charge by averaging over 50 adjacent data points, and its corresponding dQ/dV curve is shown as “1 C smooth” in (B).

6.3.2 *In situ* XRD measured during 1 C, 2 C and 5 C charging of LiVPO_4F

Given the unit cell transformation by (6.1), the $(1\bar{1}0)$ reflection of LiVPO_4F is equivalent to the (020) reflection of VPO_4F , and the $(02\bar{1})$ and $(20\bar{1})$ reflections of LiVPO_4F are

equivalent to the $(\bar{2}21)$ reflection of VPO_4F . It should be noted that $(\bar{2}21)$ and $(\bar{2}\bar{2}1)$ are symmetry equivalent in the monoclinic system. Therefore, the above reflections can be used to identify whether the phase transition is continuous or not during charge (delithiation) of LiVPO_4F : if the phase transition from $\text{Li}_{0.67}\text{VPO}_4\text{F}$ to VPO_4F is continuous, the $(1\bar{1}0)$ reflection of LiVPO_4F will shift continuously to the (020) reflection of VPO_4F , and the $(02\bar{1})$ and $(20\bar{1})$ reflections of LiVPO_4F will converge into one $(\bar{2}21)$ reflection of VPO_4F . The *in situ* XRD patterns of the aforementioned reflections during 1 C, 2 C and 5 C charging are shown as image plots in Figure 6.4. Individual diffraction patterns at certain states of charge over the same 2θ regions are shown in Figure 6.5.

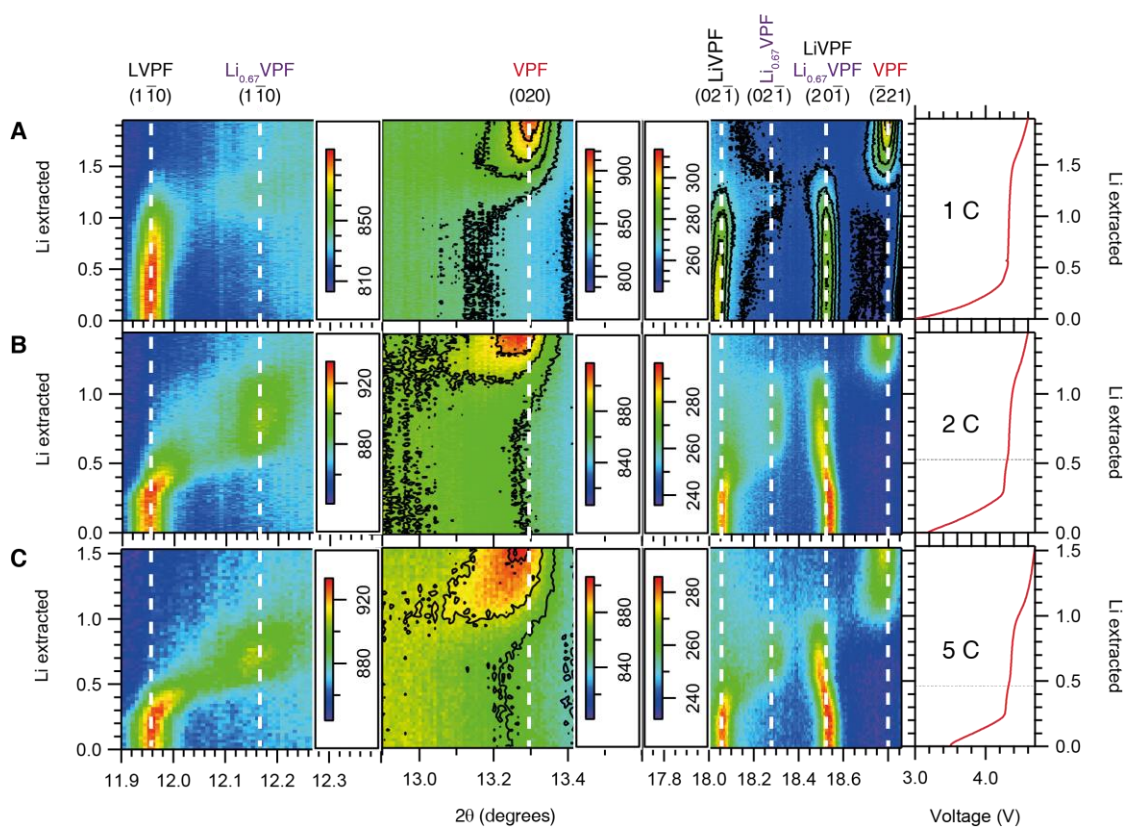


Figure 6.4. *In situ* XRD patterns collected during the (A) 1 C, (B) 2 C and (C) 5 C charging of LiVPO_4F . Three 2θ regions are selected to study the phase evolution. The graphs on the right show the electrochemical profile at the respective rate. The dashed grey line in the electrochemical profile indicates the transition between the first and the second plateaus; no line is drawn for 1 C as there is no distinct low voltage plateau. The dashed white lines indicate the positions of the indicated reflections. LVPF, $\text{Li}_{0.67}\text{VPF}$ and VPF are abbreviations for LiVPO_4F , $\text{Li}_{0.67}\text{VPO}_4\text{F}$ and VPO_4F , respectively.

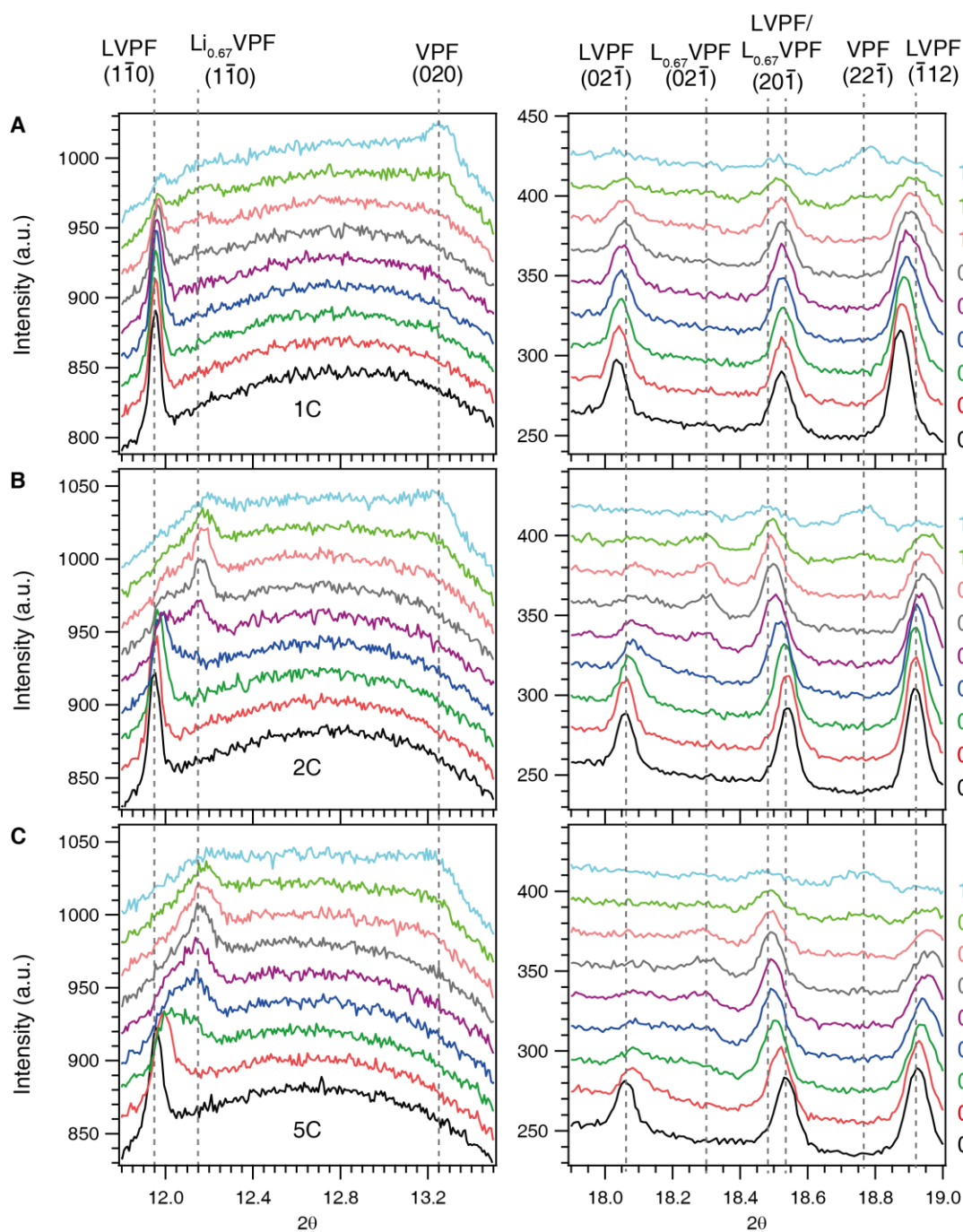


Figure 6.5 Individual *in situ* XRD patterns at different states of charge during (A) 1C, (B) 2C and (C) 5C charge. LVPF, $\text{Li}_{0.67}\text{VPF}$ and VPF are abbreviations for LiVPO_4F , $\text{Li}_{0.67}\text{VPO}_4\text{F}$ and VPO_4F , respectively. The number to the right of each pattern indicate the corresponding number of Li extracted per f.u. of LiVPO_4F .

During 1 C charging (Figure 6.4 A), $(1\bar{1}0)$, $(02\bar{1})$ and $(20\bar{1})$ reflections of LiVPO_4F do not show any change from 0 to 0.5 Li extraction per f.u. of LiVPO_4F . This is consistent with the interpretation of its electrochemistry that the sloping voltage profile during the first 0.4 Li extraction is due to capacitive charge storage, i.e. double layer capacitance, and/or SEI formation, which do not change the chemical composition of LiVPO_4F . However, as noted in Figure 6.3 B for 1 C charge, the increase in voltage from

4.25 V to 4.3 V (0.4 to 0.5 Li extraction per f.u.) is associated with a very weak peak corresponding to the transition from LiVPO_4F to $\text{Li}_{0.67}\text{VPO}_4\text{F}$, which is not observed in the *in situ* XRD pattern. Further charging from 0.5 to 1.0 Li extraction shows a decrease in intensity and a shift in position of the $(1\bar{1}0)$, $(02\bar{1})$ and $(20\bar{1})$ reflections of LiVPO_4F , indicating a decrease in the phase fraction of LiVPO_4 and a change in lattice parameters as a result of the change in Li stoichiometry. During charging from 1 to 1.5 Li extraction, weak peaks corresponding to the $(1\bar{1}0)$ and $(02\bar{1})$ reflections of $\text{Li}_{0.67}\text{VPO}_4\text{F}$ start to form and then disappear, while the $(1\bar{1}0)$ and $(02\bar{1})$ reflections of LiVPO_4F decrease in intensity and do not present noticeable shift in position, as shown in Figure 6.5 A. The lack of continuous shift of the $(1\bar{1}0)$ and $(02\bar{1})$ reflections of LiVPO_4F to the equivalent reflections of $\text{Li}_{0.67}\text{VPO}_4\text{F}$ rules out the possibility of a continuous phase transition between LiVPO_4F and $\text{Li}_{0.67}\text{VPO}_4\text{F}$, therefore, the phase transition from LiVPO_4F and $\text{Li}_{0.67}\text{VPO}_4\text{F}$ has to be first-order during 1 C charging. The weak intensities of $\text{Li}_{0.67}\text{VPO}_4\text{F}$ reflections are consistent with the small peak at 4.25 V, corresponding to the transition from LiVPO_4F to $\text{Li}_{0.67}\text{VPO}_4\text{F}$, in the dQ/dV plot in Figure 6.3 B. In addition, the (020) reflection of VPO_4F starts to form when charging reaches 1.2 Li extraction. It is noted that the formation of VPO_4F started only after charging had passed half of the high voltage plateau, i.e. after more than ~ 1 Li extraction. This shows the reaction at the local region probed by X-ray is delayed with respect to the electrochemistry. As charging goes beyond 1.5 Li extraction per f.u., the (020) and $(\bar{2}21)$ reflections of VPO_4F become more intense as Li is extracted although the voltage profile suggests the transition to VPO_4F is complete when 1.5 Li has been extracted.

For charge at 2 C (Figure 6.4 B), as with charge at 1 C, no change in the $(1\bar{1}0)$, $(02\bar{1})$ and $(20\bar{1})$ reflections of LiVPO_4F is observed during the initial charge from 0 to 0.2 Li extraction. However, further charging from 0.2 to 1.0 Li extraction shows a more pronounced effect in the shift of $(1\bar{1}0)$ reflection of LiVPO_4F towards higher 2θ angles than during 1 C charging. Examination of individual *in situ* XRD patterns at 0.49, 0.62 and 0.76 Li extraction in the 2θ region (11.8° - 12.3°) for $(1\bar{1}0)$ reflections of both LiVPO_4F and $\text{Li}_{0.67}\text{VPO}_4\text{F}$, as shown in Figure 6.5 B, reveals the existence of substantial diffraction intensity in the 2θ range between 12.0° and 12.1° , while $(1\bar{1}0)$ reflections corresponding to stoichiometric LiVPO_4F and $\text{Li}_{0.67}\text{VPO}_4\text{F}$ are at 11.95° and 12.16° , respectively. Also shown in Figure 6.5 B, the $(02\bar{1})$ reflection of LiVPO_4F broadens asymmetrically towards the position of the $(02\bar{1})$ reflection of $\text{Li}_{0.67}\text{VPO}_4\text{F}$ when 0.49 Li

per f.u. is extracted, indicating a variation of lattice parameters. As with LiFePO_4 at high rate cycling[125,133], the appearance of a continuous intensity band in the 2θ region between $(1\bar{1}0)$ reflections of both LiVPO_4F and $\text{Li}_{0.67}\text{VPO}_4\text{F}$ indicates the existence of a series of intermediate solid solution phases, $\text{Li}_x\text{VPO}_4\text{F}$, with Li composition spanning continuously from $x = 1$ to $x = 0.67$. Hence, the two-phase reaction between LiVPO_4F and $\text{Li}_{0.67}\text{VPO}_4\text{F}$ is suppressed in favour of the single-phase reaction. The final stage of 2 C charge (for extraction of more than 1 Li) proceeds by the disappearance of $\text{Li}_{0.67}\text{VPO}_4\text{F}$ and concurrent formation and growth of VPO_4F , shown as the disappearance of $(1\bar{1}0)$, $(02\bar{1})$ and $(20\bar{1})$ reflections of $\text{Li}_{0.67}\text{VPO}_4\text{F}$ and the formation and growth of (020) and $(\bar{2}21)$ reflections of VPO_4F . The (020) reflection of VPO_4F near the end of charge (from 1.2 Li extraction onwards) exhibits a shift in position, indicating a limited Li solubility for $\text{Li}_\gamma\text{VPO}_4\text{F}$ ($C2/c$ and γ is a small number). However, neither the $(1\bar{1}0)$ or the $(20\bar{1})$ reflection of $\text{Li}_{0.67}\text{VPO}_4\text{F}$ shifts continuously towards the (020) or the $(\bar{2}21)$ reflection of VPO_4F , respectively, hence, the transition from $\text{Li}_{0.67}\text{VPO}_4\text{F}$ to VPO_4F still proceeds by the two-phase reaction where VPO_4F grows at the expense of $\text{Li}_{0.67}\text{VPO}_4\text{F}$. As with 1 C charge, evolution probed by *in situ* XRD is delayed with respect to the average reaction reflected by electrochemistry.

As with 2 C charge, charge at 5 C (Figure 6.4 C) also exhibits distinct two phase transition steps: the transition from LiVPO_4F to $\text{Li}_{0.67}\text{VPO}_4\text{F}$ from 0 to 0.7 Li extraction, followed by the transition from $\text{Li}_{0.67}\text{VPO}_4\text{F}$ to VPO_4F from 0.7 Li extraction to the end of charge. It is noted the $(1\bar{1}0)$ reflection of LiVPO_4F appears to shift almost continuously into the position of the $(1\bar{1}0)$ reflection, as shown in Figure 6.5 C, indicating a more pronounced single-phase transition from LiVPO_4F to $\text{Li}_{0.67}\text{VPO}_4\text{F}$ than at 2 C charge. The transition from $\text{Li}_{0.67}\text{VPO}_4\text{F}$ to VPO_4F remains distinctly two-phase as no continuous shift is observed between the $(1\bar{1}0)$ reflection of $\text{Li}_{0.67}\text{VPO}_4\text{F}$ and the (020) reflection of VPO_4F and between the $(20\bar{1})$ reflection of $\text{Li}_{0.67}\text{VPO}_4\text{F}$ and the $(\bar{2}21)$ reflection of VPO_4F . As with both 1 C and 2 C charge, the transition probed by *in situ* XRD at 5 C is also delayed with respect to the average reaction indicated by the voltage profile.

The lag in the reaction at the region probed by X-ray with respect to the reaction indicated by electrochemistry, which has also been found in *in situ* XRD studies of LiFePO_4 [31,33,134], is associated with the spatially non-uniform reaction of the electrode: since electrochemistry measures the average voltage of the entire electrode, it

does not reflect any local variation; in contrast, XRD only probes the section of the electrode, on which the X-ray beam is incident (0.8mm x 2.5 mm X-ray beam size on a 13 mm diameter electrode, i.e. only 1.5% of the electrode is measured by X-ray in this study), hence, it does not reflect the average state of the electrode especially when reaction does not proceed uniformly across the electrode. Nonetheless, since reaction at the region probed by the X-ray beam is only delayed but not disrupted, i.e. LiVPO₄F still transforms to VPO₄F at the end of experiment, the probed region should have undergone the same processes as the rest of the electrode (not probed by X-ray) and hence is informative of the phase transitions occurred at the entire electrode. This non-uniform reaction across the electrode could be caused by the poor transport properties of the composite porous electrode, the design of the *in situ* battery cell and/or influence of the X-ray beam. In this study, the non-uniform reaction appears to be greatly influenced by the X-ray beam: there is a severe lag during discharge in the reaction at the region exposed to the X-ray beam compared to the unexposed region. A recent study has found that the low energy (17keV) X-ray beam induces non-uniformity in the reaction across the electrode[135]. The X-ray beam energy is 15keV in this study and could induce non-uniform reaction across the electrode. In fact, the influence of the X-ray beam is so severe during discharge that only a fraction of VPO₄F was converted back to LiVPO₄F at the region exposed to the X-ray beam while VPO₄F at regions not exposed to X-ray beam was almost fully converted back to LiVPO₄F (see Appendix). Therefore, the discharge process is not reported in this study due to the heavy influence of the X-ray beam.

It is also noted that three phase coexistence is observed for charging at 1 C, 2 C and 5 C, for example, at 1.27, 1.03 and 0.91 Li extraction per f.u. for 1 C, 2 C and 5 C charge, respectively, as shown in Figure 6.5. This could be brought about by concurrent transitions from LiVPO₄F to Li_{0.67}VPO₄F and from Li_{0.67}VPO₄F to VPO₄F if the reaction does not proceed uniformly in the region probed by X-ray. Besides, the small difference (0.04 V) between the voltage plateaus corresponding to LiVPO₄F to Li_{0.67}VPO₄F and Li_{0.67}VPO₄F to VPO₄F transitions means an overpotential of 0.04 V in the local region consisting of Li_{0.67}VPO₄F will drive the transition to VPO₄F.

6.3.3 Quantifying the phase transition

Visual inspection of the *in situ* XRD patterns in Figure 6.4 has found the appearance of intermediate solid solution Li_xVPO₄F (0.67 < x < 1) phases during the phase transition

from LiVPO_4F to $\text{Li}_{0.67}\text{VPO}_4\text{F}$ at 2 C and 5 C. If the d-spacing of every reflection varies linearly with x , the distribution of the intermediate phases can be quantified by modelling a single reflection. Therefore, the $(1\bar{1}0)$ reflection of $\text{Li}_x\text{VPO}_4\text{F}$ ($P-I$) was modelled with 7 pseudo-Voigt peaks that are equally spaced in d-spacing in the 2θ region between 11.95° and 12.23° , corresponding to 7 $\text{Li}_x\text{VPO}_4\text{F}$ phases with $x = 1, 0.93, 0.86, 0.80, 0.73, 0.66, 0.59$, respectively (7 was found to be the minimum number peaks that could lead to a satisfactory fit). The shape parameter and full width at half maximum (FWHM) of all peaks were constrained to be identical and allowed to vary during peak fitting. The individual intensity of each peak, which is proportional to the phase fraction of the corresponding phase, was allowed to vary independently. It should be noted that the number of variable parameters (9 in total: shape parameter, FWHM and 7 intensities) used in this method is comparable to a conventional peak fitting with 2 pseudo-Voigt peaks, which involves the use of 8 variable parameters (position, intensity, FWHM and shape of each peak). Typical fitting results are shown in Figure 6.6. The intensities obtained from the fitting are shown as contour plots in Figure 6.7 (A). It is seen that more phases appear in the intermediate composition range between $x = 0.9$ and $x = 0.7$ as charging rate increases. It is worth mentioning that at 0.53 Li extraction per f.u. whilst cycling at a charge rate of 5 C, the phases from $x = 0.86$ to $x = 0.73$ (inclusive) account for 60 % of the total phase population.

Since the reaction between $\text{Li}_{0.67}\text{VPO}_4\text{F}$ and VPO_4F remains distinctively two-phase from 1 C to 5 C charging, individual peak fitting was carried out to track the phase transition. Peak fitting was performed for the (020) , (021) and $(\bar{2}02)$ reflections of VPO_4F , which are well separated from other reflections, with pseudo-Voigt peaks. In addition, the profile for the (110) and $(11\bar{2})$ reflections of $\text{Li}_x\text{VPO}_4\text{F}$ ($0.67 < x < 1$, i.e. all low symmetry phases) were also fitted to a single peak since they are very close in position and do not present a substantial shift during the transition between LiVPO_4F and $\text{Li}_{0.67}\text{VPO}_4\text{F}$. It must be noted that the intensity of the $(11\bar{2})$ reflection is less than 0.1% of the (110) reflection, therefore, the observed peak is effectively assigned entirely to the (110) reflection of $\text{Li}_x\text{VPO}_4\text{F}$. Typical fitting results are shown in Figure 6.8. The integrated intensities and the FWHMs of the above reflections are shown in Figure 6.7 B and C, respectively. As seen in Figure 6.7 C, the FWHM of all the VPO_4F peaks decrease monotonically during charging and the width of the $\text{Li}_x\text{VPO}_4\text{F}$ peak starts to increase upon the formation of the VPO_4F phase for all rates. Since the peak width, if due solely to finite size effect, is inversely related to the domain size, this observation suggests the

VPO₄F domain size grows while the domain size of Li_xVPO₄F decreases, which is characteristic of the two-phase reaction by the nucleation and growth of a second phase, consistent with the first-order phase transition.

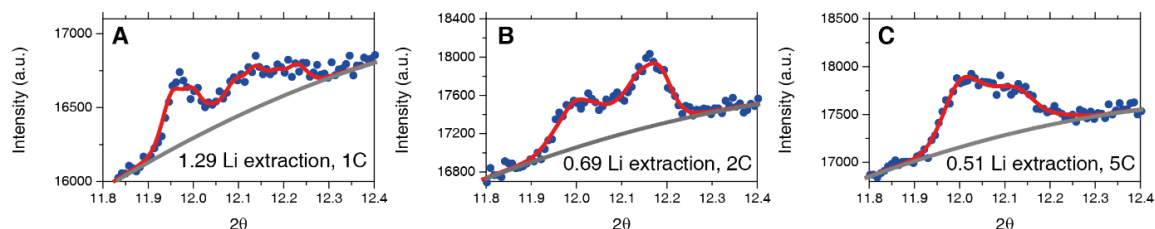


Figure 6.6 Typical fitting results for the $(1\bar{1}0)$ reflection of Li_xVPO₄F (*P-I*). The blue dots represent the observed intensities, the red curves are the fitted profiles and the grey curves are the background.

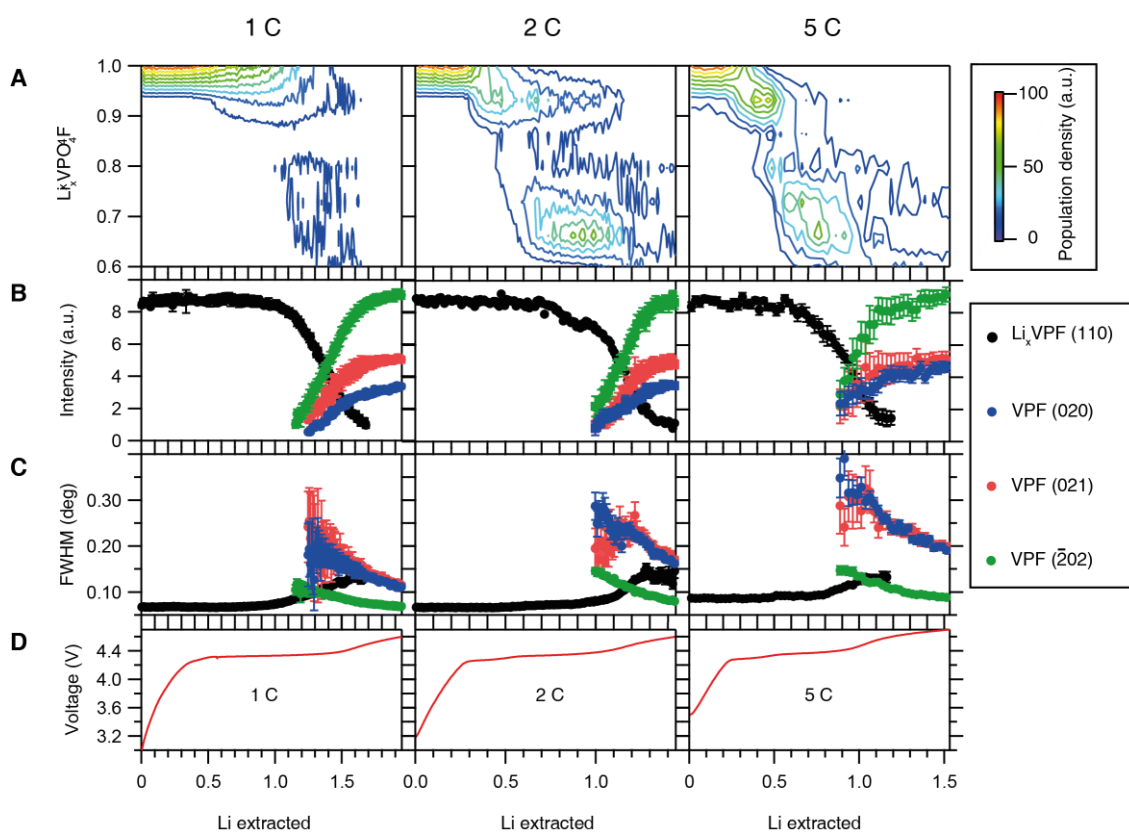


Figure 6.7. (A) Contour plots of the Li_xVPO₄F phase population extracted from fitting the $(1\bar{1}0)$ reflection profile during the charge at different rates. The spacing between two adjacent contour lines is equal to one tenth of the maximum density. The respective electrochemical profile is shown at the bottom. (B) Integrated intensities and (C) FWHMs of the Li_xVPO₄F (Li_xVPF) (110) and the VPO₄F (VPF) (020), (021) and $(\bar{2}02)$ reflections. (D) Voltage profiles during 1 C, 2 C and 5 C charging.

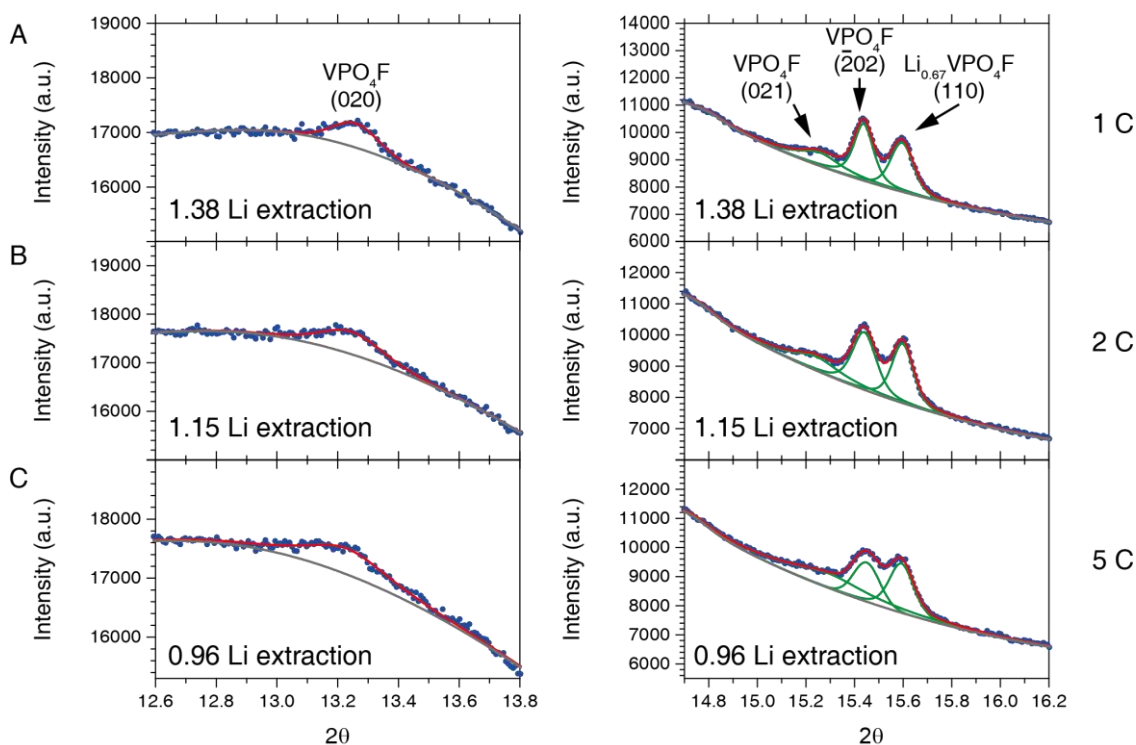


Figure 6.8 Typical peaking fitting results obtained for the (020), (021) and $(\bar{2}02)$ reflections of VPO_4F and the (110) reflection for $\text{Li}_{0.67}\text{VPO}_4\text{F}$. The blue dots are the observed intensities, the red curves are the fitted profiles, the green curves show the individual profiles and the grey curve is the background.

6.3.4 Discussion on the possibility of a continuous phase transition

As neither of the symmetry-changing phase transitions ($\alpha\text{-TiO}_2$ to $\beta\text{-Li}_{0.5}\text{TiO}_2$ in previous Chapter and $\text{Li}_{0.67}\text{VPO}_4\text{F}$ to VPO_4F) demonstrates a continuous path even at very high rates, it begs the question as to why a continuous phase transition is not observed when there is a change in crystal symmetry.

For a continuous structural phase transition to occur between two phases of different symmetries, the phase transition must be second-order, which is described classically by Landau theory[52]. In Landau theory, the structural phase transition between two symmetry-related phases is described by a continuous change in the so called order parameter, denoted as η , from 0 (representing the high symmetry phase) to a non-zero value (representing the low symmetry phase), where the order parameter represents a set of atomic displacements that conform to the symmetry operations of the low symmetry phase and lowers the symmetry of the high symmetry phase. In each of the two cases ($\alpha\text{-TiO}_2$ ($I4_1/amd$, No. 141) \rightarrow $\beta\text{-Li}_{0.5}\text{TiO}_2$ ($Imma$, No. 74) and $\text{Li}_{0.67}\text{VPO}_4\text{F}$ ($P-1$, No. 2) \rightarrow VPO_4F ($C2/c$, No. 15)) studied here, there exists an order parameter, which is allowed by Landau theory to lower the symmetry to the desired one. Because order

parameters are derived by group-theoretical approach, it does not address the energetics of the phase transition. Hence as discussed in the previous Chapter, it is possible that the continuous transition path lies too high in energy.

Another possibility based on the Landau theory is that the nature of the phase transition is changed from second-order to first-order due to the strain energies. The Landau expansion in η up to the 6th order for the excess free energy due to a phase transition is given by[52]

$$G = \frac{1}{2}A(T - T_c)\eta^2 + \frac{1}{4}B\eta^4 + \frac{1}{6}C\eta^6 \quad (6.2)$$

where T_c is the transition temperature, η is the order parameter that is 0 for the high symmetry phase and non-zero for the low symmetry phase, and A , B and C are the coefficients in the expansion. It is known that the transition becomes first-order when $B < 0$ and $C > 0$. When the spontaneous strain, which is measured against the non-distorted (high symmetry) phase, is considered and coupled with the order parameter, the coefficient B in (6.2) is modified and can become negative if the spontaneous strain strongly couples with the quadratic term of the order parameter[136]. Hence, there is the possibility that the phase transition will always be first-order due to the large strain-induced coupling effect.

In contrast, a continuous phase transition appears to be induced readily with high cycling rate when the phase transition does not involve a change in crystal symmetry. In addition to LiFePO_4 and LiVPO_4F studied here, $\text{LiNi}_{1/2}\text{Mn}_{3/2}\text{O}_4$, whose symmetry is preserved during delithiation, has also been found by X-ray diffraction to transform via non-equilibrium solid solution phases[137]. The ease of transforming via a single, solid solution, phase in LiFePO_4 , LiVPO_4F and $\text{LiNi}_{1/2}\text{Mn}_{3/2}\text{O}_4$ could be related to the relatively low energy for the formation of the non-equilibrium solid solution phases. Because phase separation is a kinetic process, the non-equilibrium solid solution phases can become kinetically stable when the driving force for phase separation is relatively small.

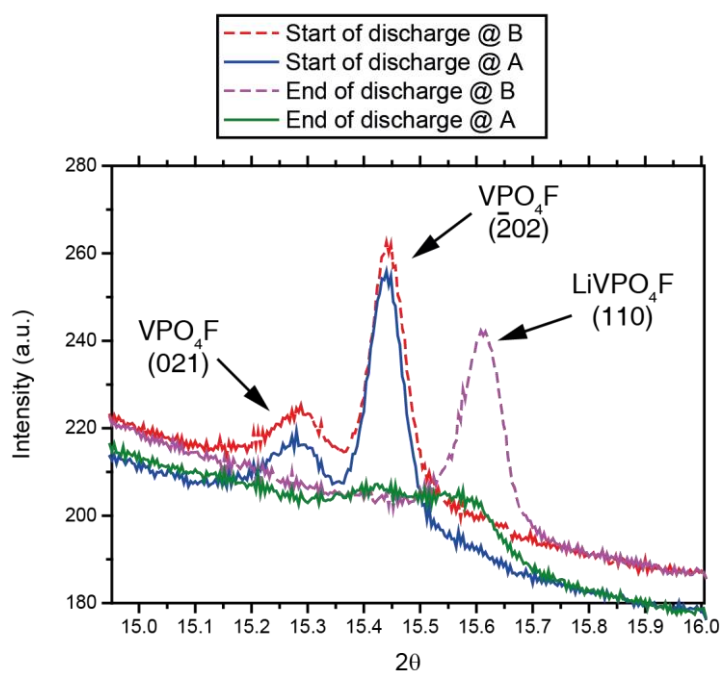
6.4 Conclusion

In situ XRD was used to study the charging (delithiation) process of LiVPO_4F as a function of charging rate. The phase transition from LiVPO_4F to $\text{Li}_{0.67}\text{VPO}_4\text{F}$ is rate

dependent: the transition proceeds via a two-phase mechanism at 1 C but becomes almost single-phase at 5 C. However, apart from some quantitative differences, further delithiation of $\text{Li}_{0.67}\text{VPO}_4\text{F}$ to transform to VPO_4F is not affected by the charging rate between 1 C and 5 C and undergoes a nucleation and growth mechanism as evidenced by the evolution of the peak widths. The failure to induce continuous structural phase transition at high charging rates when there is a change in crystal symmetry is attributed to the high energy barrier of the continuous structural phase transition path or strong coupling between strain and order parameter, which may render the continuous structural phase transition unviable.

6.5 Appendix

Region A was constantly exposed to the X-ray beam during the *in situ* experiment, and region B (1.8 mm away from region A) was not exposed to the X-ray beam during the *in situ* experiment. Before discharge, both regions were measured by XRD and show similar diffraction patterns as seen in the figure below. During discharge, region A was constantly exposed to the X-ray beam, while B was not. At the end of discharge, both regions were measured by XRD again: region B shows the diffraction pattern of LiVPO_4F while region A shows an incomplete conversion from VPO_4F to LiVPO_4F .



7 Conclusions

To understand the two-phase reaction in electrodes for Li-ion batteries, three electrode materials: LiFePO₄, anatase TiO₂ and LiVPO₄F, all of which exhibit a large Li miscibility gap at room temperature, were investigated in this thesis.

The two-phase reaction of an electrode challenges the use of conventional electrochemical methods in the determination of Li chemical diffusivity since the two-phase reaction is not accounted for in these methods. To address this issue, Li tracer diffusivity in LiFePO₄ was investigated by Li cation exchange between ⁶Li enriched LiFePO₄ and naturally abundant ⁷Li and ⁶Li LiPF₆ electrolyte. Li NMR was used to follow the extent of Li exchange as a function of time. The measured Li tracer exchange is consistent with exchange subject to single-file diffusion, which is expected for LiFePO₄. Fitting the experimental Li tracer exchange with the theoretical model yielded a Li attempt jump frequency on the order of 10⁵s⁻¹ and Li tracer diffusivity on the order of 10⁻¹⁰ cm²s⁻¹, which are in very good agreement with the values obtained from microscopic measurements of Li tracer diffusivity. The high Li tracer diffusivity allows fast Li insertion and extraction if diffusion is the only rate-limiting process.

The apparent contradiction between the high rate capability of LiFePO₄ and the presumably first-order phase transition of LiFePO₄ via kinetically limited nucleation and growth process motivated the investigation of the phase transition process of LiFePO₄ nanoparticles. Time-resolved *in situ* synchrotron XRD was used to directly probe the structural evolution of LiFePO₄ during high rate cycling. Electrochemical cycling at 10 C results in substantial asymmetrical broadening of Bragg reflections. Analysis on the diffraction peak profile reveals the existence of intermediate solid solution phases, Li_xFePO₄ (0 < x < 1), under non-equilibrium conditions, and the transition between LiFePO₄ and FePO₄ undergoes via a single-phase reaction. The existence of the facile non-equilibrium, single-phase reaction pathway explains the high rate performance of LiFePO₄.

Discovery of the non-equilibrium single-phase (continuous) transition for a phase-separating electrode at high rate cycling encouraged further investigation to determine how wide spread this non-equilibrium process is. Phase transitions of anatase TiO₂ and LiVPO₄ were investigated with the same *in situ* synchrotron XRD method as for LiFePO₄.

Li insertion of 25 nm and 100 nm TiO₂ particles was investigated at different cycling rates at room temperature and 80°C. In none of the conditions studied here (from 1 C to 5 C at room temperature and from 5 C to 20 C at 80°C) did the transition from tetragonal α -TiO₂ to orthorhombic β -Li_{0.5}TiO₂ become continuous. Increasing from room temperature to 80°C does not change the two-phase reaction mechanism of 25 nm and 100 nm particles. However, the two-phase reaction was found to occur sequentially for 25 nm particles and to undergo via the conventional nucleation and growth process for 100 nm particles.

The two phase transitions ($\text{LiVPO}_4\text{F} \rightarrow \text{Li}_{0.67}\text{VPO}_4\text{F}$ and $\text{Li}_{0.67}\text{VPO}_4\text{F} \rightarrow \text{VPO}_4\text{F}$) during the charging process of LiVPO₄F were investigated at charging rates of 1 C, 2 C and 5 C. The transition from LiVPO₄F to Li_{0.67}VPO₄F was found to depend on the charging rates: reaction at 1 C follows the two-phase mechanism but becomes increasingly single-phase with increasing charging rates. Hence, as with LiFePO₄, a single-phase reaction between LiVPO₄F to Li_{0.67}VPO₄F can be induced during high rate charging. In contrast, two-phase reaction was observed for Li_{0.67}VPO₄F \rightarrow VPO₄F for charging rates between 1 C and 5 C. Analysis on the evolution of FWHM of Bragg reflections suggests that the two-phase reaction ($\text{Li}_{0.67}\text{VPO}_4\text{F} \rightarrow \text{VPO}_4\text{F}$) takes place via a conventional nucleation and growth process.

In the phase transitions studied in this thesis, the possibility to transform via a non-equilibrium continuous path appears to be dictated by the crystal symmetry of the two end member phases: when both phases assume the same symmetry, as for LiFePO₄ \rightarrow FePO₄ and LiVPO₄F \rightarrow Li_{0.67}VPO₄F, the phase transition became continuous at high rates of cycling; when both phases assume different but group-subgroup related symmetries, as for α -TiO₂ \rightarrow β -Li_{0.5}TiO₂ and Li_{0.67}VPO₄F \rightarrow VPO₄F, no continuous phase transition was observed for the cycling conditions employed in the experiments despite the existence of continuous pathways allowed by Landau theory on group-theoretical considerations.

8 Bibliography

- [1] M. Armand, J.-M. Tarascon, *Nature* 451 (2008) 652.
- [2] B. Dunn, H. Kamath, J.-M. Tarascon, *Science* 334 (2011) 928.
- [3] P. Poizot, S. Laruelle, S. Grugeon, L. Dupont, J.-M. Tarascon, *Nature* 407 (2000) 496.
- [4] B. A. Boukamp, G. C. Lesh, R. A. Huggins, *J. Electrochem. Soc.* 128 (1981) 725.
- [5] J.N. Reimers, J.R. Dahn, *J Electrochem. Soc.* 139 (1992) 2091.
- [6] A.K. Padhi, K.S. Nanjundaswamy, J.B. Goodenough, *J. Electrochem. Soc.* 144 (1997) 1188.
- [7] S. Nishimura, G. Kobayashi, K. Ohoyama, R. Kanno, M. Yashima, A. Yamada, *Nat. Mater.* 7 (2008) 707.
- [8] M.S. Islam, D.J. Driscoll, C.A.J. Fisher, P.R. Slater, *Chem. Mater.* 17 (2005) 5085.
- [9] C. Ouyang, S. Shi, Z. Wang, X. Huang, L. Chen, *Phys. Rev. B* 69 (2004) 1.
- [10] D. Morgan, A. Van der Ven, G. Ceder, *Electrochem. Solid-State Lett.* 7 (2004) A30.
- [11] T. Maxisch, F. Zhou, G. Ceder, *Phys. Rev. B* 73 (2006) 1.
- [12] J.L. Dodd, R. Yazami, B. Fultz, *Electrochem. Solid-State Lett.* 9 (2006) A151.
- [13] A. Yamada, H. Koizumi, S.-I. Nishimura, N. Sonoyama, R. Kanno, M. Yonemura, T. Nakamura, Y. Kobayashi, *Nat. Mater.* 5 (2006) 357.
- [14] B. Kang, G. Ceder, *Nature* 457 (2009) 190.
- [15] A. Andersson, J. Thomas, *J. Power Sources* 98 (2001) 498.
- [16] V. Srinivasan, J. Newman, *J. Electrochem. Soc.* 151 (2004) A1517.
- [17] M. Wagemaker, R. van de Krol, A.P. Kentgens, A.A. van Well, F.M. Mulder, *J. Am. Chem. Soc.* 123 (2001) 11454.
- [18] G. Chen, X. Song, T.J. Richardson, *Electrochem. Solid-State Lett.* 9 (2006) A295.
- [19] C.V. Ramana, A. Mauger, F. Gendron, C.M. Julien, K. Zaghib, *J. Power Sources* 187 (2009) 555.

- [20] M. Wagemaker, D.P. Singh, W.J.H. Borghols, U. Lafont, L. Haverkate, V.K. Peterson, F.M. Mulder, *J. Am. Chem. Soc.* 133 (2011) 10222.
- [21] D.A. Cogswell, M.Z. Bazant, *ACS Nano* 6 (2012) 2215.
- [22] N. Meethong, H.-Y.S. Huang, W.C. Carter, Y.-M. Chiang, *Electrochem. Solid-State Lett.* 10 (2007) A134.
- [23] G. Kobayashi, S. Nishimura, M.-S. Park, R. Kanno, M. Yashima, T. Ida, A. Yamada, *Adv. Funct. Mater.* 19 (2009) 395.
- [24] N. Meethong, H.-Y.S. Huang, S. A. Speakman, W.C. Carter, Y.-M. Chiang, *Adv. Funct. Mater.* 17 (2007) 1115.
- [25] C. Delmas, M. Maccario, L. Croguennec, F. Le Cras, F. Weill, *Nat. Mater.* 7 (2008) 665.
- [26] G. Brunetti, D. Robert, P. Bayle-Guillemaud, J.L. Rouvière, E.F. Rauch, J.F. Martin, J.F. Colin, F. Bertin, C. Cayron, *Chem. Mater.* 23 (2011) 4515.
- [27] W. Dreyer, J. Jamnik, C. Guhlke, R. Huth, J. Moškon, M. Gaberscek, *Nat. Mater.* 9 (2010).
- [28] R. Malik, F. Zhou, G. Ceder, *Nat. Mater.* 10 (2011) 587.
- [29] P. Bai, D.A. Cogswell, M.Z. Bazant, *Nano Lett.* 11 (2011) 4890.
- [30] G. Oyama, Y. Yamada, R. Natsui, S. Nishimura, A. Yamada, *J. Phys. Chem. C* (2012).
- [31] H.-H. Chang, C.-C. Chang, H.-C. Wu, M.-H. Yang, H.-S. Sheu, N.-L. Wu, *Electrochem. Commun.* 10 (2008) 335.
- [32] H.C. Shin, K.Y. Chung, W.S. Min, D.J. Byun, H. Jang, B.W. Cho, *Electrochem. Commun.* 10 (2008) 536.
- [33] J.B. Leriche, S. Hamelet, J. Shu, M. Morcrette, C. Masquelier, G. Ouvrard, M. Zerrouki, P. Soudan, S. Belin, E. Elkaïm, F. Baudalet, *J. Electrochem. Soc.* 157 (2010) A606.
- [34] N. Sharma, X. Guo, G. Du, Z. Guo, *J. Am. Chem. Soc.* 134 (2012) 7867–7873.
- [35] X. Wang, C. Jaye, K. Nam, B. Zhang, H. Chen, J. Bai, H. Li, *J. Mater. Chem.* (2011) 11406.
- [36] X.-J. Wang, H.-Y. Chen, X. Yu, L. Wu, K.-W. Nam, J. Bai, H. Li, X. Huang, X.-Q. Yang, *Chem. Commun. (Camb)*. 47 (2011) 7170.

- [37] G.K.P. Dathar, D. Sheppard, K.J. Stevenson, G. Henkelman, *Chem. Mater.* 23 (2011) 4032.
- [38] R. Malik, D. Burch, M. Bazant, G. Ceder, *Nano Lett.* 10 (2010) 4123.
- [39] J. Chen, M.J. Vacchio, S. Wang, N. Chernova, P.Y. Zavalij, M.S. Whittingham, *Solid State Ionics* 178 (2008) 1676.
- [40] S.-Y. Chung, S.-Y. Choi, T. Yamamoto, Y. Ikuhara, *Phys. Rev. Lett.* 100 (2008) 125502.
- [41] K.M.Ø. Jensen, M. Christensen, H.P. Gunnlaugsson, N. Lock, E.D. Bøjesen, T. Proffen, B.B. Iversen, *Chem. Mater.* 25 (2013) 2282.
- [42] J. Chen, J. Bai, H. Chen, J. Graetz, *J. Phys. Chem. Lett.* 2 (2011) 1874.
- [43] J. Chen, J. Graetz, *ACS Appl. Mater. Interfaces* 3 (2011) 1380.
- [44] P.J. Baker, I. Franke, F.L. Pratt, T. Lancaster, D. Prabhakaran, W. Hayes, S.J. Blundell, *Phys. Rev. B - Condens. Matter Mater. Phys.* 84 (2011) 1.
- [45] J. Sugiyama, H. Nozaki, M. Harada, K. Kamazawa, O. Ofer, M. Månsson, J.H. Brewer, E.J. Ansaldo, K.H. Chow, Y. Ikedo, Y. Miyake, K. Ohishi, I. Watanabe, G. Kobayashi, R. Kanno, *Phys. Rev. B* 84 (2011) 1.
- [46] T.E. Ashton, J.V. Laveda, D.A. MacLaren, P.J. Baker, A. Porch, M.O. Jones, S.A. Corr, *J. Mater. Chem. A* 2 (2014) 6238.
- [47] J. Xie, N. Imanishi, T. Zhang, A. Hirano, Y. Takeda, O. Yamamoto, *Electrochim. Acta* 54 (2009) 4631.
- [48] D.Y.W. Yu, C. Fietzek, W. Weydanz, K. Donoue, T. Inoue, H. Kurokawa, S. Fujitani, *J. Electrochem. Soc.* 154 (2007) A253.
- [49] P. Prosini, M. Lisi, D. Zane, M. Pasquali, *Solid State Ionics* 148 (2002) 45.
- [50] A. V. Churikov, A. V. Ivanishchev, I.A. Ivanishcheva, V.O. Sycheva, N.R. Khasanova, E. V. Antipov, *Electrochim. Acta* 55 (2010) 2939.
- [51] R. Malik, A. Abdellahi, G. Ceder, *J. Electrochem. Soc.* 160 (2013) A3179.
- [52] L.D. Landau, E.M. Lifshitz, *Statistical Physics*, 3rd ed., Pergamon Press, Oxford, 1980.
- [53] H.T. Stokes, D.M. Hatch, B.J. Campbell, *ISOTROPY Software Suite*, iso.byu.edu.
- [54] F. Bonino, L. Busani, M. Lazzari, M. Manstretta, B. Rivolta, B. Scrosati, *J. Power Sources* 6 (1981) 261.

- [55] W.A. England, J.B. Goodenough, P.J. Wiseman, *J. Solid State Chem.* 49 (1983) 289.
- [56] C. Giacovazzo, H.L. Monaco, G. Artioli, D. Viterbo, G. Ferraris, G. Gilli, G. Zanotti, M. Catti, *Fundamentals of Crystallography*, Second Edi, Oxford University Press, Oxford, 2002.
- [57] A.L. Patterson, *Phys. Rev.* 56 (1939) 978.
- [58] W.I.F. David, M. Leoni, P. Scardi, *Mater. Sci. Forum* 651 (2010) 187.
- [59] A.R. Stokes, A.J.C. Wilson, *Proc. Phys. Soc.* 56 (1944) 174.
- [60] G.K. Williamson, W.H. Hall, *Acta Metall.* 1 (1953) 22.
- [61] B.E. Warren, B.L. Averbach, *J. Appl. Phys.* 21 (1950) 595.
- [62] A.R. Stokes, *Proc. Phys. Soc.* 61 (1948) 382.
- [63] H.M. Rietveld, *Acta Crystallogr.* 22 (1967) 151.
- [64] H.M. Rietveld, *J. Appl. Crystallogr.* 2 (1969) 65.
- [65] G. Pawley, *J. Appl. Crystallogr.* 14 (1981) 357.
- [66] A.R. Stokes, A.J.C. Wilson, *Math. Proc. Cambridge Philos. Soc.* 40 (1944) 197.
- [67] O.J. Borkiewicz, B. Shyam, K.M. Wiaderek, C. Kurtz, P.J. Chupas, K.W. Chapman, *J. Appl. Crystallogr.* 45 (2012) 1261.
- [68] M. Wagemaker, *Structure and Dynamics of Lithium in Anatase TiO₂*, Delft University, 2002.
- [69] M.M. Maricq, J.S. Waugh, *J. Chem. Phys.* 70 (1979) 3300.
- [70] C.P. Grey, N. Dupré *Chem. Rev.* 104 (2004) 4493.
- [71] M.H. Levitt, *Spin Dynamics: Basics of Nuclear Magnetic Resonance*, John Wiley & Sons, Ltd, Chichester, 2007.
- [72] J. Keeler, *Understanding NMR Spectroscopy*, John Wiley & Sons, Ltd, Chichester, 2005.
- [73] Y. Zhu, C. Wang, *J. Phys. Chem. C* 114 (2010) 2830.
- [74] N. Meethong, Y.-H. Kao, W.C. Carter, Y.-M. Chiang, *Chem. Mater.* 22 (2010) 1088.
- [75] J. Crank, *The Mathematics of Diffusion*, Clarendon Press, Oxford, 1956.

- [76] S. Vasenkov, J. Kärger, *Phys. Rev. E* 66 (2002) 052601.
- [77] P.H. Nelson, S.M. Auerbach, *J. Chem. Phys.* 110 (1999) 9235.
- [78] K. Hahn, J. Karger, *J. Phys. Chem. B* 102 (1998) 5766.
- [79] S. Yang, X. Zhou, J. Zhang, Z. Liu, *J. Mater. Chem.* 20 (2010) 8086.
- [80] C. Nan, J. Lu, L. Li, L. Li, Q. Peng, Y. Li, *Nano Res.* 6 (2013) 469.
- [81] A.A. Coelho, TOPAS v2.0: General Profile and Structure Analysis Software for Powder Diffraction Data, Karlsruhe, 2000.
- [82] M. Järvinen, *J. Appl. Crystallogr.* 26 (1993) 525.
- [83] W. Porcher, P. Moreau, B. Lestriez, S. Jouanneau, D. Guyomard, *Electrochem. Solid-State Lett.* 11 (2008) A4.
- [84] J.F. Martin, A. Yamada, G. Kobayashi, S. Nishimura, R. Kanno, D. Guyomard, N. Dupré, *Electrochem. Solid-State Lett.* 11 (2008) A12.
- [85] S. Hamelet, P. Gibot, M. Casas-Cabanas, D. Bonnin, C.P. Grey, J. Cabana, J.-B. Leriche, J. Rodriguez-Carvajal, M. Courty, S. Levasseur, P. Carlach, M. Van Thournout, J.-M. Tarascon, C. Masquelier, *J. Mater. Chem.* 19 (2009) 3979.
- [86] P. Gibot, M. Casas-Cabanas, L. Laffont, S. Levasseur, P. Carlach, S. Hamelet, J.-M. Tarascon, C. Masquelier, *Nat. Mater.* 7 (2008) 741.
- [87] M. Wagemaker, B.L. Ellis, D. Lützenkirchen-Hecht, F.M. Mulder, L.F. Nazar, *Chem. Mater.* 20 (2008) 6313.
- [88] M.C. Tucker, M.M. Doeff, T.J. Richardson, R. Fiñones, E.J. Cairns, J.A. Reimer, *J. Am. Chem. Soc.* 124 (2002) 3832.
- [89] L.J.M. Davis, I. Heinmaa, B.L. Ellis, L.F. Nazar, G.R. Goward, *Phys. Chem. Chem. Phys.* 13 (2011) 5171.
- [90] K. Zaghbi, A. Mauger, J.B. Goodenough, F. Gendron, C.M. Julien, *Chem. Mater.* 19 (2007) 3740.
- [91] J. Karger, M. Petzold, H. Pfeifer, S. Ernst, J. Weitkamp, *J. Catal.* 136 (1992) 283.
- [92] N. Yabuuchi, T. Ohzuku, *J. Power Sources* 119-121 (2003) 171.
- [93] D. Zeng, J. Cabana, J. Bréger, W. Yoon, C.P. Grey, *Chem. Mater.* 19 (2007) 6277.
- [94] I. Saadoune, C. Delmas, (1999) 1135.

- [95] L. Laffont, C. Delacourt, P. Gibot, M.Y. Wu, P. Kooyman, C. Masquelier, J.M. Tarascon, *Chem. Mater.* 18 (2006) 5520.
- [96] J.L. Allen, T.R. Jow, J. Wolfenstine, *J. Solid State Electrochem.* 12 (2008) 1031.
- [97] Y. Zhu, J. Wang, Y. Liu, X. Liu, *Adv. Mater.* 25 (2013) 5461.
- [98] B. Orvananos, R. Malik, H.C. Yu, A. Abdellahi, C.P. Grey, G. Ceder, K. Thornton, *Electrochim. Acta* 137 (2014) 245.
- [99] Y. Orikasa, T. Maeda, Y. Koyama, H. Murayama, K. Fukuda, H. Tanida, H. Arai, E. Matsubara, Y. Uchimoto, Z. Ogumi, *J. Am. Chem. Soc.* 135 (2013) 5497.
- [100] Y. Orikasa, T. Maeda, Y. Koyama, H. Murayama, K. Fukuda, H. Tanida, H. Arai, E. Matsubara, Y. Uchimoto, Z. Ogumi, *Chem. Mater.* 25 (2013) 1032.
- [101] C. Fongy, A.-C. Gaillot, S. Jouanneau, D. Guyomard, B. Lestriez, *J. Electrochem. Soc.* 157 (2010) A885.
- [102] G. Ouvrard, M. Zerrouki, P. Soudan, B. Lestriez, C. Masquelier, M. Morcrette, S. Hamelet, S. Belin, A.M. Flank, F. Baudalet, *J. Power Sources* 229 (2013) 16.
- [103] N.C. Popa, *J. Appl. Crystallogr.* 25 (1992) 611.
- [104] B.E. Warren, *X-Ray Diffraction*, Addison-Wesley, Reading, Mass., 1969.
- [105] P.S. Rudman, *Acta Crystallogr.* 13 (1960) 905.
- [106] A.L. Goodwin, M. Calleja, M.J. Conterio, M.T. Dove, J.S.O. Evans, D.A. Keen, L. Peters, M.G. Tucker, *Science* 319 (2008) 794.
- [107] G. Barsch, J. Krumhansl, *Phys. Rev. Lett.* 53 (1984) 1069.
- [108] J.W. Cahn, J.E. Hilliard, *J. Chem. Phys.* 28 (1958) 258.
- [109] C. Delacourt, P. Poizot, J.-M. Tarascon, C. Masquelier, *Nat. Mater.* 4 (2005) 254.
- [110] W.C. Chueh, F. El Gabaly, J.D. Sugar, N.C. Bartelt, A.H. McDaniel, K.R. Fenton, K.R. Zavadil, T. Tyliczszak, W. Lai, K.F. McCarty, *Nano Lett.* 13 (2013) 866.
- [111] J.D. Sugar, F. El Gabaly, W.C. Chueh, K.R. Fenton, T. Tyliczszak, P.G. Kotula, N.C. Bartelt, *J. Power Sources* 246 (2014) 512.
- [112] B. Orvananos, H. Yu, R. Malik, C.P. Grey, G. Ceder, K. Thornton, in:., 224th ECS Meet., 2013.

- [113] M. Wagemaker, G.J. Kearley, A.A. Van Well, H. Mutka, F.M. Mulder, *J. Am. Chem. Soc.* 125 (2003) 840.
- [114] D. Murphy, R. Cava, S. Zahurak, A. Santoro, *Solid State Ionics* 9-10 (1983) 413.
- [115] A.A. Belak, Y. Wang, A. Van Der Ven, *Chem. Mater.* (2012).
- [116] W.J.H. Borghols, D. Lützenkirchen-Hecht, U. Haake, E.R.H. van Eck, F.M. Mulder, M. Wagemaker, *Phys. Chem. Chem. Phys.* 11 (2009) 5742.
- [117] M. Wagemaker, W.J.H. Borghols, F.M. Mulder, *J. Am. Chem. Soc.* 129 (2007) 4323.
- [118] T. Ohzuku, T. Kodama, T. Hirai, *J. Power Sources* 14 (1985) 153.
- [119] K. Shen, H. Chen, F. Klaver, F.M. Mulder, M. Wagemaker, *Chem. Mater.* 26 (2014) 1608.
- [120] M. Wagemaker, F.M. Mulder, *Acc. Chem. Res.* 46 (2013) 1206.
- [121] X.P. Gao, Y. Lan, H.Y. Zhu, J.W. Liu, Y.P. Ge, F. Wu, D.Y. Song, *Electrochem. Solid-State Lett.* 8 (2005) A26.
- [122] G. Sudant, E. Baudrin, D. Larcher, J.-M. Tarascon, *J. Mater. Chem.* (2005) 1263.
- [123] Y.-G. Guo, Y.-S. Hu, J. Maier, *Chem. Commun. (Camb.)* (2006) 2783.
- [124] J.S. Chen, Y.L. Tan, C.M. Li, Y.L. Cheah, D. Luan, S. Madhavi, F.Y.C. Boey, L.A. Archer, X.W. Lou, *J. Am. Chem. Soc.* 132 (2010) 6124.
- [125] X. Zhang, M. van Hulzen, D.P. Singh, A. Brownrigg, J.P. Wright, N.H. van Dijk, M. Wagemaker, *Nano Lett.* (2014).
- [126] B. Orvananos, H.-C. Yu, A. Abdellahi, R. Malik, C.P. Grey, G. Ceder, K. Thornton, *J. Electrochem. Soc.* 162 (2015) A965.
- [127] J. Barker, R.K.B. Gover, P. Burns, A. Bryan, M.Y. Saidi, J.L. Swoyer, *J. Power Sources* 146 (2005) 516.
- [128] J. Barker, M.Y. Saidi, J.L. Swoyer, *J. Electrochem. Soc.* 150 (2003) A1394.
- [129] J.-M.A. Mba, L. Croguennec, N.I. Basir, J. Barker, C. Masquelier, *J. Electrochem. Soc.* 159 (2012) A1171.
- [130] J.-M.A. Mba, C. Masquelier, E. Suard, L. Croguennec, *Chem. Mater.* 24 (2012) 1223.

- [131] B.L. Ellis, T.N. Ramesh, L.J.M. Davis, G.R. Goward, L.F. Nazar, *Chem. Mater.* 23 (2011) 5138.
- [132] M. Cuisinier, N. Dupré, J.F. Martin, R. Kanno, D. Guyomard, *J. Power Sources* 224 (2013) 50.
- [133] H. Liu, F.C. Strobridge, O.J. Borkiewicz, K.M. Wiaderek, K.W. Chapman, P.J. Chupas, C.P. Grey, *Science* 344 (2014) 1252817.
- [134] M. Tang, H.Y. Huang, N. Meethong, Y.H. Kao, W.C. Carter, Y.M. Chiang, *Chem. Mater.* 21 (2009) 1557.
- [135] O.J. Borkiewicz, K.M. Wiaderek, P.J. Chupas, K.W. Chapman, *J. Phys. Chem. Lett.* 6 (2015) 2081.
- [136] E. Salje, V. Devarajan, *Phase Transit.* 6 (1986) 235.
- [137] A. Singer, A. Ulvestad, H. Cho, J.W. Kim, J. Maser, R. Harder, Y.S. Meng, O.G. Shpyrko, *Nano Lett.* 14 (2014) 5295.